Title
Integration of Sorption Enhanced Operations into Sustainable Processes

Author
Alturki, Abdulaziz Ali

Publication Date
2020

Peer reviewed|Thesis/dissertation

UNIVERSITY OF CALIFORNIA

Los Angeles

Integration of Sorption Enhanced Operations into Sustainable Processes

A dissertation submitted in partial satisfaction of the

requirements for the degree of Doctor of Philosophy

in Chemical Engineering

by

Abdulaziz Ali Alturki

2020

ABSTRACT OF THE DISSERTATION

Integration of Sorption Enhanced Operations into Sustainable Processes

by

Abdulaziz Ali Alturki

Doctor of Philosophy in Chemical Engineering

University of California, Los Angeles, 2020

Professor Dante A. Simonetti, Chair

Stabilizing atmospheric concentrations of CO_2 has become a significant focus worldwide as environmental concern continues to increase and carbon-based fuel sources continue to play a significant role in energy generation. For this reason, mitigation actions are needed to stabilize the atmospheric CO_2 concentration at 500 parts per million. The International Energy Agency has suggested the use of carbon-neutral renewable energy sources such as biomass, carbon-free sources such as hydrogen, and carbon capture and storage as effective CO_2 reduction methods. These technologies have the potential to reduce anthropogenic CO_2 during the transition towards a low-carbon energy system. This study focused on discovering a combination of these approaches that uses innovative sorption processes to achieve lower overall carbon emissions. The objectives of this work were to study the fundamental structure–function relationships for organic and inorganic synthetic materials in sorption application systems and analyze the common characteristics shared between adsorption, absorption, and ion exchange for the extraction of molecules and ions from aqueous solutions. The research also investigated applying sorption

operations in sustainable processes to improve efficiency, reduce energy, and subsequently, reduce costs through process intensification by inducing reactions simultaneously with separation. The merit of this process is attributed to efficient energy and material utilization.

The dissertation of Abdulaziz Ali Alturki is approved.

Panagiotis D. Christofides

Vasilios Manousiouthakis

Louis Bouchard

Dante A. Simonetti, Committee Chair

University of California, Los Angeles

2020

Table of Contents

List of Figures

List of Tables

Acknowledgments

I am thankful to everyone who supported me in my educational journey towards this degree. I want to take this opportunity to express my gratitude to the people who helped me complete this thesis. Many people have helped me with this research. I would like to express my gratitude Prof. Dante Simonetti, my graduate advisor, for his patience, guidance, support, and motivation, which have shaped me into the researcher I am today. I am very thankful for the countless hours he has spent with me. His patience and indulgence have given me ample time and space to mature not only as a researcher but also as an individual. I will always have pride in my heart knowing that I was a member of Dante Simonetti's research group.

Besides my advisor, I would like to thank my thesis committee members: Prof. Vasilios I. Manousiouthakis Prof. Louis Bouchard and Prof. Panagiotis Christofides, for their encouragement and insightful comments.

Most of all, I am grateful to my wife for her everlasting love and support. Because of her, I was able to focus on my research and finish this project. I would like to thank my family for their continued support and encouragement during my time as a graduate student. Thank you for giving me the strength to reach for the stars and chase my dreams. Thanks to my father, who motivated me always to pursue my desires. I am grateful to you for guiding me to achieve new heights and all your words that gave me a viewpoint and lessons which no books can teach me. Mom, I feel so honored and blessed to have you in my life. Thank you for being the kind, loving, and caring mom that you are. I would like to thank my older sister, and younger brothers for their help, love and support.

I would also like to thank my friends in the Simonetti Research Group. I have had a delightful time and shared many experiences with them. I will always cherish my memories with them.

Finally, I would like to thank Saudi Arabian Cultural Mission for the financial support during my education.

Chapter 2 is version of: Abdulaziz Alturki and Dante Simonetti. Oxygenate Adsorption onto Hydrophilic Zeolites from Aqueous Solution. In preparation.

Chapter 3 is version of: Abdulaziz Alturki and Dante Simonetti. Efficient Hydrogen Production from N-butanol Steam Reforming Obtained from ABE Fermentation Using RD. In preparation.

Chapter 4 is version of: Alturki, A., Callagon La Plante, E., Simonetti, D.; Sant, G. Sensitivity Analysis of an Intensified CO_2 Mineralization and RO Desalination Process in Ca^{2+}-/Mg^{2+}-Rich Aqueous Solutions. In preparation.

Some of the work in chapter 5 is a version in preparation for submission [Bustillos, S., Alturki, A., Prentice, D., Callagon La Plante, E., Rogers, M., Keller, M., Simonetti, D., Sant, G. Implementation of ion exchange processes on industrial waste streams for CO_2 mineralization. Low-Carbon Technologies for Petroleum Industries. 2019, In Preparation for Submission.]. A. Alturki wrote this chapter. A. Alturki and S. Bustillos performed varies experiments. A. Alturki and S. Bustillos analyzed the data and will write the manuscript. G. Sant and D. Simonetti are the PIs. The financial support for this chapter's research from the Department of Energy (DOE) is acknowledged by authors (DE- FE0031705).

Vita

2012	School of Chemical Engineering and Process Engineering
	University of Leeds, United Kingdom
	Bachelor of Engineering in Chemical Engineering
2012-2015	Process Engineer,
	Saudi Aramco
	Dhahran, Saudi Arabia
2017	Department of Chemical and Biomolecular Engineering
	University of California, Los Angeles
	Master of Science in Chemical Engineering

Publications and Presentations

Alturki, A. and Simonetti, D. Fundamentals of Competitive Adsorption Phenomena within Dilute, Multi-Component Aqueous Mixtures. In AIChE Annual Meeting, paper 458c, Minneapolis, MN; 2017.

Alturki, A. Bustillos, S Callagon La Plante, E. Simonetti, D. and Sant G. Implementation of Ion Exchange Processes on Industrial Waste Streams for CO_2 Mineralization. In AIChE Annual Meeting, paper 90c, Orlando, FL; 2019.

Bustillos, S., Alturki, A., Prentice, D., Callagon La Plante, E., Rogers, M., Keller, M., Simonetti, D., Sant, G. Implementation of ion exchange processes on industrial waste streams for CO_2 mineralization. Low-Carbon Technologies for Petroleum Industries. 2019, In Preparation for Submission.

Callagon La Plante, E., Simonetti, D., Wang, J., Alturki, A., Chen, X., Sant, G (2020). A saline-water based mineralization pathway for gigatonne-scale CO_2 management. Submitted to Joule Journal.

Alturki, A., Callagon La Plante, E., Simonetti, D.; Sant, G. Sensitivity Analysis of an Intensified CO_2 Mineralization and RO Desalination Process in Ca^{2+}-/Mg^{2+}-Rich Aqueous Solutions. AIChE Journal, In Preparation for Submission.

Chapter 1: Introduction

1.1 Motivation

Over the last two decades, population growth and economic development have resulted in increased energy demand. Living standard improvements have also heightened the need for energy.[1] Sustainable energy meets the present generation's energy demand without endangering the environment and compromising future generations' ability to meet their own needs. Concerns regarding the sustainability of current methods of energy use and production center on several areas: the depletion of nonrenewable resources, the effect of emissions on the global environment, and global instability in supply security.[2] The world's population is still growing rapidly. A move toward less environmentally harmful energy production is possible, and efficiency can be used to lower the CO_2 output per energy unit through developing economic CO_2 capture technologies that enable facilities powered by carbon-based fuels to operate but emit less CO_2 emissions.[3]

Sustainable development requires clean, convenient, and effective energy to lift billions of people out of poverty to better standards of living. However, substantial work remains to be done to make carbon-based fuel sources (i.e., coal, oil, and gas) more sustainable and more efficient, with less CO_2 emissions. Many hope for the development of renewable and new forms of energy that emit less CO_2, but realization of this hope may not come rapidly enough or be affordable enough to allow billions of people to achieve the standard of living they want and deserve. Thus, we must develop a parallel path to sustainability that entails use of both renewable and clean carbon-based fuel sources for generations to come and the expanded use of oil and gas as sources of advanced materials in addition to their use as fuels. Sustainability will play a major role in the future of energy.

1.2 Introduction and Methodology

The anthropogenic emission of CO_2, which mainly results from fossil fuel combustion, contributes to CO_2 accumulating in the atmosphere. In 2004, global CO_2 emissions totaled 27.4 Gt, and this figure increased dramatically to 33.4 Gt in 2016. Despite significant efforts to develop a renewable energy–based system, carbon-based fuel sources remain the dominant global energy provider, accounting for 82.2% of the 598 quadrillion BTUs produced in 2018. As the global economy and population expand, global demand for energy is expected to grow dramatically over the next 30 years. Energy demand is expected to increase by 40% at a rate of 1.5% per year from 2020 to 2030. The recent increase in global energy demand has been met mostly through increased fossil fuel use, resulting in a higher concentration of CO_2 in the atmosphere. As a result, the International Energy Agency (IEA) has proposed measures to remove 10–20 Gt of CO_2 per year to meet the 2 °C global temperature target.[4] They have suggested using carbon capture and storage, carbon-neutral renewable energy sources, such as biomass, and carbon-free sources, such as hydrogen, as key methods to achieve substantial reductions in CO_2 emissions. These technologies can potentially reduce anthropogenic CO_2 as part of the transition to a low-carbon energy system. These are discussed separately in turn in the following paragraphs.[5,6]

First, the massive variety of carbon capture and storage suggests that a combination of techniques would be the most practical approach.[7] Amine-based regeneration using an aqueous amine solution, such as monoethanolamine (MEA), has been widely used for several years to capture CO_2 from gas streams in natural gas, flue gas, refinery off-gases, and synthesis gas (syngas) handling.[8–13] The state-of-the-art process uses 20–30% wt % aqueous MEA to capture CO_2 and form carbamates. Although it has been commercialized in various industries, carbon capture and sequestration (CCS) is not a market-driven technology, and capture cost needs to be reduced to

facilitate adoption of CCS. The most critical challenge to the amine process remains the high energy demand to heat the solution for regeneration. The process is highly energy intensive.[14–16] Alternatively, when geological sequestration is not a viable option, these drawbacks can be overcome through mineral carbonation, which has emerged as a potential carbon capture, utilization, and storage technology solution to sequester CO_2 from medium-size emitters. These processes offer a leakage-free alternative to the geological storage of CO_2 in an environmentally friendly form that is accomplished through a procedure that requires minimal effort to monitor (Figure 1.1). In this process, CO_2 reacts chemically with materials that contain sodium, calcium, and magnesium to form stable carbonates.[17] The mineralized carbon can then be disposed of at the Earth's surface. The large carbon storage capacity, minimal environmental impact, and low risk of later CO_2 release suggest the viability of the proposed scheme as a primary means of long-term Gt-scale CO_2 waste management. The assessment of operating fossil fuel plants with carbon capture using two innovative technologies is based on advanced sorbents (ion exchange using zeolite or resin) as well as on the sodium hydroxide produced by electrolysis. The application of the two processes has been investigated for power plant flue gas and enhanced steam reforming technologies.

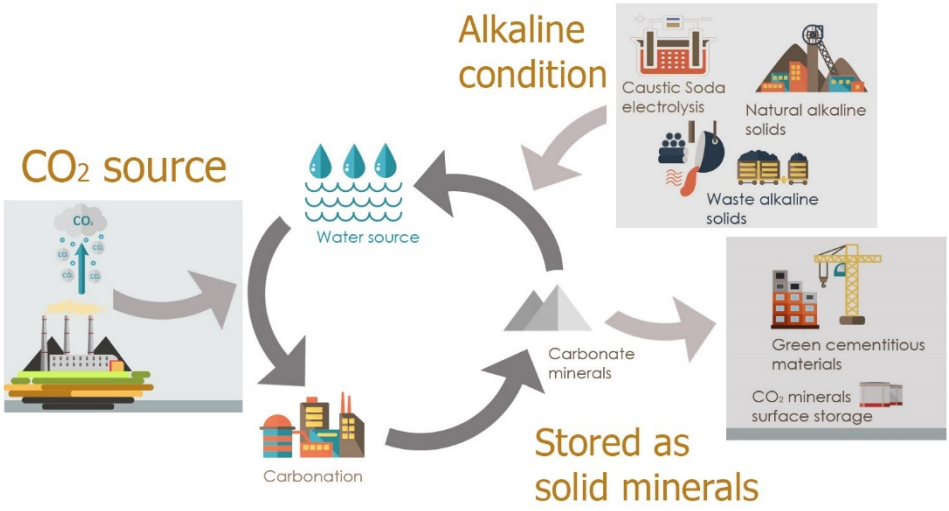

Figure 1.1. Using mineral carbonation technology to sequester CO_2 from medium size emitters by chemically reacting CO_2 with sodium-, calcium-, and magnesium-containing materials to form stable carbonates.

The second method to reduce CO_2 emissions involves biomass, which is a renewable energy source and does not contribute to CO_2 emissions as long as reforestation exceeds consumption. Using biofuels may lead to a more neutral carbon cycle, may eventually reduce net CO_2 emissions,[18] and represents a potential means by which to source liquid fuel from local biomass production. To achieve this goal, many biological processes have recently been designed for converting biomass into oxygenated molecules that can be used for fuels and chemicals. The main disadvantage of these products is that they are typically formed as a dilute aqueous solution. Adsorption using porous material is crucial in extracting these molecules and understanding how adsorption functions can assist in characterizing and rationally designing adsorbent/catalyst properties. Existing adsorption separation techniques entail high energy consumption but are still

the most economical option.[19] Integrating separation with an additional reaction process (an intensified process) to generate more valuable products is a highly attractive method that improves efficiency and reduces costs. Process intensification based on these combinations costs less because reactions induced simultaneously with separation.[20,21] This process is beneficial because of its efficient energy and material utilization.

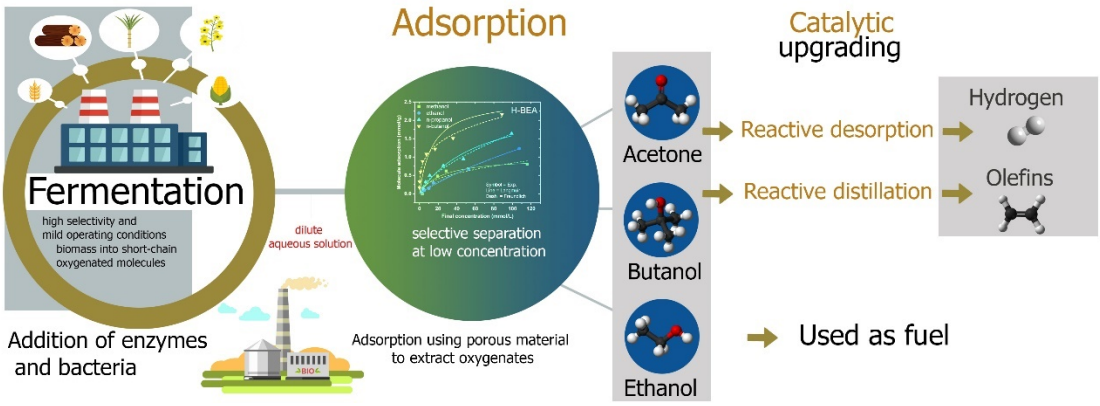

Figure 1.2. Biomass energy cycle of using adsorptive zeolitic materials and the integration potential of these materials during the desorption step.

Finally, from an energy transition perspective, natural gas can provide near-term benefits when it replaces more highly polluting fuels. Hydrogen produced from natural gas using conventional technologies such as steam methane reforming (SMR) is a clean and promising energy carrier for power generation and transportation fuel. However, carbon from this process is converted into CO_2 and released into the atmosphere. Thus, CCS is an option that could provide a near-term solution for handling greenhouse gas emissions. Calcium oxide, sodium hydroxide, and ion exchange (H^+ with Na^+) are promising acceptors of CO_2 due to the influence of carbonation on the thermodynamic equilibrium of the reforming process. The continuous withdrawal of CO_2 at the generation point shifts the equilibrium of the SMR and water–gas shift (WGS) to the right,

thus increasing the overall hydrogen yield. In addition to hydrogen generation, syngas is essential in the current and future energy mix due to its applications in the production of the chemicals such as ammonia, urea, methanol, and ethanol, among others.[22] Shale gas can be monetized through a variety of means, including the physical and chemical conversion of it to produce energy and chemicals.[23] Furthermore, the expansion of generation from wind and photovoltaic (PV) systems is predicted to help renewable energy overtake coal and natural gas in the power-generation mix by 2040. The sinking cost of renewable energy is creating opportunities for energy transitions, with wind and PV predicted to account for more than half of the electricity generation in the United States by 2040.[24] The United States has the advantage of an abundant natural gas supply, which is exploitable at low cost, as a result of the shale gas revolution.[24] Therefore, the use of natural gas and coal in the petrochemical industry provides a major opportunity to contain carbon within newly formed molecules. Consequently, value-added chemicals are provided from natural gas, and the release of CO_2 into the atmosphere is avoided. The use of methane gas in the production of olefins and other chemicals has strong potential to be a game changer in the chemical industry. A number of researchers have attempted to develop a cost-effective integrated methane-to-chemical process through syngas production.[25–27] Once syngas is produced, it can be transformed into numerous intermediates and products. Examples of chemicals that can be transformed into products include methanol,[28,29] ethylene,[30] propylene,[31] benzene,[32] and liquid transportation fuels.[33]

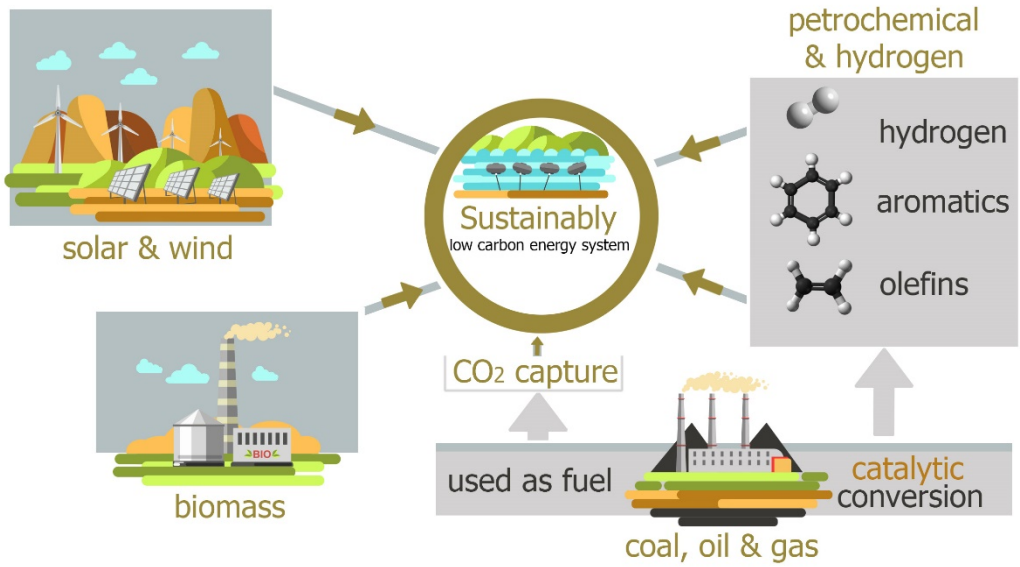

Figure 1.3. Representation of the sustainable energy system**.**

1.3 Research Objectives

The overall objective of this research was to investigate the potential use of sorption applications (absorption, adsorption, and ion exchange) to reduce CO_2 emissions using hybrid processes. Recent research has revealed some challenges to reducing anthropogenic CO_2 as the world seeks to shift to a low-carbon approach to energy production. These challenges are summarized as follows:

- A fundamental understanding of adsorption behavior in various types of adsorbents with various pore structures and multicomponent molecules is lacking.[34,35,44–46,36–43]
- Developing separation processes such as adsorption is challenging because of low production yield and high energy use.[47] In recent years, the combination of separation and reaction inside a single unit has become popular. Process intensification based on these combinations has been recognized as economically favorable because simultaneous reactions are carried out with separation.[20,21]

- It is difficult to control the alkalinity of the aqueous solution to enhance adsorption and other chemical systems such as calcium carbonate precipitation.[48–52]
- High energy costs are associated with the difficulty in capturing and storing CO_2. The most significant challenge to the amine process remains the high energy demand to heat the solution for regeneration. The process is highly energy intensive.[14–16]

This dissertation comprises seven chapters, with the current chapter being an introduction to the motivation for the research. Chapter 2 discusses experiments undertaken to investigate how the structure of zeolite influences the selectivity and adsorption capacity of oxygenates. The objective of this study was to investigate the major factors which influence of solid adsorbent materials performance in the removal of shorter-chain oxygenated molecules from aqueous solutions that comprise a variety of molecules, comparable to compositions obtained from fermentation processes. Zeolites with various Si/Al ratios were used to examine the thermodynamic, kinetic, and molecular sieve effects over a range of aqueous solution concentrations.

Chapter 3 further explores the use of zeolites for hybrid process separation and reaction using innovative reactive desorption. Results of the exploration is used to compare the benefits of CO_2 avoidance to obtain carbon-free sources such as hydrogen from carbon-neutral renewable energy sources. This study integrated n-butanol steam reforming and adsorption–desorption into a single process to enhance the efficiency of n-butanol adsorption from acetone–butanol–ethanol (ABE) and hydrogen production. The reactive desorption (RD) process optimizes the use of desorption energy to generate more valuable products and minimize the downstream processes needed to separate the hot steam from the desorbed components. This results in several

advantageous outcomes, such as an increase in reaction yield and selectivity, that overcome thermodynamic restrictions and reduce energy consumption.

Chapter 4 introduces the CO_2 mineralization approach as an alternative to CCS. Various correlation combinations are examined and validated for the thermodynamic model and the calculation of the physical properties of the MEA-H_2O-CO_2 mixture and compared with NaOH-H_2O-CO_2 and $Ca(OH)_2$-H_2O-CO_2 mixtures. Integrating CO_2 mineralization and reverse osmosis (RO) desalination pretreatment into a single process to enhance the efficiency and energy utilization of CO_2 capture is proposed. This study additionally proposes a calcium and magnesium production process that involves injecting low-concentration CO_2 (8–15 vol %) from flue gas into a carbonation process in a desalination plant. Feasibility of the overall process is analyzed through calculating the energy required for standalone desalination pretreatment and CO_2 mineralization processes compared with the hybrid process.

Chapter 5 studies the mechanism of aqueous CO_2 carbonation using the ion-exchange process. The ion-exchange capacity of several zeolites and ion-exchange resins in CO_2-saturated water was studied through batch equilibrium and column ion-exchange experiments. The analysis of solution-phase concentration and solid phases and the rate of exchange of Na^+ for H^+ were studied across a range of temperatures, solution compositions, and solution conditions (e.g., static and convectively mixed).

Chapter 6 describes the application of the CO_2 mineralization concept for enhancing the methane-reforming process and producing carbon-free H_2. The enhanced sorption steam methane process, through CO_2 mineralization, combines reaction and separation into one unit based on Le Chatelier's principle. This produces two clean products: hydrogen and calcium carbonate.

Chapter 7 presents a novel process design for converting methane into value-added chemicals with minimum carbon dioxide emissions. This work introduces the consideration of different gas-reforming technologies for methanol, such as partial oxidation (POX), SMR, autothermal reforming (ATR), and combined reforming (CR). Additionally, single-step natural gas conversion processes into olefins and higher hydrocarbons are considered. We developed a flexible approach to evaluate various technologies systematically, determine the appropriate process for converting methane into ethylene, and perform energy and economic analysis. For each reformer, specific inputs and operating conditions are analyzed to determine the syngas composition. The appropriate reformer is defined as one that can achieve the input and operating conditions' objectives.

1.4 References

1. Owusu, P. A. & Asumadu-Sarkodie, S. A review of renewable energy sources, sustainability issues and climate change mitigation. *Cogent Eng.* **3**, 1167990 (2016).

2. Tester, J. W., Drake, E. M., Driscoll, M. J., Golay, M. W. & Peters, W. A. *Sustainable Energy: Choosing Among Options*. (MIT Press, 2012).

3. MacKenzie, A., Granatstein, D. L., Anthony, E. J. & Abanades, J. C. Economics of CO2 Capture Using the Calcium Cycle with a Pressurized Fluidized Bed Combustor. *Energy & Fuels* **21**, 920–926 (2007).

4. International Energy Agency. Towards Susteinable Urban Energy Systems. 14 (2016). doi:10.1787/energy_tech-2014-en

5. Buhre, B. J. P., Elliott, L. K., Sheng, C. D., Gupta, R. P. & Wall, T. F. Oxy-fuel combustion technology for coal-fired power generation. *Prog. energy Combust. Sci.* **31**, 283–307 (2005).

6. Cabral, R. P. & Mac Dowell, N. A novel methodological approach for achieving £/MWh cost reduction of CO2 capture and storage (CCS) processes. *Appl. Energy* **205**, 529–539 (2017).

7. Pogge von Strandmann, P. A. E. *et al.* Rapid CO2 mineralisation into calcite at the CarbFix storage site quantified using calcium isotopes. *Nat. Commun.* **10**, 1983 (2019).

8. Sharma, M. M. Kinetics of reactions of carbonyl sulphide and carbon dioxide with amines and catalysis by Brönsted bases of the hydrolysis of COS. *Trans. Faraday Soc.* **61**, 681–688 (1965).

9. Vaidya, P. D. & Kenig, E. Y. CO2-Alkanolamine Reaction Kinetics: A Review of Recent Studies. *Chem. Eng. Technol.* **30**, 1467–1474 (2007).

10. Sartori, G. & Savage, D. W. Process for removing acid gases with hindered amines and amino acids. (1978).

11. Versteeg, G. F. & van Swaaij, W. P. M. On the kinetics between CO2 and alkanolamines both in aqueous and non-aqueous solutions—I. Primary and secondary amines. *Chem. Eng. Sci.* **43**, 573–585 (1988).

12. Freguia, S. & Rochelle, G. T. Modeling of CO2 capture by aqueous monoethanolamine. *AIChE J.* **49**, 1676–1686 (2003).

13. Dang, H. & Rochelle, G. T. CO2 absorption rate and solubility in monoethanolamine/piperazine/water. *Sep. Sci. Technol.* **38**, 337–357 (2003).

14. Audus, H. Greenhouse gas mitigation technology: An overview of the CO2 capture and sequestration studies and further activities of the IEA Greenhouse Gas R&D Programme. *Energy* **22**, 217–221 (1997).

15. Reiner, P., Audus, H. & Smith, A. R. Carbon dioxide capture from fossil fuel power plants, Report SR2, IEA Greenhouse Gas R&D Programme. (1994).

16. Meisen, A. & Shuai, X. Research and development issues in CO2 capture. *Energy Convers. Manag.* **38**, S37–S42 (1997).

17. Seifritz, W. CO2 disposal by means of silicates. *Nature* **345**, 486 (1990).

18. Hanaki, K. & Portugal-Pereira, J. The Effect of Biofuel Production on Greenhouse Gas Emission Reductions. in (eds. Takeuchi, K., Shiroyama, H., Saito, O. & Matsuura, M.) 53–

71 (Springer Japan, 2018). doi:10.1007/978-4-431-54895-9_6

19. Qureshi, N., Hughes, S., Maddox, I. S. & Cotta, M. A. Energy-efficient recovery of butanol from model solutions and fermentation broth by adsorption. *Bioprocess Biosyst. Eng.* **27**, 215–222 (2005).

20. Noeres, C., Kenig, E. Y. & Górak, A. Modelling of reactive separation processes: reactive absorption and reactive distillation. *Chem. Eng. Process. Process Intensif.* **42**, 157–178 (2003).

21. Agar, D. W. Multifunctional reactors: Old preconceptions and new dimensions. *Chem. Eng. Sci.* **54**, 1299–1305 (1999).

22. Claude, V., Courson, C., Köhler, M. & Lambert, S. D. Overview and Essentials of Biomass Gasification Technologies and Their Catalytic Cleaning Methods. *Energy & Fuels* **30**, 8791–8814 (2016).

23. Al-Douri, A., Sengupta, D. & El-Halwagi, M. M. Shale gas monetization – A review of downstream processing to chemicals and fuels. *J. Nat. Gas Sci. Eng.* **45**, 436–455 (2017).

24. *World Energy Outlook 2019*. (OECD, 2019). doi:10.1787/caf32f3b-en

25. Martinez-Gomez, J. *et al.* Involving economic, environmental and safety issues in the optimal purification of biobutanol. *Process Saf. Environ. Prot.* **103**, 365–376 (2016).

26. Noureldin, M. M. B., Elbashir, N. O., Gabriel, K. J. & El-Halwagi, M. M. A process integration approach to the assessment of CO2 fixation through dry reforming. *ACS Sustain. Chem. Eng.* **3**, 625–636 (2015).

27. Gabriel, K. J. *et al.* Targeting of the water-energy nexus in gas-to-liquid processes: A

comparison of syngas technologies. *Ind. Eng. Chem. Res.* **53**, 7087–7102 (2014).

28. Ehlinger, V. M., Gabriel, K. J., Noureldin, M. M. B. & El-Halwagi, M. M. Process design and integration of shale gas to methanol. *ACS Sustain. Chem. Eng.* **2**, 30–37 (2014).

29. Julián-Durán, L. M., Ortiz-Espinoza, A. P., El-Halwagi, M. M. & Jiménez-Gutiérrez, A. Techno-economic assessment and environmental impact of shale gas alternatives to methanol. *ACS Sustain. Chem. Eng.* **2**, 2338–2344 (2014).

30. Ortiz-Espinoza, A. P., Noureldin, M. M. B., El-Halwagi, M. M. & Jiménez-Gutiérrez, A. Design, simulation and techno-economic analysis of two processes for the conversion of shale gas to ethylene. *Comput. Chem. Eng.* **107**, 237–246 (2017).

31. Jasper, S. & El-Halwagi, M. A techno-economic comparison between two methanol-to-propylene processes. *Processes* **3**, 684–698 (2015).

32. Pérez-Uresti, S. I., Adrián-Mendiola, J. M., El-Halwagi, M. M. & Jiménez-Gutiérrez, A. Techno-economic assessment of benzene production from shale gas. *Processes* **5**, 33 (2017).

33. Bao, B., El-Halwagi, M. M. & Elbashir, N. O. Simulation, integration, and economic analysis of gas-to-liquid processes. *Fuel Process. Technol.* **91**, 703–713 (2010).

34. Mallon, E. E. *et al.* Correlations for adsorption of oxygenates onto zeolites from aqueous solutions. *J. Phys. Chem. B* **115**, 11431–11438 (2011).

35. Goerlitz, R. *et al.* Bio-butanol downstream processing: regeneration of adsorbents and selective exclusion of fermentation by-products. *Adsorption* **24**, 95–104 (2018).

36. Raganati, F. *et al.* Bio-butanol separation by adsorption on various materials: Assessment

of isotherms and effects of other ABE-fermentation compounds. *Sep. Purif. Technol.* **191**, 328–339 (2018).

37. Van der Perre, S. *et al.* Intensified Biobutanol Recovery by using Zeolites with Complementary Selectivity. *ChemSusChem* **10**, 2968–2977 (2017).

38. Nguyen, C. M., Reyniers, M. F. & Marin, G. B. Adsorption thermodynamics of C1-C4 alcohols in H-FAU, H-MOR, H-ZSM-5, and H-ZSM-22. *J. Catal.* **322**, 91–103 (2015).

39. Nguyen, C. M., Reyniers, M. F. & Marin, G. B. Theoretical study of the adsorption of C1-C4 primary alcohols in H-ZSM-5. *Phys. Chem. Chem. Phys.* **12**, 9481–9493 (2010).

40. Van Der Mynsbrugge, J., Hemelsoet, K., Vandichel, M., Waroquier, M. & Van Speybroeck, V. Efficient approach for the computational study of alcohol and nitrile adsorption in H-ZSM-5. *J. Phys. Chem. C* **116**, 5499–5508 (2012).

41. Milestone, N. B. & Bibby, D. M. Adsorption of alcohols from aqueous solution by ZSM-5. *J. Chem. Technol. Biotechnol. Chem. Technol.* **34**, 73–79 (1984).

42. Milestone, N. B. & Bibby, D. M. Concentration of alcohols by adsorption on silicalite. *J. Chem. Technol. Biotechnol.* **31**, 732–736 (1981).

43. Mallon, E. E., Bhan, A. & Tsapatsis, M. Driving forces for adsorption of polyols onto zeolites from aqueous solutions. *J. Phys. Chem. B* **114**, 1939–1945 (2010).

44. Mallon, E. E. Aqueous solution and vapor phase adsorption of oxygenates onto zeolites. (2012).

45. Stückenschneider, K., Merz, J. & Schembecker, G. Molecular interactions of alcohols with zeolite BEA and MOR frameworks. *J. Mol. Model.* **19**, 5611–5624 (2013).

46. Remy, T. *et al.* Adsorption and Separation of C1−C8 Alcohols on SAPO-34. *J. Phys. Chem. C* **115**, 8117–8125 (2011).

47. Ezeji, T. C., Qureshi, N. & Blaschek, H. P. Butanol fermentation research: Upstream and downstream manipulations. *Chem. Rec.* **4**, 305–314 (2004).

48. Sanna, A., Uibu, M., Caramanna, G., Kuusik, R. & Maroto-Valer, M. M. A review of mineral carbonation technologies to sequester CO2. *Chem. Soc. Rev.* **43**, 8049–8080 (2014).

49. Jones, J. D. Removing carbon dioxide from waste streams through co-generation of carbonate and/or bicarbonate minerals. (2005).

50. Klein, A. R., Baldwin, D. S., Singh, B. & Silvester, E. J. Salinity-induced acidification in a wetland sediment through the displacement of clay-bound iron(II). *Environ. Chem.* **7**, 413–421 (2010).

51. Avena, M. J. & De Pauli, C. P. Proton adsorption and electrokinetics of an Argentinean montmorillonite. *J. Colloid Interface Sci.* **202**, 195–204 (1998).

52. Robin, V. *et al.* Ion exchange reactions of major inorganic cations (H^+, Na^+, Ca^{2+}, Mg^{2+} and K^+) on beidellite: Experimental results and new thermodynamic database. Toward a better prediction of contaminant mobility in. *Appl. Geochemistry* **59**, 74–84 (2015).

Chapter 2: Oxygenate Adsorption onto Hydrophilic Zeolites from Aqueous Solution

2.1 Abstract

We collected adsorption isotherms for alcohols and aldehydes on different types of zeolites to understand the fundamentals of adsorption and apply relevant models. Zeolites with various Si/Al ratios were used to examine the thermodynamic, kinetic, and molecular sieve effects over a range of aqueous solution concentrations. Results showed that longer-chain alcohols such as n-butanol and n-propanol were able to fill the entire pore volume. Binary batch experiments showed preferential adsorption of longer-chain alcohols relative to shorter-chain alcohols allowing selective separation and removal of n-butanol from shorter-chain alcohols to be achieved at room temperature. The equilibrium concentration adsorption profiles of oxygenates were analyzed using two adsorption models: Langmuir and Freundlich for single and multi-component systems.

2.2 Introduction

The importance of biofuel formative production, such as bioethanol and biobutanol, has increased lately due to the increase in global biofuel production coupled with economic interest. In addition to the increase in global biofuel production, this interest has increased because of increasing fossil fuel costs combined with the climate change environmental impacts that face our planet. Using biofuels will lead to a more natural carbon cycle, which will eventually reduce net CO_2 emissions. This offers potential means by which to source liquid fuel from local biomass production.

Adsorption using porous material is an important process to extract oxygenated molecules that are derived from fermentation process and understanding it can assist in the characterization and rational design of adsorbent/catalyst properties. Different factors affect adsorption, such as adsorption capacity, selectivity, affinity, and desorption, which are subject to the adsorbent type. Zeolites play an essential role in catalysis[1–3] and separation[4] due to their excellent adsorption and molecular sieve properties. They are composed of a nonporous crystalline material with a well-defined pore structure. Molecules are adsorbed preferentially on the basis of the amphotericity, hydrophobicity, or hydrophilicity of the zeolite framework.[3,4]

The ability of zeolites to remain stable in severe chemical environments makes them suitable candidates for use as catalysts. Several studies have been performed to extend the principles of hydrocarbon–zeolite chemistry to oxygenate interactions to develop analogous relations between confinement and adsorption thermochemistry for oxygenated molecules.[5–7] Specifically, zeolites were investigated to probe the effects of pore size and channel shape to elucidate the effects of topology on adsorption behavior. Adsorption occurs when the volume of adsorbate is equal or close in size to the adsorbent, and this is defined as the confinement effect.

When the size of the adsorbate approaches the pore diameter of the zeolite, dispersion interactions result between the adsorbate and zeolite, causing stronger adsorption.[5,7]

Recently, significant progress has been made in the adsorption field and in understanding how zeolite properties affect adsorption behaviors. Stückenschneider et al.[8] performed experimental and theoretical studies on alcohol adsorption using BEA and MOR zeolites, and BEA was found to exhibit higher adsorption capacity than MOR, which was attributable to the pore size effect and structure differences between BEA and MOR. Remy et al.[9] studied adsorption of C_1–C_8 alcohols to the SAPO-34 molecular sieve; the study revealed favorable adsorption of shorter-chain alcohols due to the small pore size of theSAPO-34, which excluded larger adsorbates.

Previous studies have focused on the characteristics of zeolite, such as its microporous structure, acidity, and shape selectivity. However, the understanding of zeolite topology influence and adsorbate structure remains limited. Specifically, the nature and stability of oxygenate-zeolite adsorption to Brønsted acid sites remain controversial. Equilibrium adsorption studies of the Henry region have been used to explain hydrocarbon selectivity for processes such as hydrocracking and dewaxing.[10] As it approaches zero coverage, the Henry region is critical to study the intrinsic effects influenced by zeolite topology. Simple thermodynamic analysis of molecule adsorption into the zeolite pore structure could help to guide the identification of product forms and applicability of the zeolite structure for preferred catalytic application.[11]

This study investigated the factors that affect the performance of adsorbent materials extract oxygenated molecules from dilute aqueous. Langmuir and Freundlich adsorption models were applied to develop a understand quantitatively the relationship between the structure of adsorbent and their performance.[1,2]

2.3 Experimental Methods

2.3.1 Materials

Zeolites with small, medium, and large pores with various Si/Al ratios were used to examine the thermodynamic, kinetic, and molecular sieve effects and their consequences on adsorption. The ammonium forms of BEA, MOR, FER, and MFI zeolites were purchased from Zeolyst International (see Table 2.1 for formulas and Si/Al ratios) and converted to the proton forms through treatment in ambient air at 823 K (rate of 0.2 K s^{-1}) for 10 h. H-Y (FAU) zeolite from Zeolyst International was also used.

Table 2.1. Zeolite Framework and Properties.

Zeolite name	Framework	Si/Al	n
BEA	$\lvert H^+_n \rvert\ [Al_nSi_{64-n}\ O_{128}]$-*BEA	12.5	4.74
MFI	$\lvert H^+_n\ (H_2O)_{16} \rvert\ [Al_nSi_{96-n}\ O_{192}]$-MFI	11.5	7.6
FAU	$\lvert H^+_n\ (H_2O)_{240} \rvert\ [Al_{58}Si_{192-n}\ O_{384}]$-FAU	15	12
FAU	$\lvert H^+_n\ (H_2O)_{240} \rvert\ [Al_{58}Si_{192-n}\ O_{384}]$-FAU	2.6	41.2
FER	$\lvert H^+\ (H_2O)_{18} \rvert\ [Al_nSi_{36-n}\ O_{72}]$-FER	10	3.27
MOR	$\lvert H^+_n\ (H_2O)_{24} \rvert\ [Al_nSi_{48}\ O_{96}]$-MOR	10	4.36

Methanol (99.8%, Sigma-Aldrich), ethanol (95%, Sigma-Aldrich), n-propanol (99.7%, Sigma-Aldrich), n-butanol (99.4%, Sigma-Aldrich), n-butyraldehyde (99.5%, Sigma-Aldrich), n-propionaldehyde (99.4%, Sigma-Aldrich), and propanone (99.9%, Sigma-Aldrich) were purchased from Sigma-Aldrich and used as received without additional purification.

2.3.2 Batch Adsorption Equilibria Tests

Adsorption isotherms were collected using 5 mL of 0.003–0.132 M aqueous solutions of methanol, ethanol, n-propanol, n-butanol, n-butyraldehyde, n-propionaldehyde, and propanone. Zeolite samples (0.1–0.5 g) were added to these solutions and shaken periodically until equilibrium

was achieved (24–36 h). The concentration of alcohol(s) in the liquid was measured daily, and equilibrium was indicated by the concentrations remaining constant for more than 12 h. The liquid phase was analyzed through gas chromatography–mass spectrometry (GC-MS; Agilent 5980 GC coupled to 7890 MS; Agilent J&W HP-5 GC Column, 50 m, 0.32 mm, 0.52 μm). The solutions were filtered using a 3-mL Monoject syringe (Cardinal Health) fitted with a 0.2-μm polypropylene filter to remove solids before GC-MS analysis.

Initial and final liquid-phase concentrations, along with solution volumes, were used to calculate the number of molecules adsorbed onto zeolites. Measurements of molecules adsorbed into zeolites were calculated through liquid-phase measurement only. Solid-phase alcohol concentrations were expressed in terms of moles of adsorbate per mass of adsorbent, according to Equation (1).[12]

$$q = (C_e - C_0)V/W \quad (1)$$

where C_0 and C_e represent the initial and equilibrium concentration of adsorbate, respectively (mol/l), V is the volume of the solution, and W is the mass of the adsorbent.

2.3.3 Adsorption Modeling

2.3.3.1 Langmuir Isotherm

The Langmuir model was initially developed to explain gas–solid-phase adsorption in activated carbon[1]:

$$q = \frac{q_{max}K_1c_e}{1+K_1c_e} \quad (2)$$

where

q_{max} is the maximum adsorption capacity (mol/g),

K_1 is a constant related to the free energy of adsorption (L/g), and

C_e is the equilibrium concentration.

The following equation illustrates the forward and backward reactions between the adsorbed molecule (A) and the active site (*) giving the adsorbed species (A*):

$$A + * \underset{K_d}{\overset{K_a}{\rightleftharpoons}} A - * \tag{3}$$

The rate of adsorption is directly proportional to the concentration of adsorbate and the number of vacant sites on the surface, and the sites are assumed to be single and identical.

The rate of the forward reaction is expressed as follows:

$$r_a = K_a \, \mathrm{C} \, (1 - \emptyset) \tag{4}$$

where

r_a is the rate of the forward reaction normalized by the total number of sites,

K_a is the rate constant for the forward reaction (adsorption reaction),

C is the species concentration, and

$\emptyset$ is the fraction of surface sites occupied by the adsorbed molecules, which is represented as

$\emptyset = 1 \; -$ fraction of vacant sites.

The rate of the reverse reaction is as follows:

$$r_d = K_d N \emptyset \quad (5)$$

r_d is the rate of the backward reaction normalized by the total number of sites,

K_d is the rate constant for the reverse reaction (desorption reaction), and

N is the number of total sites.

$$\emptyset = \frac{Number\ of\ adsorption\ sites\ occupied}{Number\ of\ adsorption\ sites\ available} \quad (6)$$

At equilibrium, we have the following:

$$r_a = r_d \quad (7)$$

$$K_a C_e (1 - \emptyset) = K_d N \emptyset \quad (8)$$

where

$$K_1 = \frac{K_a}{K_d} \quad (9)$$

Solving Equation 8 for $\emptyset$ leads to the Langmuir equation:

$$\emptyset = \frac{K_1 C_e}{1 + K_1 e} \quad (10)$$

At a low concentration, $K_1 C_A \ll 1$, and the concentration of adsorbed species is linearly proportional to the bulk-phase concentration.

$$\emptyset = K_1 C_A \quad (11)$$

At a high concentration, $K_1\ C_A \gg 1$, and the fraction of total sites occupied by the adsorbed species approaches unity, where

q_{max} is the maximum adsorption capacity (mol/g),

K_L is a constant related to the free energy of adsorption (L/g), and

C_e is the equilibrium concentration.

2.3.3.2 Langmuir Multicomponent Isotherm

In multicomponent systems, the equilibrium adsorption of one molecule can be affected by the presence of other molecule and can be explained by Langmuir multicomponent isotherm by the following equation:

$$q = \frac{q_{max} K_{\mathrm{L}} C_{\mathrm{e}}}{1+\sum_{j=1}^{N} K_j C_j} \tag{12}$$

where K_j is the Langmuir constant for the second component, and C_j is the equilibrium constant of the second component.

2.3.3.3 Freundlich Isotherm

The Freundlich isotherm is an empirical relation between the solute concentration on the adsorbent surface and the solute concentration in the liquid.[2] As the extent of adsorption varies directly with concentration, the model may show limitations at high concentrations. The equation does not indicate a finite uptake capacity, and thus, it is functional in the low-to-medium concentration ranges. The Freundlich model is the earliest known model to describe nonideal and reversible adsorption. Unlike the Langmuir equation, which is restricted to monolayer coverage,

the Freundlich equation can apply to multilayer adsorption having a nonuniform distribution of adsorption heats and affinities over a heterogeneous surface[13]. The equation is represented as

$$q = K_F \, {C_e}^n \tag{13}$$

where

K and *n* are constants related to the adsorption intensity, and

c_e is the equilibrium constant.

The derivation of this model begins by writing the rate law of the reaction between the adsorbate and active sites:

$$\frac{dC}{dt} = k\mathrm{C}^n \tag{14}$$

Writing the equation for both reactions forward and backward results in the following:

$$\frac{dC}{dt} = -k_1\mathrm{C}^{n_1} + k_2\mathrm{q}^{n_2} \tag{15}$$

At equilibrium, the derivative is zero, and the following equations are derived[14]:

$$q = \left(\frac{k_1}{k_2}\right)^{1/n_2} {C_e}^{n_1/n_2} \tag{16}$$

$$q = K_F \, {C_e}^n \tag{17}$$

2.3.3.4 Freundlich Multicomponent Isotherm

Sheindorf et al.[15] suggested a derived multicomponent adsorption isotherm based on an assumption of an exponential distribution of adsorption energies for each component. This model

requires single-component isotherm compliance with the Freundlich model. Parameters estimated from the individual model, adsorption constant, and intensity are used for the multicomponent system:

$$q_{i,e} = K_i \times c_{i,e} \times \left(\sum_{i=1}^{N} a_{ij} \cdot c_{j,e}\right)^{\left(\frac{1}{n_i}-1\right)} \quad (18)$$

where

q is the equilibrium adsorption capacity of component i in the presence of component j,

a_{ij} is the competitive adsorption coefficient for the system components,

K_F and n are respectively the isotherm constant capacity parameter and adsorption intensity determined from the single-component system for component i, and

$c_{i,e}$ and $c_{j,e}$ are the adsorbate concentrations at equilibrium for components i and j, respectively.

N is the total number of components.

2.4 Results

2.4.1 Adsorption Equilibrium Data

Adsorption equilibrium isotherm data were collected for methanol, ethanol, n-propanol, and n-butanol at ambient temperature to compare the capacity of different adsorbents. Figure 2.1 presents the adsorption isotherms of n-butanol, n-propanol, ethanol, and methanol adsorbed on selected adsorbent materials under various loading conditions. Adsorption increased with increasing carbon number in different patterns, and n-butanol had the highest affinity for all the materials tested; this trend agrees with the results of many studies reported in the literature.[6,16–21] Methanol and ethanol had a lower affinity than the other alcohols in all zeolites studied except FER, where ethanol had a higher affinity than methanol and propanol did. Upon the basis of these experiments, we assumed in our analysis that water–zeolite interactions are negligible.

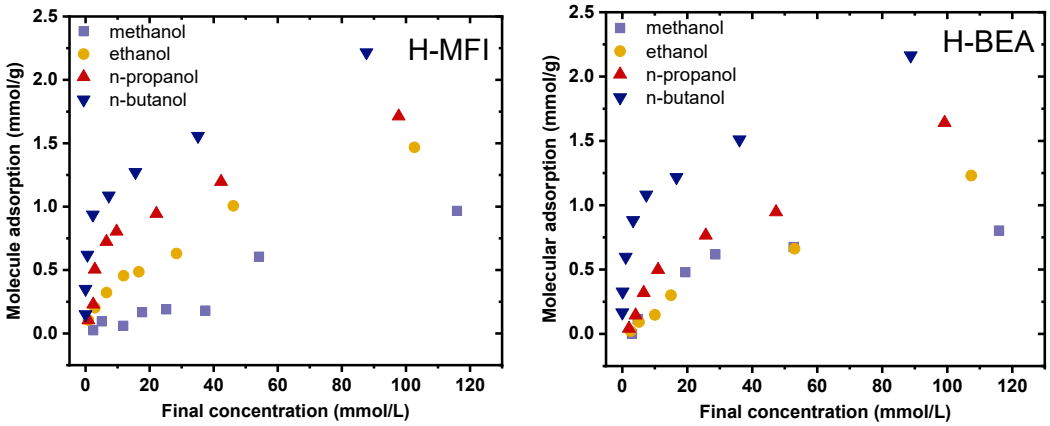

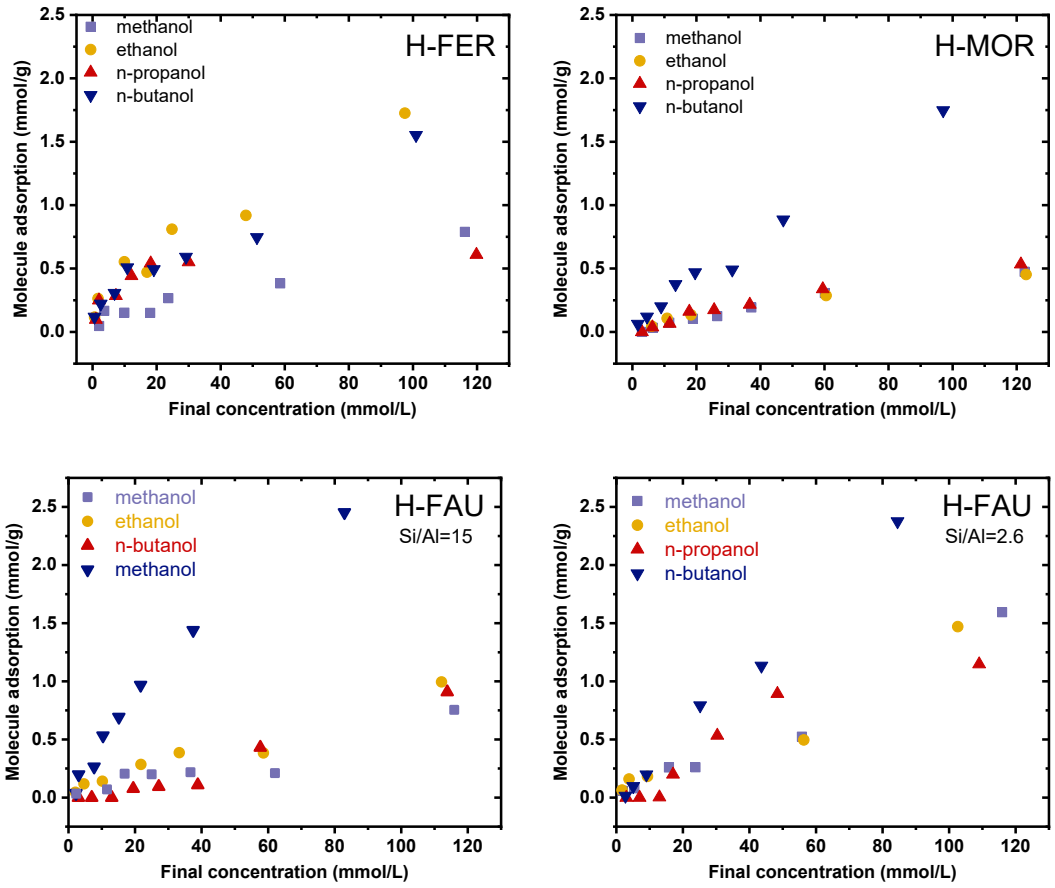

Figure 2.1. Equilibrium adsorption isotherms for single-component alcohols in aqueous solution for methanol (■ light blue), ethanol (● red), n-propanol (▲ light green), and n-butanol (▼ dark blue).

BEA, MFI, and FER tend to have a nonlinear pattern with a gradual decrease in adsorption capacity from n-butanol to methanol. At low butanol concentrations in the solution, both BEA and MFI exhibited a much steeper increase in the loading compared with other types, but then the rate of increase quickly flattened. Up to a concentration value of approximately 20 (mmol L^{-1}), both zeolites exhibited the same course, but then they began to split, finally yielding a maximum measured butanol loading of 2.21 mmol L^{-1} (at 88 mmol g^{-1}) for MFI and 2.16 mmol L^{-1} (at 89 mmol g^{-1}) for BEA. MFI is considered a medium-pore zeolite with 10-member ring pores openings and intersecting channels.[22] BEA is a large-pore zeolite with 12-member ring openings. However, BEA has channels similar to those of MFI. Pore geometry affects van der Waals interactions

between the organic substance and the framework oxygen atoms.[4] The scale of affinity observed for MFI and BEA was as expected: increasing affinity with increasing molecular weight and decreasing polarity.[16]

In FER, the n-butanol and ethanol isotherm adsorption slopes were similar, as were those of methanol and n-propanol, which had lower isotherm slopes. The same behavior was documented in earlier studies[7] when the adsorption of ethylene glycol was higher than that of propylene glycol. Another study mentioned similar trends for linear and disbranched alkanes.[23] Previous studies have demonstrated that linear alkanes with fewer than five carbons are adsorbed in both 8-member ring (MR) and 10-MR channels, whereas more than five carbons preferentially adsorb in the 10-MR channels.[24,25] In a previous study, isotherm experiments with n-butanol and ethanol using CHA (3.8 × 4.2 a) and LTA (4.2 × 4.2 a) cage types demonstrated opposite selectivity; the adsorption of ethanol was favorable on CHA (which has a similar kinematic diameter to FER 8-ring channels), whereas the LTA (which has a similar kinematic diameter to FER 10-ring channels) topology had a clear preference for n-butanol.[18] These results indicate a molecular sieving property of FER zeolites for ethanol in 8-ring channels and an n-butanol confinement preference in 10-ring channels.

MOR and FAU exhibited linear trends over the studied region. FAU is considered a large-size zeolite. However, MOR is considered a medium-size zeolite despite its 12-MR openings because its channels are straight and do not have intersections. They have highly different pore structures, but both showed linear adsorption. MOR showed an increase in the adsorption capacity with an increasing carbon number. However, this effect was abrupt at C_4 rather than proceeding gradually from C_1 to C_3. The small adsorption of C_1–C_3 in MOR suggests that side pockets are

inaccessible due to its minor axis (4.3 Å). Adsorption of n-butanol in MOR appeared to be linear and did not follow a defined pattern based on the molecule sizes.

High-alumina samples of FAU (Si/Al = 2.6) in shorter-chain alcohols exhibited higher adsorption values than normal FAU did (Si/Al = 15). Adsorption of shorter-chain alcohols in aqueous solution at lower concentrations was higher with more defects due to the considerable amount of water adsorbed into the framework. Water and shorter-chain alcohols have strong interactions within the framework that significantly enhance adsorption.[26] The adsorption of the longer-chain alcohols at lower concentrations varied slightly and even decreased with increasing aqueous-phase concentration. Hydrogen ions and water molecules occupy pore space and therefore hinder the adsorption of the alcohols at higher concentrations.[26] Hydrophilic sites had a more substantial effect on the adsorption of shorter-chain alcohols at low concentrations than on that of the longer-chain alcohols. The crossover from higher n-propanol loading to higher methanol and ethanol loading in the adsorption isotherms occurred at 20 mmol/L.

Oxygenates of various oxygen functional groups behave differently in adsorption onto zeolites. In principle, adsorption affinity is a function of adsorbate functionality.[4] Figure 2.2 shows adsorption for aldehydes and ketones on MFI and BEA. The longer nonpolar C-chain of n-butyraldehyde promotes adsorption over n-butanol and propanol in MFI and BEA types.

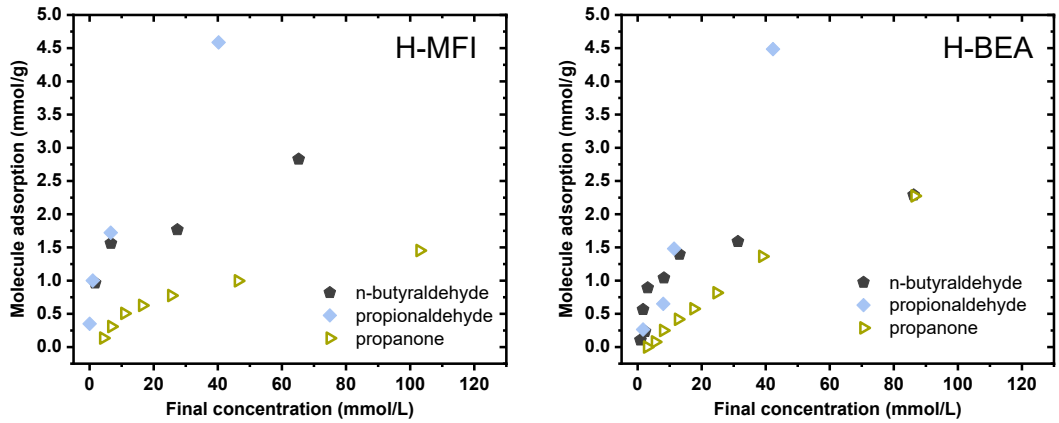

Figure 2.2. Equilibrium adsorption isotherms for single-component aldehydes and ketones in aqueous solution for n-butyraldehyde (▼ grey), n-propionaldehyde (▼ light blue), and propanone (▼orange).

Propionaldehyde has a higher loading than other oxygenates. The adsorption isotherm was steeper in MFI than in other types, with 4.6 mmol g^{-1} at an equilibrium concentration of 40.3 mmol L^{-1}. BEA had similar uptake capacities at high concentrations. However, the slope of the isotherm was much steeper at low concentrations.

By contrast, propanone adsorption with linear behavior was greater than that of n-propanol in BEA but less than that of n-butanol, n-butyraldehyde, and propionaldehyde. The n-propanone isotherm for BEA exhibited a more strongly concave downward crossover with respect to that of MFI.

Binary component adsorption tests—adsorption in aqueous solutions of two components—and multicomponent adsorption tests were conducted. The binary component is the most straightforward system in which to probe the competitiveness effect; n-butanol was studied in a binary mixture in the presence of other shorter-chain alcohols. Generally, the findings corresponded to those of the single-component results, primarily implying an unaltered concentration for n-butanol with shorter-chain alcohols, which means that the affinity of this

molecule was not affected by the presence of smaller molecules within the same functional group. High n-butanol selectivity over the other molecules was observed due to the stronger dispersive interactions with the zeolite framework. Methanol and ethanol were completely excluded, and n-propanol showed negligible competition with n-butanol. In FER, adsorption isotherms of n-butanol and ethanol were similar to those of their corresponding single-component systems, meaning that n-butanol and ethanol are adsorbed into different sites and do not compete with the same active types. The FER channels were occupied simultaneously by both molecules.

Straight-chain alcohols are compared to branched-chain alcohols in BEA in Figure 2.3. In the single-component isotherms, 2-butanol exhibited lower adsorption capacity than n-butanol did, which is consistent with the results of a previous study.[27] Shape selectivity arises through a tradeoff between entropy and enthalpy.[27] Adsorption of linear-chain butanol alcohols maximizes the enthalpy contribution and minimizes entropy losses. When both molecules are present in the mixture, n-butanol and 2-butanol adsorption occurs simultaneously.

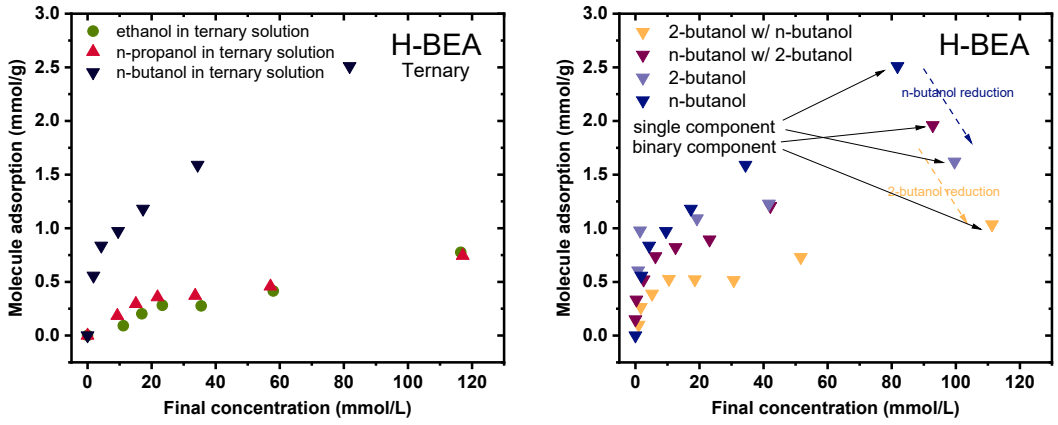

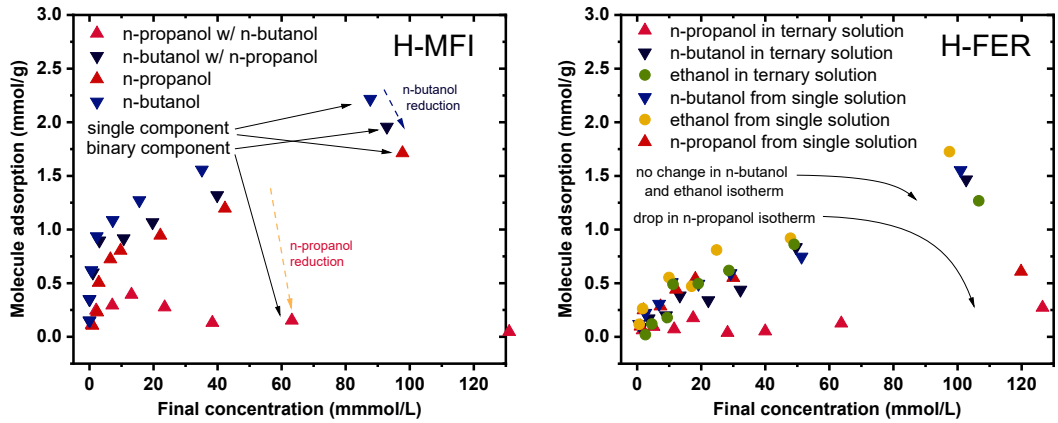

Figure 2.3. Equilibrium adsorption isotherms for multicomponent alcohols in aqueous solution for methanol (■ light blue), ethanol (● red), n-propanol (▲ light green), n-butanol (▼ dark blue), and 2-butanol (▼light blue).

The equilibrium loading of n-butyraldehyde was higher than that of butanol (Figure 2.4). The strong competition between n-butanol and n-butyraldehyde is due to their similar chemical structure, but n-butyraldehyde is more hydrophilic. N-butanol loading decreased in the presence of n-butyraldehyde for all the adsorbents.

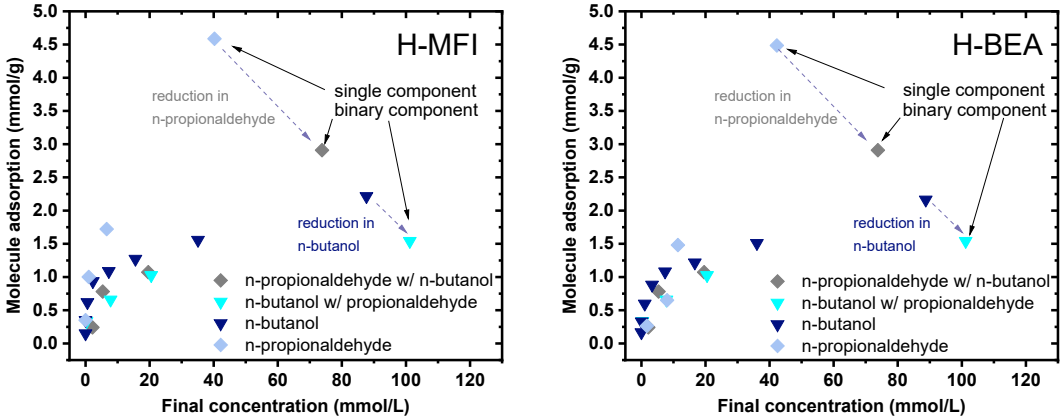

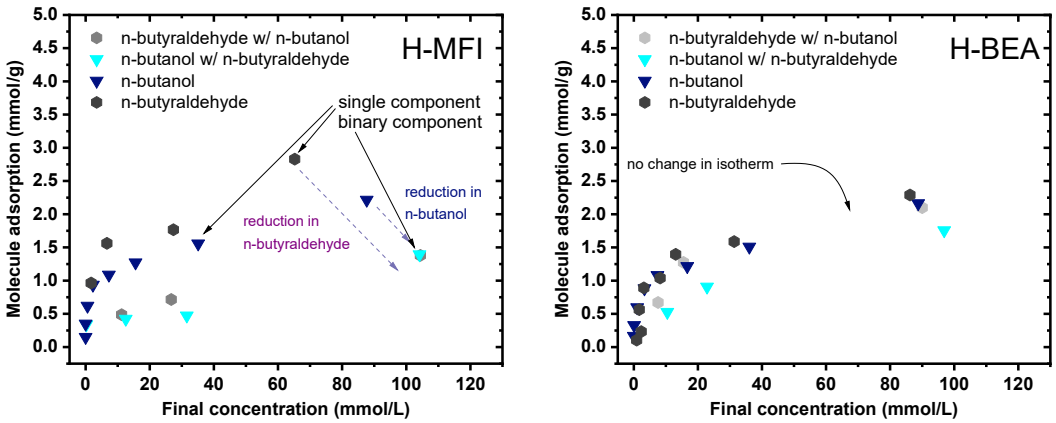

Figure 2.4. Equilibrium adsorption isotherms for multicomponent alcohols, aldehydes, and ketones in aqueous solution for methanol (■ light blue), ethanol (● red), n-propanol (▲ light green), n-butanol (▼ dark blue), n-butyraldehyde (▼ grey), and n-propionaldehyde (▼ light blue).

2.5 Discussion

2.5.1 Isotherm Modeling Results

All data were fitted to the Langmuir or Freundlich adsorption models, resulting in a set of model parameters. The terms q_{max} and K_1 are the Langmuir parameters that indicate the maximum adsorption capacity and affinity, respectively, of the adsorbent, whereas K_F and n are the Freundlich parameters. The parameter K_F is an indicator of the adsorption capacity, and n represents the heterogeneity of adsorption. The isotherms, in general, were better fit to the Freundlich model, but several isotherms had good fits for both models. This is possibly because the Langmuir and Freundlich models are not contradictory.[13,28]

2.5.2 Langmuir Model

Data were fitted with the Langmuir model, which is commonly used for modeling monolayer adsorption. The assessed adsorbent isotherm parameter saturation loading (q_{max}) and the Langmuir adsorption constant (K_L) are presented in (Tables 2.3 and 2.4, Appendix). The plots of the Langmuir model with the corresponding model parameters are displayed in Figures 2.5 and

2.6. The monolayer capacity generally increases with increasing zeolite pore size, with the q_{max} values for BEA and MFI being similar.

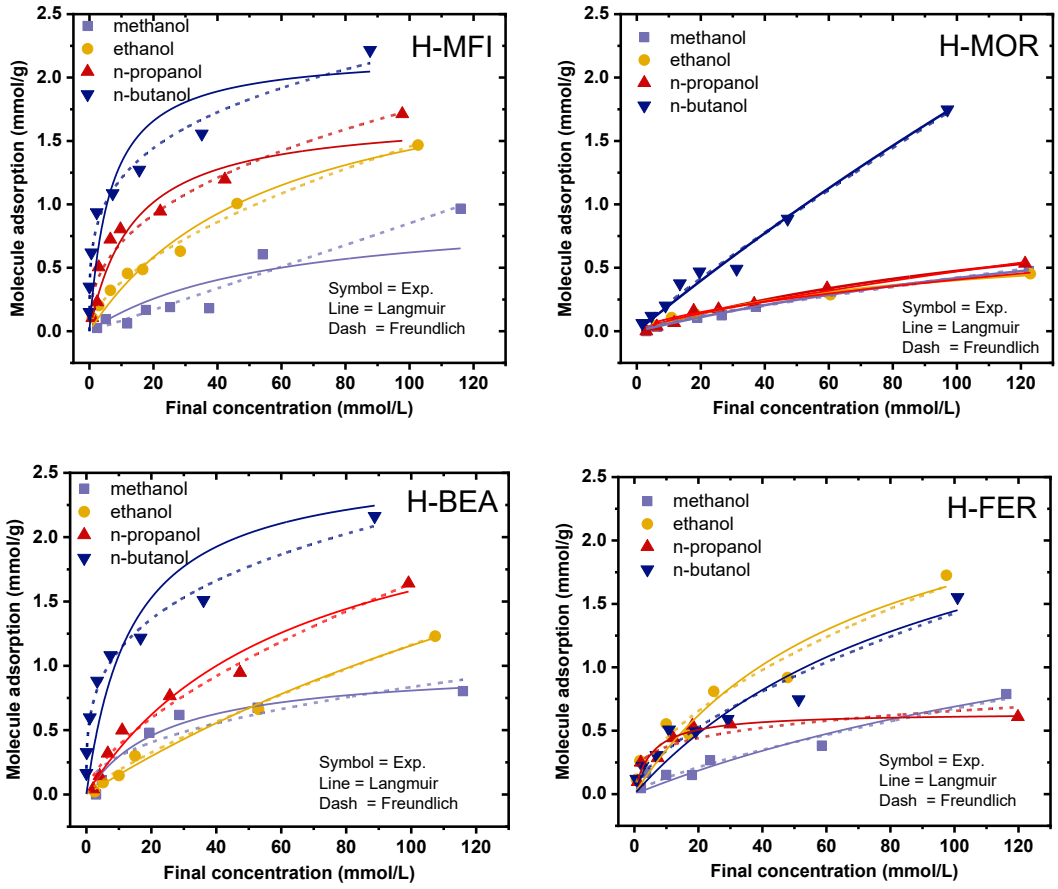

Figure 2.5. Model isotherms for single-component alcohols in aqueous solution for methanol (■ light blue), ethanol (● red), n-propanol (▲ light green), n-butanol (▼ dark blue). The symbols show experimental values, and the solid and dashed lines show the Langmuir and Freundlich model results, respectively.

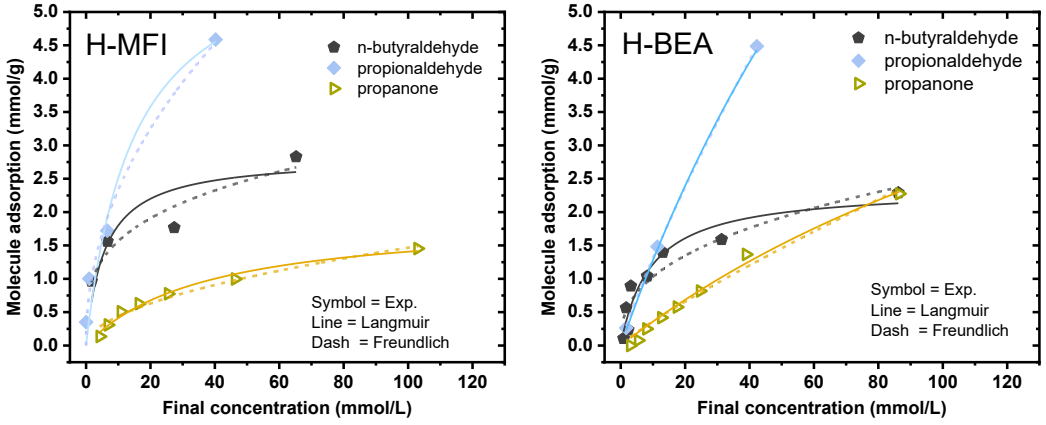

Figure 2.6. Model isotherms for single-component aldehydes and ketones in aqueous solution for n-butyraldehyde (▼ grey), n-propionaldehyde (▼ light blue), and propanone (▼ orange). The symbols show experimental values, and the solid and dashed lines show the Langmuir and Freundlich model results, respectively.

The Langmuir model assumes monolayer adsorption over adsorbent sites[1]; no further adsorption occurs after molecules occupy a site. The model can be explained by examining the loadings in terms of the number of molecules per active site to eliminate the effect of varying formula weights. Molecular clustering, which can be induced by hydrogen bonding, causes the maximum adsorption factor per alumina factor to exceed unity.[29] In MFI and BEA, more than one ethanol and one n-propanol molecule are adsorbed per site (Figure 2.7 a). By contrast, a smaller adsorption capacity for n-alcohols occurs in FAU with a Si/Al ratio of 2.6, indicating that only a certain fraction of the Brønsted acid sites are accessible to the adsorbing n-alcohol molecules (Figure 2.7 b).

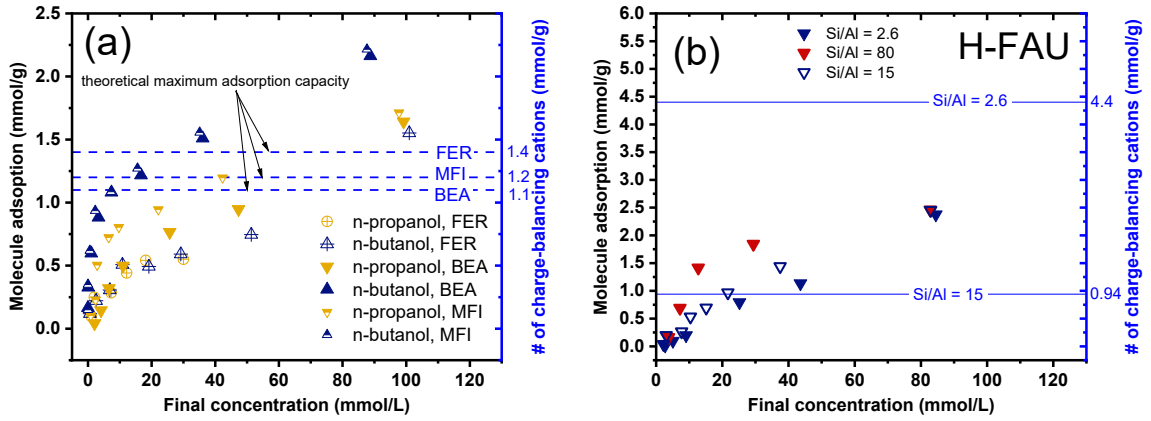

Figure 2.7. The number of charge-balancing cations for each zeolite type for (a) the comparison of n-butanol and n-propanol adsorption over FER, MFI, and BEA and (b) n-butanol adsorption with FAU with Si/Al ratios of 2.6, 15 and 80.

In FER, MFI, and BEA, the total number of molecules adsorbed exceeded the number of active sites available per gram of zeolite (Figure 2.7 a), and stronger interaction confirmed

multiple-site occupancy. This observation implies that adsorption occurs everywhere through the channel walls, not just at the Brønsted acid sites. The adsorption isotherms and energetics vary in a sophisticated manner depending on the composition of the solid adsorbent and on the size and shape of the pores that constitute the solid. A more advanced model is required to decouple adsorption at multiple types of sites, which probably limits the use of simple models to describe adsorption. The adsorption constant (K_L) for the Langmuir isotherm model in BEA and MFI revealed more robust interactions at low coverage. This is expected because of the strongly concave downward shape of these isotherms. The low adsorption constant on FAU for smaller n-alcohols can be attributed to the large size of FAU zeolites associated with a large cavity diameter of approximately 11.9 Å (Table 2.2).

Table 2.2. Zeolite topological characteristics for channels and cages.[30]

Framework	**Channels**		**Cages**		
Type	**Ring Size**	**Channel Pathway**	**Largest Cavity Diameter**	**Percentage of Pore Volume in Cages (%)**	**Pore Limiting Diameter**
ZSM-5	10	Sinusoidal	7	26	5
	10	Straight			
FER	10	Straight	7	47	5.3
	8	Straight			
FAU	12	Straight	11.9	77	6.7
BEA	12	Straight	6.9	20	6.7
	12	Straight			

2.5.3 Freundlich Adsorption Isotherm

The Freundlich isotherm models for BEA and MFI were consistent with the Langmuir isotherm; as generally reported, adsorption increases in distinct patterns for each carbon number. For both types, the Freundlich adsorption intensity parameter increased with increasing carbon number, similar to the increase in the adsorption constant in the Langmuir model. Sorption was better fitted to the Freundlich equation, which suggests that adsorption occurs at heterogeneous reactive sites and is probably a multilayer process (Tables 2.5 and 2.6, Appendix).[31] Isotherms that deviated from a Langmuir isotherm were plotted according to the Freundlich model. Simplified models such as the linear and Langmuir isotherm models are less likely to be followed for the single adsorption of alcohol in aqueous solution. These results are attributed to multilayer adsorption, especially with larger molecules. To predict the adsorption behavior of the multicomponent solution system, a multicomponent Freundlich isotherm model was used to study the experiments results of this study (Eq. 18). Parameters K_F, n, and a_{ij} for the multicomponent adsorption isotherms for each component are given in Tables 2.7–2.13 in the Appendix. The coefficients shown in these tables explain the adsorption influence of a specific molecule by the presence of the other molecule in the solution. For example, n-butanol absorption was not affected by the presence of all the other smaller n-alcohols molecules, which were mainly ethanol and methanol, whereas, in the case of oxygenates of different oxygen functional groups such as n-propionaldehyde and n-butyraldehyde, the presence of other components on n-butanol adsorption was rather high. Figure 2.8 shows the Freundlich competitive adsorption coefficient for binary n-butanol in the presence of each molecule for various zeolite types. For n-propanol, competitive adsorption coefficients were estimated to be 0.133 for MFI. Because ethanol and methanol have no significant influence on the parameter, their estimated parameter coefficient was negligible and

omitted. Figure 2.8 a, also indicates that the coefficient value (effect) increases with carbon numbers from methanol (a_{ij} = 0.0013) to 2-butanol (a_{ij} = 1.51) for BEA zeolite. The same trend was noticed in H-MFI (Figure 2.8 b). However, n-butyraldehyde had more effect on n-butanol (a_{ij} = 1.77). Results indicated that the model fit the data obtained from all experiments relatively well and could be applied to study and predict the adsorption behavior of multicomponent system present in an ABE fermentation solution that is obtained from the biomass route.

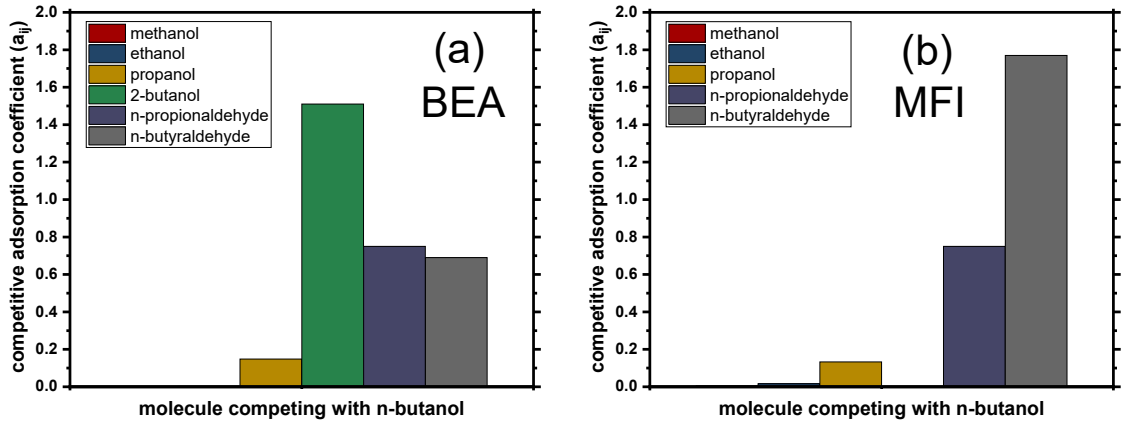

Figure 2.8. Competitive adsorption coefficients for methanol, ethanol, n-propanol, n-propionaldehyde, n-butyraldehyde, and 2-butanol with n-butanol for (a) BEA and (b) MFI.

2.6 Conclusion

We demonstrated that adsorption on zeolites from aqueous solution is a viable and attractive method for separation. Five types of commercial zeolites were assessed as possible options for n-butanol recovery. Adsorption isotherms of n-butanol, n-propanol, ethanol, and methanol were determined. By adopting the Langmuir model, underlying assumptions can be applied to understand conceptual meaning of the model due its physical means. However, providing a complete theoretical assessment is complicated, and thus, reasonable assumptions have been used to simplify the explanations of the Langmuir model. Langmuir isotherm models were

less likely to follow the single-adsorption mechanism of alcohol in aqueous solution. These results were due to multilayer adsorption, especially for longer-chain alcohols. Isotherms deviating from the Langmuir isotherm were plotted according to the Freundlich model. Competitive adsorption coefficients were correlated to the influence of the other molecules present. However, due to the empirical basis of the Freundlich model, the model could not be correlated to physical adsorption interactions and zeolite sizes. The topology of a zeolite plays a role in allowing smaller molecules to enter small channels and larger ones to be adsorbed preferentially, leading to different active site adsorption in a heterogeneous system.

2.7 Appendix

Table 2.3. Langmuir parameters for a single component system for BEA, MFI, and FER.

Zeolite type	BEA		MFI		FER	
Sample	K_L (L mol^{-1})	q_{max} (mmol g^{-1})	K_L (L mol^{-1})	q_{max} (mmol g^{-1})	K_L (L mol^{-1})	q_{max} (mmol g^{-1})
methanol	42 ± 15	1.01 ± 0.13	18.0 ± 5.8	0.96 ± 0.0	4.7 ± 4.3	2.15 ± 1.42
ethanol	3.8 ± 1.8	4.2 ± 1.4	17.6 ± 4.4	2.24 ± 0.3	14.0 ± 7.8	2.83 ± 0.88
n-propanol	15.7 ± 5.1	2.6 ± 0.44	73.0 ± 0.01	1.7 ± ± 0.0	180 ± 5	0.64 ± 0.05
n-butanol	71.3 ± 18	2.6 ± 0	153 ± 52	2.2 ± 0.01	9.8 ± 6.6	2.90 ± 1.20
n-propionaldehyde	7.3 ± 0.06	18.8 ± 0.14	67 ± 44	6.2 ± 1.5	-	-
n-butyraldehyde	106 ± 33	2.4 ± 0.3	174 ± 71	2.8 ± 0	-	-
propanone	4.7 ± 1.8	7.9 ± 2.3	27 ± 4.2	1.9 ± 0.13	-	-

Table 2.4. Langmuir parameters for a single component system for MOR and FAU.

Zeolite type	MOR		FAU (Si/Al=15)	
Sample	K_L (L mol^{-1})	q_{max} (mmol g^{-1})	K_L (L mol^{-1})	q_{max} (mmol g^{-1})
methanol	4.5 ± 1.0	1.36 ± 0.22	-	-
ethanol	11.0 ± 3.0	0.77 ± 0.11	-	-
n-propanol	6.3 ± 1.5	1.23 ± 0.20	-	-
n-butanol	15.0 ± 14.7	13.6 ± 12.0	8.9 ± 1.4	5.8 ± 0.6
n-propionaldehyde	-	-	-	-
n-butyraldehyde	-	-	-	-
propanone	-	-	-	-

Table 2.5. Freundlich parameters for a single component system for BEA, MFI, and FER**.**

Zeolite type	BEA		MFI		FER	
Sample	K_F (L mol^{-1})	n	K_F (L mol^{-1})	n	K_F (L mol^{-1})	n
methanol	0.11 ± 0.05	2.2 ± 0.6	0.008 ± 0	0.99 ± 0.14	0.02 ± 0.01	1.39 ± 0.20
ethanol	0.03 ± 0.06	1.3 ± 0.7	0.10 ± 0.01	1.74 ± 0.09	0.12 ± 0.04	1.72 ± 0.23
n-propanol	0.09 ± 0.02	1.6 ± 0.1	0.28 ± 0.05	2.53 ± 0.28	0.21 ± 0.04	4.07 ± 1.01
n-butanol	0.58 ± 0.03	3.5 ± 0.2	0.67 ± 0.10	3.87 ± 0.63	0.08 ± 0.02	1.62 ± 0.22
n-propionaldehyde	0.18 ± 0.01	1.17 ± 0.02	0.78 ± 0.21	2.1 ± 0.4	-	-
n-butyraldehyde	0.42 ±0.09	2.6 ± 0.4	0.82 ± 0.2	3.5 ± 0.88	-	-

propanone	0.05 ± 0.01	1.15 ± 0.08	0.13 ± 0.02	1.91± 0.17	-	-

Table 2.6. Freundlich parameters for a single component system for MOR and FAU.

Zeolite type	MOR		FAU (Si/Al=15)	
Sample	K_F (L mol^{-1})	n	K_F (L mol^{-1})	n
methanol	0.01 ± 0.00	1.27 ± 0.002	0.005 ± 0.005	0.96 ± 0.22
ethanol	0.02 ± 0.002	1.62 ± 0.006	0.018 ± 0.010	1.2 ± 0.20
n-propanol	0.014 ± 0.003	1.32 ± 0.096	0.005 ± 0.003	0.96 ± 0.003
n-butanol	0.027 ±0.006	1.10 ± 0.071	0.083 ± 0.012	1.31 ± 0.072
n-propionaldehyde	-	-	-	-
n-butyraldehyde	-	-	-	-
propanone	-	-	-	-

Table 2.7. Competitive adsorption coefficients for methanol, ethanol, and n-propanol with n-butanol.

	coefficient value					
single coefficient	K=0.82 n=3.5					
a_{ii}	1	1	1	1	1	1
a_{ij}	0.0051	0.0013	0.0164	0.00245	0.133	0.148
main Molecule	methanol		ethanol		n-propanol	
other Molecule	n-butanol					
conc. Ratio	1	1	1	1	1	1
R^2	0.94	0.98	0.91	0.94	0.86	0.92
zeolite type	H-MFI	H-BEA	H-MFI	H-BEA	H-MFI	H-BEA

Table 2.8. Competitive adsorption coefficients for n-propionaldehyde and n-butyraldehyde with n-butanol.

	coefficient value			
single coefficient	K=0.18 n=1.17		K=0.82 n=3.5	
a_{ii}	1	1	1	1
a_{ij}	285.42	285.42	2.51	0.62
main Molecule	n-propionaldehyde		n-butyraldehyde	
other Molecule	n-butanol			
conc. Ratio	1	1	1	1
R^2	0.94	0.94	0.91	0.91

zeolite type	H-BEA	H-MFI	H-MFI	H-BEA

Table 2.9. Competitive adsorption coefficients for 2-butanol and n-butanol in binary solutions of n-butanol and 2-butanol.

coefficient value		
single coefficient	K=0.42 n=3.50	K=0.73 n=6.31
a_{ii}	1	1
a_{ij}	1.51	0.85
main Molecule	n-butanol	2-butanol
other Molecule	2-butanol	n-butanol
conc. Ratio	1	1
R^2	0.83	0.87
zeolite type	H-BEA	H-BEA

Table 2.10. Competitive adsorption coefficients for n-butanol in binary solutions with n-propionaldehyde and n-butyraldehyde.

coefficient value				
single coefficient	K=0.42 n=3.50			
a_{ii}	1	1	1	
a_{ij}	0.75	0.75	1.77	0.69
main Molecule	n-butanol		n-butanol	
other Molecule	n-propionaldehyde		n-butyraldehyde	
R^2	0.91	0.91	0.56	0.75
zeolite type	H-MFI	H-BEA	H-MFI	H-BEA

Table 2.11. Competitive adsorption coefficients for n-propionaldehyde and n-butyraldehyde with n-butanol.

coefficient value				
single coefficient	K=0.18 n=1.17		K=0.82 n=3.5	
a_{ii}	1	1	1	1
a_{ij}	285.42	285.42	2.51	0.62
main Molecule	n-propionaldehyde		n-butyraldehyde	
other Molecule	n-butanol			
conc. Ratio	1	1	1	1
R^2	0.94	0.94	0.91	0.91
zeolite type	H-BEA	H-MFI	H-MFI	H-BEA

2.8 References

1. Bates, S. P.; Van Well, W. J. M.; Van Santen, R. A.; Smit, B. Energetics of N-Alkanes in Zeolites: A Configurational-Bias Monte Carlo Investigation into Pore Size Dependence. *J. Am. Chem. Soc.* **1996,** *118,* 6753–6759.
2. Eder, F.; Lercher, J. A. On the Role of the Pore Size and Tortuosity for Sorption of Alkanes in Molecular Sieves. *J. Phys. Chem. B* **1997,** *101,* 1273–1278.
3. First, E. L.; Gounaris, C. E.; Wei, J.; Floudas, C. A. Computational Characterization of Zeolite Porous Networks: An Automated Approach. *Phys. Chem. Chem. Phys.* **2011,** *13,* 17339–17358.
4. Foo, K. Y.; Hameed, B. H. Insights into the Modeling of Adsorption Isotherm Systems. *Chem. Eng. J.* **2010,** *156,* 2–10.
5. Freundlich, H. Über Die Adsorption in Lösungen. *Zeitschrift für Physikalische Chemie* **1907,** *57U,* 385.
6. Goerlitz, R.; Weisleder, L.; Wuttig, S.; Trippel, S.; Karstens, K.; Goetz, P.; Niebelschuetz, H. Bio-Butanol Downstream Processing: Regeneration of Adsorbents and Selective Exclusion of Fermentation by-Products. *Adsorption* **2018,** *24,* 95–104.
7. Janda, A.; Vlaisavljevich, B.; Smit, B.; Lin, L.-C.; Bell, A. T. Effects of Pore and Cage Topology on the Thermodynamics of N-Alkane Adsorption at Brønsted Protons in Zeolites at High Temperature. *J. Phys. Chem. C* **2017,** *121,* 1618–1638.
8. Krishna, R.; Van Baten, J. M. Hydrogen Bonding Effects in Adsorption of Water−Alcohol Mixtures in Zeolites and the Consequences for the Characteristics of the Maxwell−Stefan Diffusivities. *Langmuir* **2010,** *26,* 10854–10867.
9. Kulprathipanja, S. *Zeolites in Industrial Separation and Catalysis;* John Wiley & Sons, 2010.

10. Langmuir, I. The Adsorption of Gases on Plane Surfaces of Glass, Mica and Platinum. *J. Am. Chem. Soc.* **1918,** *40,* 1361–1403.

11. Mallon, E. E. Aqueous Solution and Vapor Phase Adsorption of Oxygenates onto Zeolites. Thesis, University of Minnesota, 2012.

12. Mallon, E. E.; Babineau, I. J.; Kranz, J. I.; Guefrachi, Y.; Siepmann, J. I.; Bhan, A.; Tsapatsis, M. Correlations for Adsorption of Oxygenates onto Zeolites from Aqueous Solutions. *J. Phys. Chem. B* **2011,** *115,* 11431–11438.

13. Mallon, E. E.; Bhan, A.; Tsapatsis, M. Driving Forces for Adsorption of Polyols onto Zeolites from Aqueous Solutions. *J. Phys. Chem. B* **2010,** *114,* 1939–1945.

14. Nguyen, C. M.; Reyniers, M.-F.; Marin, G. B. Theoretical Study of the Adsorption of C1–C4 Primary Alcohols in H-Zsm-5. *Phys. Chem. Chem. Phys.* **2010,** *12,* 9481–9493.

15. Nguyen, C. M.; Reyniers, M.-F.; Marin, G. B. Theoretical Study of the Adsorption of the Butanol Isomers in H-Zsm-5. *J. Phys. Chem. C* **2011,** *115,* 8658–8669.

16. Nguyen, C. M.; Reyniers, M.-F.; Marin, G. B. Adsorption Thermodynamics of C1–C4 Alcohols in H-Fau, H-Mor, H-Zsm-5, and H-Zsm-22. *J. Catal.* **2015,** *322,* 91–103.

17. Raganati, F.; Procentese, A.; Olivieri, G.; Russo, M. E.; Salatino, P.; Marzocchella, A. Bio-Butanol Separation by Adsorption on Various Materials: Assessment of Isotherms and Effects of Other Abe-Fermentation Compounds. *Sep. Purif. Technol.* **2018,** *191,* 328–339.

18. Remy, T.; Cousin Saint Remi, J.; Singh, R.; Webley, P. A.; Baron, G. V.; Denayer, J. F. M. Adsorption and Separation of C1−C8 Alcohols on Sapo-34. *J. Phys. Chem. C* **2011,** *115,* 8117–8125.

19. Sheindorf, C.; Rebhun, M.; Sheintuch, M. A Freundlich-Type Multicomponent Isotherm. *J. Colloid Interface Sci.* **1981,** *79,* 136–142.

20. Skopp, J. Derivation of the Freundlich Adsorption Isotherm from Kinetics. *J. Chem. Educ.* **2009,** *86,* 1341.

21. Smit, B.; Maesen, T. L. M. Towards a Molecular Understanding of Shape Selectivity. *Nature* **2008,** *451,* 671–678.

22. Stückenschneider, K.; Merz, J.; Schembecker, G. Molecular Interactions of Alcohols with Zeolite Bea and Mor Frameworks. *J. Mol. Model.* **2013,** *19,* 5611–5624.

23. Van den Bergh, M.; Van de Voorde, B.; De Vos, D. Adsorption and Selective Recovery of Citric Acid with Poly(4-Vinylpyridine). *ChemSusChem* **2017,** *10,* 4864–4871.

24. Van der Mynsbrugge, J.; Hemelsoet, K.; Vandichel, M.; Waroquier, M.; Van Speybroeck, V. Efficient Approach for the Computational Study of Alcohol and Nitrile Adsorption in H-Zsm-5. *J. Phys. Chem. C* **2012,** *116,* 5499–5508.

25. Van Koningsveld, H. High-Temperature (350 K) Orthorhombic Framework Structure of Zeolite H-Zsm-5. *Acta Crystallogr., Sect. B* **1990,** *46,* 731–735.

26. Van Well, W. J. M.; Cottin, X.; de Haan, J. W.; Smit, B.; Nivarthy, G.; Lercher, J. A.; van Hooff, J. H. C.; Van Santen, R. A. Chain Length Effects of Linear Alkanes in Zeolite Ferrierite. 1. Sorption and 13c Nmr Experiments. *J. Phys. Chem. B* **1998,** *102,* 3945–3951.

27. Van der Perre, S.; Gelin, P.; Claessens, B.; Martin-Calvo, A.; Cousin Saint Remi, J.; Duerinck, T.; Baron, G. V.; Palomino, M.; Sánchez, L. Y.; Valencia, S.; Shang, J.; Singh, R.; Webley, P. A.; Rey, F.; Denayer, J. F. M. Intensified Biobutanol Recovery by Using Zeolites with Complementary Selectivity. *ChemSusChem* **2017,** *10,* 2968–2977.

28. Weitkamp, J.; Puppe, L. *Catalysis and Zeolites: Fundamentals and Applications;* Springer: Berlin Heidelberg, 2013.

29. Worch, E. *Adsorption Technology in Water Treatment: Fundamentals, Processes, and Modeling;* De Gruyter: Berlin, 2012.

30. Xiong, R.; Sandler, S. I.; Vlachos, D. G. Molecular Screening of Alcohol and Polyol Adsorption onto Mfi-Type Zeolites. *Langmuir* **2012,** *28,* 4491–4499.

31. Yu, S.; Wang, X.; Yao, W.; Wang, J.; Ji, Y.; Ai, Y.; Alsaedi, A.; Hayat, T.; Wang, X. Macroscopic, Spectroscopic, and Theoretical Investigation for the Interaction of Phenol and Naphthol on Reduced Graphene Oxide. *Environ. Sci. Technol.* **2017,** *51,* 3278–3286.

Chapter 3: Efficient Hydrogen Production from N-butanol Steam Reforming Obtained from ABE Fermentation Using RD

3.1 Abstract

An increase in n-butanol production is a consequence of the growth in biomass production and makes utilizing n-butanol as a feedstock attractive (e.g., for the production of hydrogen). Here, we report integrating n-butanol steam reforming and adsorption–desorption into a single process as a potential approach to enhance the efficiency of n-butanol adsorption from ABE and hydrogen production. A base case process, operating with normal butanol reforming, was investigated. A thermodynamic analysis was used to compare n-butanol steam reforming with and without integration with the adsorption–desorption process, highlighting higher efficiency for hydrogen production and energy utilization. This report recommends a reforming temperature of 800 °C and a steam-to-carbon ratio of 10 to ensure the lowest energy usage to generate a particular amount of hydrogen.

3.2 Introduction

Growing population and economic development have resulted in more energy demand over the last two decades. Living standard improvements have also strengthened the need for energy.[1] Among the various sources of energy, petroleum is the most significant. Its derivatives are significant in transportation, electricity, and raw materials for the petrochemical industry. These resources are facing an inevitable increase in demand, and their usage is becoming a major concern.[2]

Plants produce 128 billion metric tons of carbohydrate biomass every year through photosynthesis.[3] Several potential biologically based routes to synthesize commodity chemicals from biomass exist.[4] Biomass is one of the world's single largest renewable energy resources, contributing to 10% of the world's primary energy supply.[5] Compared with other emerging liquid fuel sources, biomass is thought to have the most potential. With the gradual shift toward a more carbohydrate-based economy, in 2030, it is anticipated that 20% of transportation fuels and 25% of chemicals, including 45 billion pounds of biobased chemicals and bioproducts, will be produced from biomass.[3] Due to its abundance and growing production, biomass could help alleviate concerns regarding energy security and climate change. The mitigation of climate change is achieved by offsetting the carbon produced by fuel burning and reducing greenhouse gas emissions. Because CO_2 emissions from combustion are consumed by plants during the process of photosynthesis, more biomass is produced, and biomass has the potential to reduce 550 million tons of CO_2 every year.[3]

The composition of biomass contains two major carbohydrates, cellulose and hemicellulose, which are bound together by polymeric lignin. The three resulting biopolymers are valuable because of their ability to extract energy from the sun. Lignocellulosic biomass is often

referred to as a second-generation feedstock and is one of the most significant applications of biorefineries for the production of biofuels due to its abundance and affordability; moreover, its use does not affect the food supply. The potential biomass energy to be produced in 2050 has been estimated to be in the range of 150–450 exajoule/year, representing an equivalent amount of 76×10^9 barrels of oil equivalent.[3,6] Lignocellulosic biomass is a nonedible residue obtained from agriculture, forestry, urban, and industrial reuses.[7] It can be converted into solid, liquid, and gaseous fuels through various technologies of thermal, thermochemical, and biochemical conversion. Different reactions are involved in these steps, including hydrolysis, dehydration, isomerization, oxidation, dehydrogenation, and hydrogenation, which occur in processes such as combustion, pyrolysis, gasification, alcoholic fermentation, and liquefaction.[8]

In the biochemical conversion process, lignocellulosic biomass follows two production routes (those using ABE and isopropanol–butanol–ethanol). These production routes are challenged by low production yield and high energy use for separation.[9] Therefore, alternative separation techniques to distillation are more attractive and promising for integration. Several online recovery methods have been studied, including adsorption, liquid–liquid extraction, pervaporation, and gas stripping. Among them, adsorption is the most promising separation process to separate the required molecules from fermentation broths.[10] The material and energy balances reported by Qureshi et al. suggest that the energy needed to recover n-butanol from fermentation broth using zeolites as adsorbents is 1,948 kcal/kg compared to 5,789 kcal/kg through distillation or gas stripping.[11] The process of adsorption involves adsorbing the required molecules on the surface of the adsorbent (zeolite in this study) and then desorbing them by increasing the temperature. Different factors affect adsorption, such as adsorption capacity, selectivity, affinity, and desorption, which are subject to adsorbent type.[12] Existing adsorption separation techniques

are directly connected with high energy consumption but are still the most economical option.[11] However, these techniques are connected with cyclic work and the consumption of a substantial amount of steam for regeneration. Operating adsorption equipment requires regenerating part or all of the adsorbed components to be diverted to downstream facilities with a hot stream that may not be an economical choice. Increasing the temperature of the regeneration stream through a series of heat exchangers leads to higher consumption of steam and electricity, ultimately requiring more energy. This approach substantially increases operational costs, making it highly difficult to operate this separation process without having to reduce the energy associated with the process. Integrating separation with an additional reaction process (intensified process) to generate more valuable products is a highly attractive route for improving efficiency and thereby reducing costs. To address the impact of adsorption–desorption efficiency, the RD process optimizes the use of desorption energy to generate more valuable products and minimize the downstream processes needed to separate the hot stream from the desorbed components. This process has the potential to yield more valuable products and reduce equipment size and throughput. In this process, the desorbed outlet stream is integrated with an n-butanol steam reforming unit. There are two steps in the operation of this reaction system: adsorption and RD. In the first step, the fermentation stream is fed into an adsorber, and the adsorbent becomes slowly saturated with n-butanol. In the second step, the n-butanol is desorbed from the adsorbent by means of an inert regeneration gas (e.g., N_2) and an increase in temperature. The amount of heat released during the regeneration step is used for the integration with endothermic n-butanol steam reforming. The key point of this step is to use the energy used for adsorbent regeneration in the subsequent reaction step. The N_2 in the effluent may be used as a carrier gas.

Steam reforming is one primary routes for n-butanol that involves a strongly endothermic reaction ($\Delta H_{298}^{\circ} = 206.2$ and 558.3 kJ mol^{-1} for natural gas and n-butanol steam reforming, respectively); thus, the desorbed stream is useful for reducing this energy requirement.[13,14] N-butanol can be converted into H_2 through steam reforming,[15,16] POX,[17] dry reforming (DR),[18] and ATR. POX and ATR have faster start-up times due to exothermic reactions. However, the steam reforming process provides more H_2 yield and fewer side reactions. This process is conducted in two steps: first, n-butanol is converted to H_2, CO, and CO_2; then, CO is converted to CO_2 in the WGS reaction. Several studies have been conducted on steam reforming of n-butanol, and these have revealed that hydrogen-rich gas production from renewable biomass or biomass-derived chemicals is a promising hydrogen production direction.[19,20] To improve hydrogen production, minimize methane formation, and avoid coke deposition, thermodynamic analysis suggests operating the reforming process at a high temperature (>900 K), a high steam-to-n-butanol ratio (>9), and atmospheric pressure. However, under these operating conditions, the produced gas contains a high content of CO; thus, the WGS reaction is used to convert CO to CO_2. It is thermodynamically possible to perform steam reforming of oxygenates with a C:O ratio of 1:1 at 200–400 K less than that required by alkanes with a similar carbon number.[21] Oxygenated hydrocarbon reforming presents several advantages related to natural availability, including renewable production from several biomass utilization resources that require a dedicated and flexible processing facility. Like most industrial applications, this process is driven by economic constraints and sustainability criteria, such as low-cost operation and resource-efficient use. Therefore, the challenge is to produce environmentally friendly products with small carbon numbers having at least comparable or better properties than fossil fuels at competitive prices. Combining several processes in an integrated manner is useful for process optimization, and hence,

generating valuable marketable products.[22] One of the major challenges for efficient biomass processing is the ability to optimize product extraction. Currently used extraction and fractionation techniques may cause a dramatic loss of potential value for biomass components due to the pretreatment and separation steps. Hence, more research should focus on the maximization and process development of value extraction to establish cost-effective biorefinery operations for separation and upgrading as well as to meet the current infrastructure of fuel systems. Here, we present a current and potential application of adsorption by zeolites in process intensification. The objective of this paper is to outline and illustrate an alternative intensified process separation technique. In the initial stage of the study, the adsorption of n-butanol molecules from fermentation aqueous solution were investigated. Building on this foundation, an investigation of a possible integration process for a more intensified process of upgrading was undertaken. A thermodynamic approach to steam reforming of oxygenated n-butanol and a mixture of n-butanol and butene obtained from desorption[23,24] was studied to determine favorable operating conditions to produce hydrogen. The influences of steam, steam-to-fuel, and feed molar ratios and temperature on the product gas concentration were investigated. This effort to integrate experimental work with process simulation to develop a comprehensive design for separation and reaction of the system has rarely been discussed in the literature, and yet, further process improvements remain to be discovered. The analysis in this report includes product recovery specifications and process operations, and they are presented for two possible cases of integration. Finally, anticipated problems and further recommendations are mentioned.

3.3 Process Description

3.3.1 Baseline

3.3.1.1 Adsorption Process

Adsorption is defined as a separation process that involves two phases in which two components are separated. It is the result of interactive forces of physical attraction between surfaces of porous solids and component molecules being removed from the bulk phase.[25] First, the adsorption process is accomplished in a fixed bed using zeolites. Adsorption in liquid adsorbents is accomplished by passing the liquid down through a bed of zeolites in a liquid absorber. Another liquid absorber is used in the regeneration cycle. Zeolites have a strong affinity for some molecules, as determined by isotherm analysis.[26] Once zeolites are saturated, the liquid adsorber must be taken off-stream and regenerated using a hot-flow stream such as nitrogen. This occurs in every full cycle of adsorption until equilibrium conditions are approached and may also be influenced by bed performance and feed conditions. Adsorption is described through isotherms, which are functions that connect the amount of adsorbate taken by the adsorbent with the adsorptive equilibrium concentration c and temperature T, with all other parameters being constant.[27]

This connection is based on the pressure of the gas phase and the concentration of the liquid phase. In actual practice, adsorption isotherms represent the equilibrium states of an adsorption system. They give useful information about adsorbates, adsorbents, and adsorption processes.[28] This usefulness may be extended to the determination of adsorbent surface area, pore volume, and size distribution.[29] Furthermore, these isotherms give more information on the magnitudes of adsorption enthalpy as well as the relative adsorbability of a molecule on a solid surface at specific

standards. Different isotherm equations, such as those of Langmuir[30] and Freundlich,[31] might be used to represent the adsorption data. Figure 3.1 shows a simplified flow diagram of the adsorption process.

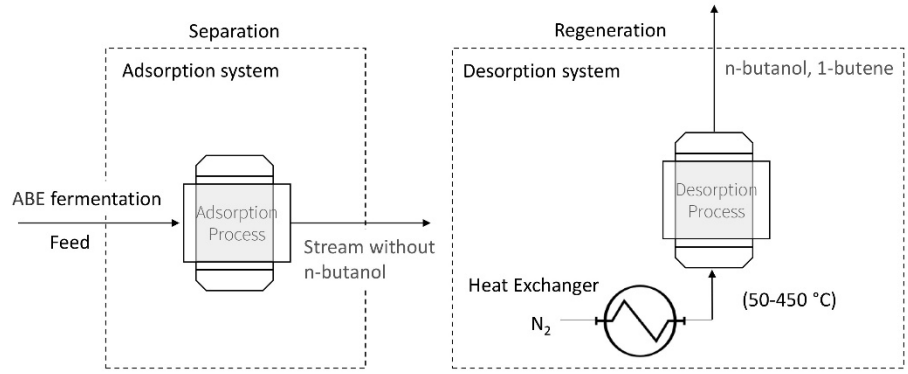

Figure 3.1. Simplified flow diagram of the adsorption process.

3.3.1.2 Steam Reforming Process

As shown in Figure 3.2, n-butanol is vaporized, mixed with steam, and heated to the inlet temperature of the reformer in the preheater. At lower temperatures, steam reforming of oxygenated hydrocarbons is favored thermodynamically to that of nonoxygenated hydrocarbons because the former is more exothermic.[32] The stoichiometric reaction of maximum hydrogen production is

$$C_xH_yO_z + (2x - z)H_2O \longrightarrow (2x - z + 0.5y)H_2 + xCO_2 \quad (1)$$

Steam reforming of oxygenated hydrocarbons involves complicated reaction systems that produce undesirable reaction paths.[33] To obtain the maximum hydrogen yield, the steam reforming process is completed in three steps: oxygenated hydrocarbon conversion to H_2, CH_4, CO, and CO_2;

a lower temperature step that converts CO to CO_2 and H_2 through the WGS reaction; and conversion of the remaining CO into CO_2 through preferential CO oxidation in a third reactor.[34]

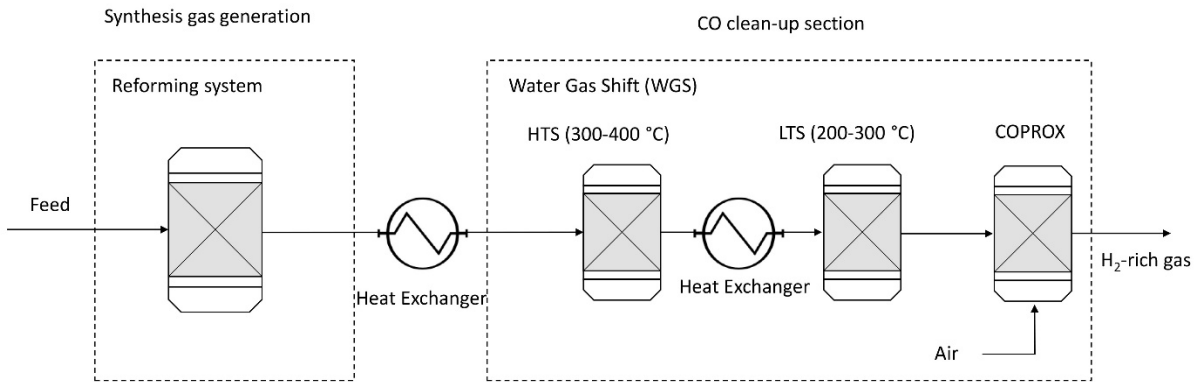

Figure 3.2. Simplified flow diagram of H_2 production from the n-butanol steam reforming process.

3.3.2 Advanced Process

Desorption is the reverse process of adsorption in which adsorbates are desorbed by increasing the temperature to produce concentrated adsorbates in the outlet stream.[35] Four common processes can be applied for desorption of adsorbed species: pressure swing, purge gas stripping, desorption displacement, and thermal swing operation. The first two processes are not practical in the case of n-butanol desorption due to the low vapor pressure of n-butanol at ambient temperature.[10,24] The RD process optimizes the use of desorption energy to generate more valuable products and minimize the downstream processes needed to separate the hot stream from the desorbed components. In this process, a regeneration gas is fed to the adsorbents from the compressor and hot gas stream. Reported desorption temperatures in the literature range from 200 to 450 °C for a desorption composition mixture of n-butanol and 1-butene.[24] Experimental recovery of n-butanol by desorption from adsorbates has resulted in an endothermic peak due to a

dehydration chemical reaction, leading to 1-butene formation.[23,24] Table 3.1 presents the compositions of n-butanol, 1-butene, and water desorbed from 0.385 g of dry extrudate at different temperatures. At 150 °C, 80% of the adsorbed n-butanol was desorbed, and the remaining 18% was desorbed as 1-butene at temperatures >250 °C.[23] A comparison of the two previous basic configurations suggests that a hybrid process should be explored to combine the advantages of the two basic configurations.

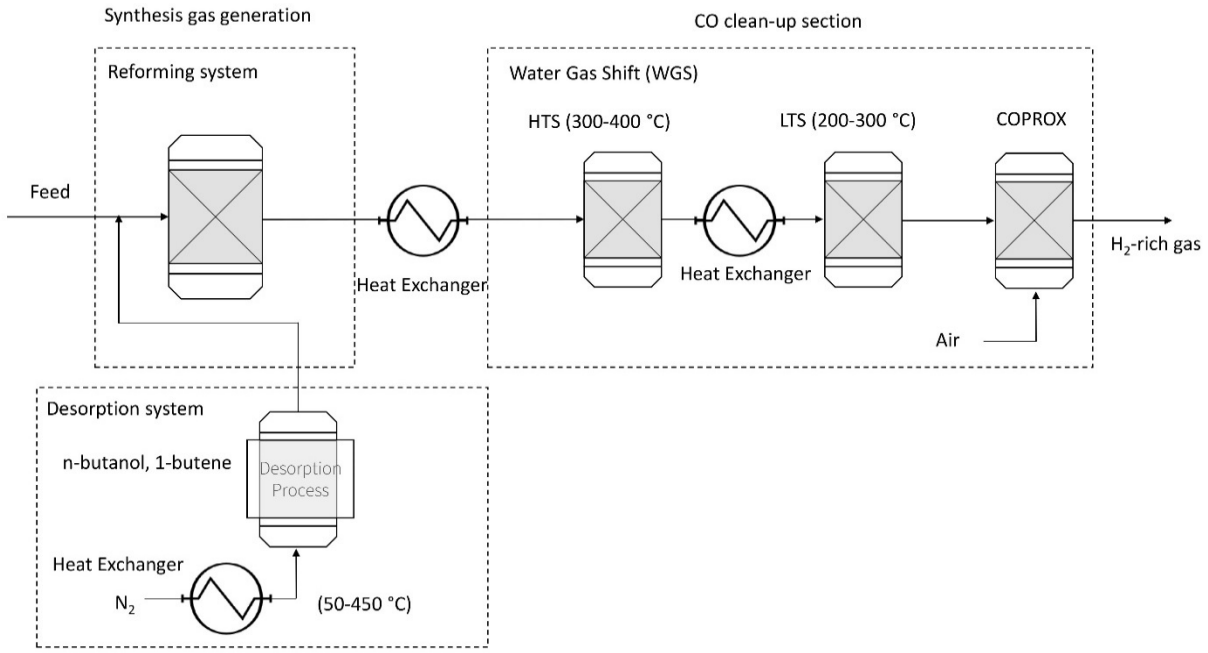

Figure 3.3. Simplified flow diagram of the integrated approach; the combined desorber–reactor system operation includes a desorption outlet feed to the steam reforming reactor.

Table 3.1. Compositions of n-butanol, 1-butene, and water desorbed from 0.385 g of dry extrudate (containing 0.308 g of zeolite) at different temperatures. The table was normalized in mmol/g of solid using the data in Saravanan (2009).[23]

Temperature (˚C)	Composition (mmol/g)		
	n-butanol	1-butene	water
50	0.33	0.0	16.01
150	1.24	0.0	0.29
250	0.0619	0.075	0.13
350	0.007	0.008	0.10
450	0	0.003	0.05

3.4 Modeling Methodology

3.4.1 Aspen Plus Flowsheet

Figure 3.4 shows an Aspen Plus flowsheet of the n-butanol steam reformer. Aspen Plus was used to perform all the equilibrium composition calculations. A "Gibbs reactor" was used to calculate the product composition and the heat of the overall reaction.

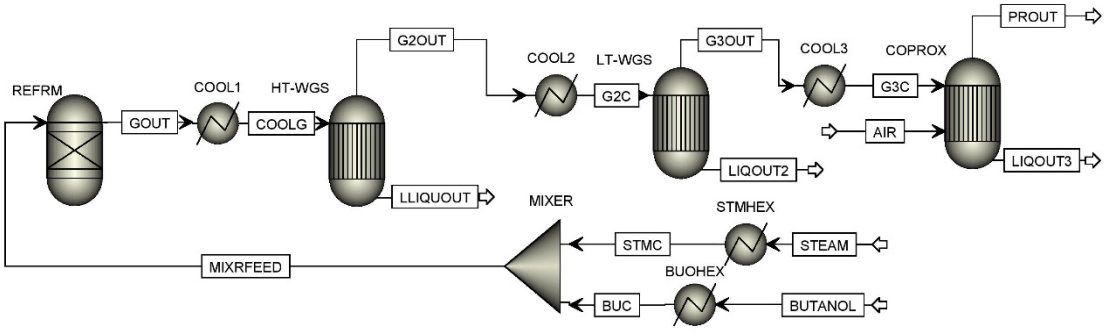

Figure 3.4. Aspen Plus flowsheet of the n-butanol steam reformer.

3.4.2 Minimization of Gibbs Free Energy

Minimization of the total Gibbs free energy is a suitable approach for calculating the equilibrium composition of any reaction system.[36] This approach accounts for the many simultaneous reactions that occur.

The Gibbs free energy of a system is given by

$$G^t = \sum_{i=1}^{N} n_i G_i = \sum_{i=1}^{N} n_i \mu_i = \sum_{i=1}^{N} \mu_i G_i^0 + RT \sum n_i \ln \frac{f_i}{f_i^0} \quad (2)$$

$$\mu_i = \Delta G_{fi}^0 + RT \ln \frac{f_i}{f_i^0} \quad (3)$$

where G^t is the total Gibbs free energy, N in the reaction system number of species, n_i is the moles of species i, μ_i is the chemical potential, ΔG_{fi}^0 is the standard Gibbs function of the formation of species i, R is the molar gas constant, T is the temperature of the system, f_i is the fugacity in the system, and f_i^0 is the standard-state fugacity. The equilibrium reaction in the gas phase is represented as

$$f_i = y_i \phi_i P, f_i^0 = P_0 \quad (4)$$

where P is the pressure of the system, ϕ_i is the fugacity coefficient of species i, y_i is the molar fraction of species i, and P_0 is the standard-state pressure.

By using the method of Lagrange multiplier, the minimum Gibbs free energy of the total system can be expressed as

$$\sum_{i=1}^{N} n_i a_{ik} = b_k \qquad k = 1, \dots M \quad (5)$$

$$\sum_{i=1}^{N} n_i \left(\Delta G_{fi}^0 + RT \ln \frac{f_i}{f_i^0} + \sum_k \lambda_i \alpha_{ik} \right) = 0 \quad (6)$$

A Gibbs reactor was used to calculate product compositions under conditions to minimize Gibbs free energy. The equation of state used for fugacity calculations was the Peng–Robinson method. In the simulations, the reaction temperature was varied in the range of 500–800 °C and 1 atm. The inlet steam-to-fuel molar ratio ranged from 1:1 to 20:1.

3.4.3 N-Butanol Reforming

The possible reactions of n-butanol steam reforming are described by Eqs. 7–25. The steam reforming process of $C_4H_{10}O$ produces H_2 and CO (Eq. 7). This is a strongly endothermic reaction

($\Delta H_{298}^{0} = -558.32\ kJ/mol$).[15,16] $C_4H_{10}O$ can dehydrogenate to butanal according to Eq. 18 ($\Delta H_{298}^{0} = -86.47\ kJ/mol$).

The n-butanol steam reforming process involves the following reactions[14,20]:

N-butanol steam reforming reaction

$$C_4H_{10}O + 3H_2O \leftrightharpoons 4CO + 8H_2 \qquad \Delta H_{298}^{0} = 558.32\ kJ/mol \qquad (7)$$

$$C_4H_{10}O + 7H_2O \leftrightharpoons 4CO + 12H_2 \qquad \Delta H_{298}^{0} = 394\ kJ/mol \qquad (8)$$

WGS reaction

$$CO + H_2O \leftrightharpoons CO_2 + H_2 \qquad \Delta H_{298}^{0} = -41.09\ kJ/mol \qquad (9)$$

Hydrogenation of carbon monoxide

$$CO + 3H_2 \leftrightharpoons CH_4 + H_2O \qquad \Delta H_{298}^{0} = -205.21\ kJ/mol \qquad (10)$$

$$CO + 4H_2 \leftrightharpoons CH_4 + 2H_2O \qquad \Delta H_{298}^{0} = -164.95\ kJ/mol \qquad (11)$$

$$2CO + 2H_2 \leftrightharpoons CO_2 + CH_4 \qquad \Delta H_{298}^{0} = -260.5\ kJ/mol \qquad (12)$$

Hydrogenation of carbon dioxide

$$CO_2 + 4H_2 \leftrightharpoons CH_4 + 2H_2O \qquad \Delta H_{298}^{0} = -165.0\ kJ/mol \qquad (13)$$

Methane steam reforming

$$CH_4 + H_2O \leftrightharpoons CO + 3H_2 \qquad \Delta H_{298}^{0} = 206\ kJ/mol \qquad (14)$$

$$CH_4 + 2H_2O \leftrightharpoons CO + 4H_2 \qquad \Delta H_{298}^{0} = 164.95\ kJ/mol \qquad (15)$$

Methane dry reforming

$$CH_4 + CO_2 \leftrightharpoons 2CO + 2H_2 \qquad \Delta H_{298}^0 = 247\ kJ/mol \qquad (16)$$

Reverse WGS (RWGS) reaction

$$CO_2 + H_2 \leftrightharpoons CO + H_2O \qquad \Delta H_{298}^0 = 41.09\ kJ/mol \qquad (17)$$

Dehydrogenation of n-butanol

$$C_4H_{10}O \leftrightharpoons C_4H_8O + H_2 \qquad \Delta H_{298}^0 = -86.47\ kJ/mol \qquad (18)$$

Dehydration of n-butanol

$$C_4H_{10}O \leftrightharpoons C_4H_8 + H_2O \qquad \Delta H_{298}^0 = -24.04\ kJ/mol \qquad (19)$$

Decomposition of n-butanol to propane

$$C_4H_{10} \rightleftharpoons C_3H_8 + CO + H_2O \qquad \Delta H_{298}^0 = 11.98\ kJ/mol \qquad (20)$$

Ethylene production

$$C_3H_8O \rightleftharpoons C_2H_4 + CH_4 \qquad \Delta H_{298}^0 = 81.65\ kJ/mol \qquad (21)$$

Ethylene to hydrogen

$$C_2H_4 \rightleftharpoons C_2H_2 + H_2 \qquad \Delta H_{298}^0 = 175.0\ kJ/mol \qquad (22)$$

Butene isomerization

$$C_4H_8 \leftrightharpoons i - C_4H_{10} \qquad (23)$$

$$C_4H_8 \leftrightharpoons cis - 2 - C_4H_{10} + trans - 2 - C_4H_{10} \qquad (24)$$

$$cis - 2 - C_4H_{10} + trans - 2 - C_4H_{10} \leftrightharpoons i - C_4H_{10} \qquad (25)$$

Butene hydrogenation

$$C_4H_8 + H_2 \leftrightharpoons C_4H_{10} \quad (26)$$

Butene reforming

$$C_4H_8 + 4H_2O \leftrightharpoons 4CO + 8H_2 \quad (27)$$

The equilibrium conversions of reactants and hydrogen yield

$$\text{Conversion of } C_4H_{10}O\ (\%) = \frac{F_{n-butanol,in} - F_{n-butanol,out}}{F_{n-butanol,in}} \times 100 \quad (28)$$

$$\text{Conversion of } H_2O\ (\%) = \frac{F_{H_2O,in} - F_{H_2O,out}}{F_{H_2O,in}} \times 100 \quad (29)$$

$$H_2 \text{ yield } (\%) = F_{H_2,in}/F_{C_4H_{10}O,in} \times 1/8 \quad (30)$$

The model described was used to perform sensitivity analysis. During sensitivity analysis, the model input values were kept the same, and a parameter was varied. The calculation procedure for thermal efficiency was based on the approach developed by He and collaborators.[19] In the conversion of fuel into hydrogen using a steam reforming process, the efficiency of the reaction can be calculated as follows:

$$\eta = \frac{n_{H_2}^{out} \cdot LHV_{H_2}}{\left(n_{fuel}^{in} \cdot LHV_{fuel} + Q_{input,SR} + n_{steam}^{in} \cdot \Delta H_{latent}\right)} \quad (31)$$

where $n_{H_2}^{out}$ is the number of moles of H_2 in the outlet stream at equilibrium, n_{fuel}^{in} and n_{steam}^{in} are the numbers of moles of fuel and steam in the inlet stream, respectively, ΔH_{latent} is the latent energy of the feed stream, LHV_{H_2} is the lower heating value of hydrogen, and LHV_{fuel} is the lower heating value of the fuel. The lower heating value of n-butanol is 2444.6 kJ mol^{-1}, and the lower heating value of hydrogen is 239.2 kJ mol^{-1}.

3.5 Experimental Methods

3.5.1 Materials

Zeolites with small-, medium-, and large-size pores and various Si/Al ratios were used to examine the thermodynamic, kinetic, and molecular sieve effects and their consequences on adsorption. The ammonium forms of BEA and MFI zeolites were purchased from Zeolyst International (see Table 3.2 for formulas and Si/Al ratios) and converted to the proton form through treatment in ambient air at 823 K (rate of 0.2 K s^{-1}) for 10 h. Methanol (99.8%, Sigma-Aldrich), ethanol (95%, Sigma-Aldrich), n-propanol (99.7%, Sigma-Aldrich), and n-butanol (99.4%, Sigma-Aldrich) were purchased and used as received without additional purification.

Table 3.2. Zeolite frameworks and properties.

Zeolite name	Framework	Si/Al	n
BEA	$\lvert H^+_n \rvert\ [Al_nSi_{64-n}O_{128}]$-*BEA	12.5	4.74
MFI	$\lvert H^+_n (H_2O)_{16} \rvert\ [Al_nSi_{96-n}O_{192}]$-MFI	11.5	7.6

3.5.2 Batch Adsorption Equilibria Tests

Adsorption isotherms were collected using 5 mL of 0.003–0.132 M aqueous solutions of methanol, ethanol, n-propanol, and/or n-butanol. Zeolite samples (0.1–0.5 g) were added to these solutions, and the solutions were shaken periodically until equilibrium was achieved (24–36 h). The concentration of alcohol(s) in the liquid was measured daily, and equilibrium was determined to have been reached when concentrations remained constant for more than 12 h. Analysis of the liquid phase was conducted using GC-MS (Agilent 5980 GC coupled to 7890 MS; Agilent J&W HP-5 GC Column, 50 m, 0.32 mm, 0.52 μm). The solutions were filtered using a 3-mL Monoject syringe fitted with a 0.2-μm polypropylene filter to remove solids before GC-MS analysis. Initial

and final liquid-phase concentrations, along with solution volumes, were used to calculate the number of molecules adsorbed onto zeolites. Measurements of molecules adsorbed into zeolites were only calculated through liquid-phase measurements. Solid-phase alcohol concentrations were expressed in terms of moles of adsorbate per mass of adsorbent, according to equation 31[37]:

$$q = (C_e - C_0)V/W \tag{32}$$

where C_0 and C_e represent the initial and equilibrium concentrations of adsorbate, respectively (mol/l), V is the volume of solution, and W is the mass of adsorbent.

3.6 Results and Discussion

3.6.1 Adsorption Capacities

Alcohols and water were absorbed in different types of zeolites. Zeolites exhibit molecular sieve properties due to well-defined pore and cavity structures. The effective channel detects whether a molecule that has a specific critical molecular diameter can diffuse into the cage and adsorb.

The maximum capacity for each individual component was estimated to be 2.2 and 1.7 [mmol/g] for n-butanol and n-propanol (Figure 3.5), respectively. A binary component system is the most straightforward system with which to study the effects of a multicomponent system. Competitive adsorption was noticed between n-butanol and n-propanol in their binary system. This is a simple illustration of the competitive adsorption case in which n-butanol affinity is much higher than that of methanol, leading to full active site occupation by n-butanol. In this case, the n-butanol adsorption isotherm was studied to account for the presence of other molecules.

Generally, the findings correspond to the single-component results and imply unaltered concentrations for n-butanol, meaning that the affinity of such molecules was not affected by the presence of smaller molecules within the same functional group. However, smaller molecules exhibited lower adsorption capacity in the presence of n-butanol, and these findings are in agreement with a previously concluded on a factor affecting adsorption performance, confinement.[26,38–43] The adsorption isotherms of n-butanol on MFI zeolites in the presence of methanol, ethanol, and n-propanol in binary solutions, each with n-butanol, show similar behavior as in those of the individual components, except for n-propanol with increased competitiveness to be presented. This finding could be attributed to the competition between these additional molecules for the same active sites that n-butanol is attracted to. The binary mixture of n-butanol and methanol exhibited almost identical adsorption constants. The second-most simplified competitive adsorption was that between n-butanol and n-propanol in BEA. Both molecules showed high adsorption capacity in their individual component systems, and as expected, they competed for the same active site, but the sites had high affinity towards n-butanol due to confinement and other effects, as indicated earlier. The presence of some interactions between different system components may have affected this result and changed the saturation adsorption capacity. In a multicomponent system, confinement has a major impact on competitiveness factors.

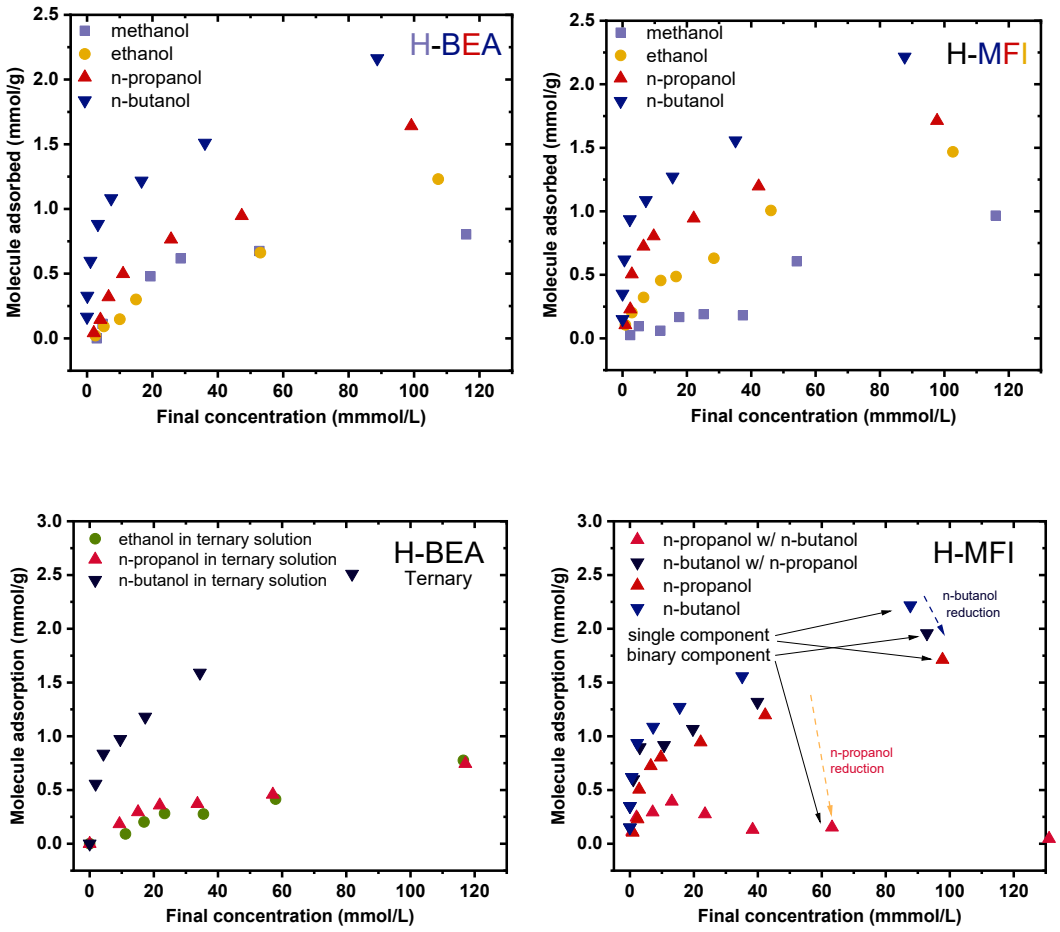

Figure 3.5. Equilibrium adsorption isotherms for single-component and multicomponent alcohols in aqueous solution for methanol (■ light blue), ethanol (● red), n-propanol (▲ light green), and n-butanol (▼ dark blue).

3.6.2 Steam Reforming

3.6.2.1 Baseline

A traditional steam n-butanol reforming (SBR)-based hydrogen production flowsheet is shown in Figure 3.4; its thorough material stream and energy flow data is provided in Tables 3.4-3.12. The baseline SBR design consists of the following reactor building blocks: SBR, high-temperature shift reaction, and low-temperature shift reaction. Each of these reactors operates near equilibrium and is modeled using a Gibbs free energy minimization reactor in Aspen Plus. The

overall flow sheet inlets are 1 kmol/h $C_4H_{10}O$ with varies flow rates of kmol/h H_2O, and the overall flow sheet outlets are 12 kmol/h H_2.The $C_4H_{10}O$ and H_2O streams are heated to 500–800 °C and then mixed to form the reformer feed, which has a $H_2O/C_4H_{10}O$ molar ratio of 2:20; the reformer operating pressure and temperature are1 bar and 500-800 °C, respectively.

Thermodynamic analysis predicts that during n-butanol reforming, hydrogen can be produced from steam reforming of n-butanol, as illustrated by reaction 1 (Eq. 7), reaction 2 (Eq. 8), the WGS reaction (Eq. 9), SMR and DR of methane (DRM; Eqs. 14, 15, and 16), and dehydrogenation of n-butanol (Eq. 18). Figure 3.6 shows the effects of the H_2O/C_4H_9OH ratio and temperature on n-butanol and H_2O conversion and H_2 yield. N-butanol conversion increased with an increase in either the H_2O/C_4H_9OH ratio or temperature (500–800 °C). More n-butanol was converted at higher temperatures due to endothermic steam reforming. An increase in temperature contributed to steam reforming and RWGS. The latter results in more H_2O generation, whereas the former reaction results in more H_2O consumption. The WGS reaction is endothermic, which means that with increasing temperature, CO and H_2 increase. The H_2 yield increases at low temperatures due to steam reforming and WGS. At a higher temperature of approximately 700 °C, the H_2 yield increases to its maximum value. Both steam reforming and RWGS are endothermic. The optimum steam reforming condition is determined by the maximization of reactant (C_4H_9OH and H_2O) conversion and H_2 yield. At low temperatures, carbon monoxide was low due to consumption in the carbon monoxide hydrogenation reaction (Eqs. 10, 11, and 12). Increasing temperature increased carbon monoxide yield as a result of SMR and DRM (Eqs. 14, 15, and 16) and RWGS (Eq. 17). This suggests that carbon monoxide formation can be inhibited at low temperatures. Increasing the amount of steam shifted the equilibrium toward the WGS reaction and the RWGS reaction toward hydrogen production. Figure 3.6 illustrates the effects of the

H_2O/C_4H_9OH ratio and temperature on CO conversion and H_2 yield. At low temperatures, almost no carbon monoxide was observed. However, carbon dioxide and methane are the predominant species to occur. Methane production is highest at the lowest temperature due to the methanation reaction (Eqs. 12–15). As the temperature increases, more H_2 is produced above 700 °C because of the inhibition of the exothermic WGS reaction (Eq. 9).

The hydrogen content in the effluent is high for reformer temperatures above 700 °C and increases slightly with increasing steam-to-n-butanol ratio. At temperatures >700 °C, the methane concentration decreases while the CO concentration increases, reaching a maximum at a low steam-to-n-butanol ratio and high temperature (T > 700 °C and H_2O/C_4H_9OH ratio of 2:1 to 3:1). The high concentration of CO is attributed to the WGS reaction behavior (reverse of Eq. 9). The RWGS reaction and SMR are predominant at reaction temperatures above 800 K (527 °C).[44] The addition of water increases H_2 and CO_2 while reducing CO and methane.

Figure 3.6 (d) shows the effects of temperature and the water/n-butanol molar ratio on the reaction conversion and product selectivity. It is evident that n-butanol converted to hydrogen more often at higher temperatures (>600 °C) and water conversion increased with temperature. Figure 3.6 (a) shows that energy increases have more impact with temperature than steam ratio, suggesting that temperature has the higher impact.

Analysis of the basic configuration through energy estimation (Figure 3.7) suggests that process designs with more complex arrangements should be explored to further reduce energy.

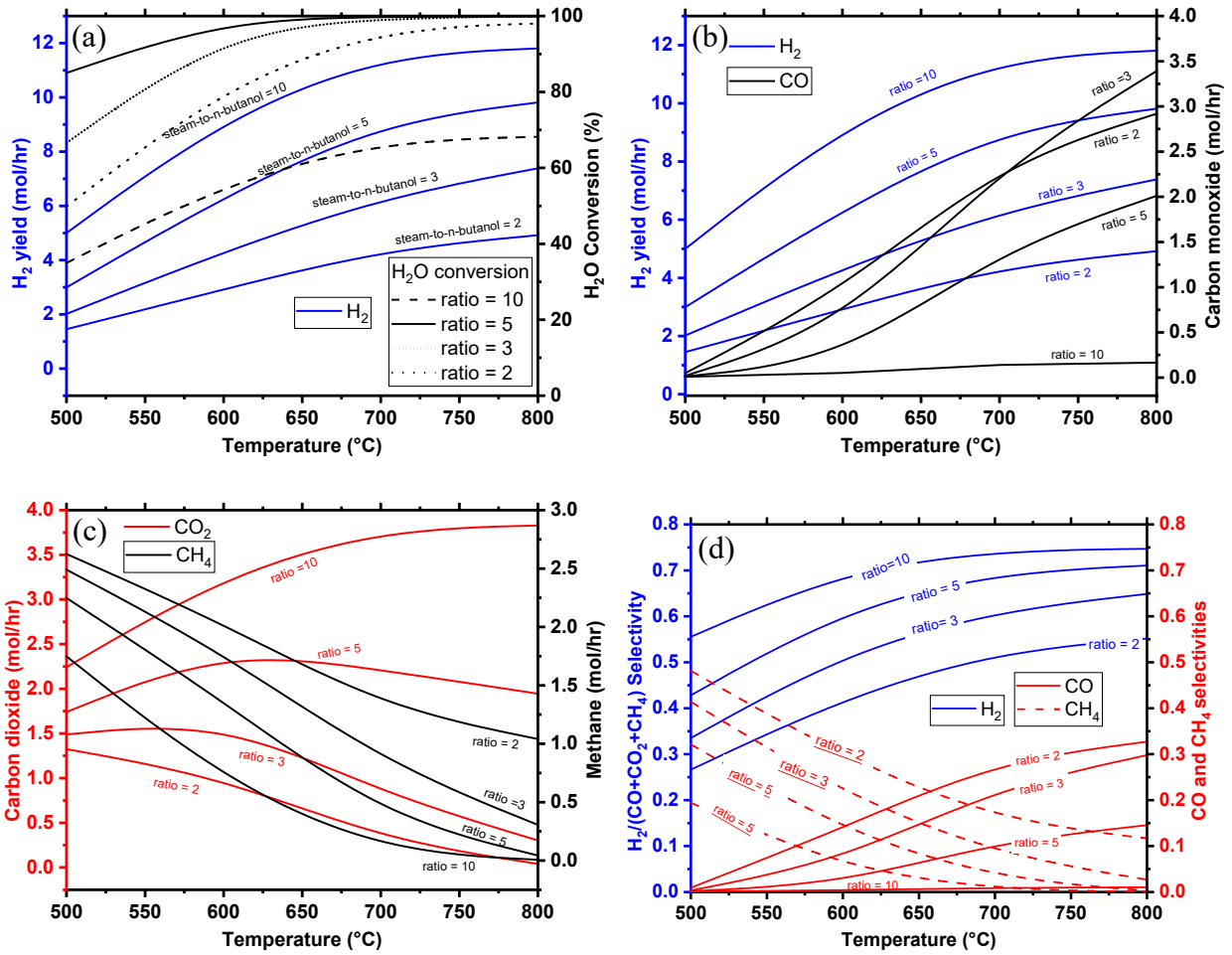

Figure 3.6. Effects of temperature and steam-to-n-butanol (H_2O/C_4H_9OH) molar ratio on the dry basis molar concentration flow rate of (a) H_2 and H_2O conversion, (b) H_2 and CO, (c) CO_2 and CH_4, and (d) H_2, CH_4, and CO product selectivities.

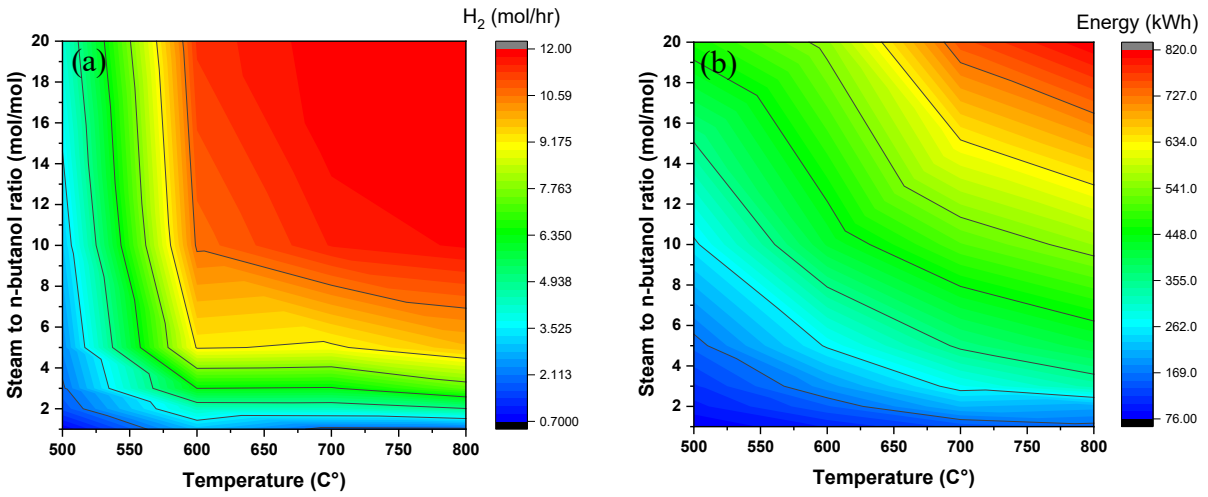

Figure 3.7. Influence of the reformer operating temperature and steam-to-n-butanol ratio on (a) hydrogen production and (b) total energy consumption by the process to obtain hydrogen yield in (a).

In this study, modeling was extended to evaluate the performance of a system with a complex arrangement. Heat integration analysis for SBR-based hydrogen production was performed for the baseline, and the integrated approach and results are shown in Figure 3.8. The heat integration method used in this paper was based on the Aspen Energy Analyzer using the pinch analysis methodology. Process data are presented as a set of streams with supply and target temperature and heat loads. Heating and cooling must be specified. For this process, the hot oil stream is hot enough to satisfy the heating load of the units. The composite curve is used to determine a minimum energy target for a given process system. These curves are profiles for heat availability (shown by the hot composite curve) and heat demand (shown by the cold composite curve). The potential heat for recovery through integration is measured by the overlap between the curves. Figure 3.9 shows the hot stream plotted on the temperature enthalpy diagram. Pinch analysis enables the target for minimum energy consumption for a detailed heat exchanger network to be set for energy-saving potential. The optimum heat exchanger design network that minimizes

cost and energy consumption is composed of eight heat exchangers. The results show that 290 MJ/s exothermic heat in the range of 500–700 °C is available to heat the baseline case. In addition, the integrated approach requires approximately 114 MJ/s of heat to increase the temperature of the reformer feed to 800 °C. Data obtained from the Aspen Energy Analyzer were used to determine the best heat integration strategy by using pinch analysis. Heat transfer demands determine the model flowsheet requirement for Aspen Plus (Figure 3.10). When heat integration is employed, process-to-process heat recovery leads to a reduction in the utility load and, consequently, operating costs. According to the model results, the integrated heat exchanger system exhibited lower energy consumption. The calculation results for the integrated process are presented in Figure 3.11. Both hydrogen yield and energy consumption were evaluated as a function of temperature and steam-to-n-butanol ratio. They were evaluated at five different values: 2, 3, 5, 10, and 15. The color corresponds to the ratio of severity. It is apparent that the curve of specific energy moves toward higher energy as the value of the steam-to-n-butanol ratio increases. Consequently, operating at 800 °C and a steam-to-n-butanol ratio of 10 creates the optimum condition that ensures the highest hydrogen yield and acceptable energy demand.

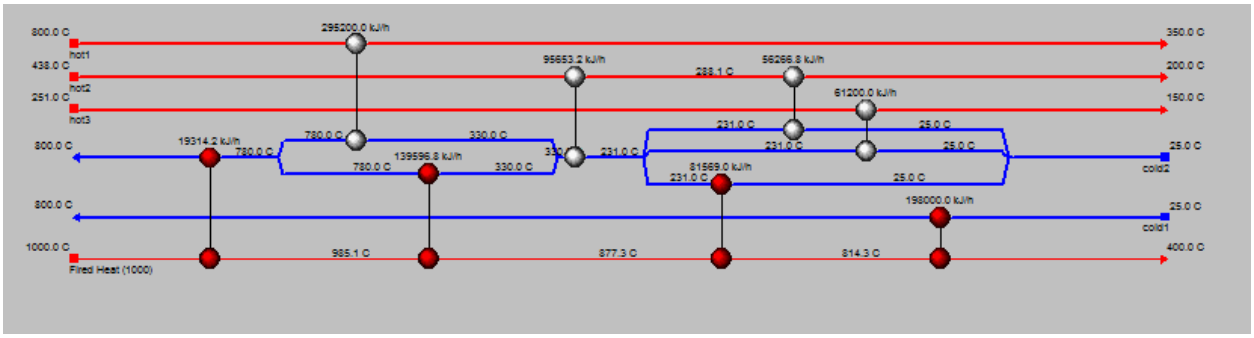

Figure 3.8. Heat exchanger network design of the n-butanol reformer.

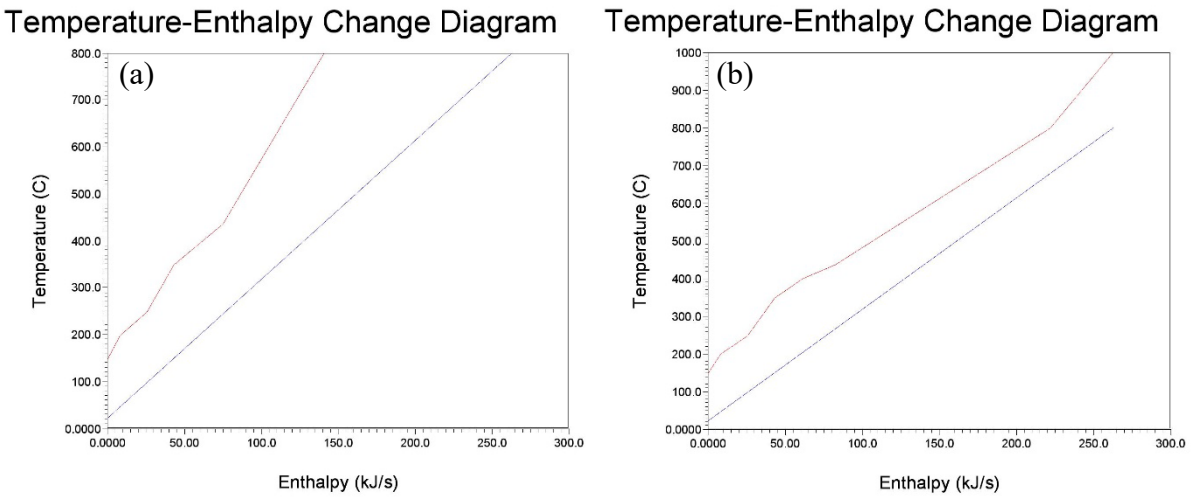

Figure 3.9. Heat exchanger network for (a) the baseline and (b) integrated approach showing the temperature−enthalpy change diagram.

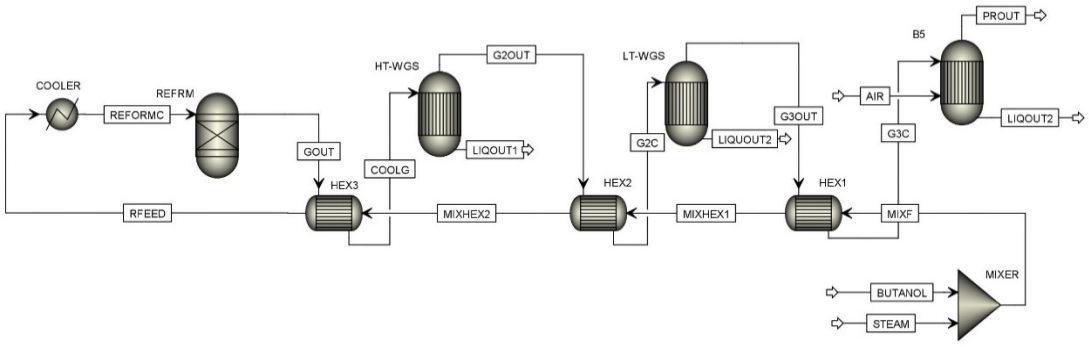

Figure 3.10. Integrated heat exchanger system.

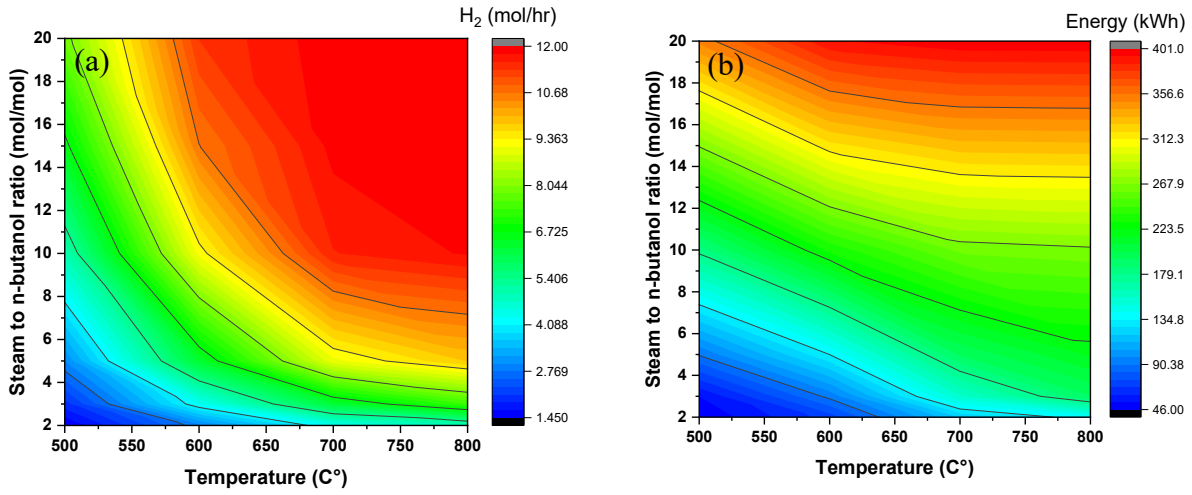

Figure 3.11. Influence of the reformer operating temperature and steam-to-n-butanol ratio on the (a) hydrogen production and (b) total energy consumption by the process to obtain hydrogen yield in (a).

From the analyzed temperature and steam-to-n-butanol feed ratio, hydrogen production increases when the temperature or steam-to-n-butanol ratio increases [Figure 3.12 (a)]. The best conditions for hydrogen production occur at T > 600 °C and a steam-to-n-butanol ratio of 10:1. Under these conditions, methane production is minimized, and carbon formation is inhibited thermodynamically. Above this temperature, the n-butanol conversion was always higher than 99.9%; that is, it can be conclude that conversion was completed in all cases.

Analysis of the product distributions obtained at different temperatures (500–800 °C) indicated that methane selectivity is equal to carbon selectivity, suggesting that n-butanol decomposition to CO, CH_4, and H_2 (Eq. 18) is the main reaction. Lower selectivity to CO_2 could be produced by either the WGS reaction or n-butanol reforming reaction. Increasing the temperature from 500 to 800 °C increases the conversion of water and yields more CO_2 as CO decreases. This means that n-butanol reforming (Eqs. 7 and 8) becomes more significant than n-butanol decomposition (Eq. 20) at 600 °C. When the temperature increases from 500 to 700 °C,

methane selectivity decreases while carbon monoxide and hydrogen selectivity increase. CO is mainly produced from SMR (Eqs. 14 and 15). If WGS occurs at 500 °C, then the CO_2/CO molar ratio increases with increasing steam-to-n-butanol ratio (Figure 3.12). By increasing the n-butanol/water feed ratio from 1 to 20, methane selectivity decreases (from 0.29 to 0.25), but hydrogen selectivity increases significantly.

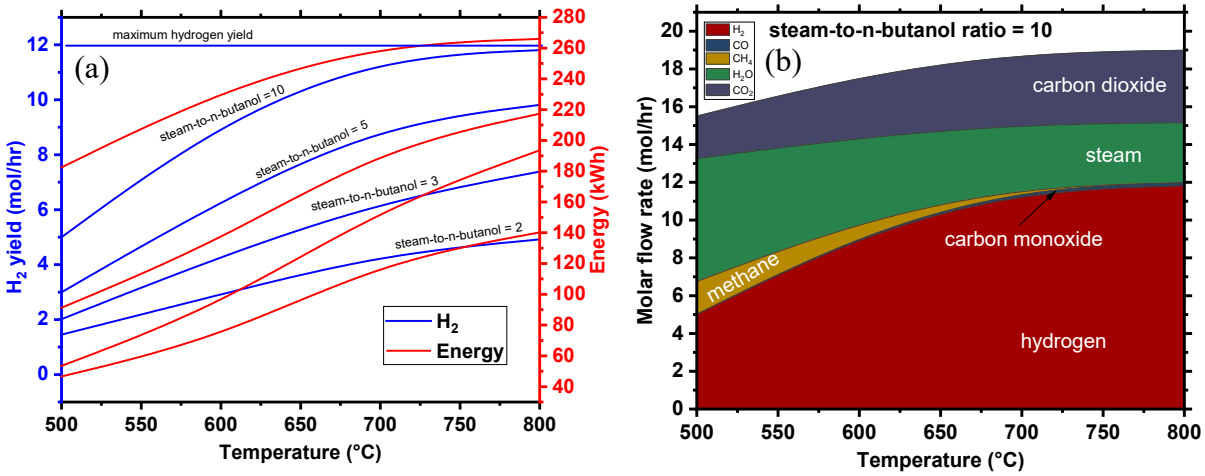

Figure 3.12. Effect of temperature on the reformer product proportions of H_2, CH_4, CO, H_2O, and CO_2. The shaded regions represent the molar hydrogen, carbon monoxide, carbon dioxide, and methane conversion from n-butanol and the unreacted steam.

Figure 3.13 illustrates the effect of temperature on the efficiency of the process. When the temperature increased from 300 to 700 °C, the efficiency increased from 20 to 90% until reaching a maximum value of 90%. H_2 production increased with increasing temperature, reached a maximum, and then stabilized. This is because the steam reforming process is an endothermic process, and at higher temperatures, the equilibrium is shifted toward the products yielding more H_2. By contrast, WGS and methanation reactions are exothermic, and these reactions shift toward the reactants when the temperature increases, causing more H_2 production and consumption during

the steam reforming process. Competition between the steam reforming reaction and the WGS and methanation reactions results in a plateau in H_2 productivity. The steam-to-n-butanol ratio provides no significant performance advantage. The efficiency increases and then decreases slightly. The equilibria of SR and WGS shift toward the product side, resulting in higher H_2 yield. With increasing steam-to-n-butanol ratio, the number of moles on the reactant side (Eqs. 7, 8, and 9) increases, and the equilibria of the steam reforming and WGS reactions shift to the right, producing more hydrogen.

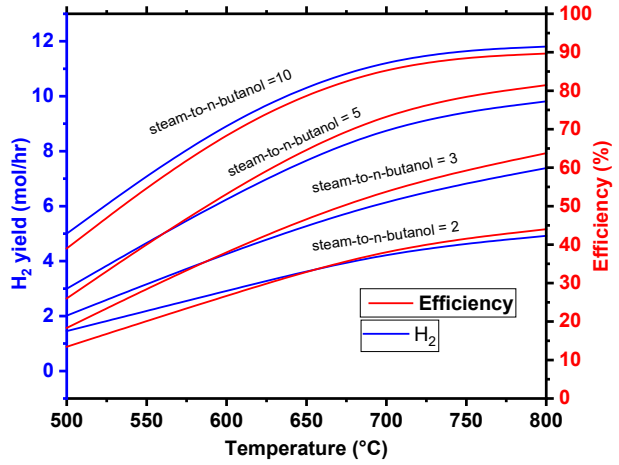

Figure 3.13. Effect of temperature on the thermal efficiency of the process (thermal efficiency is based on the approach developed by He and collaborators[19]).

3.6.3 Proposed RDSBR

The proposed reactive desorption steam n-butanol reforming (RDSBR) hydrogen production flow sheet is shown in Figure 3.14, and detailed material stream and energy flow information for three alternative RDSBR designs (all processing the same flowsheet) is provided in Tables S8, S9, S10, and S11. In this case, the temperature of the steam reformer was chosen to be 800 °C with a steam-to-n-butanol ratio of 10, as this was the optimum condition that produced

the highest yield of hydrogen. Then, the regeneration stream from desorption was fixed as 0.5 mol/h n-butanol (with 3 mol/h N_2), and the other 0.5 mol/h n-butanol was supplied from fresh feed. One of the advantages of the novel process is improving the energy of the process to desorb n-butanol and simultaneously make hydrogen. The application of product recovery through RD demonstrated that significant improvement can be achieved. In this process, the steam reformer harvests the energy from n-butanol desorption, which has nitrogen that enhances the reaction as well as n-butanol supplied at an elevated temperature. To obtain a better understanding of the process, the total energy consumption was divided into separate parts, thereby illustrating that the energy consumed by the steam reformer feed heater dropped from a value of 114 kWh to a value of 89 kWh for the case of coupling the desorber. An increase in the harvested energy can be achieved by changing the ratio of n-butanol obtained from the desorption of the ABE stream to n-butanol fresh feed. The calculation of results for SBR is first presented. The results exhibited superior (in reducing specific energy consumption) performance to that of the steam n-butanol reformer only. As indicated by the above analysis, more energy can be harvested in the RDSBR process. This indicates that improved designs can potentially be developed by coupling the desorption process with steam reforming.

Table 3.3. Performance Summary of Baseline SBR and Proposed RDSBR.

Performance summary	Baseline SBR (case a)	Baseline SBR with heat integration (case b)	Proposed RDSBR
Cooler 1, kW	82	-	-
Cooler 2, kW	42	-	-
Cooler 3, kW	17	-	-
Reformer feed heater, kW	263	114	89
Reformer, kW	151	151	151
Net power, MW	555	265	240

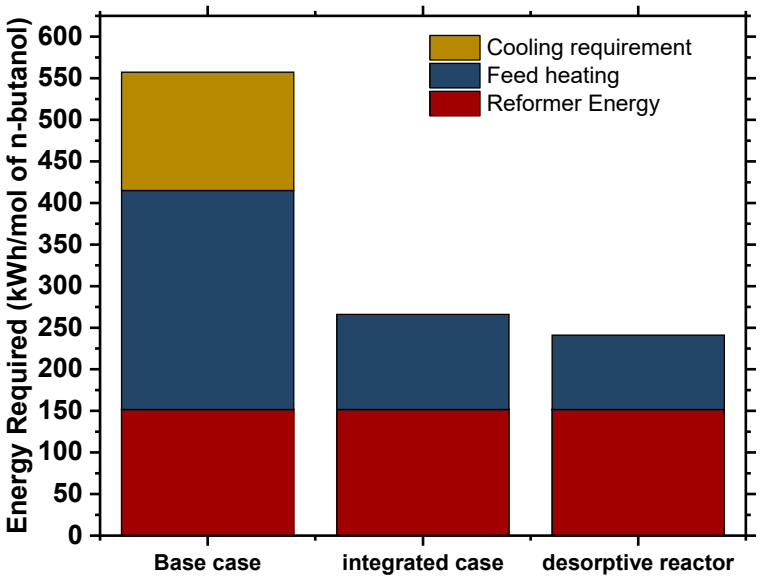

Figure 3.14. Specific power requirements for the n-butanol reforming process are divided into components (the orange color represents the cooling requirement, dark blue represents n-butanol feed heating, and dark red represents the reformer energy required to keep the temperature constant at 800 °C).

3.7 Conclusion

The intensification of an adsorption–desorption unit with an SBR process was investigated through the implementation of a combined RD reforming reactor. An Aspen simulation model was used for an intensified reactive desorber. The effect of varying temperature and steam injection on product composition was investigated. The thermodynamic equilibrium of n-butanol reforming was studied by employing Gibbs free energy minimization approach as a function of H_2O:C_4H_9OH ratio, CO_2:C_4H_9OH ratio, and reforming temperature. At a reforming temperature of 800 °C, the thermodynamic calculation result demonstrated good reaction performance within the region studied. The two reaction processes were SBR with and without the coupling reactive desorber. Favorable hydrogen production was obtained by using the scheme of a desorber with a steam reformer. The hydrogen yield in both processes can be enhanced by adding more steam to the reaction system. A comparison of the energy of the RDSBR process with that of an individual SBR indicates that RDSBR is a more effective process. This process enables energy reduction by 9.4% in hydrogen production. The study showed that integrating separation with an additional reaction process (an intensified process) to generate more valuable products was attractive method that improved efficiency and consequently costs. Process intensification based on these combinations costs less because reactions was induced simultaneously with separation. This process was beneficial because of its efficient energy and material utilization.

3.8 Appendix

Table 3.4. Energy Load information for Baseline Design of SBR (P=1 bar, T=500 °C) for 1 mol/h of initial n-butanal.

$C_4H_{10}O_{(i)}$ = 1 mol/h		Heat Load (kJ/s)					
Inlet H_2O (mol/h)	Outlet H_2 (mol/h)	n-butanol feed heater	steam feed heater	reformer energy	Cooler 2	Cooler 3	Cooler 4
1	0.73	35.49	17.46	0.00	-11.55	-9.17	-2.87
2	1.71	35.49	35.49	0.00	-12.71	-12.33	-5.35
3	2.03	35.49	52.39	0.00	-13.09	-13.75	-5.08
5	2.39	35.49	87.32	0.00	-13.46	-16.20	-5.40
10	3.02	35.49	174.63	0.00	-14.43	-23.32	-7.60
15	3.57	35.49	261.95	0.00	-15.66	-30.86	-10.03
20	4.09	35.49	349.27	0.00	35.49	35.49	-12.51

Table 3.5. Energy Load information for Baseline Design of SBR (P=1 bar, T=600 °C) for 1 mol/h of initial n-butanal.

$C_4H_{10}O_{(i)}$ = 1 mol/h		Heat Load (kJ/s)					
Inlet H_2O (mol/h)	Outlet H_2 (mol/h)	n-butanol feed heater	steam feed heater	reformer energy	Cooler 2	Cooler 3	Cooler 4
1	2.92	41.71	18.55	19.18	-16.59	-9.43	-2.86
2	4.32	41.71	37.10	34.08	-19.93	-13.68	-4.94
3	6.35	41.71	55.64	46.82	-23.14	-17.37	-7.89
5	9.23	41.71	92.74	67.98	-29.36	-23.11	-10.96
10	10.67	41.71	185.48	102.41	-44.17	-33.49	-12.40
20	11.36	41.71	278.22	119.19	-58.30	-41.35	-13.68

Table 3.6. Energy Load information for Baseline Design of SBR (P=1 bar, T=700 °C) for 1 mol/h of initial n-butanal.

$C_4H_{10}O_{(i)}$ = 1 mol/h		Heat Load (kJ/s)					
Inlet H_2O (mol/h)	Outlet H_2 (mol/h)	n-butanol feed heater	steam feed heater	reformer energy	Cooler 2	Cooler 3	Cooler 4
1	1.92	48.30	19.67	38.98	-24.19	-9.17	-2.84
2	4.36	48.30	39.34	82.76	-29.41	-13.00	-4.03
3	6.29	48.30	59.00	109.84	-34.24	-17.61	-5.85
5	9.08	48.30	98.34	134.38	-43.12	-26.41	-12.03
10	11.55	48.30	196.68	143.71	-63.45	-39.54	-16.58
15	11.87	48.30	295.02	141.65	-82.93	-46.59	-15.27
20	11.94	48.30	393.36	139.30	-102.12	-52.52	-16.00

Table 3.7. Energy Load information for Baseline Design of SBR (P=1 bar, T=800 °C).

$C_4H_{10}O_{(i)}$ = 1 mol/h		Heat Load (kJ/s)					
Inlet H_2O (mol/h)	Outlet H_2 (mol/h)	n-butanol feed heater	steam feed heater	reformer energy	Cooler 2	Cooler 3	Cooler 4
1	2.00	55.21	20.82	41.19	-31.87	-9.08	-2.84
2	4.92	55.21	41.65	55.21	-38.80	-12.12	-3.88
3	7.39	55.21	62.47	146.42	-45.37	-16.23	-5.10
5	9.82	55.21	104.11	158.06	-56.39	-27.51	-11.34
10	11.81	55.21	208.23	151.62	-82.23	-42.28	-17.71
15	11.95	55.21	312.34	146.84	-107.52	-49.74	-15.90
20	11.98	55.21	416.46	143.66	-132.57	-55.69	-16.31

Table 3.8. Equilibrium SBR Inlet and Outlet Conditions of reformer and WGS reactions (P=1 bar, T=500 °C) integrated case.

Inlet (mol/h)				Outlet (mol/h)				Heat Load (kJ/s)	
$C_4H_{10}O$	H_2O	CO	CH_4	H_2O	CO_2	H_2	$C_4H_{10}O$	reformer	heater
1	2	0.050	2.625	0.300	1.325	1.451	5.11E-19	-6.60	40.05
1	3	0.020	2.491	1.002	1.489	2.017	1.65E-19	-0.28	53.21
1	5	0.013	2.248	2.509	1.739	2.995	3.77E-20	11.87	79.43
1	10	0.010	1.748	6.505	2.243	5.000	3.68E-21	37.44	145.06
1	15	0.009	1.350	10.708	2.641	6.592	6.67E-22	57.83	211.04
1	20	0.008	1.030	15.068	2.962	7.873	1.51E-22	74.20	277.35

Table 3.9. Equilibrium SBR for Inlet and Outlet Conditions of reformer and WGS reactions (P=1 bar, T=600 °C) integrated case.

Inlet (mol/h)				Outlet (mol/h)				Heat Load (kJ/s)	
$C_4H_{10}O$	H_2O	CO	CH_4	H_2O	CO_2	H_2	$C_4H_{10}O$	reformer	heater
1	2	0.963	2.030	0.022	1.008	2.919	9.689E-19	34.08	37.62
1	3	0.572	1.779	0.130	1.649	4.313	3.052E-19	46.82	46.05
1	5	0.192	1.365	0.922	2.443	6.347	5.105E-20	67.98	66.85
1	10	0.051	0.681	4.413	3.268	9.226	1.511E-21	102.40	130.66
1	15	0.028	0.325	8.679	3.647	10.671	6.724E-23	119.19	198.00
1	20	0.019	0.157	13.333	3.824	11.353	3.856E-24	126.29	266.39

Table 3.10. Equilibrium SBR for Inlet and Outlet Conditions of reformer and WGS reactions (P=1 bar, T=700 °C) integrated case.

Inlet (mol/h)				Outlet (mol/h)				Heat Load (kJ/s)	
$C_4H_{10}O$	H2O	CO	CH4	H2O	CO2	H2	$C_4H_{10}O$	reformer	heater
1	2	2.369	1.317	0.003	0.314	4.362	5.75E-19	82.76	38.26
1	3	2.314	0.850	0.015	0.836	6.285	8.1E-20	109.84	46.05
1	5	1.408	0.379	0.166	2.213	9.076	3.23E-21	134.38	60.46
1	10	0.140	0.078	3.296	3.782	11.548	8.49E-24	143.70	118.63
1	15	0.040	0.025	8.089	3.936	11.861	1.18E-25	141.65	189.78
1	20	0.021	0.010	13.042	3.968	11.938	4.24E-27	139.30	260.32

Table 3.11. Equilibrium SBR Inlet and Outlet Conditions reformer and WGS reactions (P=1 bar, T=800 °C) integrated case.

Inlet (mol/h)				Outlet (mol/h)				Heat Load (kJ/s)	
$C_4H_{10}O$	H_2O	CO	CH_4	H_2O	CO_2	H_2	$C_4H_{10}O$	reformer	heater
1	2	2.919	1.040	0.000	0.040	4.919	5.99E-19	101.22	39.01
1	3	3.392	0.306	0.004	0.302	7.385	7.73E-21	146.42	47.20
1	5	2.011	0.043	0.098	1.946	9.816	1.17E-23	158.06	59.35
1	10	0.166	0.006	3.178	3.828	11.809	1.27E-26	151.62	114.39
1	15	0.042	0.002	8.046	3.956	11.950	1.92E-28	146.84	185.62
1	20	0.022	0.001	13.024	3.977	11.975	7.96E-30	256.41	143.65

Table 3.12. Base Case Material and Energy Stream Information.

Stream name	T (°C)	$C_4H_{10}O$ (mol/h)	CO (mol/h)	CO_2 (mol/h)	H_2O (mol/h)	H_2 (mol/h)	CH_4 (mol/h)
$C_4H_{10}O$ feed	307.6	1	0	0	0	0	0
steam feed	307.6	0	0	0	10	0	0
reformer feed	800	1	0	0	10	0	0
reformer outlet	800	0	2.452	1.542	5.465	9.523	0.006
HT WGS outlet	438.15		0.971	3.023	3.983	11.004	0.006
LT WGS outlet	251.06		0.160	3.833	3.173	11.815	0.006
Stream name	Energy Flow (kJ/s)						
n-butanol feed heater	55.21						
steam feed heater	208.23						
Reformer duty	151.62						
Cooler 2	-82.23						
Cooler 3	-42.28						
Cooler 4	-17.71						

Table 3.13. Integrated Case Material and Energy Stream Information.

Stream name	T (°C)	$C_4H_{10}O$ (mol/h)	CO (mol/h)	CO2 (mol/h)	H2O (mol/h)	H2 (mol/h)	CH4 (mol/h)
$C_4H_{10}O$ feed	307.6	1	0	0	0	0	0
steam feed	307.6	0	0	0	10	0	0
reformer feed	800	1	0	0	10	0	0
reformer outlet	800	0	2.452	1.542	5.465	9.523	0.006
HT WGS inlet	320	0	2.452	1.542	5.465	9.523	0.006
HT WGS outlet	416.08	0	0.855	3.139	3.867	11.120	0.006
LT WGS inlet	210	0	0.855	3.139	3.867	11.120	0.006
LT WGS outlet	251.06	0	0.166	3.828	3.178	11.809	0.006
LT WGS outlet cooled	110	0	0.166	3.828	3.178	11.809	0.006
Stream name	Energy Flow (kJ/s)						
Reformer feed heater	114.39						
Reformer duty	151.62						

Table 3.14. Reactive Desorption Case Material and Energy Stream Information.

Stream name	T (°C)	$C_4H_{10}O$ (mol/h)	CO (mol/h)	CO_2 (mol/h)	H_2O (mol/h)	H_2 (mol/h)	CH_4 (mol/h)	N_2 (mol/h)
$C_4H_{10}O$ fresh feed	307.6	0.5	0	0	0	0	0	0
$C_4H_{10}O$ feed from desorption	450	0.5	0	0	0	0	0	3
steam feed	307.6	0	0	0	10	0	0	0
reformer feed	800	1	0	0	10	0	0	3
reformer outlet	800	0	2.454	1.542	5.463	9.527	0.005	3
HT WGS inlet	320	0	2.454	1.542	5.463	9.527	0.005	3
HT WGS outlet	406.8		2.454	1.542	5.463	9.527	0.005	3
LT WGS inlet	210	0	0.807	3.188	3.817	11.174	0.005	3
LT WGS outlet	246.3		0.149	3.846	3.158	11.832	0.005	3
LT WGS outlet cooled	110	0	0.149	3.846	3.158	11.832	0.005	3
Stream name	Energy Flow (kJ/s)							
Reformer feed heater	89.42							
Reformer duty	151.62							

3.9 References

1. Owusu, P. A.; Asumadu-Sarkodie, S. A Review of Renewable Energy Sources, Sustainability Issues and Climate Change Mitigation. *Cogent Eng.* **2016**, *3* (1), 1167990. https://doi.org/10.1080/23311916.2016.1167990.
2. Asif, M.; Muneer, T. Energy Supply, Its Demand and Security Issues for Developed and Emerging Economies. *Renew. Sustain. Energy Rev.* **2007**, *11* (7), 1388–1413. https://doi.org/10.1016/j.rser.2005.12.004.
3. Corma, A.; Iborra, S.; Velty, A. Chemical Routes for the Transformation of Biomass into Chemicals. *Chem. Rev.* **2007**, *107* (6), 2411–2502. https://doi.org/10.1021/cr050989d.
4. Werpy, T.; Petersen, G. *Top Value Added Chemicals from Biomass: Volume I -- Results of Screening for Potential Candidates from Sugars and Synthesis Gas*; United States, 2004. https://doi.org/10.2172/15008859.
5. IEA; Eisentraut, A.; Brown, A. Technology Roadmap: Bioenergy for Heat and Power. *Manag. Environ. Qual. An Int. J.* **2012**, *24* (1), 1–41. https://doi.org/10.1108/meq.2013.08324aaa.005.
6. Huber, G. W.; Iborra, S.; Corma, A. Synthesis of Transportation Fuels from Biomass: Chemistry, Catalysts, and Engineering. *Chem. Rev.* **2006**, *106* (9), 4044–4098. https://doi.org/10.1021/cr068360d.
7. Nanda, S.; Azargohar, R.; Dalai, A. K.; Kozinski, J. A. An Assessment on the Sustainability of Lignocellulosic Biomass for Biorefining. *Renew. Sustain. Energy Rev.* **2015**, *50*, 925–941.
8. Foust, T. D.; Aden, A.; Dutta, A.; Phillips, S. An Economic and Environmental Comparison of a Biochemical and a Thermochemical Lignocellulosic Ethanol Conversion Processes. *Cellulose* **2009**, *16* (4), 547–565. https://doi.org/10.1007/s10570-009-9317-x.
9. Ezeji, T. C.; Qureshi, N.; Blaschek, H. P. Butanol Fermentation Research: Upstream and

Downstream Manipulations. *Chem. Rec.* **2004**, *4* (5), 305–314. https://doi.org/10.1002/tcr.20023.

10. Oudshoorn, A.; Van Der Wielen, L. A. M.; Straathof, A. J. J. Assessment of Options for Selective 1-Butanol Recovery from Aqueous Solution. *Ind. Eng. Chem. Res.* **2009**, *48* (15), 7325–7336. https://doi.org/10.1021/ie900537w.
11. Qureshi, N.; Hughes, S.; Maddox, I. S.; Cotta, M. A. Energy-Efficient Recovery of Butanol from Model Solutions and Fermentation Broth by Adsorption. *Bioprocess Biosyst. Eng.* **2005**, *27* (4), 215–222. https://doi.org/10.1007/s00449-005-0402-8.
12. Bonenfant, D.; Kharoune, M.; Niquette, P.; Mimeault, M.; Hausler, R. Advances in Principal Factors Influencing Carbon Dioxide Adsorption on Zeolites. *Sci. Technol. Adv. Mater.* **2008**, *9* (1), 13007. https://doi.org/10.1088/1468-6996/9/1/013007.
13. Chen, Z.; Po, F.; Grace, J. R.; Jim Lim, C.; Elnashaie, S.; Mahecha-Botero, A.; Rakib, M.; Shirasaki, Y.; Yasuda, I. Sorbent-Enhanced/Membrane-Assisted Steam-Methane Reforming. *Chem. Eng. Sci.* **2008**, *63* (1), 170–182. https://doi.org/https://doi.org/10.1016/j.ces.2007.09.031.
14. Wang, W.; Cao, Y. Hydrogen Production via Sorption Enhanced Steam Reforming of Butanol: Thermodynamic Analysis. *Int. J. Hydrogen Energy* **2011**, *36* (4), 2887–2895. https://doi.org/https://doi.org/10.1016/j.ijhydene.2010.11.110.
15. Nahar, G. A.; Madhani, S. S. Thermodynamics of Hydrogen Production by the Steam Reforming of Butanol: Analysis of Inorganic Gases and Light Hydrocarbons. *Int. J. Hydrogen Energy* **2010**, *35* (1), 98–109. https://doi.org/https://doi.org/10.1016/j.ijhydene.2009.10.013.
16. Bimbela, F.; Oliva, M.; Ruiz, J.; García, L.; Arauzo, J. Catalytic Steam Reforming of Model Compounds of Biomass Pyrolysis Liquids in Fixed Bed: Acetol and n-Butanol. *J. Anal. Appl.*

Pyrolysis **2009**, *85* (1), 204–213. https://doi.org/https://doi.org/10.1016/j.jaap.2008.11.033.

17. Wang, W.; Cao, Y. Hydrogen-Rich Gas Production for Solid Oxide Fuel Cell (SOFC) via Partial Oxidation of Butanol: Thermodynamic Analysis. *Int. J. Hydrogen Energy* **2010**, *35* (24), 13280–13289. https://doi.org/https://doi.org/10.1016/j.ijhydene.2010.09.031.
18. Wang, W. Hydrogen Production via Dry Reforming of Butanol: Thermodynamic Analysis. *Fuel* **2011**, *90* (4), 1681–1688. https://doi.org/10.1016/j.fuel.2010.11.001.
19. He, L.; Parra, J. M. S.; Blekkan, E. A.; Chen, D. Towards Efficient Hydrogen Production from Glycerol by Sorption Enhanced Steam Reforming. *Energy Environ. Sci.* **2010**, *3* (8), 1046–1056. https://doi.org/10.1039/B922355J.
20. Hartley, U. W.; Amornraksa, S.; Kim-Lohsoontorn, P.; Laosiripojana, N. Thermodynamic Analysis and Experimental Study of Hydrogen Production from Oxidative Reforming of N-Butanol. *Chem. Eng. J.* **2015**, *278*, 2–12. https://doi.org/10.1016/j.cej.2015.02.016.
21. Huber, G. W.; Dumesic, J. A. An Overview of Aqueous-Phase Catalytic Processes for Production of Hydrogen and Alkanes in a Biorefinery. *Catal. Today* **2006**, *111* (1–2), 119–132. https://doi.org/10.1016/j.cattod.2005.10.010.
22. Agrimi; Alexopoulou, E.; Bartzoka, E. D.; Buonerba, A.; Cavani, F.; Christou, M.; Colucci, A.; Couturier, J.-L.; Crestini, C.; Dubois, J.-L. *Biorefineries: An Introduction*; Walter de Gruyter GmbH & Co KG, 2015.
23. Saravanan, V.; Waijers, D. A.; Ziari, M.; Noordermeer, M. A. Recovery of 1-Butanol from Aqueous Solutions Using Zeolite ZSM-5 with a High Si/Al Ratio; Suitability of a Column Process for Industrial Applications. *Biochem. Eng. J.* **2010**, *49* (1), 33–39. https://doi.org/https://doi.org/10.1016/j.bej.2009.11.008.
24. Oudshoorn, A.; van der Wielen, L. A. M.; Straathof, A. J. J. Desorption of Butanol from Zeolite

Material. *Biochem. Eng. J.* **2012**, *67*, 167–172. https://doi.org/10.1016/j.bej.2012.06.014.

25. Thomas, W. J.; Crittenden, B. *The Development of Adsorption Technology*; Butterworth-Heinemann, 1998. https://doi.org/10.1016/b978-075061959-2/50002-1.
26. Mallon, E. E.; Babineau, I. J.; Kranz, J. I.; Guefrachi, Y.; Siepmann, J. I.; Bhan, A.; Tsapatsis, M. Correlations for Adsorption of Oxygenates onto Zeolites from Aqueous Solutions. *J. Phys. Chem. B* **2011**, *115* (39), 11431–11438. https://doi.org/10.1021/jp208143t.
27. Koble, R. A.; Corrigan, T. E. Adsorption Isotherms for Pure Hydrocarbons. *Ind. Eng. Chem.* **1952**, *44* (2), 383–387.
28. Dąbrowski, A. Adsorption—from Theory to Practice. *Adv. Colloid Interface Sci.* **2001**, *93* (1–3), 135–224.
29. Chapter 12 The Use of Adsorption Methods for the Assessment of the Surface Area and Pore Size Distribution of Heterogeneous Catalysts. In *Catalysis*; Moulijn, J. A., van Leeuwen, P. W. N. M., van Santen, R. A. B. T.-S. in S. S. and C., Eds.; Elsevier, 1993; Vol. 79, pp 419–438. https://doi.org/https://doi.org/10.1016/S0167-2991(08)63816-1.
30. Langmuir, I. THE ADSORPTION OF GASES ON PLANE SURFACES OF GLASS, MICA AND PLATINUM. *J. Am. Chem. Soc.* **1918**, *40* (9), 1361–1403. https://doi.org/10.1021/ja02242a004.
31. Freundlich, H. Über Die Adsorption in Lösungen. *Zeitschrift für Physikalische Chemie*. 1907, p 385. https://doi.org/10.1515/zpch-1907-5723.
32. Sutton, D.; Kelleher, B.; Ross, J. R. H. Review of Literature on Catalysts for Biomass Gasification. *Fuel Process. Technol.* **2001**, *73* (3), 155–173. https://doi.org/10.1016/S0378-3820(01)00208-9.
33. Sun, J.; Wang, Y. Recent Advances in Catalytic Conversion of Ethanol to Chemicals. *ACS*

Catal. **2014**, *4* (4), 1078–1090.

34. Lima da Silva, A.; Müller, I. L. Hydrogen Production by Sorption Enhanced Steam Reforming of Oxygenated Hydrocarbons (Ethanol, Glycerol, n-Butanol and Methanol): Thermodynamic Modelling. *Int. J. Hydrogen Energy* **2011**, *36* (3), 2057–2075. https://doi.org/https://doi.org/10.1016/j.ijhydene.2010.11.051.
35. Brauer, H.; Varma, Y. B. G. Design and Operation of Adsorption Equipment BT - Air Pollution Control Equipment; Brauer, H., Varma, Y. B. G., Eds.; Springer Berlin Heidelberg: Berlin, Heidelberg, 1981; pp 307–333. https://doi.org/10.1007/978-3-642-67905-6_10.
36. Perry, J. H. Chemical Engineers' Handbook. ACS Publications 1950.
37. Worch, E. *Adsorption Technology in Water Treatment*; De Gruyter, 2012. https://doi.org/10.1515/9783110240238.
38. Goerlitz, R.; Weisleder, L.; Wuttig, S.; Trippel, S.; Karstens, K.; Goetz, P.; Niebelschuetz, H. Bio-Butanol Downstream Processing: Regeneration of Adsorbents and Selective Exclusion of Fermentation by-Products. *Adsorption* **2018**, *24* (1), 95–104. https://doi.org/10.1007/s10450-017-9918-x.
39. Raganati, F.; Procentese, A.; Olivieri, G.; Russo, M. E.; Salatino, P.; Marzocchella, A. Bio-Butanol Separation by Adsorption on Various Materials: Assessment of Isotherms and Effects of Other ABE-Fermentation Compounds. *Sep. Purif. Technol.* **2018**, *191*, 328–339. https://doi.org/10.1016/j.seppur.2017.09.059.
40. Van der Perre, S.; Gelin, P.; Claessens, B.; Martin-Calvo, A.; Cousin Saint Remi, J.; Duerinck, T.; Baron, G. V.; Palomino, M.; Sánchez, L. Y.; Valencia, S.; et al. Intensified Biobutanol Recovery by Using Zeolites with Complementary Selectivity. *ChemSusChem* **2017**, *10* (14), 2968–2977. https://doi.org/10.1002/cssc.201700667.

41. Nguyen, C. M.; Reyniers, M. F.; Marin, G. B. Adsorption Thermodynamics of C1-C4 Alcohols in H-FAU, H-MOR, H-ZSM-5, and H-ZSM-22. *J. Catal.* **2015**, *322*, 91–103. https://doi.org/10.1016/j.jcat.2014.11.013.

42. Nguyen, C. M.; Reyniers, M. F.; Marin, G. B. Theoretical Study of the Adsorption of C1-C4 Primary Alcohols in H-ZSM-5. *Phys. Chem. Chem. Phys.* **2010**, *12* (32), 9481–9493. https://doi.org/10.1039/c000503g.

43. Van Der Mynsbrugge, J.; Hemelsoet, K.; Vandichel, M.; Waroquier, M.; Van Speybroeck, V. Efficient Approach for the Computational Study of Alcohol and Nitrile Adsorption in H-ZSM-5. *J. Phys. Chem. C* **2012**, *116* (9), 5499–5508. https://doi.org/10.1021/jp2123828.

44. Adhikari, S.; Fernando, S.; Gwaltney, S. R.; Filip To, S. D.; Mark Bricka, R.; Steele, P. H.; Haryanto, A. A Thermodynamic Analysis of Hydrogen Production by Steam Reforming of Glycerol. *Int. J. Hydrogen Energy* **2007**, *32* (14), 2875–2880. https://doi.org/10.1016/j.ijhydene.2007.03.023.

Chapter 4: Sensitivity Analysis of an Intensified CO_2 Mineralization-based Scheme and RO Desalination Process in Ca^{2+}/Mg^{2+}-Rich Aqueous Solutions for CO_2 Management

4.1 Abstract

A CO_2 capture process which is based on the use of MEA absorption was simulated using Aspen Plus and compared with proposed CO_2 mineralization in Ca^{2+}/Mg^{2+}-rich aqueous solutions that enable carbon capture. This paper proposes two baseline reference CO_2-capturing technologies: conventional carbon capture and storage technology (CCS) and CO_2 mineralization technology. For sensitivity analysis, simulations were conducted that kept all parameters constant except for the studied parameter to evaluate the degree to which economic feasibility was influenced by the studied parameter. A process design that achieved maximum CO_2 utilization was considered as the base case in which all of the used CO_2 was converted to carbonates, $MgCO_3$, $CaCO_2$, and $NaHCO_3$. Here, we propose integrating CO_2 mineralization and RO desalination pretreatment into a single process as a potential approach to enhance the efficiency and energy utilization of CO_2 capture. This study proposes a calcium and magnesium production process that involves injecting low-concentration CO_2 (8–15 vol %) from flue gas into a carbonation process in a desalination plant. The feasibility of the overall process was analyzed by calculating the energy required for a standalone desalination pretreatment process and a standalone CO_2 mineralization process to the hybrid process.

4.2 Introduction

Anthropogenic emission of CO_2, mainly induced by fossil fuel combustion, contributes to CO_2 accumulation in the atmosphere. In 2004, global CO_2 emissions were 27.4 Gt and have been increasing dramatically since then, reaching 33.4 Gt in 2016. Consequently, mitigation efforts to achieve atmospheric CO_2 concentration stabilization at 500 ppm are needed.[1] Different geoengineering techniques have been proposed for the direct decarbonization of the global atmosphere, each with different costs and environmental consequences.[2] The large scale of CCS suggests a combination of different techniques would be most practical.[3]

Mineral carbonation has been emerging as a potential carbon capture, utilization, and storage technology solution to sequester CO_2 from medium-size emitters when geological sequestration is not a viable option. These processes offer a leakage-free alternative to geological storage of CO_2 and represent an environmentally friendly process that requires little effort to monitor. In this process, CO_2 is chemically reacted with sodium-, calcium-, and magnesium-containing materials to form stable carbonates.[4] The mineralized carbon can then be disposed of at the Earth's surface. The large carbon storage capacity, minimal environmental impact, and low risk of late CO_2 release suggest the viability of the proposed scheme as a primary means of long-term Gt-scale CO_2 waste management.

Initially, CO_2 mineralization was developed by the reaction between CO_2 and natural alkaline silicate ores, such as serpentine [$Mg_3Si_2O_5(OH)_4$],[4–7] wollastonite ($CaSiO_3$),[8–12] olivine [$(Fe_x,Mg_{1-x})_2SiO_4$],[13–16] dolomite,[10,17–19] and albite.[20] Mineral carbonation of Mg-Ca-Fe-silicates has high carbonation potential (>10,000 Gt C)[21] and typically requires 2 tons of silicate mineral per ton of CO_2 capture. A carbonation reaction occurs when a metal oxide such as calcium oxide or magnesium oxide reacts with CO_2 to yield calcium or magnesium carbonate.

$CaO + CO_2 \rightarrow CaCO_3$ $\Delta H = -179$ (KJ/mol) (1)

$MgO + CO_2 \rightarrow MgCO_3$ $\Delta H = -118$ (KJ/mol) (2)

Olivine (forsterite)

$Mg_2SiO_4 + 2CO_2 \rightarrow 2MgCO_3 + SiO_2$ $\Delta H = -89$ (KJ/mol) (3)

Wollastonite

$CaSiO_3 + CO_2 \rightarrow CaCO_3 + SiO_2$ $\Delta H = -87$ (KJ/mol) (4)

Serpentine

$Mg_3Si_2O_5(OH)_4 + 3CO_2 \rightarrow 3MgCO_3 + 2SiO_2 + 2H_2O$ $\Delta H = -64$ (KJ/mol) (5)

Although these approaches can stably store CO_2 for thousands of years, their low reaction rate and high energy consumption limit the application of these methods in industrial implementation, which entails large-scale mining and disposal operations. For example, an 18 ton/day mining operation would be able to capture 18 Mt of CO_2 per year, enough to serve roughly five 500-MWe-fired power stations.[22]

Apart from mining-based applications, alkaline waste from various industrial applications is used as feedstock in CO_2 mineral carbonation. Recent studies have demonstrated an ability to improve the mineralization process using natural minerals and solid waste.[8,23–26] Kodama et al.[27] used steelmaking slag and ammonium chloride solution to convert CO_2 to $CaCO_3$. Nduagu et al.[28] used magnesium silicates and ammonium sulfate to produce magnesium hydroxide that absorbs CO_2 and produces $MgCO_3$. Xie et al.[29,30] used phosphogypsum waste, magnesium chloride, and potash feldspar to mineralize CO_2 and produce valuable products. Although quantities of waste are not available at the Gt scale for a mineral carbonation feedstock, the quantities are still substantial enough to warrant integration in industries that produce the waste to reduce emissions. These wastes contain a significant amount of calcium oxide or hydroxide (15% for concrete waste,

40% for steel slag). Many of these waste products have reusable values of 5–10 ($/ton), making them comparable to or possibly higher than the expected cost of natural mineral feedstock. These processes use less energy and produce higher value–added products. Energy and cost of solid alkaline materials are primarily dependent on the plant's scale, operating conditions, and operation modulus, including pretreatments such as grinding, thermal activation, and product disposal.[31,32] A multiwaste treatment integration approach is implemented using CO_2 in the flue gas as a chemical stabilizer for active components in alkaline solid wastes. From an economic perspective, the carbonation reaction reduces the treatment cost associated with wastewater and increases the value of alkaline solid waste simultaneously. Energy-intensive processes associated with feedstock preparation, including process heating and slurry stirring, can be compensated by the exothermic carbonation process, making the process economically viable.[33]

Aqueous sources such as seawater, subsurface brine, and industrial effluents are also Mg^{2+}/Ca^{2+}-rich aqueous solutions and can potentially be applied for CO_2 mineralization.[34,35] In this process, CO_2 is transformed into carbonate precipitates and permanently stored as value-added products.[36] Wastewater or brine solution could be used as a liquid agent in the carbonation reaction.[37,38]

Oil-field brine is another significant waste from oil and gas production, which is mainly disposed of.[39] In the United States, 18 billion barrels (2.12 billion m^3) are produced yearly.[40] The primary disposal strategy for about 65% of this water is reinjection, which costs between $0.015 and $3 per barrel.[41] Consequently, the management and disposal of oil-field brine costs $1.5 billion per year in the United States.

Some brine has high concentrations of Ca, Mg, and Fe, which react with CO_2 to form $CaCO_3$(s), $MgCO_2$(s), and $FeCO_3$(s) and other products under favorable conditions.[42] Together,

these suggest the possibility of using the cations in saline wastewater and subsurface brine as potential sources for CO_2 mineralization to form carbonates.

Motivated by the current status of CO_2 utilization technologies, this study proposes a calcium and magnesium production process that involves injecting low-concentration CO_2 (8–15 vol %) from flue gas into a carbonation process in a desalination plant. The feasibility of the overall process is analyzed by calculating the energy required for a standalone desalination pretreatment process and a standalone CO_2 mineralization process to the hybrid process. Previous experiments demonstrated that seawater is a viable option for precipitating 90% of Ca and Mg ions in seawater, which is equivalent to 0.06 mol of CO_2 that can be captured per liter in the natural seawater process. Additionally, two to three times higher CO_2 fixation potential could be achieved with more concentrated water.[43] Valuable by-products, such as magnesite and strontianite, can be precipitated to reduce the operating cost of oil production.

4.3 Process Modeling and Simulation

4.3.1 Overall Description

Aspen Plus was used as the main simulator because necessary chemical units are available from its library, and eRNTL was selected as the thermodynamic property method.[44] The method considers Hilgard thermodynamics, CO_2 MEA reaction kinetics, and other mass transfer phenomena associated with system mixture. The model explicitly accounts for solution chemistry, which includes dissociations of H_2O, NaOH, $CaCl_2$, and CO_2; the formation of bicarbonate; and precipitation of calcium carbonate.

The main design schemes of the model include the following:

- CO_2 mineralization plant (Baseline)
- CO_2 amine-capture unit (Baseline)
- The advanced process to reduce power consumption baseline

4.3.2 Thermodynamic Framework

4.3.2.1 CO_2 Amine-Capture Unit

The adsorption process was described by the zwitterion mechanism, is followed by the hydration of CO_2 to form HCO_3^-/CO_3^{2-}, and is supplemented by the hydrolysis of carbamate as shown in equations 6 and 7.

$$CO_2 + RNH_2 \rightleftharpoons RNH_2{}^+COO^- \quad (6)$$

$$RNH_2{}^+COO^- + RNH_2 \rightleftharpoons RNHCOO^- + RNH_2{}^+ \quad (7)$$

Performing CO_2 desorption through a heating process of the MEA solution that is saturated with CO_2 to perform the reverse process of absorption.

$$CO_3{}^{2-} + 2H^+ \xrightarrow{heating} CO_2(g) + H_2O \quad (8)$$

$$HCO_3{}^- + H^+ \xrightarrow{heating} CO_2(g) + H_2O \quad (9)$$

$$2HCO_3{}^- + RNH_2{}^+ \xrightarrow{heating} RNHCOO^- + CO_2(g) + H_2O \quad (10)$$

4.3.2.2 CO_2 Absorption Using Alkaline

CO_2 reacts with brine metal cations to form carbonate precipitates through the following reaction sequence. The aqueous solution is first brought into contact with the flow of flue gas in a contactor where it takes up CO_2. To promote mineral carbonate precipitation, precipitation of calcium carbonate requires the speciation of aqueous CO_2 to CO_3^{2-}.

$$CO_3^{2-} + H_2O \rightleftharpoons HCO_3^- + H^+ \quad (11)$$

$$HCO_3^- + H^+ \rightleftharpoons CO_3^{2-} + H_2O \quad (12)$$

$$CO_2 + OH^- \rightleftharpoons HCO_3^- \quad (13)$$

$$HCO_3^- \rightleftharpoons CO_2 + OH^- \quad (14)$$

$$H^+ + OH^- \rightleftharpoons H_2O \quad (15)$$

$$HCO_3^- + OH^- \rightleftharpoons CO_3^{2-} + H_2O \quad (16)$$

$$Ca^{2+} + CO_3^{2-} \rightleftharpoons CaCO_3 \quad (17)$$

$$CaCO_3 + H^+ \rightleftharpoons Ca^{2+} + HCO_3^- \quad (18)$$

The pH determines the steps that control sequence of the reaction and the proportions of carbonate species. At low pH of approximately 4, production of H_2CO_3 dominates; at mid pH of around 6, HCO_3^- production dominates; then when the pH increases to a higher level around 9, CO_3^{2-} dominates.[37] Therefore, precipitation of calcium carbonate is predominant at a basic pH because of the carbonate ions that are available. Conversely, carbonate dissociates as a solution and becomes more acidic. Several factors affect the efficiency of carbonate-forming processes, such as brine composition, temperature, pressure, and pH. The purpose of this study was to optimize the process conditions that form mineral carbonates using Aspen Plus by changing temperature, pH, and solution composition. This study can help to determine the relationship between aqueous solution composition and the formation of precipitates.

4.4 Results and Discussion

4.4.1 Base Case

4.4.1.1 CO_2 Capture and Sequestration

A traditional CO_2-removing unit process flow sheet is shown in Figure 4.1. The baseline consists of the following building blocks: amine absorber, stripper, cooler. Clean flue gas is extracted from the top of the absorber while the rich solvent stream is extracted from the bottom.[45–47] The rich amine is pumped through a lean/rich heat exchanger to recover the heat from incoming lean amine. Afterward, additional heat is provided by the stripper reboiler to release CO_2 from a liquid solvent. The CO_2-lean stream is pumped to the main heat exchanger to recover heat from the incoming CO_2-rich amine and then cooled and recycled to the absorber.[45–47] The reboiler heats rich amine to an appropriate temperature to break the chemical bonds and deliver a vapor stream that acts as a stripping fluid. The overhead condenser provides a reflux liquid stream to the column and purifies the CO_2-rich gas as much as possible. The CO_2-rich gas released from the stripper is finally compressed and sent for storage.

4.4.1.1.1 Model Description

A CO_2 capture plant was simulated in this work using Aspen Plus. The operating conditions are presented in Table 4.1. The simulation was modeled using an electrolyte non-random two-liquid (NRTL) property package.[44]

Table 4.1. Breakdown of specific power requirements represented in Figure 4.1.

Component	Power Consumption (MWh/t of CO_2)
Recycle pumping	0.05
CO_2 compression	0.22
Heating requirement	0.25
Cooling requirement	0.25

Work was calculated by summing work from heating, cooling, and compression. The energy required for CO_2 capture was based on the sum of the minimum energy required for CO_2 capture using amine, which is 1.26 MWh per t of CO_2, and additional energy for CO_2 sequestration, here estimated as 0.22 MWh per t of CO_2: the energy needed to pressurize a 100% CO_2 gaseous stream from atmospheric pressure to 14 MPa. The primary energy consumers were compression and heating[48] (Table 4.1). Additional energy can be reduced to lower the energy of CO_2 capture to 0.5 MWh per t of CO_2 by maximizing heat integration between the lean–rich heat exchanger and reducing the energy in the reboiler through heat integration.

Power demand was estimated using a four-stage centrifugal compressor with interstage coolers on the basis of Dresser-Rand data. CO_2 compression is an auxiliary load; the effect of the pressure requirement should be specified on the basis of pressure for pipeline transport customers. The majority of the captured CO_2 must be sequestered, and a fraction of the captured CO_2 can be used as raw material for manufacturing and producing polymers and liquid fuels.[49] The energy

consumption per t of CO_2 captured tends to decrease as the concentration of CO_2 in the flue gas increases.

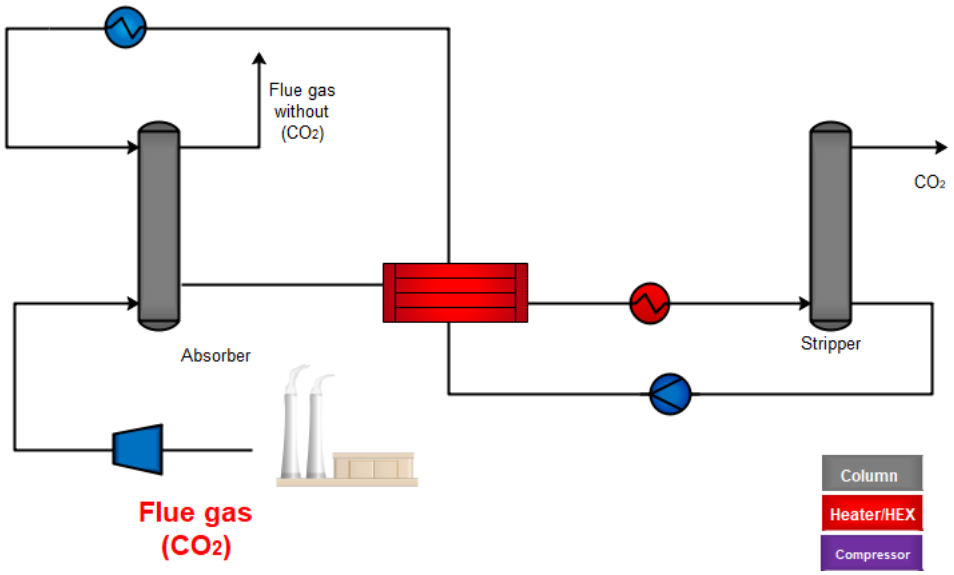

Figure 4.1. Process flow diagram of the amine unit flue gas being fed to the absorber and contacted with a lean solvent, removing 90 wt % of the CO_2 from flue gas. The rich solvent is heated by incoming lean amine in a heat exchanger (HEX).

The efficiency of removing CO_2 in the absorber is a function of several factors that affect the gas–liquid equilibrium. One factor governing CO_2 capture is amine efficiency (i.e., the number of amine moles required to capture one mole of CO_2). The amine efficiency of an amine dictates the form of CO_2 absorbed [Figure 4.2 (blue curve)]. The efficient use of amine results in a reduction in the overall cost of the CO_2 capture process. Among the alkanol amines, there are three main categories: primary, secondary, and tertiary. Primary amines, such as MEA, form relatively stable carbamate (Figure 4.2a), and according to the simulation, 0.64 moles are absorbed per one mole of amine (blue curve, Figure 4.2b). However, the stable formation of carbamate takes more heat energy and regenerates the absorbent (Figure 4.2b). Alternatively, tertiary amine (methyl diethanolamine; MDEA) forms unstable carbamate, and an alternate reaction leads to the bicarbonate ion formation [Figure 4.2b (red curve)] but lowers the capacity to 0.3 moles of CO_2

per mole of amine. Based on this analysis, MEA was chosen as a solvent due to low energy consumption.

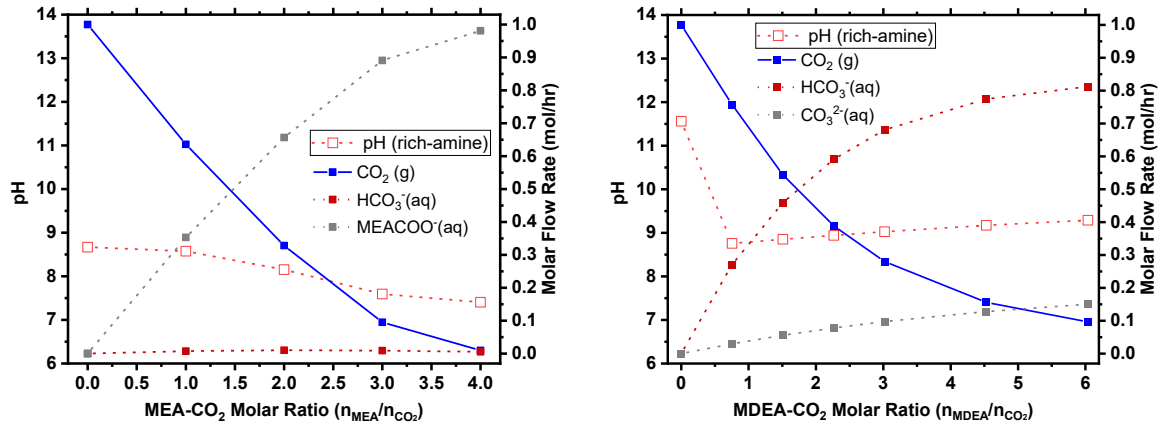

(a) (b)

Figure 4.2. CO_2 absorption isotherm for (b) tertiary amine (MDEA) compared with (a) conventional absorbent (MEA). Amine/CO_2 ratio (x-axis) is based on the inlet streams of flue gas and lean amine entering the absorber. Blue line represents the concentration of CO_2 in the stream leaving the absorber, and square dotted lines represent the rich amine pH solution (□ red), $MEACOO^-$ (■ grey), and HCO_3^- (■ dark red) leaving the absorber.

4.4.1.2 CO_2 Desorption via Electrolysis

The amine-electrolyze process is proposed here as a more efficient process than the standard amine post-combustion CCS technology. Electrodialytic desorption of CO_2 gas from aqueous solution has the potential to improve the efficiency of CO_2 separation. In this process, seawater is processed through a bipolar membrane electrodialysis (BPMED) system, providing two output streams, acidified seawater, and basified seawater (Figure 4.3). The acidified seawater stream produces HCl, which is added to rich amine leaving the absorber, and a portion of CO_2 is subsequently stripped, producing a stream of pure CO_2 gas. The depleted CO_2-amine solution leaving the stripper can be combined with a basified solution, creating an alkaline pH solution that can be used back in the absorber. For this, the rich-amine solution is treated with different HCl

molar concentration. This estimates that H^{+} is needed from the electrolysis process to desorb the CO_2 rich amine. The purpose of this case study is to investigate the thermodynamic dissociation of MEA-rich solution upon CO_2 absorption and to determine the possibility to convert rich into lean amine without any need for the heating step. For this process, CO_2 in the incoming flue gas to the absorber was fixed at 1 mol/h, and the amine added to the absorber was with the following proportions 4.17, 0.90 and 0.87 mol/h for MEA, MEA^{+}, and $MEACOO^{-}$ respectively. Figure 4.4a shows the effect of adding HCl (H^{+}:CO_2 molar ratio) to a rich amine solution. The blue curve in Figure 4.4a represents the amount of CO_2 stripped from the amine solution for every additional mole of H^{+} added. Results show that CO_2 concentration in the flash stream increased with the addition of H^{+}.

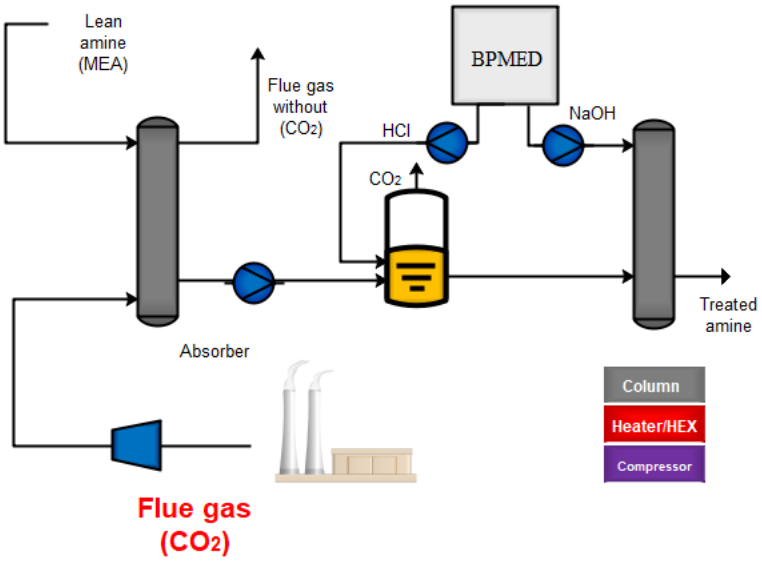

Figure 4.3. Process flow diagram of the amine unit flue gas being fed to the absorber and contacted with a lean solvent, removing the CO_2 from flue gas. The rich solvent is treated by being mixed with HCl solution generated from BPMED process followed by a treatment by NAOH generated from the same BPMED process.

Increasing H^{+} decreases the pH of amine from 8.5 to 7.25, and $MEACOO^{-}$ concentration decreases in a similar trend to pH. According to the stoichiometric proportion of the solution and Eq 6, 7, 8, and 9, CO_2 was a result of $MEACOO^{-}$ + HCO_3^{-} from solution. At H^{+} = 0 mol/h,

$MEACOO^-$ + HCO_3^- = 1.86 mol/h which equals the number of total CO_2 resulted from $H^+ \geq 6$ mol/h. Following HCl addition, an acidic lean amine stream was treated with NaOH to probe the effect of restoring the rich-amine-$^+$ back to rich-amine. For this analysis, the rich amine solution that was treated with the 4.5 mol HCl from the above analysis was used to study the effect of adding NaOH to restore the amine$^+$ back to the amine. Figure 4.4b shows the effect of adding (OH^- :CO_2 molar ratio) to acidic, rich amine solution compared to the previous case of H+ addition (Figure 4.4a). The additional NaOH increases the pH of the solution from 7.28 to 9.93, which is similar to the pH of Figure 4.4a with no HCl added, pH = 8.67, where acidity was a result of CO_2 absorbed in this stream. As pH continues to increase with NaOH, MEA^+ flow rate decreases from 5.43 to 1 mol/h HCO_3^- from 0.41 to 0.04 mol/h. On the other hand, MEA increased from 0.8 to 4.07 and $MEACOO^-$ mol/h from 0.41 to 0.86 mol/h.

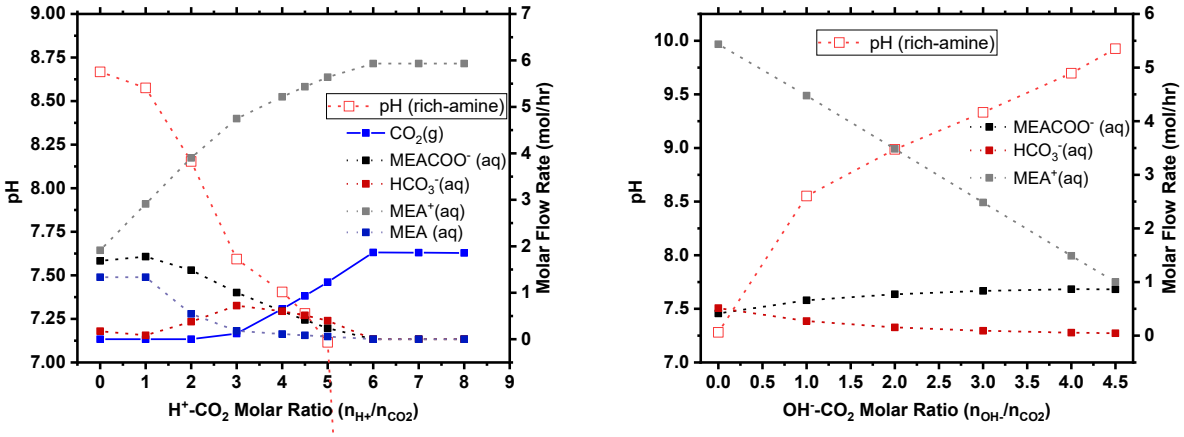

Figure 4.4 (a) the amount of CO_2 stripped (flash stream) from an amine solution for every additional mole of H^+ added. Data shows that CO_2 concentration in the flash stream increases with the addition of H^+. Increasing H^+ decreases the pH of amine from 8.5 to 7.25, and $MEACOO^-$ concentration decreases in a similar trend to pH. **(b)** addition of OH^- through NaOH to rich-amine-$^+$ to convert back to rich-amine.

4.4.1.3 CO_2 Mineralization

Alkali metal hydroxide bases, such as sodium hydroxide, calcium hydroxide, and magnesium hydroxide, have a high affinity to capture CO_2 from both concentrated and dilute sources. In this process, CO_2 contained in the flue gas is captured using an alkali capture solution such as NaOH. CO_3^{2-} is precipitated by the reaction with Ca^{2+} or Mg^{2+} to form Ca-$MgCO_3$. The objective of this section is to study the step-change flow rate of the base with a fixed CO_2 flow to trace the reaction process and understand the changes more clearly.

4.4.1.1.1 Model Description

The CO_2 mineralization plant was simulated in this work using Aspen Plus. Figure 4.5 shows one possible configuration of the plant equipment for this process. Aspen Plus was used as the main simulator to provide the necessary chemical units from its library, and eRNTL was selected as the thermodynamic property method.[44]

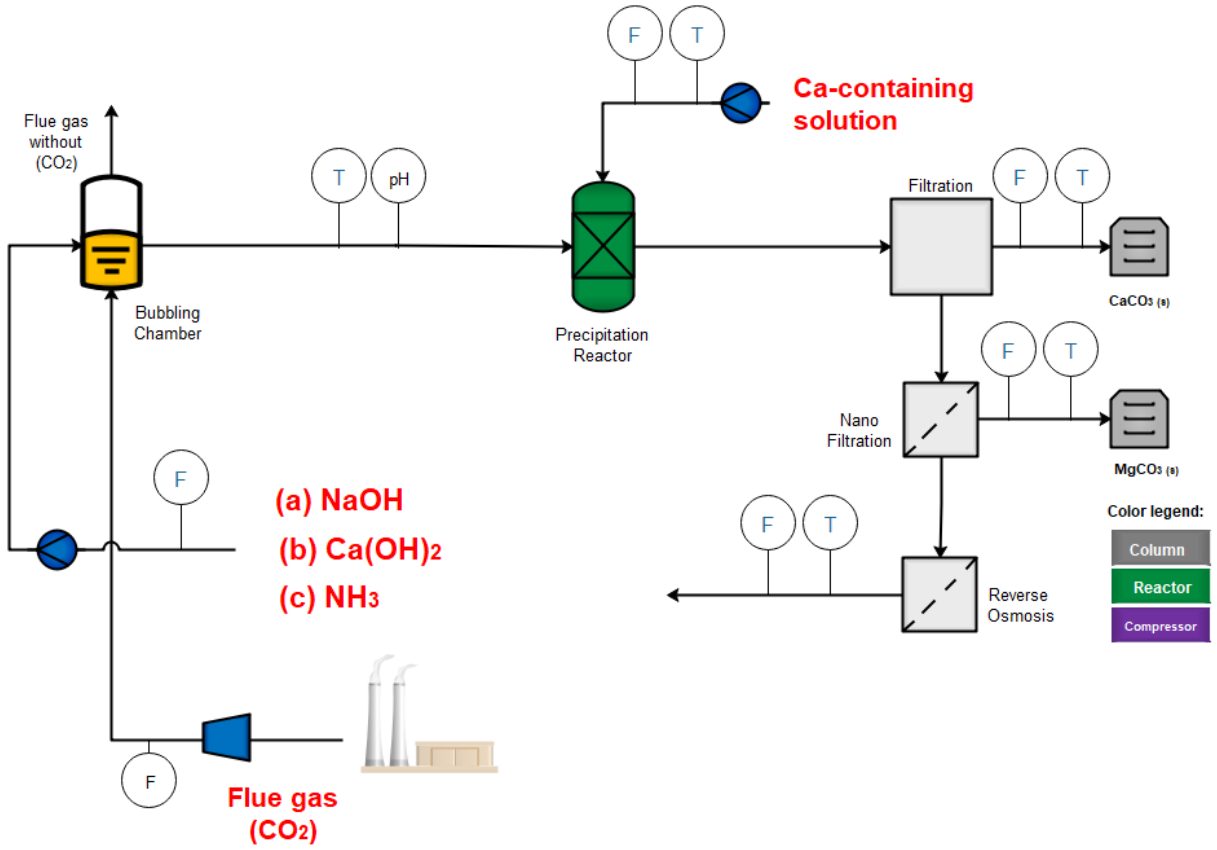

Figure 4.5. Process flow diagram of continuous aqueous carbonation on Ca-containing solution with carbonation reactor and absorption. Flue gas is contacted with a lean alkali metal hydroxide–based solution in all cases; (a) using NaOH hydroxide, (b) using Ca-$Mg(OH)_2$ hydroxide, and (c) using NH_3 to remove 90 wt % of the CO_2 from flue gas. In the carbonation reactor, the processes of coagulation and flocculation occur, resulting in the precipitation of $CaCO_3$ and $MgCO_3$.

A sensitivity analysis was used to determine the optimum flow ratio to remove 90 wt % of the CO_2 from flue gas. The ratio was varied between 1–6, and the CO_2 concentration from flue gas was monitored to study the possibilities of reducing energy. This process entailed thorough competitive energy estimation for the MEA-based process. The significant energy advantage of CO_2 mineralization is the use of a cheap sorbent derived from seawater (e.g., priced at 2.5 MWh/kg for NaOH,[50] compared with 5 MWh/kg for MEA).[51] Changing the use of NaOH to $Ca(OH)_2$ and $Mg(OH)_2$ has led to a decrease in both molar ratio and, consequently, energy demand.

The carbonation reaction can be improved by raising the pH or CO_2 partial pressure, thereby converting Ca^{2+} and Mg^{2+} ions in the solution through precipitation to the forms of Mg-$CaCO_3$. When alkaline is added into Ca^{2+}/Mg^{2+}-rich aqueous solutions, the equilibrium of CO_2 dissolution is broken. Sodium hydroxide solution was employed as a medium to remove CO_2 from flue gas. Figure 4.6a reflects the carbonation process when CO_2 was continuously in contact with the aqueous alkaline solution (NaOH) with different flow ratios compared to CO_2 from flue gas. It is evident that with the increase of alkaline molar ration to CO_2, the pH of the solution increased accordingly, reaching pH = 10–11, favoring more carbonate ions proportion that are available for precipitation at a molar ratio of 2 NaOH to 1 mol of CO_2. Based on this analysis, the molar ratio of NaOH consumed to sequester CO_2 as CO_3^{2-} is at least approximately 2. However, excess CO_2 in incoming flue gas (more than 0.5 moles of CO_2 per 1 mole of NaOH) renders CO_2 in flue gas leaving the absorber.

This case was compared to that in which NH_3 is added with respect to impact on the pH of the solution. There were obvious changes in the concentrations of CO_3^{2-}, HCO_3^-, and NH_2COO^- species. After adding 1.5 mol/h of NH_3 to the flue gas containing 1 mol/h CO_2, the concentration of CO_2 in the outlet CO_2 stream was substantial, achieving 90% CO_2 removal. Studies of the CO_2 capture process typically assume capture efficiency in the range of 85% to 90%.[48,52] As the NH_3 ratio to CO_2 continued to increase even after capturing nearly all of the CO_2, the concentrations of CO_3^{2-}, HCO_3^-, and NH_2COO^- species increased. The initial pH of the solution was set to 12.17 because of ammonium's solubility in water.

$Ca(OH)_2$ aqueous solution was used as an effective solvent to absorb CO_2. The amount of CO_2 absorbed was linearly increased with respect to $Ca(OH)_2$ concentration due to the formation of $CaCO_3$. In contrast to the two previous examples, NH_3 and NaOH, mineralization using

$Ca(OH)_2$ aqueous solution formed instant $CaCO_3$ precipitates and included many individual reactions, such as $Ca(OH)_2$ dissolution and HCO_3^- production. According to the simulated results, at least one mole of Ca(OH) per CO_2 is required to convert one mole of CO_2 to $CaCO_3$.

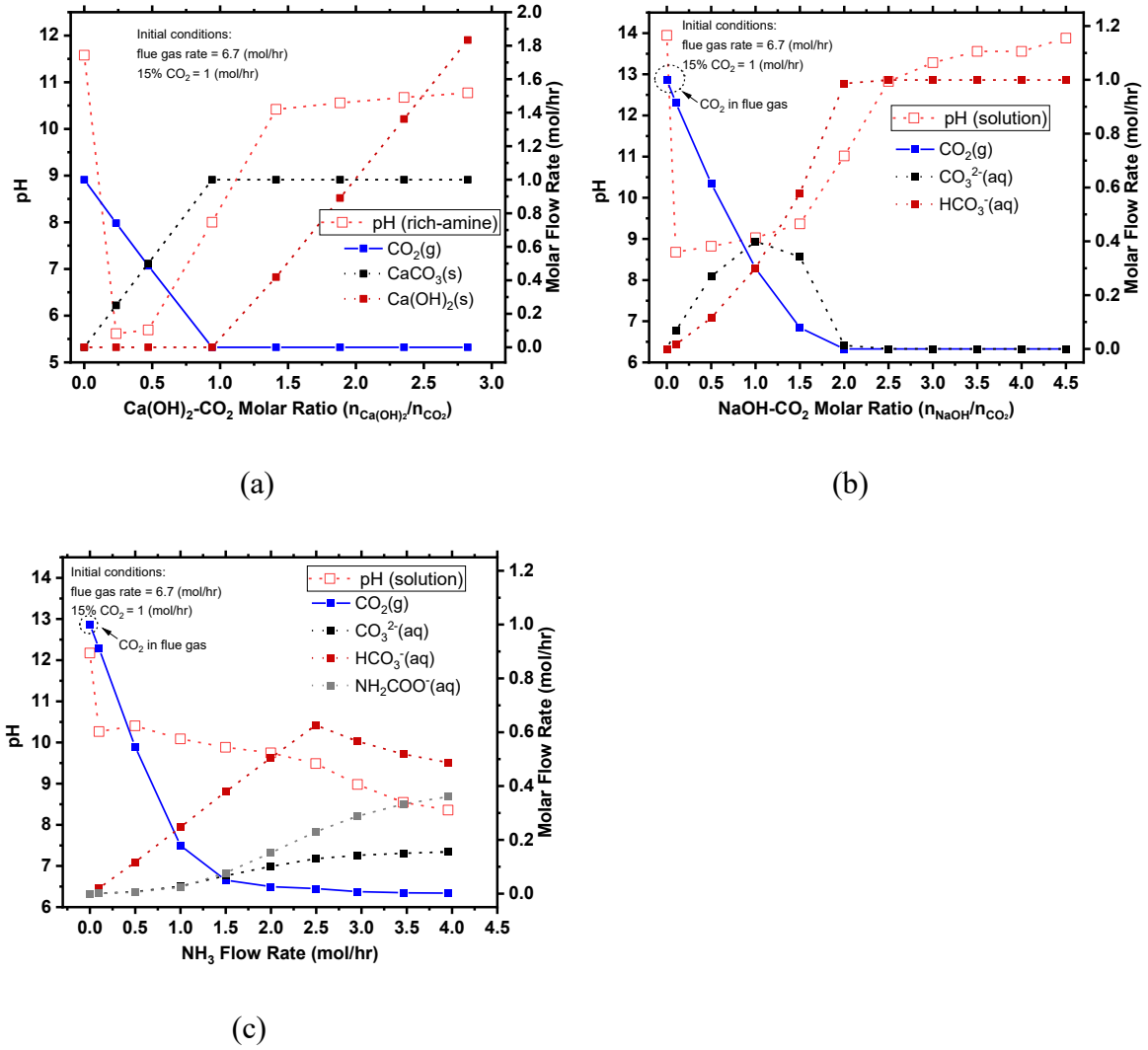

Figure 4.6. Aspen Plus simulation of fixed CO_2 at 1 mol/h shows changes of outlet CO_2 composition, pH (□ red), and other dissociations. $MEACOO^-$ (■ grey) and HCO_3^- (■ dark red) with (a) varying NaOH:CO_2 flow rates, (b) varying $Ca(OH)_2$:CO_2 flow rates, and (c) varying NH_3:CO_2 flow rates.

4.4.1.1.1 Thermodynamic Modeling of the NaOH:CO_2:H_2O Ratio

The heatmap in Figure 4.7 shows the optimization analysis of changing the concentrations of $CaCl_2$ and NaOH with 1 mole of CO_2 initially in the coming flue gas. The heatmap shows the probability of converting 1 mole of CO_2 to $CaCO_3$. Changing the ratios of NaOH:CO_2:$CaCl_2$ to form $CaCO_3$ is reflected by the colors of the map; red indicates the highest conversion yield, and blue indicates the minimum conversion yield of $CaCO_3$ with 1 being the highest possible conversion yield. A higher NaOH/CO_2 ratio leads to higher CO_3^{2-} concentration. For instance, under a condition of 2 moles NaOH:CO_2 and 1 mole $CaCl_2$:CO_2, the precipitation reaction of $CaCO_3$ is thermodynamically favorable to convert CO_2 in the flue gas initially (1 mol) to 1 mole precipitated calcium carbonate. This is indicated in the red region (Figure 4.7a), which shows a higher probability of forming $CaCO_3$ solid, according to the Aspen Plus simulation. Thus, conversion of 1 mol CO_2 to 1 mol $CaCO_3$ requires, at minimum, 2 mol NaOH (Figure 4.7a). If alkalinity and CO_2 are sufficient, the carbonate yield becomes limited by the concentration of divalent in the feed. Fixing the NaOH to CO_2 molar ratio at 2 (x-axis, Figure 4.7a) provides sufficient alkalinity, and then, carbonation is limited by Ca in the solution (y-axis, Figure 4.7a). Less than 2 mol NaOH per mol of CO_2 results in less than 100% conversion of CO_2. Figure 4.7b shows the final pH of the solution after each combination of NaOH:CO_2 and $CaCl_2$:CO_2. Precipitation of calcium carbonate is favored at a basic pH because of the carbonate ions, and as carbonate ions are consumed, the pH of the solution drops. The graph model is useful to predict the pH for the downstream process treatment following the carbonation reactor.

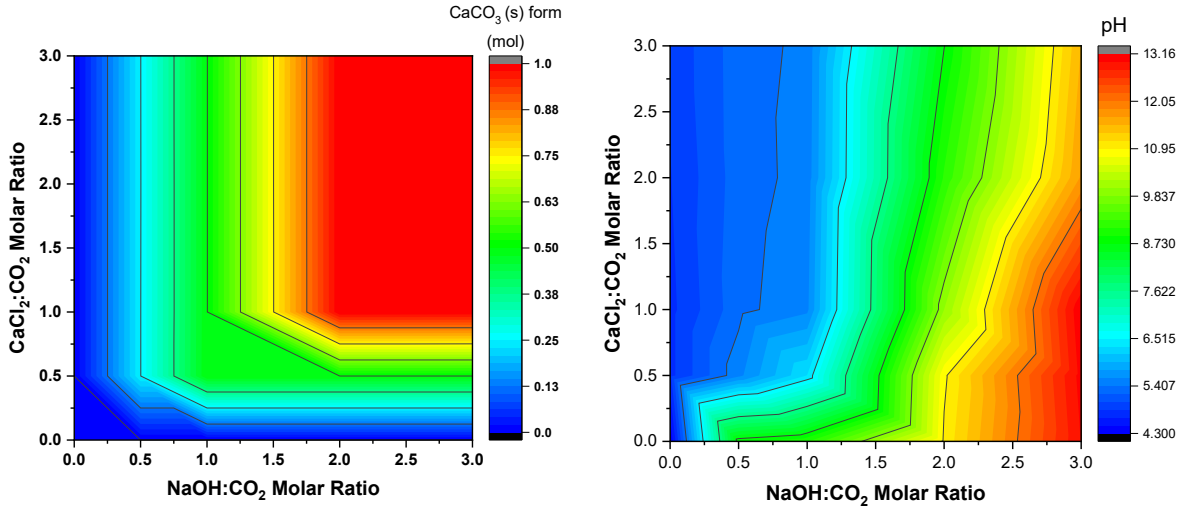

(a) (b)

Figure 4.7. Heatmap of (a) pH changes and (b) calcium carbonate precipitation formation in aqueous solution leaving the absorber when changing the inlet concentrations of $CaCl_2$ and NaOH with 1 mole of CO_2 initially in the coming flue gas.

The energy demand for the CO_2 mineralization process was simulated in this work using Aspen Plus and was then compared with values from existing industrial-scale technologies. In total, water processing consumes roughly 0.14 kWh per m^3 or 50 kWh per t of CO_2, assuming a seawater feed. The synthesis of a consumable base taken as NaOH via the Chlor-alkali process demands 2.5 MWh per t of NaOH.[50] Based on these assumptions, we estimated that the total energy demand for CO_2 mineralization with the baseline process is 4.55 MWh per t of CO_2 for current best-in-class Chlor-alkali process-generated NaOH. The theoretical minimum energy demand for NaOH generation is 0.7 MWh per t of NaOH for a direct HCl–NaOH generation from HCl.[53] These energy estimations were based on converting CO_2 to $CaCO_3$. Another possible process approach is to convert CO_3 to either a pure $NaHCO_3$ product or a mixture of a $CaCO_3$/$NaHCO_3$ solution. Figure 4.8 shows the energy needed for a stream containing a specific $CaCl_2$/CO_2 molar ratio (x-axis, Figure 4.8). Varying the x-axis indicates the energy needed to obtain a specific composition

of the outlet product. The y-axis shows the composition of the product as a $CaCO_3/NaHCO_3$ ratio. Red regions indicate the higher energy process approach to form CaCO3 products, and blue regions indicate the lower energy process approach to form an $NaHCO_3$ solution.

Figure 4.9 shows the specific power requirement for the two baseline cases: CO_2 capture and sequestration and CO_2 mineralization. Advancements in electrolysis technology should lead to higher energy efficiency in the CO_2 mineralization process and make it more competitive for CO_2 capture and sequestration. Solvent-based capture has higher costs than CO_2 mineralization due to the solvent needed to make up for any losses.[67,68] Additionally, amine stripping uses a large amount of water relative to the flow of flue gas for the CO_2 removal and circulation process. For a typical amine unit, to remove 800 t of CO_2/day, approximately 6,000 t of water/day is required for circulation with 10% make-up water needed, which affects operating costs significantly and makes this approach challenging at the Gt level due to the large amount of solvent make-up needed.[22] By contrast, CO_2 mineralization technology uses a low concentration of CO_2 with no additional energy requirement.

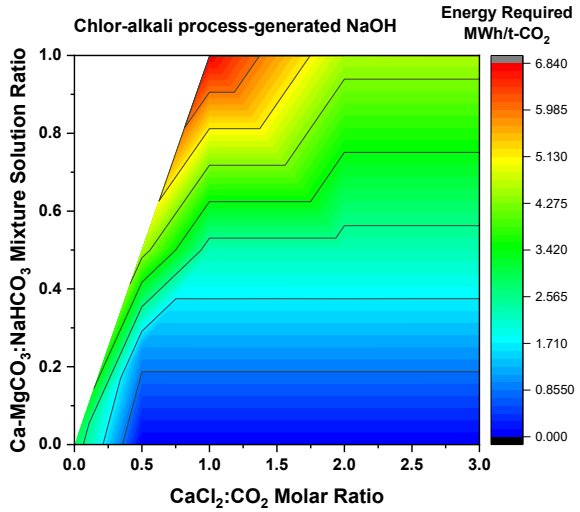

Figure 4.8. Heatmap of energy demand as a function of $CaCl_2$ concentration in the inlet CO_2 mineralization plant and produced mixture of Ca-$MgCO_3$:$NaHCO_3$ using Chlor-alkali process energy demand for NaOH generation.[50]

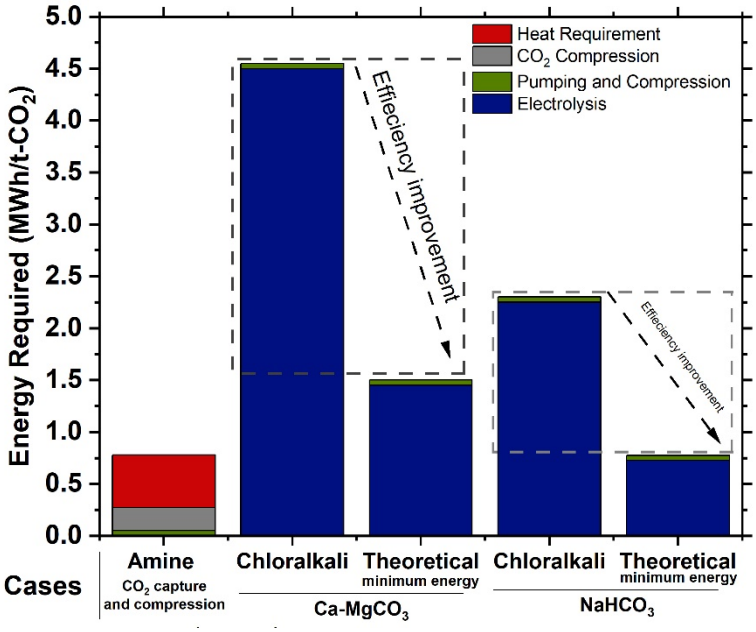

Figure 4.9. Energy requirements for CO_2 sequestration by (a) capture and injection in geologic formations (red and grey) and (b) baseline concept for carbon dioxide mineralization and disposal. Through NaOH generation by the Chlor-alkali process,[50] this route entails two possible subroutes for CO_2 converted products, $NaHCO_3$ and $CaCO_3$. The theoretical energy requirement for NaOH generation from NaCl has been shown to indicate the minimum energy needed.[53]

4.4.2 Advanced Cases

4.4.2.1 Reducing Power Consumption Below Baseline

Several process configurations were tested to reduce the power requirement for the CO_2 mineralization process. The key feature of the advanced concept is to enhance the efficiency, energy utilization, and possibility for process integration within existing and future desalination plants, simultaneously addressing the issues of CO_2-driven climate change and water supply.

A seawater reverse osmosis (SWRO) plant has been the dominant desalination technology used to remove $Mg^{2+/}Ca^{2+}$-rich aqueous solutions from seawater in the industry due to the low process cost.[54] The energy cost of desalinating seawater can be estimated as 3.5 kWh/m^3, considering that the best current seawater RO process requires 2–2.5 kWh/m^3 and additional

energy[54]; >1.0 kWh is consumed mainly by the intake and pretreatment of the desalination plant.[40] Of these stages, the pretreatment of fresh seawater before it is fed into RO accounts for most of the energy used. Seawater pretreatment consumes 0.3–1.0 kWh/m^3, and as the salinity of water increases, so does the required energy for pretreatment. For example, the energy required for brackish water is 0.8–1.7 kWh/m^3.[54] Recent analysis has shown that there is a small marginal potential for further energy saving in any desalination process.[55,56] Nevertheless, the total energy consumption of sea water reverse osmosis plants is around three to four times higher than the minimum theoretical energy due to the involvement of pretreatment steps. Eliminating or reducing the pretreatment stage would reduce the energy consumption of SWRO plants and reduce the chemicals used that pose environmental hazards to creatures when discharged into the aquatic environment.[57,58] Aqueous sources such as seawater, subsurface brine, and industrial effluents are also $Mg^{2+/}Ca^{2+}$-rich aqueous solutions and potentially applied for CO_2 mineralization.[34,35] Figure 4.9 compares the energy required for seawater and brackish water. Figure 4.10 illustrates that there is an area to integrate the pretreatment step of RO desalination plants with CO_2 mineralization, leading to lower energy requirements. Our proposed alternative is to use the CO_2 mineralization unit in the pretreatment step of RO desalination plants to enhance the efficiency and energy utilization of the CO_2 capture and pretreatment process. Integrating the CO_2 mineralization unit in the pretreatment stage improves the energy efficiency of the SWRO plant because thermodynamics sets the boundary of the desalination step energy requirement.[56] Brackish water is also a $Mg^{2+/}Ca^{2+}$-rich aqueous solution that can be integrated with CO_2 mineralization to reduce high disposal costs and limited disposal options.[59–61] Previous experiments have shown that seawater is a viable option to precipitate 90% of Ca and Mg ions in seawater, equivalent to 0.06

mol of CO_2 that can be captured per liter of the natural seawater process. Additionally, two to three times more CO_2 fixation can potentially be achieved with more concentrated water.[43]

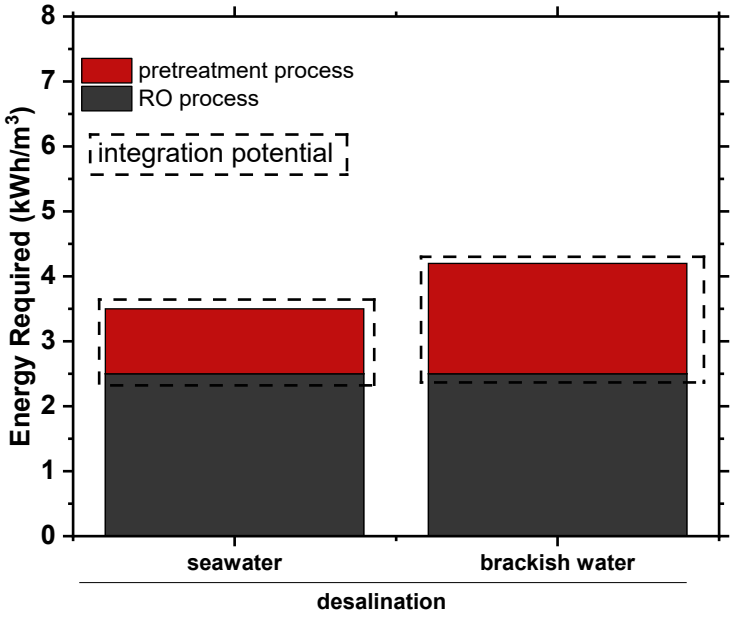

Figure 4.10. Specific energy required to treat different sources of wastewater (seawater and brackish water) broken down into components (red for pretreatment process prior to RO and green for the RO process energy requirements).[40,54]

In this section, we discuss changes in concentrated seawater composition (Ca, Mg; Table 4.2) with pH and CO_2 flow rate and precipitation of carbonates. We evaluated a carbon capture plant treating 45 kg/h of flue gas containing 15% (v/v) of CO_2 from a supercritical pulverized coal power plant. The coal-fired flue gas composition was 15% CO_2, 4.0% H_2O, 4.0% O_2, and 77% N_2 at 25 °C and 0.1 MPa. The plant was assumed to run 335 days per year at 100% capacity, with 90% capture efficiency of the emitted carbon from the power plant. A solution containing Ca^{2+} and Mg^{2+}, which originate in sources such as waste brine produced by salt and potassium carbonate industries (Table 4.2),[62,63] was used as a continuous flow source (fixed at 1 m^3/h) for a Ca^{2+}/Mg^{2+}-

rich aqueous solution for the integration approach. The constraints of this study were to achieve >90% CO_2 and >90% Ca-Mg^{2+} on outlet flue gas and concentrated seawater streams, and thus, the CO_2 flow rate was adjusted to the value that gave the highest carbonation potential based on concentrated seawater concentration. CO_2 mineralization by this method is analogous in several respects to water treatment. First, adequate mixing and CO_2 equilibration can be enabled using aeration tanks similar to those used in the activated sludge process in wastewater treatment plants. Second, NaOH can be blended into the CO_2-rich water, as in the processes of coagulation and flocculation for water treatment, resulting in the precipitation of $CaCO_3$ and $MgCO_3$. The precipitates are then separated from the solution by sedimentation, and the discharge solids can either be further dewatered using techniques that are currently employed in water treatment, such as rotary drum filters, or expelled into the ocean in a manner similar to brine disposal in desalination plants.

The flue gas flow rate was chosen to be 45 kg/h to ensure that minimum carbon was available to precipitate products. The pH of the concentrated seawater was adjusted by adding sodium hydroxide medium while maintaining a constant flue gas flow (45 kg/h). After the addition of 7 kg/h of NaOH, the concentration of Ca and Mg ions was reduced to less than 10% in the treated brine solution (Figure 4.11). Beyond the addition of 7 kg/h, no more precipitates were expected from the solution because nearly all the Mg and Ca had been already removed.

Table 4.2. Concentrated seawater compounds.[62,63]

Compound	Concentration (g/L)	Compound	Concentration (g/L)
NaCl	46.88	KBr	0.196
$MgCl_2$	10.16	H_3BO_3	0.054
$CaCl_2$	2.25	$SrCl_2$	0.048
Na_2SO_4	7.99	NaF	0.006
KCl	1.33	$NaHCO_3$	0.392

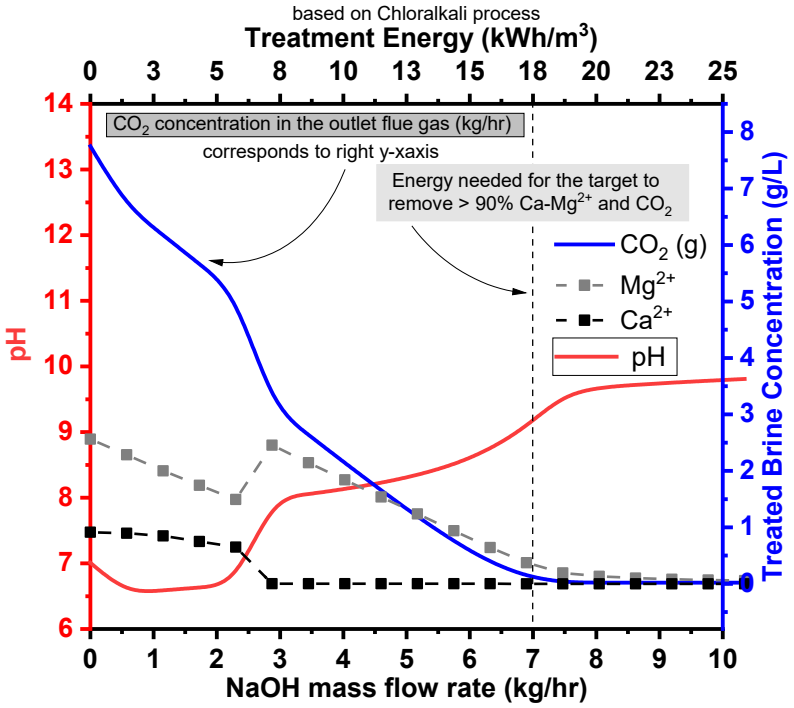

Figure 4.11. Effect of adding NaOH (bottom x-axis) to a concentrated brine composition (Ca, Mg) to adjust pH (left y-axis) that is in contact with flue gas at 45 kg/h to calculate carbonate precipitation. Effluent speciation (right y-axis) shows the reduction in Mg^{2+} (■ grey) and Ca^{2+} (■ black) for the solution as they form carbonates. Top x-axis shows the energy used and correlated to NaOH is added to solution.

Oil-field brine is another wastewater source that was used in this study. Oil-field brine composition was based on a water treatment plant that collects oil-field brine and underground deep natural gas brine from various wells in Pennsylvania, USA.[31] A similar approach to

concentrated seawater was developed for this case; the results of this study are reported in the following section 3.2.2.

Table 4.3 Oil-field brine compounds.[31]

Compound	Concentration (g/L)	Compound	Concentration (g/L)
NaCl	62.780	$FeCl_3$	0.43
$MgCl_2$	1.837	$SrCl_2$	10.04
$CaCl_2$	33.45	$BaCl_2$	0.89
KCl	2.350		

4.4.2.2 Integration Approach

The potential of using integration to fix CO_2 was evaluated according to the following equation.[43,62] The calculation was based on Mg, Ca in an aqueous solution of concentrated brine (Table 4.2) in addition to any bicarbonate formation in the solution. CO_2 fixation comes from Mg^{2+} and Ca^{2+} in a concentrated solution.

$$C_{fixation} = C_{CaCO_3} + C_{MgCO_3} + C_{NaHCO_3} \quad (19)$$

where $C_{fixation}$ is the total CO_2 fixed in the process by carbonate precipitation and bicarbonate formation.

The value of $C_{fixation}$ has been calculated as 0.18 mol of CO_2/m^3 of concentrated seawater. This is the carbon fixation where 1 m^3 of concentrated seawater can capture roughly 8 kg of CO_2 under standard conditions. Oil-field brine has higher Ca and Mg concentrations (Table 4.3), and thus more, CO_2 capture potential per m^3 of solution (23 kg of CO_2/m^3 of oil-field brine solution).

Figures 4.12 and 4.13 show the effect of NaOH mass flow rate on the carbonate products proportions of $MgCO_3$, $MgCO_3 \cdot 3H_2O$, $CaCO_3$, and $NaHCO_3$ for two wastewater sources: concentrated seawater and oil-field brine solutions, respectively. The simultaneous addition of NaOH results in the precipitation of calcite and nesquehonite, up to roughly 89 mmol nesquehonites and approximately 23 mmol calcite/m^3 of treated concentrated seawater solution

and approximately 296 mmol calcite and roughly 16 mmol nesquehonites/m^3 of treated oil-field brine solution. The shaded regions represent the percentage of nesquehonite, calcite, and bicarbonate converted from CO_2 to carbonates, and the blue curve represents the decrease in the CO_2-treated flue gas flow rate with the addition of NaOH.

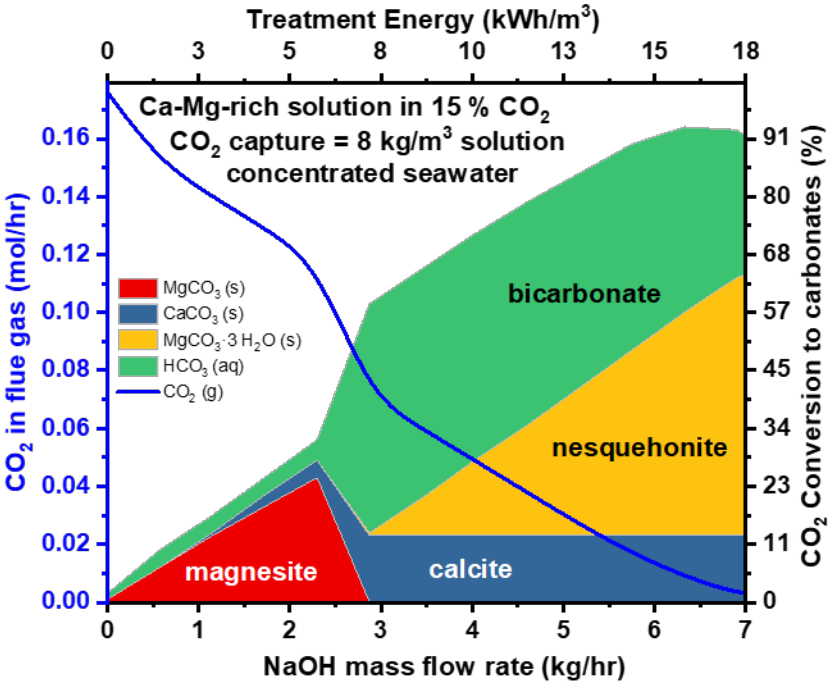

Figure 4.12. Effect of NaOH mass flow rate (bottom x-axis) to the carbonate products proportions of $MgCO_3$ (red region), $MgCO_3 \cdot 3H_2O$ (orange region), $CaCO_3$ (blue region), and $NaHCO_3$ (green region). The change in CO_2 flue gas concentration for the stream leaving the absorber is shown in the blue line; at 7 kg/h NaOH, CO_2 is completely removed.

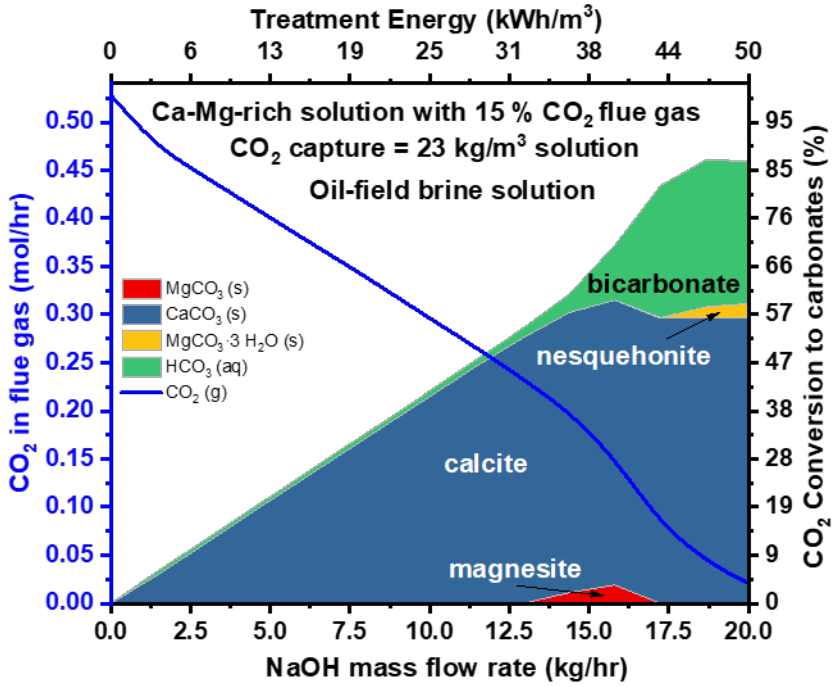

Figure 4.13. Effect of NaOH mass flow rate (bottom x-axis) to the carbonate products proportions of $MgCO_3$ (red region), $MgCO_3 \cdot 3H_2O$ (orange region), $CaCO_3$ (blue region), and $NaHCO_3$ (green region). The change in CO_2 flue gas concentration for the stream leaving the absorber is shown in the blue line; at 20 kg/h NaOH, CO_2 is completely removed.

4.4.2.3 Energy Advantage

No energy is needed for phase separation, nor is heat required. The primary energy sources are a pump required to transfer concentrated seawater and energy for electrolysis. For a typical process, 125 m^3 of concentrated seawater is needed for 1 ton of CO_2 fixation. This requires 29.29 kWh of pumping energy to drive the 125 m^3 of concentrated brine. Oil-field brine requires 10.2 kWh, which is even less pumping energy to fix 1 ton of CO_2 of 43.5 m^3 of the oil-field brine solution.

Any resulting precipitation is removed before reaching the RO unit. From the base case scenario, most of the energy in this process comes from the synthesis of a consumable base, such as NaOH via the Chlor-alkali process, which demands 2.5 MWh per t of NaOH. It is apparent that

the CO_2 mineralization approach with integration improves efficiency and reduces costs. Efficiency is increased by 10% relative to CO_2 mineralization only.

An efficient process integration to reduce extra pretreatment requirements for Ca^{2+}/Mg^{2+}-rich aqueous solutions while capturing CO_2 at the same time to form carbonate solution was investigated. This resulted in a reduction in total power consumption for the process if each were treated independently. In an integrated mineralization pretreatment–desalination process, the total energy can be estimated as 18 kWh/m^3 of concentrated seawater and 7 kg of CO_2 stored, which is equivalent to a net energy reduction of the overall process by 10% considering that standalone concentrated seawater pretreatment requires 1.7 kWh/m^3.[40,54] Oil-field brine uses more energy to remove 90% of Ca and Mg from the solution (50 kWh/m^3); however, it has higher CO_2 capture potential per m^3 of wastewater solution (Figure 4.13). Operating expense has a direct relationship with NaOH synthesis energy; thus, further improvement in electrolysis technology can enable this integration route to be more competitive as a replacement for the current desalination pretreatment process (Figure 4.14). Recycled wastewater may indeed emerge as one of the most important water supplies in the future, particularly for water-scarce regions.

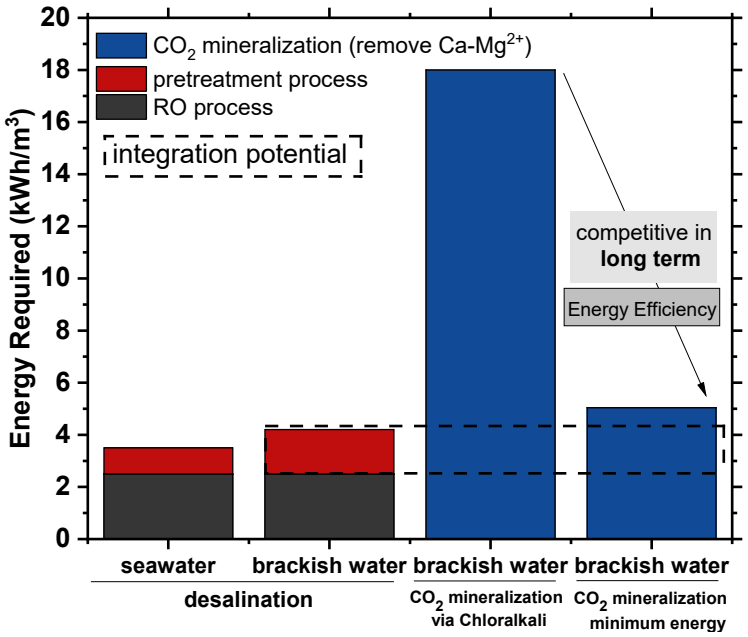

Figure 4.14. Specific energy requirement to treat different sources of wastewater broken down into components (red for pretreatment process prior to RO and green for the RO process energy requirements) compared with energy required to treat the same wastewater sources through CO_2 mineralization approach. Dotted rectangle shape shows the integration potential to reduce energy required to treat water (kWh/m^3) by combined CO_2 mineralization and RO plants.

4.5 Conclusion

We can conclude from our assessment about an amine-unit CO_2 capture plant that although it has been widely used to capture CO_2, the energy used for amine regeneration still represents a significant challenge. In addition to regeneration energy used in the amine unit, in some cases, we need to pressurize a 100% CO_2 gaseous stream from atmospheric pressure to 140 bar to store it underground, and the energy demand used for compression was estimated using a four-stage compressor with inter-stage coolers, which require 0.22 MWh per t-CO_2. Alternatively, CO_2 can be fixed by the production of insoluble carbonate salt through the carbonation process of a caustic solution's absorbing CO_2, which is another option for CO_2 capture. Distinct from the carbon capture and sequestration, the mineralization approach does not necessitate overcoming the energy of separating CO_2 from a mixture of gases and can be utilized without energy rise over a wide range of CO_2 concentrations and temperatures.

In the framework of an integrated CO_2 mineralization plant, Ca-Mg^{2+} can be mineralized and integrated with the desalination plant. The intensification of the CO_2 capture process with a desalination plant was explored through the integration of CO_2 mineralization with a pretreatment plant. This study proposed a CO_2 mineralization process that integrates low-concentration CO_2 (15 vol %) obtained from coal-fired power plants with wastewater treatment and produces carbonate materials. It was found that the CO_2 configuration yielded a 10% decrease in the total energy of separation required. The process shows that a concentrated solution containing Ca^{2+}/Mg^{2+} solution can be used to fix CO_2 using the hydroxide produced by electrolysis.

4.6 References

1. Heuberger, C. F.; Staffell, I.; Shah, N.; Mac Dowell, N. Impact of Myopic Decision-Making and Disruptive Events in Power Systems Planning. *Nat. Energy* **2018**, *3* (8), 634–640. https://doi.org/10.1038/s41560-018-0159-3.
2. Shepherd, J. G. *Geoengineering the Climate: Science, Governance and Uncertainty*; Royal Society, 2009.
3. Pogge von Strandmann, P. A. E.; Burton, K. W.; Snæbjörnsdóttir, S. O.; Sigfússon, B.; Aradóttir, E. S.; Gunnarsson, I.; Alfredsson, H. A.; Mesfin, K. G.; Oelkers, E. H.; Gislason, S. R. Rapid CO2 Mineralisation into Calcite at the CarbFix Storage Site Quantified Using Calcium Isotopes. *Nat. Commun.* **2019**, *10* (1), 1983. https://doi.org/10.1038/s41467-019-10003-8.
4. Seifritz, W. CO2 Disposal by Means of Silicates. *Nature* **1990**, *345* (6275), 486.
5. Alexander, G.; Maroto-Valer, M. M.; Gafarova-Aksoy, P. Evaluation of Reaction Variables in the Dissolution of Serpentine for Mineral Carbonation. *Fuel* **2007**, *86* (1–2), 273–281.
6. Dlugogorski, B. Z.; Balucan, R. D. Dehydroxylation of Serpentine Minerals: Implications for Mineral Carbonation. *Renew. Sustain. Energy Rev.* **2014**, *31*, 353–367.
7. Park, A.-H. A.; Fan, L.-S. CO2 Mineral Sequestration: Physically Activated Dissolution of Serpentine and PH Swing Process. *Chem. Eng. Sci.* **2004**, *59* (22–23), 5241–5247.
8. Kakizawa, M.; Yamasaki, A.; Yanagisawa, Y. A New CO2 Disposal Process via Artificial Weathering of Calcium Silicate Accelerated by Acetic Acid. *Energy* **2001**, *26* (4), 341–354.
9. Huijgen, W. J. J.; Witkamp, G.-J.; Comans, R. N. J. Mechanisms of Aqueous Wollastonite Carbonation as a Possible CO2 Sequestration Process. *Chem. Eng. Sci.* **2006**, *61* (13), 4242–4251.

10. Daval, D.; Martinez, I.; Corvisier, J.; Findling, N.; Goffé, B.; Guyot, F. Carbonation of Ca-Bearing Silicates, the Case of Wollastonite: Experimental Investigations and Kinetic Modeling. *Chem. Geol.* **2009**, *265* (1–2), 63–78.
11. Huijgen, W. J. J.; Comans, R. N. J.; Witkamp, G.-J. Cost Evaluation of CO2 Sequestration by Aqueous Mineral Carbonation. *Energy Convers. Manag.* **2007**, *48* (7), 1923–1935. https://doi.org/https://doi.org/10.1016/j.enconman.2007.01.035.
12. Ghoorah, M.; Dlugogorski, B. Z.; Balucan, R. D.; Kennedy, E. M. Selection of Acid for Weak Acid Processing of Wollastonite for Mineralisation of CO2. *Fuel* **2014**, *122*, 277–286.
13. Munz, I. A.; Kihle, J.; Brandvoll, Ø.; Machenbach, I.; Carey, J. W.; Haug, T. A.; Johansen, H.; Eldrup, N. A Continuous Process for Manufacture of Magnesite and Silica from Olivine, CO2 and H2O. *Energy Procedia* **2009**, *1* (1), 4891–4898.
14. Zevenhoven, R.; Fagerlund, J.; Songok, J. K. CO2 Mineral Sequestration: Developments toward Large-Scale Application. *Greenh. Gases Sci. Technol.* **2011**, *1* (1), 48–57. https://doi.org/10.1002/ghg3.7.
15. Fagerlund, J.; Teir, S.; Nduagu, E.; Zevenhoven, R. Carbonation of Magnesium Silicate Mineral Using a Pressurised Gas/Solid Process. *Energy Procedia* **2009**, *1* (1), 4907–4914.
16. Koukouzas, N.; Gemeni, V.; Ziock, H. J. Sequestration of CO2 in Magnesium Silicates, in Western Macedonia, Greece. *Int. J. Miner. Process.* **2009**, *93* (2), 179–186. https://doi.org/10.1016/j.minpro.2009.07.013.
17. Oelkers, E. H.; Gislason, S. R.; Matter, J. Mineral Carbonation of CO2. *Elements* **2008**, *4* (5), 333–337.
18. Oelkers, E. H. An Experimental Study of Forsterite Dissolution Rates as a Function of Temperature and Aqueous Mg and Si Concentrations. *Chem. Geol.* **2001**, *175* (3–4), 485–494.

19. Krevor, S. C.; Lackner, K. S. Enhancing Process Kinetics for Mineral Carbon Sequestration. *Energy Procedia* **2009**, *1* (1), 4867–4871.

20. Mei, Z. H.; Mei, S. Y. Novel Economical Chemical Engineering Reactions for Mineralization of CO2 to Combat Global Warming. In *Advanced Materials Research*; Trans Tech Publ, 2012; Vol. 524, pp 3302–3307.

21. Sanna, A.; Uibu, M.; Caramanna, G.; Kuusik, R.; Maroto-Valer, M. M. A Review of Mineral Carbonation Technologies to Sequester CO2. *Chem. Soc. Rev.* **2014**, *43* (23), 8049–8080. https://doi.org/10.1039/c4cs00035h.

22. Rackley, S. A. 2 - Overview of Carbon Capture and Storage; Rackley, S. A. B. T.-C. C. and S. (Second E., Ed.; Butterworth-Heinemann: Boston, 2017; pp 23–36. https://doi.org/https://doi.org/10.1016/B978-0-12-812041-5.00002-7.

23. Lackner, K. S.; Wendt, C. H.; Butt, D. P.; Joyce Jr, E. L.; Sharp, D. H. Carbon Dioxide Disposal in Carbonate Minerals. *Energy* **1995**, *20* (11), 1153–1170.

24. Moriyoshi, Y.; Fukawa, J.; Ishibe, E.; Ikegami, T. Fixation of Carbon Dioxide with Wollastonite and Its Reaction Products. *Trans Mater Res Soc Jpn* **1999**, *24* (4), 611–614.

25. Landrot, G.; Ajo-Franklin, J. B.; Yang, L.; Cabrini, S.; Steefel, C. I. Measurement of Accessible Reactive Surface Area in a Sandstone, with Application to CO2 Mineralization. *Chem. Geol.* **2012**, *318*, 113–125.

26. Rendek, E.; Ducom, G.; Germain, P. Carbon Dioxide Sequestration in Municipal Solid Waste Incinerator (MSWI) Bottom Ash. *J. Hazard. Mater.* **2006**, *128* (1), 73–79.

27. Kodama, S.; Nishimoto, T.; Yamamoto, N.; Yogo, K.; Yamada, K. Development of a New PH-Swing CO2 Mineralization Process with a Recyclable Reaction Solution. *Energy* **2008**, *33* (5), 776–784. https://doi.org/https://doi.org/10.1016/j.energy.2008.01.005.

28. Nduagu, E.; Björklöf, T.; Fagerlund, J.; Wärnå, J.; Geerlings, H.; Zevenhoven, R. Production of Magnesium Hydroxide from Magnesium Silicate for the Purpose of CO2 Mineralisation–Part 1: Application to Finnish Serpentinite. *Miner. Eng.* **2012**, *30*, 75–86.
29. Xie, H.-P.; Xie, L.-Z.; Wang, Y.-F.; Zhu, J.-H.; Liang, B.; Ju, Y. CCU: A More Feasible and Economic Strategy than CCS for Reducing CO2 Emissions. *J. Sichuan Univ. Eng. Sci. Ed.* **2012**, *44* (4), 1–5.
30. Xie, H.; Wang, Y.; Ju, Y.; Liang, B.; Zhu, J.; Zhang, R.; Xie, L.; Liu, T.; Zhou, X.; Zeng, H. Simultaneous Mineralization of CO2 and Recovery of Soluble Potassium Using Earth-Abundant Potassium Feldspar. *Chinese Sci. Bull.* **2013**, *58* (1), 128–132.
31. Sanna, A.; Dri, M.; Hall, M. R.; Maroto-Valer, M. Waste Materials for Carbon Capture and Storage by Mineralisation (CCSM) – A UK Perspective. *Appl. Energy* **2012**, *99*, 545–554. https://doi.org/https://doi.org/10.1016/j.apenergy.2012.06.049.
32. Pan E.E. and Chiang, Pen-Chi, S.-Y. and C. CO2 Capture by Accelerated Carbonation of Alkaline Wastes: A Review on Its Principles and Applications. *Aerosol Air Qual. Res.* **2012**, *12* (5), 770–791. https://doi.org/10.4209/aaqr.2012.06.0149.
33. Pan, S.-Y.; Chiang, P.-C.; Chen, Y.-H.; Chen, C.-D.; Lin, H.-Y.; Chang, E.-E. Systematic Approach to Determination of Maximum Achievable Capture Capacity via Leaching and Carbonation Processes for Alkaline Steelmaking Wastes in a Rotating Packed Bed. *Environ. Sci. Technol.* **2013**, *47* (23), 13677–13685. https://doi.org/10.1021/es403323x.
34. Rau, G. H. CO2 Mitigation via Capture and Chemical Conversion in Seawater. *Environ. Sci. Technol.* **2010**, *45* (3), 1088–1092.
35. Sanna, A.; Uibu, M.; Caramanna, G.; Kuusik, R.; Maroto-Valer, M. M. A Review of Mineral Carbonation Technologies to Sequester CO2. *Chem. Soc. Rev.* **2014**, *43* (23), 8049–8080.

https://doi.org/10.1039/C4CS00035H.

36. Zevenhoven, R.; Eloneva, S.; Teir, S. Chemical Fixation of CO2 in Carbonates: Routes to Valuable Products and Long-Term Storage. *Catal. Today* **2006**, *115* (1), 73–79. https://doi.org/https://doi.org/10.1016/j.cattod.2006.02.020.
37. Druckenmiller, M. L.; Maroto-Valer, M. M. Carbon Sequestration Using Brine of Adjusted PH to Form Mineral Carbonates. *Fuel Process. Technol.* **2005**, *86* (14), 1599–1614. https://doi.org/https://doi.org/10.1016/j.fuproc.2005.01.007.
38. Liu, Q.; Mercedes Maroto-Valer, M. Investigation of the Effect of Brine Composition and PH Buffer on CO2 -Brine Sequestration. *Energy Procedia* **2011**, *4*, 4503–4507. https://doi.org/https://doi.org/10.1016/j.egypro.2011.02.406.
39. Roach, R. W.; Carr, R. S.; Howard, C. L.; Cain, B. W.; Carrý, R.; Station, C. Assessment of Produced Water Impacts in Galveston Bay System. *US Fish Wildl. Report, Clear Lake Ecol. Serv. Off. Houston, TX* **1992**.
40. Puder, M. G.; Veil, J. A. Options, Methods, and Costs for Offsite Commercial Disposal of Exploration and Production Wastes. *SPE Proj. Facil. Constr.* **2007**, *2* (04), 1–5.
41. Soong, Y.; Fauth, D. L.; Howard, B. H.; Jones, J. R.; Harrison, D. K.; Goodman, A. L.; Gray, M. L.; Frommell, E. A. CO2 Sequestration with Brine Solution and Fly Ashes. *Energy Convers. Manag.* **2006**, *47* (13), 1676–1685. https://doi.org/https://doi.org/10.1016/j.enconman.2005.10.021.
42. Kharaka, Y. K.; Leong, L. Y. C.; Doran, G.; Breit, G. N. Can Produced Water Be Reclaimed? Experience with Placerita Oil Field, California. In *Proceedings of the 5th international petroleum environmental conference, Albuquerque, NM*; 1998.
43. Wang, W.; Hu, M.; Zheng, Y.; Wang, P.; Ma, C. CO2 Fixation in Ca2+-/Mg2+-Rich Aqueous

Solutions through Enhanced Carbonate Precipitation. *Ind. Eng. Chem. Res.* **2011**, *50* (13), 8333–8339. https://doi.org/10.1021/ie1025419.

44. Chen, C.-C.; Song, Y. Generalized Electrolyte-NRTL Model for Mixed-Solvent Electrolyte Systems. *AIChE J.* **2004**, *50* (8), 1928–1941. https://doi.org/10.1002/aic.10151.
45. Bui, M.; Tait, P.; Lucquiaud, M.; Mac Dowell, N. Dynamic Operation and Modelling of Amine-Based CO2 Capture at Pilot Scale. *Int. J. Greenh. Gas Control* **2018**, *79*, 134–153.
46. Mota-Martinez, M. T.; Brandl, P.; Hallett, J. P.; Mac Dowell, N. Challenges and Opportunities for the Utilisation of Ionic Liquids as Solvents for CO2 Capture. *Mol. Syst. Des. Eng.* **2018**, *3* (3), 560–571.
47. Cui, Q.; Lu, H.; Li, C.; Singh, S.; Ba, L.; Zhao, X.; Ku, A. Y. China Baseline Coal-Fired Power Plant with Post-Combustion CO2 Capture: 1. Definitions and Performance. *Int. J. Greenh. Gas Control* **2018**, *78*, 37–47.
48. Rao, A. B.; Rubin, E. S. A Technical, Economic, and Environmental Assessment of Amine-Based CO2 Capture Technology for Power Plant Greenhouse Gas Control. *Environ. Sci. Technol.* **2002**, *36* (20), 4467–4475. https://doi.org/10.1021/es0158861.
49. MacDowell, N.; Florin, N.; Buchard, A.; Hallett, J.; Galindo, A.; Jackson, G.; Adjiman, C. S.; Williams, C. K.; Shah, N.; Fennell, P. An Overview of CO2 Capture Technologies. *Energy Environ. Sci.* **2010**, *3* (11), 1645–1669.
50. Chlistunoff, J. Advanced Chlor-Alkali Technology. **2004**.
51. Cabral, R. P.; Heldebrant, D. J.; Mac Dowell, N. A Techno-Economic Analysis of a Novel Solvent-Based Oxycombustion CO2 Capture Process. *Ind. Eng. Chem. Res.* **2019**, *58* (16), 6604–6612. https://doi.org/10.1021/acs.iecr.9b00305.
52. Singh, D.; Croiset, E.; Douglas, P. L.; Douglas, M. A. Techno-Economic Study of CO2

Capture from an Existing Coal-Fired Power Plant: MEA Scrubbing vs. O2/CO2 Recycle Combustion. *Energy Convers. Manag.* **2003**, *44* (19), 3073–3091. https://doi.org/10.1016/S0196-8904(03)00040-2.

53. Thiel, G. P.; Kumar, A.; Gómez-González, A.; Lienhard, J. H. Utilization of Desalination Brine for Sodium Hydroxide Production: Technologies, Engineering Principles, Recovery Limits, and Future Directions. *ACS Sustain. Chem. Eng.* **2017**, *5* (12), 11147–11162. https://doi.org/10.1021/acssuschemeng.7b02276.
54. Bartels, C. R.; Andes, K. Consideration of Energy Savings in SWRO. *Desalin. Water Treat.* **2013**, *51* (4–6), 717–725.
55. Song, L.; Hu, J. Y.; Ong, S. L.; Ng, W. J.; Elimelech, M.; Wilf, M. Emergence of Thermodynamic Restriction and Its Implications for Full-Scale Reverse Osmosis Processes. *Desalination* **2003**, *155* (3), 213–228.
56. Elimelech, M.; Phillip, W. A. The Future of Seawater Desalination: Energy, Technology, and the Environment. *Science (80-.).* **2011**, *333* (6043), 712–717.
57. Council, N. R. Committee on Advancing Desalination Technology. *Desalin. a Natl. Perspect.* **2008**.
58. Lattemann, S.; Höpner, T. Environmental Impact and Impact Assessment of Seawater Desalination. *Desalination* **2008**, *220* (1), 1–15. https://doi.org/https://doi.org/10.1016/j.desal.2007.03.009.
59. Benko, K. L.; Drewes, J. E. Produced Water in the Western United States: Geographical Distribution, Occurrence, and Composition. *Environ. Eng. Sci.* **2008**, *25* (2), 239–246.
60. Consulting, A. L. L. Handbook on Coal Bed Methane Produced Water: Management and Beneficial Use Alternatives. *Prep. Groundw. Prot. Res. Found. US Dep. Energy, Natl. Pet.*

Technol. Ofce, Bur. L. Manag. July **2003**.

61. Veil, J. A.; Puder, M. G.; Elcock, D.; Redweik Jr, R. J. *A White Paper Describing Produced Water from Production of Crude Oil, Natural Gas, and Coal Bed Methane.*; Argonne National Lab., IL (US), 2004.
62. Wang, W.; Liu, X.; Wang, P.; Zheng, Y.; Wang, M. Enhancement of CO2 Mineralization in Ca2+-/Mg2+-Rich Aqueous Solutions Using Insoluble Amine. *Ind. Eng. Chem. Res.* **2013**, *52* (23), 8028–8033. https://doi.org/10.1021/ie400284v.
63. Millero, F. J. *Chemical Oceanography*; CRC press, 2016.

Chapter 5: Application of Ion-Exchange Processes for CO_2 Mineralization

5.1 Abstract

We propose a new process to produce an alkali solution that is subsequently utilized for the mineralization of carbon dioxide using an ion-exchange approach. In this scheme, the capacities for ion exchange of various zeolites and ion-exchange resins in CO_2-saturated water were studied through batch equilibrium and column ion-exchange experiments. The analysis of solution-phase concentration and solid phases and the rate of exchange of Na^+ for H^+ were studied across a range of temperatures, solution compositions, and solution conditions (i.e., static and convectively mixed). For all the tested materials, weakly acidic ion exchangers exhibited superior Na^+/H^+ exchange capacity in comparison to the highly acidic ion exchangers. Ion-exchange resins that contains weakly acidic functional groups such as carboxylic acid exhibited higher affinity for H^+, increasing pH from 4 to 11.3 and surpassing the pH shift induced by the zeolitic materials. The equilibrium ion exchange isotherms for Na^+/Ca^{2+}, Na^+/Mg^{2+}, and Na^+/Fe^{2+} aqueous solutions were also collected to assess the possibility of using ion exchange to increase the pH of carbonated water in an industrial flue gas stream with the presence of ions other than H^+ such as Ca^{2+}, Mg^{2+}, and Fe^{2+}.

5.2 Introduction

CO_2 mineralization is attractive to sequester CO_2 as it captures it as an insoluble carbonate mineral, imitating the rock weathering natural process. CO_2 mineralization is described in Eqs. (1)–(4). Alkaline pH is essential for the change in speciation of CO_2 to CO_3^{2-}, as shown in Eqs. (2) and (3), which reacts with calcium and magnesium ions for precipitation as shown in Eq. (4). This approach involves the conversion of CO_2 to carbonate minerals, offering an advantage in terms of energy savings and storage capacity as solid carbonate minerals, which alleviates the risk of gas leakage over an extended period of time.[1] Precipitation of calcite in aqueous solutions is favored by high Ca^{2+} and CO_3^{2-} concentrations and pH. Precipitation of calcite involves a decrease in pH, which eventually limits further precipitation according to the following equations:

$$\mathrm{CO_2\ (g)} \rightleftharpoons CO_2\ (aq) \quad (1)$$

$$CO_2\ (aq) + OH^-\ (aq) \rightarrow HCO_3^-\ (aq) \quad (2)$$

$$HCO_3^-\ (aq) + OH^-\ (aq) \rightarrow H_2O + CO_3^{2-}\ (aq) \quad (3)$$

$$Ca^{2+}/\ Mg^{2+}\ (aq) + CO_3^{2-}\ (aq) \rightarrow Ca/Mg\ carbonates\ (s) + heat \quad (4)$$

The main challenge in this process is to maintain the alkalinity during carbonation. The use of hydroxide (OH−) in alkaline aqueous solution to capture CO_2 has received attention recently as part of the viable carbon capture and sequestration (CCS) approach.[2] The increase of alkalinity makes a more thermodynamic environment to precipitate calcite. Mineral carbonation has been demonstrated in Ca-rich solids that are rich in Ca^{2+} such as slags,[3,4] other calcium silicates,[5] and waste concrete.[6] Mineral carbonation has also been demonstrated in processes that utilize brines as the Ca source.[1] The potential simplicity and low-cost implementation of using an alkaline solution for the CCS approach represent a substantial opportunity to mitigate CO_2 emissions.[2]

Previous studies have relied on the costly and unsustainable consumption of alkalinity sources such as natural minerals and solid waste.[7–11] Kodama et al.[12] used steelmaking slag and ammonium chloride solution to convert CO_2 to $CaCO_3$. The major disadvantage of these methods is the continuous need to add NaOH and secondary waste production. Ion-exchange processes can be used as an alternative method to the addition of stoichiometric inorganic bases such as sodium hydroxide to provide alkalinity for the consequential precipitation of $CaCO_3$. In this process, we used regenerable solids to increase the water pH through ion exchange and provide alkalinity. In principle, ions exchange between an electrolyte solution source and the similar charged ions fixed in an ion exchange material through a stoichiometric reversible ion-exchange reaction. Previous research has shown that both the forward and reverse H^+/Na^+ exchanges can occur.[13–15]

Ion exchange technology is usually used water purification by eliminating the dissolved ions through sorption by ion-exchange materials that have several physical forms.[16,17] An ion exchanger is a soluble material that has a functional group that traps and releases ions. The occurrence of a mobile ion having a charge that is opposite to the fixed ions neutralizes the ion's electrical charges.[16] Due to the specific structural feature of zeolites, all zeolites can serve as ion exchangers. However, only a limited number of these are used for practical applications. Ion-exchange efficiency is directly associated with content of aluminum in the zeolite. High-alumina zeolites are favored for ion-exchange applications.[18] The most commonly used synthetic zeolites in ion-exchange applications are Linde Type A (LTA) [19] and Linde Type X (FAU)[20] due to their high alumina content and easily accessible pore systems.[21] Ion exchange and selectivity in zeolites are mainly influenced by the exchangeable cations properties, the concentration of the solution, presence of other cations, and characteristics of zeolite such as channels and Si/Al ratio.[22] There are no separate ionogenic groups of zeolites; their lattice consists of SiO_4 and AlO_4 tetrahedra,

which have an oxygen atom in shared. Since aluminum is trivalent, the lattice has a negative electric charge which is balanced by alkali and alkaline earth cations that do not inhabit fixed sites but are able to move in the framework channels. Zeolite has been used because of its large number of active sites and large surface area. Synthetic resins are typically cast as porous beads with so-called matrix consisting of hydrocarbon chains with considerable external and porous surfaces where ions can bind. They contain ionizable groups placed along their chains. These radicals are fixed in the framework and are ionogenic groups of the resins. They can be classified, based on the functional group, into strongly and weakly acidic materials. Ion-exchange resins that contain phosphorate acid ($–PO_3$) groups and sulfonate ($–SO_3$) groups are strongly acidic resins. By contrast, materials containing phenolic (–OH) groups are weakly acidic and resins containing carboxyl groups (–COO) are in between strong and weak acidic exchangers.[23] Each of these major classes imitates the ionization extent, with the pH of the solution imparting different physical and chemical properties.[24]

In this work, we investigated a mineralization route that capture flue gas CO_2 using ion exchange technique through aqueous waste streams to convert CO_2 into carbonate precipitation. Maintaining alkalinity during carbonation is a prime challenge for CO_2 mineralization. Therefore, an ion-exchange cycle is developed to provide alkalinity. This section discusses the demonstration of these processes by identifying suitable materials and process parameters. The primary objective was to increase the pH of aqueous solution through the exchange of Na^+ within the ion-exchange material with H^+. Therefore, to better understand these aspects, monovalent exchange was studied across a range of H^+ concentrations at different temperatures (i.e., 5 °C, 25 °C, and 40 °C) and different solution conditions (i.e., static and convectively mixed).

5.3 Experimental Procedure

5.3.1 Materials

Sodium hydroxide (96%, PRS grade) and nitric acid (65% w/w, Pa grade) were supplied by Sigma-Aldrich. Demineralized water was used with a conductivity value of less than 5 μScm^{-1}. A variety of ion-exchange resins and zeolites were assessed for their ability to increase the pH of carbonated water. The resins used in this study were from different functional groups and in the Na^+ form. The strongly acidic cationic exchange resins used were with sulfonic groups fixed on the polystyrene divinylbenzene matrix such as synthetic Amberlite IR-120 in sodium form (16–45 mesh size), synthetic Lewatit Mono Plus SP 112 in sodium form, synthetic Amberlite 200 C in sodium form, and synthetic Diaion SK11, all of which were obtained from Sigma-Aldrich. Weakly acidic resins such as Lewatit TP-260 with di-Na^+ (aminomethyl) phosphonic acid groups and Lewatit TP-207 in the sodium form with iminodiacetic acid groups. The physical properties and chemical properties of the resins are summarized in Table 1. Commercially available zeolites 13X and 4A were obtained in sodium form from Thermo Fisher Scientific. Zeolites with a porous structure that can accommodate a wide variation of cations, such as Na^+, K^+, Ca^{2+}, and Mg^{2+}, and can be exchanged readily with other cations in a solution were used. Their lattice consists of SiO_4 and AlO_4 tetrahedra, which have an oxygen atom in common. The lattice has a negative electric charge that is balanced by cations that do not occupy fixed positions but are free to move within the channels of the framework. These cations act as counterions to the fixed anion and can be substituted by other cations.[24] Therefore, the negative charge of zeolites is not localized but is uniformly distributed in the framework. Unlike the charge in resin, the framework charge does not depend on the external conditions.

Table 5.1. Characteristics of the chelating resins.

	TP 207	IRA 120	SP 112
Structure	Macroporous weak acid	Gel of strong acid Cation exchange resin	Macroporous Cross-linked polystyrene
Matrix	Cross-linked polystyrene	Styrene–divinylbenzene copolymer	Cross-linked polystyrene
Functional group	Iminodiacetic acid	Sulfonic acid	Sulfonic acid
Average particle size	0.61 mm	0.5 mm	0.65 mm
Bulk density	0.72 g/cm^3		1.24 g/L
Density	1.1 g/cm^3		
Total exchange capacity	2.2 meq/g	1.9 meq/m	1.7 eq/L
pH range	pH 0–14	0–14	

	200C	IRA 120	TP 260
Structure	Macroporous cross-linked polystyrene	Styrene	Macroporous weak acid
Matrix	Cross-linked polystyrene	Styrene–divinylbenzene copolymer	Cross-linked polystyrene
Functional group	Iminodiacetic acid	Sulphonic	Aminomethylphosphonic acid
Average particle size	0.60–0.850 mm	0.3–1.2 mm	0.4–1.25 mm
Bulk density	0.72 g/cm^3	1.27 g/mL	0.72 g/cm^3
Density	1.1 g/cm^3		
Total exchange capacity	2.2 meq/g	1.80 mequiv/L	2.3 mequiv/L
pH range	pH 0–14	0–14	0–14

5.3.2 Experiments

5.3.2.1 Batch Experiments

Batch equilibrium experiments were performed in CO_2-saturated solutions and in HCl solutions to determine the effect of the counterion in the ion exchange step at 25 °C. First, ion exchange was carried out by immersing resin and zeolites in CO_2-rich solution in various liquid to solid mass ratios and stored in high-density polyethylene containers. Solutions for ion exchange

for both batch equilibrium and dynamic experiments were performed by bubbling CO_2 into Milli-Q water to reach saturation (pCO_2 = 1.0 atm, pH = 4). Herein, the amount of the ion exchanger varied from 0.025 to 5 g while the other parameters, such as pH (4), solution volume (20 mL), agitation speed (0 rpm), and proton concentration (64 mmol/L) were kept constant. Additionally, batch equilibrium experiments were performed using various concentrations of HCl, diluted from 12% HCl purchased from Sigma-Aldrich. A Thermo Scientific Orion pH electrode was used to measure initial and final pH values for ion-exchange experiments. NaCl (≥99.0%) used was purchased from Thermo Fisher Scientific. $CaCl_2 \cdot 2\ H_2O$ (≥99.0%) and $MgCl_2 \cdot 6\ H_2O$ (≥98.0%) that were used for competitive ion-exchange experiments were purchased from Thermo Fisher Scientific. Cation concentrations in solution were measured by inductively coupled plasma–optical emission spectroscopy (ICP-OES) using an Avio 200 ICP Optical Emission Spectrometer from Perkin Elmer. Solutions for ICP-OES were diluted in 5% HNO_3 (diluted from 70% HNO_3 obtained from Sigma-Aldrich).

Second, equilibrium resin-loading data were generated for Na^+/Ca^{2+}, Na^+/Mg^{2+}, and Na^+/H^+ systems. Ion-exchange experiments were performed on ion-exchange materials in batch reactions using MCl (M is the cation) concentrations varying from 0.001 M to 1 M at 25 °C. In order to obtain these data, 20 mL of carbonated water solution of known pH was added into each of the several flasks that contained different known masses of resin in Na^+ form and weighing ± 0.0001 g. The containers were either shaken after each sampling or left unstirred. A 2-mL solution aliquot was collected at different times and passed through a 0.2-µm filter to remove residual solids, and the chemical composition was measured using ICP-OES. To determine the optimum conditions for the exchange of Na^+ by H^+, the experimental set was hermetically sealed and submerged in a temperature-controlled thermostatic bath. The effect of contact time (0–360 min),

temperature (5–50 °C), initial concentration (1–30 mmol/L), weight (0.5–10 g/L), and initial pH (2–13) on ion exchange was investigated. The exchange amount was determined using the following equation:

$$Q_e = (C_0 - C_e)V/W \quad (5)$$

5.3.2.2 Dynamic Experiments with Ion-Exchange Column

A home-built ion-exchange column was constructed to study ion-exchange performance for sorbents. A schematic of the constructed ion-exchange experiment can be seen in Figure 5.1. Liquid is introduced through a BioLogic LP peristaltic pump and passes through a 3.2-mm tube into the column. An aqueous solution is introduced through an in-line port and then fed into the ion-exchange column with a bed height of 24.1 cm and a bed diameter of 3.5 cm, varying flow rates from 2–20 mL/min. The outlet stream, post ion exchange, is sent to ICP-OES for measurement of elemental concentrations of Si, Al, Ca, K, and Na in solution. Furthermore, a pH meter was used to measure the pH of the outlet stream.

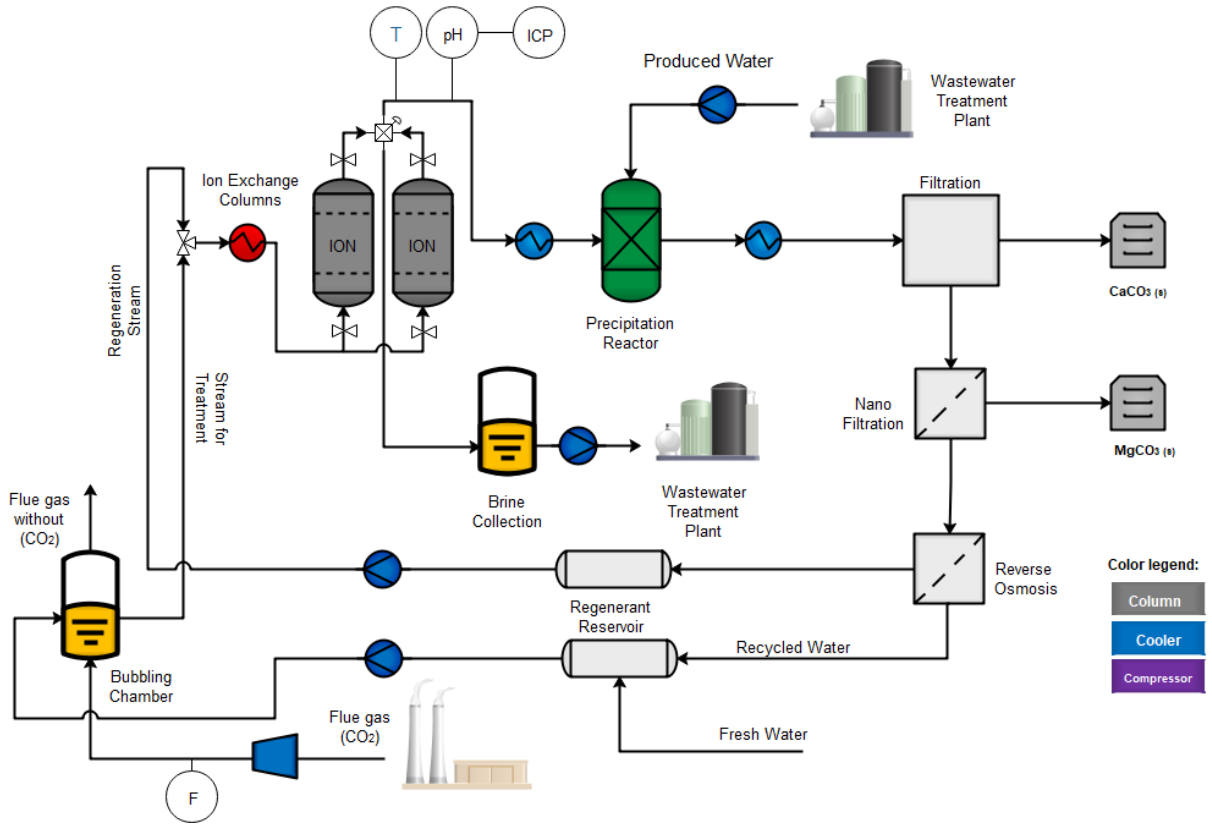

Figure 5.1. Process flow diagram of ion-exchange setup for precipitation experiments. Flue gas is contacted with a either fresh water or ca-containing solution.

5.3.3 Solution Phase Analysis

The elemental concentrations of Si, Al, Ca, K, and Na in solution were measured by ICP-OES using the Avio 200 instrument (PerkinElmer, USA). The filtered solution was diluted in 5% vol. nitric acid matrix. Three spectra were obtained for each sample and then converted to molar concentration by interpolation with standard solutions. An analytical balance (Mettler PM 400, Switzerland) was used to weigh the resins and other reagents. A portable pH/mV meter (Thermo Scientific Ross Ultra Electrode) with a glass electrode was used for pH measurements. The pH electrode was calibrated using four points of calibration with a reference (buffer) solution covering the range of $3 \leq pH \leq 13$ at 25 ± 3 °C.

5.3.4 Modeling

Ion-exchange isotherms explain equilibrium by representing counterion concentrations in the exchanger as a function of the concentration in their electrolyte solution at a constant temperature. The desire to optimize the ion-exchange process motivates covering all the possible experimental conditions accurately. The number of works done for the multicomponent system in comparison to the binary system is rather small due to the complexity of these systems. Interactions between counterions in the solution and with the exchanger, exchanger surface heterogeneity, and the amount of dissociation of exchangeable ions affect the complexity of the system.[25]

Ion-exchange models that describe the system fall into four groups:

Groups 1: ion exchange is described in the law of mass action and treated as a chemical reaction. The exchanger is assumed to be homogeneous. Activity coefficients of the ions describe nonidealities of the system in solution and solid phases. This group is called homogenous mass action models (see Dranoff and Lapidus,[26] Klein et al.,[27] Smith and Woodburn, [28] Sengupta and Paulvv,[28] Shallcross et al.,[29 30] Mehablia et al.,[31] Ioannidis et al., [32] Mumford et al.,[33] Borba et al.,[34] and Aniceto et al.[35,36]).

Group 2: ion exchange is considered as an adsorption process. Early efforts used Langmuir's and Freundlich's model isotherms followed by more through models. In this approach, deviation from ideality is elucidated in terms of the functional groups' energetic heterogeneity of ions. This group is called heterogeneous adsorption models. In this approach, empirical and semiempirical isotherms such as those of Langmuir and Frendulich are used.[37,38,47–49,39–46] Deviation from ideal adsorption is explained by heterogeneity of the functional group. Altin et al. presented a review of the successful application of isotherm models in binary equilibrium data between heavy metal and clay mineral.[45] Petrus and Warchol used Langmuir models to fit and

study solution containing $Pb^{2+}/Cd^{2+}/Cu^{2+}$ ions using a sodium ion form of the zeolitic clinoptilolite.[46] Ku et al. applied both Langmuir and Freundlich adsorption models to study the equilibrium solution of phenols in the presence of Purolite A-510 in chlorine form.[47] Uptake was considered to occur through resin active sites through either ion exchange or adsorption. The value of pH influence equilibrium because phenol acts as a weak acid. Therefore, other factors such as species distribution, ionization reaction, and acidity constant were considered. Carmona et al. observed the performance of phenol removal from aqueous solution using IRA 420. They advanced a better model to account for ion exchange and the adsorption mechanism in the overall uptake. For both phenomena, the Langmuir equation was adopted. Moreover, Langmuir and Freundlich models were used to study equilibria of phenol from aqueous solution using strong and weak anion exchangers.[49] Both models have been used widely to study of Hg^{2+} and Cd^{2+} equilibria in aqueous solutions on ETS-10 and ETS-4.[37–41,43,44]

Group 3: these models are derived from Melis et al.[50] Models are based on mass action law, which accounts for the heterogeneity of ion-exchange sites. These models are called heterogeneous mass action models.

In this study, we used adsorption models to explain the ion exchange process as explained in the following subsections.

5.3.4.1 Kinetic Sorption Modeling for Fixed-Bed Experiments

The aqueous phase flows through a packed bed of ion exchangers whose properties change in space and time as the process progresses.

Cations travel from the bulk of the aqueous phase to the surface and diffuse through layers of solid phase and pores until it reaches the surfaces available for ion exchange. At the surface, incoming cations exchange with ion-exchanger solids. The complexity of this multiscale process has led to the progress of various models such as the pore model, which aims to capture the integrated diffusion process accurately.[51] Nevertheless, simpler models such as linear driving force models may be used to describe the system less rigorously without losing relevant parameters.

5.4.2.1.1 Linear Driving Force Models

Linear driving force models are derived from analyzing adsorption column dynamics. Models provide an adequate quantitative approximation for sorption systems when the equilibrium constant is sufficiently large.[52]

Ione exchange of cations from an aqueous phase mass balance is represented as follows:

$$v\left(\frac{\delta C}{\delta Z}\right)_t + \left(\frac{\delta C}{\delta t}\right)_z + \frac{1-\varepsilon}{\varepsilon} \cdot \left(\frac{\delta q}{\delta t}\right)_z = 0 \qquad (6)$$

where v is the axial velocity of fluid through the column, z is the axial distance in the direction of the flow, C is the incoming cations concentration in the bulk fluid, t is time, ε is the bed void fraction, and q is the average concentration of incoming cations in the solid phase (maximum capacity). The derivation of this equation was based on several assumptions. First, dispersive terms are negligible due to the large axial aspect ratio, $L/d_p > 50$, where L is the bed depth and d_p is the particle diameter. With the assumption of axial dispersion neglected, the flow is assumed to be a plug flow with a constant velocity in the axial direction.[53] Therefore, velocity and concentration are constant in the radial direction. The high D/d_p ratio, where D is reactor diameter, causes

minimal channeling effects and constant interstitial velocity. Finally, the system is assumed to be isothermal, with temperature constant along the length of the bed. Bohart and Adams proposed describing the overall ion exchange rate $\left(\frac{\delta q}{\delta t}\right)$ by a linear rate law as follows[54]:

$$\frac{\delta q}{\delta t} = k_a C(q_s - q) \tag{7}$$

where k_a is the ion exchange rate constant and q_s is the maximum exchange capacity. The resulting concentration profile is

$$\frac{C}{C_0} = \frac{e^{\tau}}{e^{\tau} + e^{\mathfrak{z}} - 1} \tag{8}$$

where $\tau = k_a C_0 \left[t - {}^{L}/_{v}\right]$, $\mathfrak{z} = (k_a q_s L/v)((1-\varepsilon)/\varepsilon)$, C_0 is the concentration of the inlet cations, and ε is bed void fraction.

The overall ion exchange rate is described as follows[55]:

$$\frac{\delta q}{\delta t} = k(q_s - q) \tag{9}$$

where k is the ion exchange rate parameter. The analytical solution system is represented as follows:

$$\frac{C}{C_0} = 1 - \mathfrak{z} e^{-\tau}, \ \mathfrak{z} \leq 1 \tag{10}$$

$$\frac{C}{C_0} = 1 - e^{\mathfrak{z}-\tau-1}, 1 \leq \mathfrak{z} \leq 1+\tau \tag{11}$$

$$\frac{C}{C_0} = 0, \mathfrak{z} \geq 1+\tau \tag{12}$$

where $\tau = k\left[t - {}^{L}/_{v}\right]$ and $\mathfrak{z} = (k q_s L/C_0 v)((1-\varepsilon)/\varepsilon)$. These models relate the properties of the material and the experimental conditions to the concentration–time profile (breakthrough

curve) of the incoming cations in the effluent of the ion-exchange column. The two parameters [the sorption rate parameter (k) and the maximum exchange capacity (q_s)] are regressed from breakthrough curve data in the nonlinear least squares solver.

The rate parameter (k) contribute to three coefficients: the diffusion of cations in the bulk liquid phase fluid, diffusion inside the pores of the zeolite or polymer, and diffusion at the surface of the ion-exchanger phase:

$$\frac{1}{kK} = \frac{R_p}{3k_f} + \frac{R_p^2}{15\varepsilon_p D_p} + \frac{1}{k_{ex}} \tag{13}$$

where R_p is the radius of the ion-exchanger particles, D_p is the effective diffusivity of the incoming cations inside the pores of the solids, k_f is the mass transfer coefficient for fluid film mass, and ε_p is the porosity of the solid particles. The distribution parameter (K) is the ratio of the incoming cations in the solid phase to those in the fluid phase at equilibrium (q_s/C_0). The ion-exchange rate (k_{ex}) contains contributions from the ion-exchange interface at the solid surface and diffusion of ions.

The term k_f is determined using the Sherwood equation in which D_M is the ion diffusivity of the incoming ion in the bulk fluid, Sc is the Schmidt number, and Re is the Reynolds number[56]:

$$k_f = \frac{D_M Sh}{2R_p} \qquad Sh = 2 + 1.1Sc^{1/3}Re^{0.6} \tag{14}$$

$$D_M = \frac{0.00266T^{3/2}}{PM_{AB}^{1/2}\sigma_{AB}^2\Omega_D} \tag{15}$$

Diffusion in pores is determined by the value for D_p from the sum of diffusion in the macropores and mesopores of the solid according to

$$D_p = \frac{D}{\tau} \qquad \frac{1}{D} = \frac{1}{D_M} + \frac{1}{D_K} \tag{16}$$

where D_K is the Knudsen diffusivity given by $D_K = 9700r(\frac{T}{M})^{1/2}$ (r is the pore radius, T is temperature, and M is the molecular weight of the diffusing species), and τ is the tortuosity.

5.3.4.2 Kinetic Sorption Modeling for Batch Experiments

5.3.4.2.1 Pseudo-First Order

The equation of pseudo-first order is as follows[57]:

$$q = q_e[1 - exp(-k_1 t)] \quad (17)$$

$$\frac{dq_t}{dt} = k_1 \times (q_e - q_t) \quad (18)$$

$$log(q_e - q_t) = \log q_e - \frac{k_1}{2.303} \times t \quad (19)$$

where q is the number of ions exchanged, q_e is the number of ions at equilibrium, and k_1 is the pseudo-first order rate constant.

5.3.4.2.2 Pseudo-Second Order

The equation of pseudo-second is as follows[58]:

$$q = \frac{t}{\frac{1}{k_2 {q_e}^2} + \frac{t}{q_e}} \quad (20)$$

$$\frac{dq_t}{dt} = k_1 \times (q_e - q_t)^2 \quad (21)$$

$$\frac{q_t}{t} = \frac{1}{k_1 \times {q_e}^2} + \frac{t}{q_e} \quad (22)$$

where k_2 is the pseudo-second order rate constant.

The terms k_1 and k_2 are the rate constants for the pseudo-first and pseudo-second order equations, and q_e and q_t are uptake mmol per weight unit of the sorbent at equilibrium and at time t, respectively.[59] Plotting $logk_2$ as a function of $1/T$ is useful to obtain the activation energy (E_a) using the Arrhenius equation:

$$k = A \times e^{-(\frac{Ea}{R} \times T)} \tag{23}$$

where k is the rate coefficient, A is constant, E_a is the activation energy, R is the universal gas constant, and T is the temperature (in Kelvin). Activation energy values between 5 and 20 kJ mol^{-1} characterize the sorption process and are controlled by diffusion, and the chemical reaction–controlled process requires more than 20 kJ $mole^{-1}$ energy.[60,61]

5.4 Results and Discussion

5.4.1 Selection of Ion-Exchange Materials

In the preliminary studies, different chelating ion exchangers containing such functional groups as iminodiacetate (Lewatit TP 207), aminomethyl phosphonate (Lewatit TP 260), sulfonic groups (Amberlite 200 C, Lewatit MonoPlus SP 112, Diaion SK112, and Amberlite IR120), and zeolites (13X, 4A) were used. The proton uptake by ion-exchange materials was studied by varying the amount of the ion exchanger from 0.25 to 5.0 g while keeping the other parameters such as pH (4), solution volume (20 mL), agitation speed (0 rpm), and proton concentration (64 mmol/L) constant. The H^+–Na^+ ion exchange was conducted in CO_2-saturated water (pCO_2 = 1 atm, pH 4; Figure 5.2). As the water equilibrated with the CO_2 gas stream, dissolved CO_2 acidified the water by forming H_2CO_3. As the H^+ concentration in the water increased, it exchanged with monovalent ions contained in the ion-exchanger solid (Na^+) until equilibrium was achieved, which prevented a further increase in pH. The achievement of equilibrium was checked by taking repeated samples as well as by letting the system approach the equilibrium state. Liquid samples were withdrawn and analyzed by ICP-OES. The pH and sodium concentration of the solution after equilibrium was reached were also determined.

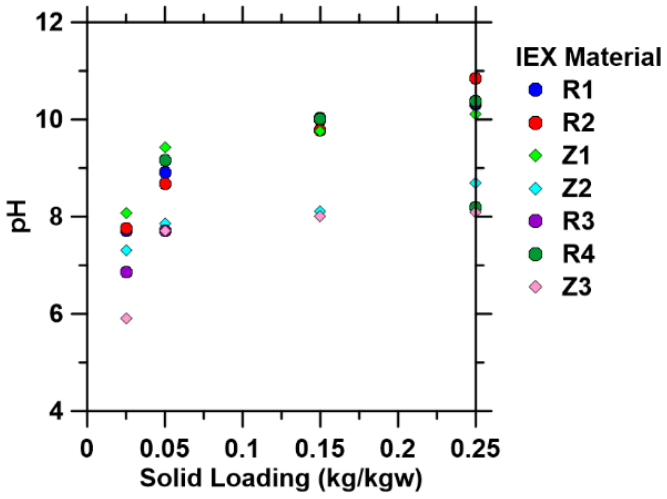

Figure 5.2. Effect of material solid loading on the pH of materials.

Increasing the ratio of the solid to liquid resulted in increasing proton removal. The increase in pH with the increasing solid-to-liquid ratio was due to the larger surface sites numbers accessible for interaction. In all ion-exchange materials, as pH increase, it was coupled also with an increase in concentration of Na, demonstrating the feasibility of the forward ion-exchange process and illustrating that significant basicity can be generated. The cationic resins that contained sulfonic groups (Amberlite 200 C) did not achieve high proton removal percentages (i.e., the pH did not meet the minimum pH = 8 required for calcium carbonate precipitation). Amberlite IR-120, Diaion SK112, and Lewatit Mono Plus SP 112 obtained unsatisfactory results, with maximum obtained pH values equal to 6, 5.5 , and 7, respectively.

Compared with the strongly acidic ion exchange materials, weakly acidic resins exhibited higher ion-exchange capacity and higher affinity for protons. The affinity of the ion exchanger to dissociate sodium and exchange it with a proton was higher for the weak acidic cation exchange resin than for the strong acidic resin. Strong acid resin is highly dissociated; thus, a considerable excess of acid is needed to convert the sodium form into the hydrogen form. Strongly acidic material imposes lower ion-exchange potential performance than does the weakly acidic resin. Weak-to-moderate acidic ion exchangers, such as zeolite (13X and 4A), have less hydrogen affinity than weakly acidic resin does but are able to convert dissolved carbonic acid into $NaHCO_3$.

Lewatit TP 207(Na) and Lewatit 260 were superior in terms of ion exchange and increasing the alkalinity of the solution from 4 to approximately 10. They were followed by weak ion exchangers such as zeolite 13X and 4A. Thus, in the next stages, the following ion exchangers were investigated: Lewatit TP 207 and Lewatit TP 260, zeolite 13X, and zeolite 4A. Lewatit TP

207 and Lewatit TP 260 resins are both weakly acidic and in the Na^+ form but contain different active groups. In the case of Lewatit TP 260 resin, the proton uptake was higher than that exhibited in TP 207. TP 260 is a weak acidic macroporous resin that contains chelating aminomethylphosphonic acid groups.[62] The aminomethylphosphonic acid group is a tridentate ligand that has two connection sites attached to phosphonic acid group and one coordination site at the nitrogen atom. Depending on the pH, the aminomethylphosphonic acid chelating group occurs in the forms shown in Figure 5.3. The presence of the methylene group increases the electron density on the atom of nitrogen of the amine groups, which promotes its protonation.[63–66] Lewatit TP 207 is a weakly acidic resin with chelating iminodiacetate.[66] At low pH, the excess proton competes for the binding site. When pH increases, the H^+ is displaced from the functional group of the resin, allowing ion exchange to occur in the resin. The pH values dictate the occurrence of iminodiacetate groups in the forms presented in Figure 5.4.[67,68] At pH values of approximately 2 (or less), both carboxylic groups and nitrogen atoms occur in the protonated forms. At higher pH (~12), both carboxylic groups are deprotonated, and the ion exchanger behaves as a typical cation exchanger. The number of cations exchanged at low pH values is lower than the number of ions exchanged at high pH values. This is due to the iminodiacetic functional groups of the resin, which tend to remain protonated in low pH solutions, and thus, the ions are less preferred by the resin under these conditions.[69–71]

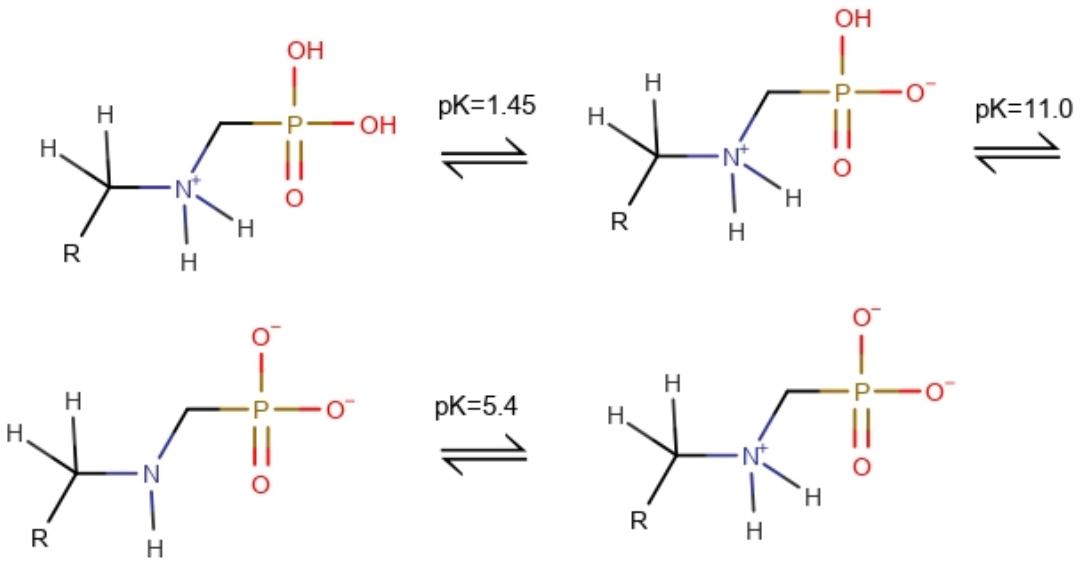

Figure 5.3. Aminomethylphosphonic acid chelating groups that occur (drawing made using MarvinSketch).[63–66]

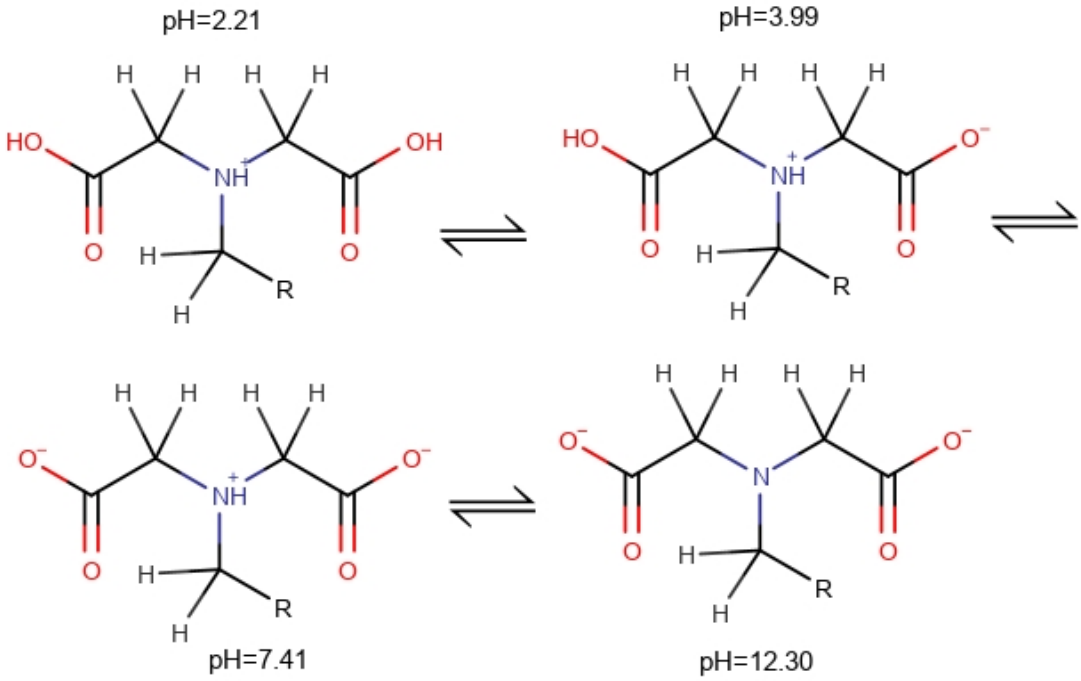

Figure 5.4. Iminodiacetate groups that occur in Lewatit TP 207 (drawing made using MarvinSketch).[67,68]

The ion exchanger was also able to increase the pH of the natural pH water. The rise in pH was attributed to the exchange between Na^+ and H^+ from the water solution (Figure 5.5). This shows that the ion-exchange process can also be used to increase the pH of deionized (DI) water before adding the CO_2 to the solution, which is an alternative to the previous step in which CO_2 was initially equilibrated with the solution before ion-exchange materials were added. When 1 g of NaR (where R is the exchanger matrix) was added into 20 mL of DI water, a small amount of Na^+ was released, and the pH became alkaline. This indicated that Na^+ was retained to compensate for the negative charge of zeolite that was released to the aqueous phase, followed by H^+ uptake, which originated for the dissociation of water.

The ion speciation of hydrolysable ions changes with changes in pH levels. Hydrolysis is a common phenomenon with inorganic and weakly acidic organic ion exchangers. In a hydrolysis reaction, the exchanger (NaR, where R is the exchanger matrix) takes up proton ions from water.[72] The more selective the exchanger for hydronium ions is (i.e., the more weakly acidic the exchanger is), the more pronounced it is for hydrolysis. Hydrolysis increases the pH and alters the ionic composition of dilute solutions. The resulting carbonic acid consumes the hydroxyl ions that are produced by hydrolysis to yield HCO_3^- and CO_3^{2-} in solution. Thus, The H^+–Na^+ ion exchange was conducted in neutral water (pCO_2 = 400 ppm, pH 7). As the solid load increases, basicity increases toward a maximum of 12.

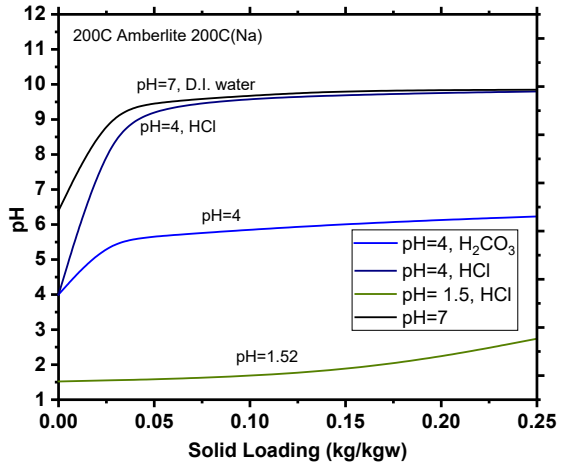

Figure 5.5. Effect of solid loading on the pH of solution at various initial concentrations.

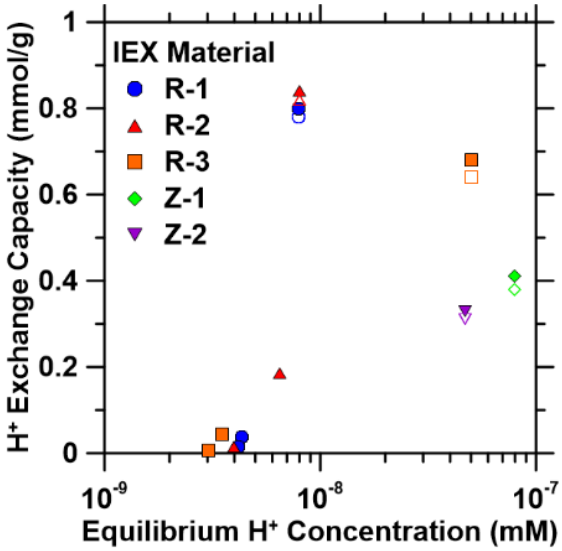

Figure 5.6. Cation exchange capacity of various concentrations of materials.

The scale of such cation exchange is known as cation exchange capacity (CEC) and is usually measured in terms of moles of exchangeable cation per gram (or per 100 grams). Using CEC expressed in terms of mmol per gram makes it easy to compare the amount of cation that can be exchanged with zeolite or resin. Thus, results of investigating the effect of increasing the ionic strength of protons and their effect on proton uptake are presented in this section.

Equilibrium uptake isotherms were collected for the batch equilibrium experiments. Figure 5.6 shows the exchange capacities of the ion-exchange materials in various concentrations of HCl solutions and CO_2-saturated solutions. CO_2 concentrations by volume from point sources are roughly 3% for natural gas–fired power plants; 15% for coal-fired power plants and iron and steel mills; 20% for cement plants; and >90% for ammonia, ethanol, and hydrogen plants.[73] Therefore, we used the reference concentrations of 5%, 20%, and 100% in the above analysis. In this case, the total number of cations in the systems was supposedly constant using 1 g of an ion exchanger. Changing the concentration of CO_2 from 15% to 100% resulted in lower equilibrium concentrations and thus lower exchange capacities. The maximum exchange capacity was achieved at the initial CO_2 concentration of 14% with 2.1 mmol/g. This follows the same trend observed with Na^+/H^+ exchange in HCl solutions. Maximum exchange capacity with organic exchange resin was achieved at 1 M HCl (~3 mmol/g Na released) with a high Na release from the zeolites due to dissolution. Overall, weakly acidic function groups provided higher ion-exchange capacities than zeolitic materials did; this may have been a result of the available exchange sites and hydrogen affinity. Zeolite Na-X had a CEC of 0.6 mmol g^{-1}. It had a lower exchange capacity than did Na-A and did not proceed to a full exchange. Exchange capacity was higher than solid loading but lower than the HCl experiment's exchange capacity. This is because HCl represented the highest exchange capacity so far.

5.4.2 Ion-Exchange Selectivity

Produced water contains various types of polyvalent cations that can inhibit ion exchange and compete with and affect the sorption behavior of ion-exchange materials for H^+ uptake. Therefore, it was essential to investigate the effect of coexisting ions on H^+ uptake. Single and binary component exchange isotherms were collected to probe the selectivity for the exchange of Na^+ with H^+ in the presence of produced water ions, such as Ca^{2+} and Mg^{2+}. The organic cation exchange resins used in this study have a high affinity for divalent cations because of their chelating-like functional groups. These resins are commonly used for water hardness removal (i.e., removal of Ca and Mg ions from water) because of their high affinities for divalent cations. Their high affinities for divalent cations may hinder H^+ uptake when using a produced water feed for swinging the pH. In quantifying the effect on H^+ uptake due to the presence of calcium cations, the most prominent divalent cation found in produced water streams, for all materials, determines the composition of the feed stream required to swing the pH of a stream containing CO_2. Shown in Figure 5.7 a and b is the effect of calcium in solution on H^+ uptake within HCl- and CO_2-saturated water, respectively.

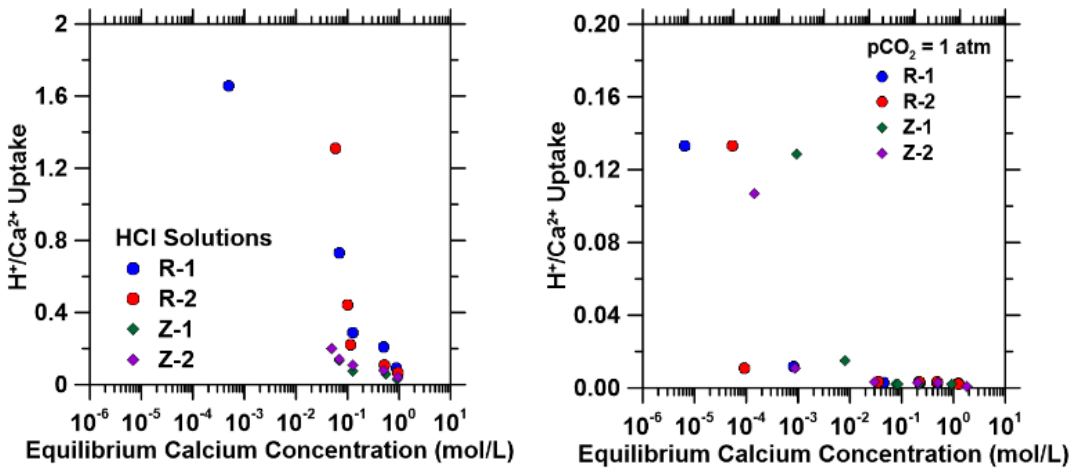

Figure 5.7. H^+ uptake reduction as a function of equilibrium calcium concentrations increasing in solution in (a) HCl and (b) saturated CO_2 solution.

The ion-exchange capacity for H^+ appears to be very similar to that of Ca^{2+} at a low concentration of Ca^{2+} in the solution for both HCl- and CO_2-saturated solutions. A similar capacity suggests that there is no significant selectivity of Ca^{2+} over H^+. However, as the concentration of Ca^{2+} increased in the solution, the uptake of H^+ started to decrease, reaching minimum levels when the concentration of Ca^{2+} increased over 10^{-3} (mol/L). Divalent cation uptake is only hindered by the presence of other divalent cations or large concentrations of monovalent ions. The increase can be explained by decreased competition between protons and Ca^{2+} for the same functional group and by a decrease in the positive surface charge in resin resulting in lower electrostatic repulsion between the surface of resin and calcium or magnesium ions.[74] Selectivity could be the result of several factors that affect ion-exchange behavior in the zeolite and resin. One factor is the structure of the zeolite; the dimensions of channels formed by tetrahedral units need to be large enough to allow hydrated ions to approach active sites. The specificity of a surface containing fixed charges for alkali ions was accounted for in terms of ion hydration and electrostatic bond energies.[75] The metal-binding strength increases as the radius of the hydrated metal ion decreases and the charge of the metal ion increases. A strong electrostatic field effect may become the dominant factor for ion affinity, such that small ions with a higher charge density are bound more strongly. An alternative explanation for the difference in selectivity involving two ions with the same radius is the dehydration phenomena,[76] in which hydrated ions initially overcome the energy barrier to be able to enter zeolite channels. This energy barrier is mainly composed of the energy required to dehydrate ions during collusion at the pore entrance.

As shown in Figure 5.7 a and b, the divalent cations found in produced water had a detrimental effect on the ion-exchange process, resulting in a decrease in H^+ uptake efficiency. These ions have a stronger attraction to the active site than an H^+. H^+ uptake decreased with increasing equilibrium calcium concentrations because of the higher affinity for divalent cations of the ion-exchange materials. Due to the higher affinities for divalent cations, it was difficult to develop a pH swing process using an integrated process configuration (i.e., carbonation reactor integrated with an ion-exchange process).

5.4.3 Batch Kinetic Results

The kinetics of ion exchange describe the rate of ion uptake on the ion-exchange resin and zeolites, and this rate controls the equilibrium time. The kinetic factor is required to select optimum operating conditions for a full-scale batch process. To evaluate the differences in the ion-exchange kinetic rates and the ion recoveries, the kinetics of ion uptake were described with a pseudo-first order and pseudo-second order model. The pseudo-first order model assumes a diffusion-controlled process inside the particles, whereas the pseudo-second order model assumes that the process is controlled by ion exchange at liquid–solid interface in the adsorbent.[77,78] The results of the sorption kinetics experiments for the zeolites studied are presented in Figure 5.8. For the zeolites studied, the sorption process was rapid. Zeolite 13X had the fastest sorption due to its large pore structure and slow diffusion. Equilibrium was reached after 3 h (1.2 mmol/g). For 4A, equilibrium was achieved after 16 h. The results revealed a faster kinetic rate for the organic polymer.

The diffusion rate of the ion exchanger can be limited with the interdiffusion of the exchanged counterions within the ion exchanger (i.e., particle diffusion) or with an adjacent liquid film that is not affected by the agitation of the solution (i.e., film diffusion). Large crystals, such

as 13X, were compared to 4A and exhibited a similar rate of release of Na^+, indicating that this release was not particle diffusion control (Figure 5.8; Table 5.2 and 5.3).

The kinetic experiments of ion exchange in zeolite indicated slower exchange rates for larger crystallites. Zeolite has a subnanometer porous structure that involves mechanisms of ion transport other than nonporous polymer resin. Due to the space confinement in the channels and strong interactions between water, ions, and pore surface, the mobility of water and ions are mutually affected. As shown in Figure 5.8, the exchange of Na^+ with H^+ proceeds faster with the smaller crystallites (4A), whereas their ion-exchange equilibrium is identical. With smaller pores, a faster exchange is observed.[79] A kinetic exchange between cations diffusing through the micropores and cations bound to a specific site could be the rate-determining step. However, this requires that the rate of exchange of ions at sites within the zeolite channels is slower than the rate at which ions diffuse through the micropores.

The chemical exchange reaction at fixed ionic sites is not the rate-limiting step. Several studies have shown that the Na^+/H^+ exchange reaction in natural solution is rapid, and equilibrium is attainable within a few minutes.[80,81] Furthermore, the kinetic reaction is not a first-order reaction.[82] To confirm the fast exchange process, kinetic experiments were carried out at temperatures of 5 °C, 25 °C, and 50 °C (Figure 5.8). A distinct positive effect of temperature on the sorption rate was observed in addition to exchange capacity. The constant rate k_2 for temperatures of 5 °C to 50 °C indicated that higher temperatures favor the driving force of the exchange process, and it increased from 0.027 to 0.040 (mmol/min) for TP207, from 0.011 to 0.017 (mmol/min) for TP260, from 0.016 to 0.029 (mmol/min) for 4A, and from 0.012 to 0.016 (mmol/min) for 13X. The activation energy was determined from the slope of a linear plot. The values calculated were less than 20 kJ mol^{-1} (Table 5.4), which may indicate the diffusion-limited

process. Generally, activation energy values between 5 to 20 kJ mol^{-1} characterize the ion-exchange process that is controlled by diffusion, while the chemical reaction–controlled process requires more than 20 kJ $mole^{-1}$ of energy.[60,61]

The increase in ion exchange with temperature may be attributed to the increasing rate of the intraparticle diffusion of ions into pores that are adsorbent at higher temperatures. If the interdiffusion of exchangeable species in solid or bulk solution is the rate-determining step, then the rate constant will be equal when static and mixing and independent of mixing. Under convective mixing, the ion-exchange rate increases exponentially with an increase in mixing speed. This signifies the importance of the role of transport in ion exchange. At a strong mixing rate, the resistance of the boundary layer that surrounds the sorbents weakens. As can be observed by the k_2 constant, the ion-exchange rate is faster at a higher mixing rate. In solid-state exchange reactions, a small amount of water can increase the speed of the reaction.[83] Therefore, the ion-exchange reaction has been modeled as diffusion limited.[84] When diffusion is the rate-controlling step, then the rate-controlling diffusion process may not be within the micropores themselves but instead may be limited by transport via a near-static boundary layer that is inserted between the external solution and crystalline surface. This process is described as a film or boundary layer diffusion.[85]

In our results, weakly ionic resins, such as TP207 and 260 kinetics, were significantly enhanced by mixing but were not when remaining static, which suggests a surface-controlled reaction. This was proved to be correct because we did not have any pores that could limit the diffusion. By contrast, data for 4A and 13X were not significantly affected by mixing, which may suggest a solid-phase diffusion-controlled mechanism. Furthermore, the static and mixed solution conditions led to the same activation energy; hence, the diffusion of ions through the Nernst's

diffusion layer is the rate-limiting step. This is because solution viscosity would not influence ion transport.

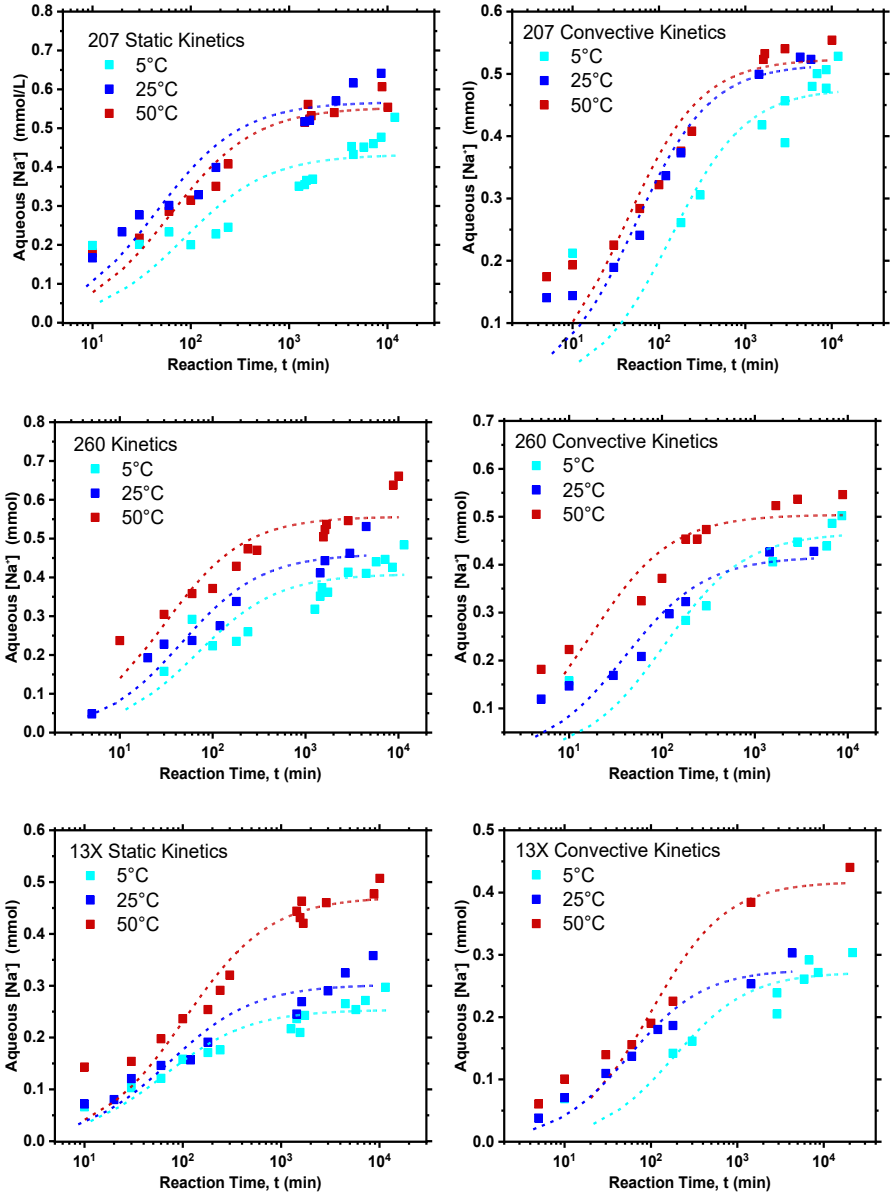

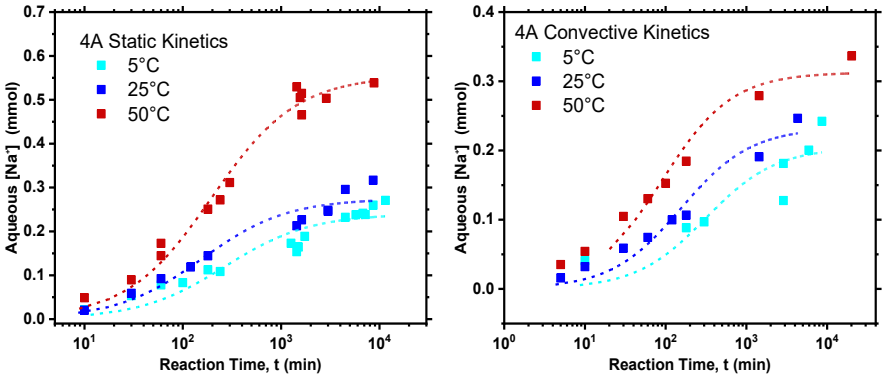

Figure 5.8. Na^+ release and exchange with H^+ from solution as functions of time for TP207, TP260, 4A, and 13X undergoing ion exchange under static and convective (stirred) mixing conditions for an initial CO_2 concentration of 34 mmol/L.

Table 5.2. Ion exchange reactions for different materials over time from 5 °C to 50 °C under static conditions.

Material	**TP-207**	**TP-260**	**Zeolite 4A**	**Zeolite 13X**
Temperature (°C)	K (mmol/min)	K (mmol/min)	K (mmol/min)	K (mmol/min)
5	0.027	0.011	0.016	0.012
25	0.030	0.013	0.022	0.014
50	0.040	0.017	0.029	0.016

Table 5.3. Ion exchange reactions for different materials over time from 5 °C to 50 °C under convective conditions.

Material	**TP-207**	**TP-260**	**Zeolite 4A**	**Zeolite 13X**
Temperature (°C)	K (mmol/min)	K (mmol/min)	K (mmol/min)	K (mmol/min)
5	0.015	0.009	0.015	0.020
25	0.032	0.060	0.027	0.065
50	0.045	0.12	0.035	0.024

Table 5.4. Activation enthalpies of ion-exchange reactions for materials.

Material	ΔH (kJ/mol) Static	ΔH (kJ/mol) Convective
TP-207	----	17.4
TP-260	6.6	43
Zeolite 4A	9.5	9.9
Zeolite 13X	4.9	----

5.4.4 Polyvalent Ion-Exchange Kinetics

The results obtained for calcium, magnesium, and iron kinetics indicate a different mechanism from that for Ca/Mg uptake. In general, the amount of sodium released materials and exchanged with ions from solutionis higher for Ca/Mg than for that of Fe. Figures 5.9–5.11 show the kinetics of metal exchange with ion-exchange materials. The plots represent the rate of ion exchange over time, showing the amount of sodium release as it is exchanged by the ions placed in the solution, whether Ca, Mg, or Fe. Although ions started initially with the same concentration, Tables 5.5–5.7 show the correlation coefficients of the kinetic first-order (first order) and pseudo-second order (second order) models for Ca^{2+}, Mg^{2+}, and Fe^{3+} sorption on the four materials and their exchange with Na^{+} attached to the functional groups of these materials. In all materials, the first-order equation of Lagergren did not apply well throughout the entire range of contact times, which can be seen in Figures 5.9–5.11. Results presented in Tables 5.5 and 5.6 show faster kinetics for Mg^{2+} (4.7E-02, 4.3E-02, 5.2E-03, 5.32E-2 mmol/g for TP207, TP260, 4A and 13X, respectively) compared with Ca^{2+} (3.23E-03, 4.91E-03, 1.48E-02, 6.78E-3 mmol/g for TP207, TP260, 4A, and 13X, respectively). The slow rate of Ca^{2+} ion exchange compared to Mg^{2+} is primarily attributed to the smaller hydration energy of the Ca^{2+} ion. This ion has approximately

the same Pauling radius as Na^+ ion (0.99 vs. 0.95 Å).[86] Based on the ionic radius, Ca^{2+} diffuses freely into small cavities of the zeolites while the hydrated ion of Mg^{2+} (0.300 nm), in comparison with Ca^{2+} (0.260 nm), is too large to diffuse through the 2.5 Å cavities, and energy is required to remove the shell due hydration of the Mg^{2+} ions.[87] The hydration energy is 140.2 kcal/g of ion.[88] Ionic radius also has an effect on ion-exchange capacity; as shown for Fe^{3+}, the concentration does not go to zero, which is similar to Ca^{2+} and Mg^{2+}, indicating that not all of the Na^+ attached to functional groups is exchanged with all of the Fe^{3+} in the solution. The Fe^{3+} exchange could be attributed to the initial Fe^{3+} exchange with ions of sodium in the available super cages at higher Fe^{3+} ion concentrations. Fe^{3+} has a radius of 0.223 nm corresponding to molecules of water in the hydrated zeolite A large cavities,[89] and this radius has similar order as the diameter of the Y zeolite.

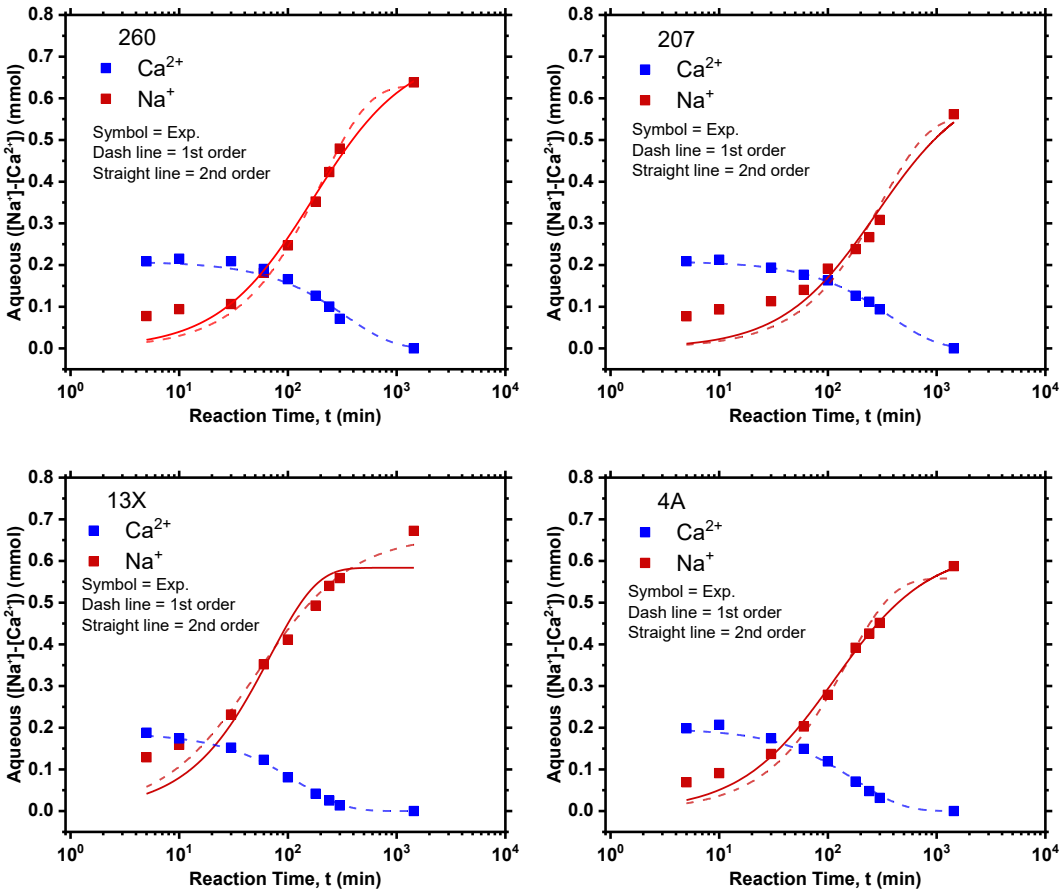

Figure 5.9. Na^+ exchanged by Ca^{2+} concentrations as functions of time for TP207, TP260, 4A, and 13X undergoing ion exchange under static conditions.

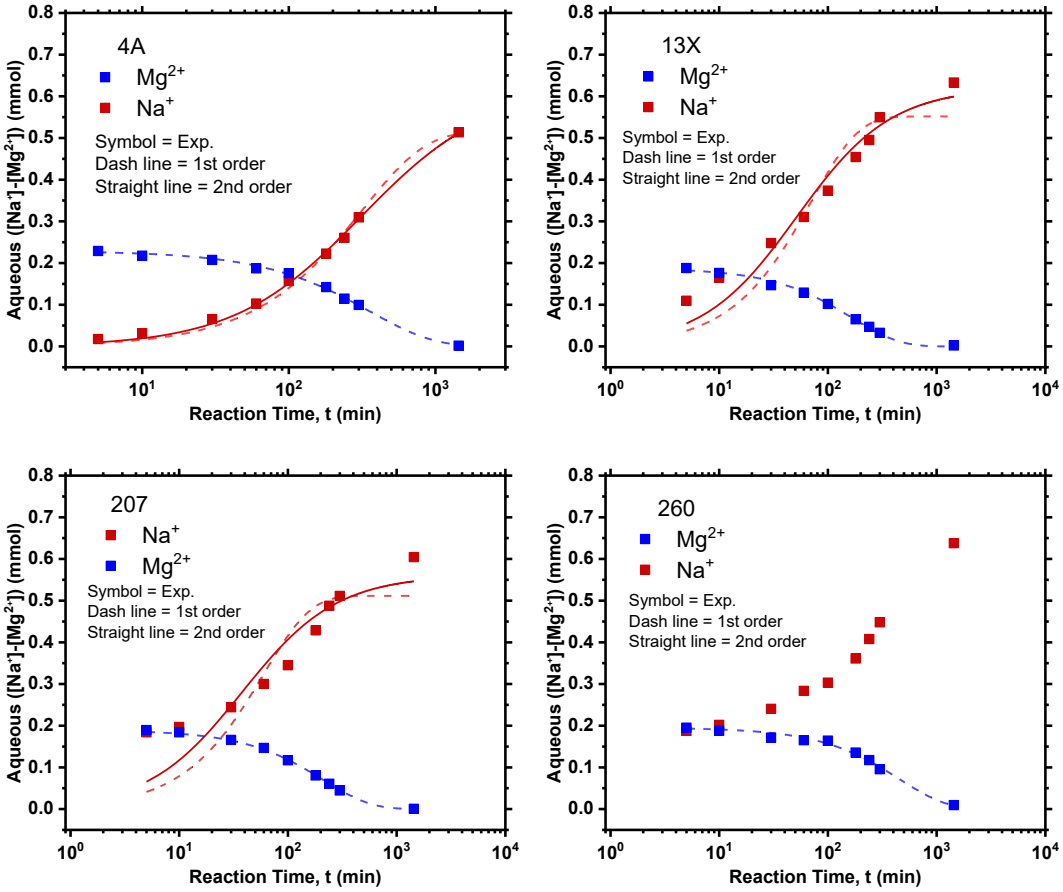

Figure 5.10. Na^+ exchanged by Mg^{2+} concentrations as functions of time for TP207, TP260, 4A, and 13X undergoing ion exchange under static conditions.

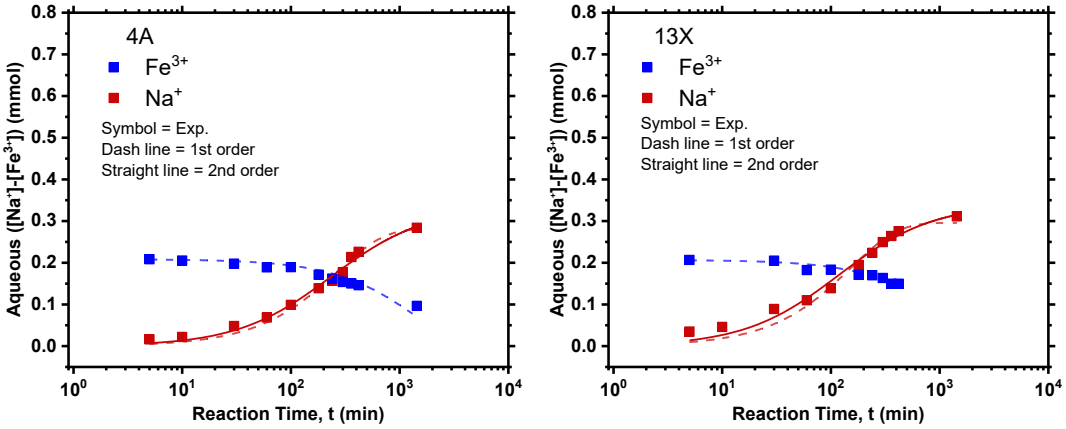

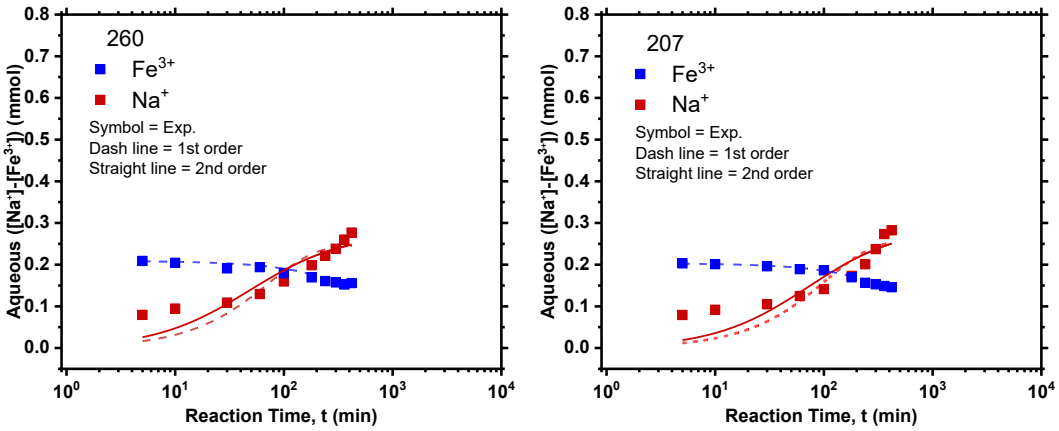

Figure 5.11. Na^+ exchanged by Fe^{3+} concentrations as functions of time for TP207, TP260, 4A, and 13X undergoing ion exchange under static conditions.

Table 5.5. Correlation coefficients of the kinetic pseudo-first-order (first order) and pseudo-second-order (second order) models for Ca^{2+} sorption on the four materials.

Material	First order, k_{Na} (mmol/g)	Second order, k_{Na} (mmol/g)	First order, k_{Ca} (mmol/g)
207	3.23E-03	5.51E-03	2.01E-01
260	4.91E-03	8.82E-03	2.92E-03
4A	1.48E-02	2.91E-02	1.88E-01
13X	6.78E-03	1.39E-02	1.99E-01

Table 5.6. Correlation coefficients of the kinetic pseudo-first-order (first order) and pseudo-second-order (second order) models for Mg^{2+} sorption on the four materials.

Material	First order, k_{Na} (mmol/g)	Second order, k_{Na} (mmol/g)	First order, k_{Ca} (mmol/g)
207	4.7E-02	-	-
260	4.3E-02	-	-
4A	5.2E-03	-	-

13X	5.32E-2	-	-

Table 5.7. Correlation coefficients of the kinetic pseudo-first-order (first order) and pseudo-second-order (second order) models for Fe^{3+} sorption on the four materials.

Material	First order, k_{Na} (mmol/g)	Second order, k_{Na} (mmol/g)	First order, k_{Fe} (mmol/g)
207	9.52E-03	4.74E-02	2.03E-01
260	1.39E-02	7.48E-02	2.09E-01
4A	3.79E-03	1.27E-02	2.08E-01
13X	6.60E-03	2.49E-02	2.07E-01

5.4.5 Column Experiments

Bohart-Adams is a simple model that combine bulk partial differential equation in time and in distance with a rate expression that describe the pickup (exchange capacity in ion exchange case) and in a rate expression called linear drive force model which assumes the pickup is linear allowing the estimation of two parameter model which are maximum capacity (q_s) and average sorption rate (k) and all of the things that could delay the pickup is summed in one parameter. The model was analyzed by changing the flow rate to evaluate the efficiency of ion-exchange materials in a continuous process. The effect of varying flow rate on H^+ uptake capacities and ion exchange diffusion parameters in saturated CO_2, with no other cations present besides H^+ from the carbonic acid (H_2CO_3), feeds were quantified at flow rates from 20–60 SCCM. As shown in Figure 5.12, at lower flow rates, higher exchange capacity is achieved consistently for all ion-exchange materials. This may be a result of the increase in the speed of the ion exchange zone with increasing flow

rate, which results in a decrease in the time required to reach breakthrough concentration. The zeolitic materials Z-1 and Z-2 exhibited faster breakthrough times than resin materials R-1 and R-2. The breakthrough curve showed a positive shift in breakthrough time with the increase in flow rate from 20–60 SCCM. Increasing the flow rate decreased contact time for exchange and caused a reduction in the exchange capacity and service time of the bed. At a lower flow rate, contact time between the exchanger and ions was higher, leading to higher exchange capacity, specifically an increase from 1.31 to 1.45 mmol/g for R-1, from 1.26 to 1.44 mmol/g for R-2, from 0.68 to 0.91 mmol/g for Z-1, and from 0.062 to 0.75 mmol/g for Z-2. Organic cation exchange resins displayed larger H^+ uptake capacities compared to zeolites across all flow rates. This is consistent with the batch equilibrium exchange capacities that exhibited slightly larger capacities for the resins compared to the zeolites. Additionally, there was a significant decrease in dynamic exchange capacities compared to batch equilibrium exchange capacities for all materials. This likely was the effect of operating at high flow rates, reducing contact times, and ion uptake.

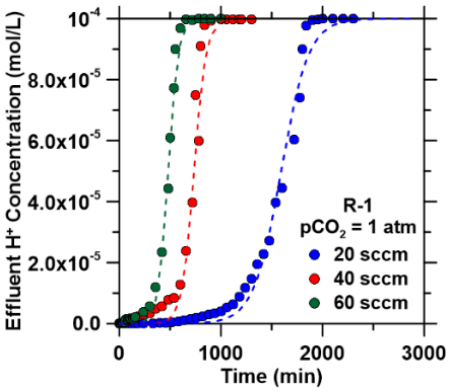

(a)

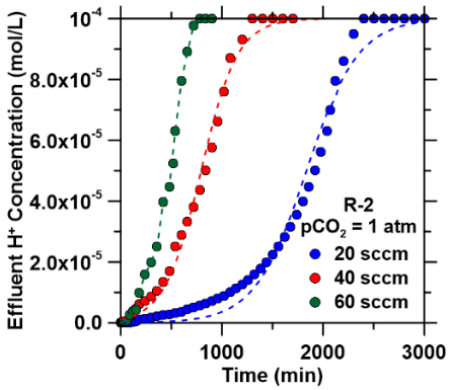

(b)

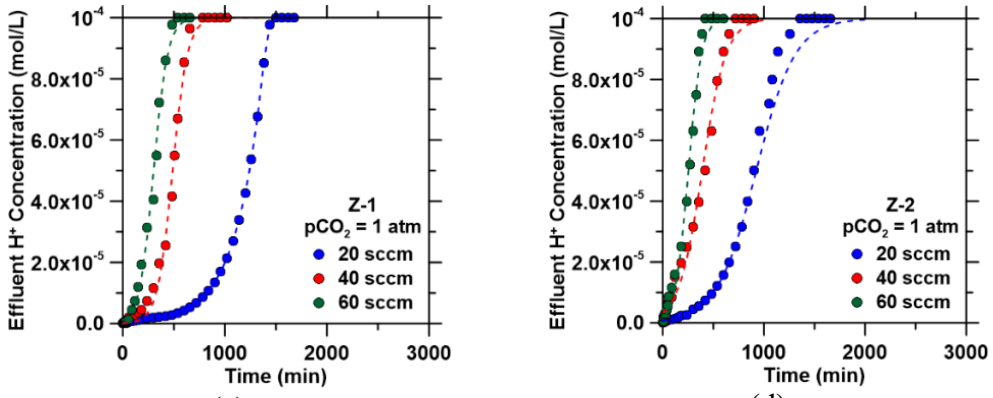

Figure 5.12. Breakthrough curves for the alkalinity-inducing reaction at different flow rates for (a) R-1 (TP 207), (b) R-2 (TP 260), (c) Z-1 (Zeolite 4A), and (d) Z-2 (Zeolite 13X). Dashed lines represent Bohart–Adams model predictions for breakthrough curves.

As the flow rate increases, so does the Reynolds number (Re), furthermore Re directly proportional to the Sherwood number (Sh), and the mass transfer coefficient is directly proportional to the Sh number. Therefore, when Re increases, the Sh increases, and then the mass transfer number increases. The Peclet number increases with the Reynolds number and with flow rate. Increasing the Péclet number (Pe) number makes the breakthrough steeper.

According to Eq. 13, there are have three resistances for the kinetics of ions throughout the ion exchange process, and one of these resistances should be the rate-limiting step; as indicated previously, the ion exchange process in this study is not an ion exchange limited process (the ion exchange between Na^+ from solids and ions from the liquid is much faster than either the diffusion in bulk of liquid or throughout the film) because ion exchange is very fast. The parameter defined in equation 13 for the radius (R_p) is inversely proportional to the overall transfer coefficient (kK) which means that smaller pore size give higher transfer coefficient and higher kinetic. The other factor within the film transfer coefficient (k_f), is directly proportional to Dm (diffusivity which is related to ion diffusion property) and we have Sh is directly proportional to Re and flow rate

Therefore, higher flow rate increases Re which in turn increase Sh that increase k_f which is directly proportional to the overall transfer coefficient (kK). Then, higher k_f gives higher kK value and higher kinetics is associated with higher flow rate (Table 5.8).

Table 5.8. Bohart–Adams parameters for the materials used in this study at varying flow rates in the column ion-exchange process.

Material	Flow Rate (SCCM)	q_s [H^+ Uptake Capacities] (mmol/g)	k (cm^3/mmol/s)
R1 (TP 207)	20	1.45	0.021
	40	1.33	0.048
	60	1.31	0.056
R2 (TP 260)	20	1.44	0.011
	40	1.42	0.019
	60	1.26	0.027
Z1 (Zeolite 4A)	20	0.91	0.023
	40	0.73	0.038
	60	0.68	0.041
Z2 (Zeolite 13X)	20	0.75	0.015
	40	0.064	0.024
	60	0.062	0.044

5.5 Conclusion

Our discoveries show that the ion-exchange process can be used to induce alkalinity through the system to a degree where precipitation is favored. The work evaluated the use of cation exchange resin and zeolites to remove protons from aqueous solution. The effect of parameters such as the amount of resin, contact time, isotherm studies, and kinetic models were studied. From the batch study, it was observed that ion-exchange capacity increased in proportion to the amount of ion-exchange material. The ion exchange has a range of efficiencies, but weak acid resin was the most effective at certain conditions. The ion-exchange kinetic was fast for the low-acid resin and relatively slow for zeolites. Weakly acidic resins, such as TP206 and TP260, have a very high potential for proton uptake from acidic solution due to their high exchange capacity. By comparison, the strongly acidic resin exhibited lower sorption capacity.

The different affinities can be described by their chemistry. TP 207 contains the carboxylic functional group, whereas 200 C contains sulfonic groups with oxygen as a donor atom. Following an initial assessment, the ion-exchange processes were performed at different initial concentrations and temperatures. The kinetic models showed that the ion-exchange processes proceeded according to the pseudo-second order kinetic model. Based on the kinetic models, the step controlling the rate of the ion-exchange process was found to be film diffusion. These results can be used to understand and optimize the process of CO_2 mineralization using the ion-exchange process.

5.6 References

1. Sanna, A., Uibu, M., Caramanna, G., Kuusik, R. & Maroto-Valer, M. M. A review of mineral carbonation technologies to sequester CO_2. *Chem. Soc. Rev.* **43**, 8049–8080 (2014).

2. Aziz, M. & Kwabi, D. G. pH Swing Cycle for CO_2 Capture Electrochemically Driven through Proton-Coupled Electron Transfer. (2019). doi:10.26434/chemrxiv.7853414.v1

3. Teir, S., Eloneva, S., Fogelholm, C. J. & Zevenhoven, R. Dissolution of steelmaking slags in acetic acid for precipitated calcium carbonate production. *Energy* **32**, 528–539 (2007).

4. Mattila, H. P. & Zevenhoven, R. Design of a continuous process setup for precipitated calcium carbonate production from steel converter slag. *ChemSusChem* **7**, 903–913 (2014).

5. Teir, S., Eloneva, S. & Zevenhoven, R. Production of precipitated calcium carbonate from calcium silicates and carbon dioxide. *Energy Convers. Manag.* **46**, 2954–2979 (2005).

6. Van der Zee, S. & Zeman, F. Production of carbon negative precipitated calcium carbonate from waste concrete. *Can. J. Chem. Eng.* **94**, 2153–2159 (2016).

7. Lackner, K. S., Wendt, C. H., Butt, D. P., Joyce Jr, E. L. & Sharp, D. H. Carbon dioxide disposal in carbonate minerals. *Energy* **20**, 1153–1170 (1995).

8. Moriyoshi, Y., Fukawa, J., Ishibe, E. & Ikegami, T. Fixation of carbon dioxide with Wollastonite and its reaction products. *Trans Mater Res Soc Jpn* **24**, 611–614 (1999).

9. Kakizawa, M., Yamasaki, A. & Yanagisawa, Y. A new CO_2 disposal process via artificial weathering of calcium silicate accelerated by acetic acid. *Energy* **26**, 341–354 (2001).

10. Landrot, G., Ajo-Franklin, J. B., Yang, L., Cabrini, S. & Steefel, C. I. Measurement of accessible reactive surface area in a sandstone, with application to CO2 mineralization.

Chem. Geol. **318**, 113–125 (2012).

11. Rendek, E., Ducom, G. & Germain, P. Carbon dioxide sequestration in municipal solid waste incinerator (MSWI) bottom ash. *J. Hazard. Mater.* **128**, 73–79 (2006).

12. Kodama, S., Nishimoto, T., Yamamoto, N., Yogo, K. & Yamada, K. Development of a new pH-swing CO_2 mineralization process with a recyclable reaction solution. *Energy* **33**, 776–784 (2008).

13. Klein, A. R., Baldwin, D. S., Singh, B. & Silvester, E. J. Salinity-induced acidification in a wetland sediment through the displacement of clay-bound iron(II). *Environ. Chem.* **7**, 413–421 (2010).

14. Avena, M. J. & De Pauli, C. P. Proton adsorption and electrokinetics of an Argentinean montmorillonite. *J. Colloid Interface Sci.* **202**, 195–204 (1998).

15. Robin, V. *et al.* Ion exchange reactions of major inorganic cations (H^+, Na^+, Ca^{2+}, Mg^{2+} and K^+) on beidellite: Experimental results and new thermodynamic database. Toward a better prediction of contaminant mobility in. *Appl. Geochemistry* **59**, 74–84 (2015).

16. Harland, C. E. & Britain), R. S. of C. (Great. *Ion Exchange: Theory and Practice*. (Royal Society of Chemistry, 1994).

17. Nasef, M. In Separation and Purification. *Polym. Grafting Crosslink.* 233–272 (2008). doi:10.1002/9780470414811.ch10

18. Inglezakis, V. J. The concept of "capacity" in zeolite ion-exchange systems. *J. Colloid Interface Sci.* **281**, 68–79 (2005).

19. Breck, D. W., Eversole, W. G., Milton, R. M., Reed, T. B. & Thomas, T. L. Physical and

Inorganic Chemistry: Crystalline Zeolites. I. The Properties of a New Synthetic Zeolite, Type A. *J. Am. Chem. Soc.* **78**, 5963–5972 (1956).

20. Beaumont, R. & Barthomeuf, D. X, Y, aluminum-deficient and ultrastable faujasite-type zeolites: I. Acidic and structural properties. *J. Catal.* **26**, 218–225 (1972).

21. Nery, J. G., Mascarenhas, Y. P. & Cheetham, A. K. A study of the highly crystalline, low-silica fully hydrated zeolite P ion exchanged with (Mn2+, Cd2+, Pb2+, Sr2+, Ba2+) cations. *Microporous Mesoporous Mater.* **57**, 229–248 (2003).

22. Kirov, G. & Filizova, L. Cationic hydration impact on zeolite formation and properties: A review and discussion. Geochemistry. *Mineral. Petrol. - Sofia* **49**, 65–82 (2012).

23. Zagorodni, A. A. *Ion exchange materials: properties and applications*. (Elsevier, 2007).

24. Helfferich, F. G. *Ion exchange*. (Courier Corporation, 1995).

25. Shallcross, D. C. Modelling Multi-Component Ion Exchange Equilibrium Behaviour. *J. Ion Exch.* **14**, 5–8 (2003).

26. Dranoff, J. & Lapidus, L. Equilibrium in Ternary Ion Exchange Systems. *Ind. Eng. Chem.* **49**, 1297–1302 (1957).

27. Klein, G., Tondeur, D. & Vermeulen, T. Multicomponent Ion Exchange in Fixed Beds. General Properties of Equilibrium Systems. *Ind. Eng. Chem. Fundam.* **6**, 339–351 (1967).

28. Smith, R. P. & Woodburn, E. T. Prediction of multicomponent ion exchange equilibria for the ternary system SO-NO-Cl from data of binary systems. *AIChE J.* **24**, 577–587 (1978).

29. Shallcross, D. C., Herrmann, C. C. & McCoy, B. J. An improved model for the prediction of multicomponent ion exchange equilibria. *Chem. Eng. Sci.* **43**, 279–288 (1988).

30. de Lucas Martínez, A., Cañizares, P. & Díaz, J. Z. Binary ion exchange equilibrium for Ca^{2+}, Mg^{2+}, K^{+}, Na^{+} and H^{+} ions on amberlite IR-120. *Chem. Eng. Technol.* **16**, 35–39 (1993).

31. Mehablia, M. A., Shallcross, D. C. & Stevens, G. W. Prediction of multicomponent ion exchange equilibria. *Chem. Eng. Sci.* **49**, 2277–2286 (1994).

32. Ioannidis, S., Anderko, A. & Sanders, S. J. Internally consistent representation of binary ion exchange equilibria. *Chem. Eng. Sci.* **55**, 2687–2698 (2000).

33. Mumford, K. A., Shallcross, D. C., Snape, I. & Stevens, G. W. Application of a Temperature-Dependent Semiempirical Thermodynamic Ion-Exchange Model to a Multicomponent Natural Zeolite System. *Ind. Eng. Chem. Res.* **47**, 8347–8354 (2008).

34. Borba, C. E., Silva, E. A., Spohr, S., Santos, G. H. F. & Guirardello, R. Ion Exchange Equilibrium Prediction for the System Cu^{2+}–Zn^{2+}–Na^{+}. *J. Chem. Eng. Data* **55**, 1333–1341 (2010).

35. Aniceto, J. P. S., Cardoso, S. P., Faria, T. L., Lito, P. F. & Silva, C. M. Modeling ion exchange equilibrium: Analysis of exchanger phase non-ideality. *Desalination* **290**, 43–53 (2012).

36. Aniceto, J. P. S., Lito, P. F. & Silva, C. M. Modeling Sorbent Phase Nonideality for the Accurate Prediction of Multicomponent Ion Exchange Equilibrium with the Homogeneous Mass Action Law. *J. Chem. Eng. Data* **57**, 1766–1778 (2012).

37. Barreira, L. D. *et al.* Effect of pH on cadmium (II) removal from aqueous solution using titanosilicate ETS-4. *Chem. Eng. J.* **155**, 728–735 (2009).

38. Ferreira, T. R. *et al.* Cadmium(II) removal from aqueous solution using microporous titanosilicate ETS-4. *Chem. Eng. J.* **147**, 173–179 (2009).

39. Camarinha, E. D. *et al.* Cadmium(II) removal from aqueous solution using microporous titanosilicate ETS-10. *Chem. Eng. J.* **155**, 108–114 (2009).

40. Lopes, C. B. *et al.* Mercury removal with titanosilicate ETS-4: Batch experiments and modelling. *Microporous Mesoporous Mater.* **115**, 98–105 (2008).

41. Lopes, C. B. *et al.* Removal of low concentration Hg^{2+} from natural waters by microporous and layered titanosilicates. *Microporous Mesoporous Mater.* **103**, 325–332 (2007).

42. Lopes, C. B. *et al.* Effect of pH and temperature on Hg2+ water decontamination using ETS-4 titanosilicate. *J. Hazard. Mater.* **175**, 439–444 (2010).

43. Lopes, C. B. *et al.* Removal of Hg^{2+} ions from aqueous solution by ETS-4 microporous titanosilicate—Kinetic and equilibrium studies. *Chem. Eng. J.* **151**, 247–254 (2009).

44. Otero, M. *et al.* Priority pollutants (Hg^{2+} and Cd^{2+}) removal from water by ETS-4 titanosilicate. *Desalination* **249**, 742–747 (2009).

45. Altın, O., Özbelge, H. Ö. & Doğu, T. Use of General Purpose Adsorption Isotherms for Heavy Metal–Clay Mineral Interactions. *J. Colloid Interface Sci.* **198**, 130–140 (1998).

46. Petrus, R. & Warchoł, J. K. Heavy metal removal by clinoptilolite. An equilibrium study in multi-component systems. *Water Res.* **39**, 819–830 (2005).

47. Lee, K. & Wang, W. Removal of Phenols from Aqueous Solutions by Purolite A-510 Resin AU - Ku, Young. *Sep. Sci. Technol.* **39**, 911–923 (2005).

48. Carmona, M., Lucas, A. De, Valverde, J. L., Velasco, B. & Rodríguez, J. F. Combined

adsorption and ion exchange equilibrium of phenol on Amberlite IRA-420. *Chem. Eng. J.* **117**, 155–160 (2006).

49. Caetano, M., Valderrama, C., Farran, A. & Cortina, J. L. Phenol removal from aqueous solution by adsorption and ion exchange mechanisms onto polymeric resins. *J. Colloid Interface Sci.* **338**, 402–409 (2009).

50. Melis, S., Cao, G. & Morbidelli, M. A New Model for the Simulation of Ion Exchange Equilibria. *Ind. Eng. Chem. Res.* **34**, 3916–3924 (1995).

51. Favergeon, L., Morandini, J., Pijolat, M. & Soustelle, M. *A General Approach for Kinetic Modeling of Solid-Gas Reactions at Reactor Scale: Application to Kaolinite Dehydroxylation*. *Oil & Gas Science and Technology* **68**, (2013).

52. Vermeulen, T. Theory for Irreversible and Constant-Pattern Solid Diffusion. *Ind. Eng. Chem.* **45**, 1664–1670 (1953).

53. Reyes, S. & Jensen, K. F. Modeling of catalytic char gasification. *Ind. Eng. Chem. Fundam.* **23**, 223–229 (1984).

54. Bohart, G. S. & Adams, E. Q. SOME ASPECTS OF THE BEHAVIOR OF CHARCOAL WITH RESPECT TO CHLORINE.1. *J. Am. Chem. Soc.* **42**, 523–544 (1920).

55. Cooper, R. S. Slow Particle Diffusion in Ion Exchange Columns. *Ind. Eng. Chem. Fundam.* **4**, 308–313 (1965).

56. Bartkowicz, I. & Stokłosa, A. Kinetics of copper, nickel, cobalt and iron sulfidation by a modified “pellet” method. The effect of reaction at the metal/scale interface. *Solid State Ionics* **24**, 51–59 (1987).

57. Lagergren, S. Y. *Zur Theorie der sogenannten Adsorption gelöster Stoffe*. (1898).

58. Ho, Y. S. & McKay, G. Pseudo-second order model for sorption processes. *Process Biochem.* **34**, 451–465 (1999).

59. Liu, Y. & Liu, Y.-J. Biosorption isotherms, kinetics and thermodynamics. *Sep. Purif. Technol.* **61**, 229–242 (2008).

60. Ho, Y. S., Ng, J. C. Y. & McKay, G. Removal of lead (II) from effluents by sorption on peat using second-order kinetics. *Sep. Sci. Technol.* **36**, 241–261 (2001).

61. Geng, B., Jin, Z., Li, T. & Qi, X. Kinetics of hexavalent chromium removal from water by chitosan-Fe0 nanoparticles. *Chemosphere* **75**, 825–830 (2009).

62. Coşkun, G., Şimşek, İ., Arar, Ö., Yüksel, Ü. & Yüksel, M. Comparison of chelating ligands on manganese (II) removal from aqueous solution. *Desalin. Water Treat.* **57**, 25739–25746 (2016).

63. Kertman, S. V., Kertman, G. M. & Leykin, Y. A. A thermochemical study of complex formation in chelating ion-exchange resins. *Thermochim. Acta* **256**, 227–235 (1995).

64. Kertman, S. V., Kertman, G. M., Amelin, A. N. & Leykin, Y. A. Heats of the immersion of Co2+ and Cu2+ contained chelating ion-exchange resins. *Thermochim. Acta* **297**, 49–56 (1997).

65. Nesterenko, P. N., Shaw, M. J., Hill, S. J. & Jones, P. Aminophosphonate-functionalized silica: A versatile chromatographic stationary phase for high-performance chelation ion chromatography. *Microchem. J.* **62**, 58–69 (1999).

66. Kołodyńska, D., Hubicki, Z. & Gęca, M. Application of a new-generation complexing agent

in removal of heavy metal ions from aqueous solutions. *Ind. Eng. Chem. Res.* **47**, 3192–3199 (2008).

67. Rengan, K. Chelating resins: Sorption characteristics in chloride media. *J. Radioanal. Nucl. Chem.* **219**, 211–215 (1997).

68. Arroza, E. & Rengan, K. Sorption characteristics of chelating resins. *J. Radioanal. Nucl. Chem.* **242**, 379–385 (1999).

69. Valverde, J. L., de Lucas, A., Carmona, M., González, M. & Rodríguez, J. F. Equilibrium data of the exchange of Cu^{2+}, Cd^{2+} and Zn^{2+} ions for H^{+} on the cathionic exchanger Lewatit TP-207. *J. Chem. Technol. Biotechnol.* **79**, 1371–1375 (2004).

70. Mijangos, F. & Diaz, M. Metal-Proton Equilibrium Relations in a Chelating Iminodiacetic Resin. *Ind. Eng. Chem. Res.* **31**, 2524–2532 (1992).

71. Horst, J., Höll, W. H. & Eberle, S. H. Application of the surface complex formation model to exchange equilibria on ion exchange resins. Part I. Weak-acid resins. *React. Polym.* **13**, 209–231 (1990).

72. Lehto, J. & Harjula, R. Experimentation in ion exchange studies - the problem of getting reliable and comparable results. *React. Funct. Polym.* **27**, 121–146 (1995).

73. Florin, N. H., Blamey, J. & Fennell, P. S. Synthetic CaO-based sorbent for CO2 capture from large-point sources. *Energy & Fuels* **24**, 4598–4604 (2010).

74. Reddad, Z., Gerente, C., Andres, Y. & Le Cloirec, P. Adsorption of several metal ions onto a low-cost biosorbent: Kinetic and equilibrium studies. *Environ. Sci. Technol.* **36**, 2067–2073 (2002).

75. Eisenman, G. Cation selective glass electrodes and their mode of operation. *Biophys. J.* **2**, 259–323 (1962).

76. Li, L., Dong, J. & Nenoff, T. M. Transport of water and alkali metal ions through MFI zeolite membranes during reverse osmosis. *Sep. Purif. Technol.* **53**, 42–48 (2007).

77. Simonin, J.-P. On the comparison of pseudo-first order and pseudo-second order rate laws in the modeling of adsorption kinetics. *Chem. Eng. J.* **300**, 254–263 (2016).

78. Pignatello, J. J. & Xing, B. Mechanisms of slow sorption of organic chemicals to natural particles. *Environ. Sci. Technol.* **30**, 1–11 (1996).

79. vR Borgstedt, E., Sherry, H. S. & Slobogin, J. P. Ion-exchange behavior of zeolite NaA and maximum aluminum zeolite NaP. in *Studies in Surface Science and Catalysis* **105**, 1659–1666 (Elsevier, 1997).

80. Breck, D. W. Crystalline molecular sieves. *J. Chem. Educ.* **41**, 678 (1964).

81. Drummond, D., De Jonge, A. & Rees, L. V. C. Ion-exchange kinetics in zeolite A. *J. Phys. Chem.* **87**, 1967–1971 (1983).

82. Helfferich, F. & Plesset, M. S. Ion Exchange Kinetics. A Nonlinear Diffusion Problem. *J. Chem. Phys.* **28**, 418–424 (1958).

83. Dyer, A. & Gettins, R. B. The mobility of cations in synthetic zeolites with the faujasite framework — III: Self-diffusion of cations into X and Y zeolites from non-aqueous solutions. *J. Inorg. Nucl. Chem.* **32**, 2401–2410 (1970).

84. Gaines, G. L. & Thomas, H. C. Adsorption Studies on Clay Minerals. II. A Formulation of the Thermodynamics of Exchange Adsorption. *J. Chem. Phys.* **21**, 714–718 (1953).

85. Townsend, R. P. Chapter 10 Ion Exchange in Zeolites. in *Studies in Surface Science and Catalysis* **58**, 359–390 (Elsevier, 1991).

86. Pauling, L. & Wheland, G. W. *The Nature of the Chemical Bond. V*. *Journal of Chemical Physics* **2**, (Cornell university press Ithaca, NY, 1934).

87. Kiriukhin, M. Y. & Collins, K. D. Dynamic hydration numbers for biologically important ions. *Biophys. Chem.* **99**, 155–168 (2002).

88. Rosseinsky, D. R. Electrode potentials and hydration energies. Theories and correlations. *Chem. Rev.* **65**, 467–490 (1965).

89. Firor, R. L. & Seff, K. Hydrolysis in zeolites. Five-coordinate aluminum(III). Investigations of two hydrated partially ion-exchanged zeolite A crystal structures, Ni(II)Na-A and Fe(II)Na-A. *J. Phys. Chem.* **82**, 1650–1655 (1978).

Chapter 6: Application of Process Reactor Design Using CO_2 Mineralization to Enhance Methane Reforming Process and Produce Carbon-free H_2

6.1 Abstract

The aim of this work is to study the implementation of the CO_2 mineralization concept in the production of hydrogen through SMR. The study provides an overview of the steam methane reforming process and methods for performance improvement by selective removal of CO_2 using sorption applications. A simulation model was developed using Aspen Plus to predict the performance of the enhanced steam methane reforming process. The model was built for conventional and sorption enhanced steam reforming process to obtain mass and energy balances that are required to assess comparative energy analysis. Equilibrium calculations employing Gibbs free minimization energy were conducted for steam methane reforming at various operating temperatures (650–1200 K), steam-to-methane ratios (1:1–10:1), and pressure (1–5 ATM) to obtain the optimum condition for achieving the highest possible hydrogen yield with lowest possible energy usage. Experimental and simulation precipitation tests were performed to analyze the effect of CO_2 mineralization on hydron yield production. A carbon mineralization process enhanced the conversion of the reforming and water gas-shift reaction processes based on Le Chatelier's principle. The chapter details the equilibrium composition for all species as a function of temperature, pressure and steam-to-methane ratio for a range of process conditions that can be applied industrially. Based on energy analysis, sorption enhanced steam methane reforming has shown a significant reduction in energy compares to steam methane reforming utilizing the exothermic carbonation reaction and obtaining high H_2 levels at temperatures below those obtained by steam methane reforming.

6.2. Introduction

Among the alternative energy sources, hydrogen is considered by researchers to be a clean and efficient promising energy carrier for power generation and transportation fuel. Hydrogen is currently used in various applications, such as proton-exchange fuel cells, hydrocracking, and the production of methanol and ammonia.[1,2] Almost 50% of the worldwide production of hydrogen comes from natural gas.[3] The conventional methods that produce hydrogen from natural gas sources include partial oxidation, steam reforming and autothermal reforming.[4] Natural gas steam reforming route, introduced previously as SMR, represents the most common source of hydrogen production. Its advantages arise from its highly efficient processing and low operation and production costs.[3]

Today, 50% of the world's hydrogen demand is provided by SMR, 30% is generated from naphtha in oil refinery industrial off-gas, 18% from coal gasification and 3.9% from water electrolysis[5]. However, SMR releases a significant amount of CO_2 emissions into the atmosphere.[5] The average SMR hydrogen plant that produce 1 million m^3 of hydrogen per day produces around 0.4 million m^3 of CO_2 per day as capacity, which is usually emitted to the atmosphere. This emission of CO_2 that is associated with hydrogen production may weaken the environmental appeal of using hydrogen as a clean, ecologically friendly fuel.[6] Therefore, to enhance the efficiency of hydrogen production, three options to mitigate the CO_2 emissions problem associated with hydrogen generation are available: (1) the use of renewable energy for water electrolysis or thermochemical water-splitting cycles; (2) the separation and sequestration of CO_2 that is produced by SMR plants; and (3) the thermal dissociation of hydrocarbon into hydrogen and carbon.[7] As a departure from the disadvantage of the conventional SMR process and its resulting CO_2 emissions, the promising method termed the "sorption enhanced reaction process (SERP)" is desirable for the

production of hydrogen.[8,9] The investigation of a reactor concept that combines the functionalities of two processes into a single unit has received considerable attention recently.[10–14] The separation of CO_2 that is produced through SMR sorption is achieved by an enhanced reaction process (SERP) that involves the addition of sorbent to the SMR effluent to enhance the equilibrium conversion by the uptake of one of the products, according to Le Chatelier's principle.[15] In this application, enhanced hydrogen production is achieved through the separation of CO_2 in the WGS reaction.

We propose that the SERP process, through CO_2 mineralization, can combine reaction and separation in a single unit to energetically enhanced the reforming process. The definition of an Energetically Enhanced Process (EEP) has been previously described as the process that has decrease or elimination on its energy consumption at high temperatures even if the reduction in energy necessitates higher energy consumption at lower temperature.[16] Previous work by Manousiouthakis's team explored energetic intensification of a network that detail the energetic intensification of a traditional SMR process, and quantifies the parametric conditions required for this intensification.[16–18] Al-Bassam et al. applied the concept of EEP initially by changing the endothermicity level of the SMR process through the inclusion of carbon monoxide and steam into the SMR feed.[16]Pichardo and Manousiouthakis's work focused on the implementation of membrane reactors in the production of hydrogen through steam–methane reforming (SMR) by applying the concept of "energetically enhanced steam methane reforming (EER)," to allow the use of a hybrid (methane combustion/renewable energy) energy supply in the production of hydrogen to be intensified.[18] Given the aforementioned definition, this study aims to pursue the work and seek EESMR, which aims to improve the environmental profile of an SMR process by the continuous removal of CO_2 and the economics of this process by reducing the energy consumption at high temperature, endothermic heat load on the reformer based on Le Chatelier's

principle, favoring the reaction equilibrium toward hydrogen production upon CO_2 removal and shifting the equilibrium reversible reforming reaction and WGS reaction beyond the conventional thermodynamic limit. Some studies were previously carried out, but it was difficult to see the impact of CO_2 removal for H_2 generation and energy enhanced process.[19–21] Therefore, the system was analyzed by adding a reformer followed by a separator that selectively splits the CO_2. Sequential reformers were added to react the unreacted methane and CO following the removal of CO_2 until an enhancement on H_2 with a set of six reactors was achieved, and any additional reactor didn't not change the yield.

The proposed mineralization routes integrate CO_2 utilization and SMR to reduce the economic burden of hydrogen production, CO_2 capture, and water treatment facilities. To examine the viability of the scheme, we performed an analysis (in terms of mass balances, carbon removal capacity and energy requirement) for the following scenarios. The impact on SMR was carried using six stages reformer followed by CO_2 separator in each stage to show the effect of removing CO_2 (CO_2 removal was calculated using splitter) on H_2 yield to probe the EEP by reducing energy consumption at high temperature. Then, when EEP is identified, the addition of sorbent particle to the reformer reactor selectively remove CO_2 examined. This not only shifts the chemical equilibrium of the reversible reaction toward higher yield such as H_2 in based on Le Chatelier's principle but also provides a means of heat via the exothermic reaction that can be applied to the reformer. The reaction releases heat due to the exothermic CO_2 sorption process, which supplied the endothermic steam methane reforming, thereby reducing the net external heat provided to the reformer. It also leads to a process intensification, as it reduces the size of the downstream separation stages or may eliminate them. Balasubramanian has experimentally demonstrated the possibility performing the three reactions SMR, WGS, and carbonation in a single reactor and

produces hydrogen with >95% purity.[22] over a range of temperatures, 650 °C was the optimal for hydrogen generation from methane in a single step reactor with the presence of CaO.

Finally, CO_2 removal using aqueous phase absorber is examined using NaOH solution or ion exchange approach to provide the alkalinity. CO_2 mineralization using NaOH and a Ca-or Mg-rich stream considers solid and liquid sources of Ca and Mg (desalination brines, Ca-rich groundwater, solid industrial byproducts, and waste). The H^+-ion-exchange scenario uses regenerable materials. This study explored the possibility of reforming methane thermodynamically with the simulated removal of CO_2 through mineralization. The equilibrium concentrations of different species were calculated by minimizing Gibbs free energy. The thermal energy requirements of the reforming system were evaluated by performing material and energy balance. Precipitation was calculated thermodynamically for the CO_2 mineralization process using NaOH and experimentally for the ion-exchange effluent precipitation stream.

Energy consumption in the NaOH process is primarily associated with the addition of alkalinity that is provided by electrolysis, whereas the ion-exchange process increases alkalinity or reduces acidity without involving consumable reagents. Ion-exchange processes use novel solid ion exchangers that are capable of reversibly capturing CO_2 from the steam reformer effluent stream. Ion-exchange materials are commonly used for the removal of heavy metal cations and hardness (e.g., zeolites, resins, and clays) from wastewater; these materials have also been used for the treatment of acid mine drainage, which results in slight pH increases after the removal of metals, implying that pH swing via ion-exchange can be achieved.[23]

The regeneration energy requirement for CO_2 capture using solid ion exchangers is significantly less than that of dry solid adsorbent and aqueous amine-based processes. The inherent advantage of the ion-exchange process is that it is simple to operate. Unlike the adsorption process,

only ion exchange requires vessels that are able to withstand the ion-exchange process. As with the adsorption process, the ion-exchange process has a regenerative material that can be reused. Furthermore, zeolite-based sorbents are low cost and require low regeneration energy. Previous research has shown that both a forward and reverse H^+/Na^+ exchange can occur.[24–26] The present process of a precipitated calcium carbonate production approach involves three essential steps (Figure 6.1): the calcination of high-purity natural limestone to produce lime, the slaking of lime to produce hydrated lime, and the carbonation of hydrated lime with CO_2 in water to precipitate $CaCO_3$.[27,28]

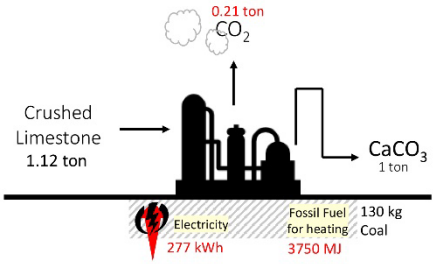

Figure 6.1. The conventional process of precipitated calcium carbonate production.[29]

6.3 Materials and Methods

6.3.1 Experimental Solutions

Solutions for forwarding ion-exchange experiments for both batch equilibrium and dynamic experiments were performed by bubbling CO_2 into high-purity water that had been purified by a Milli-Q system to reach saturation (pCO_2 = 1.0 ATM, pH = 4). Additionally, batch equilibrium experiments were performed using various concentrations of HCl, diluted from 12% HCl purchased from Sigma-Aldrich. A Thermo Scientific Orion pH electrode was used to measure initial and final pH values for the ion-exchange experiments. The NaCl (≥99.0%) used for the regeneration experiments was purchased from Thermo Fisher Scientific. The $CaCl_2 \cdot 2\ H_2O$ (≥99.0%) and $MgCl_2 \cdot 6\ H_2O$ (≥98.0%) used for competitive ion-exchange experiments were purchased from Thermo Fisher Scientific. Cation concentrations in solution were measured by ICP-OES using an Avio 200 ICP Optical Emission Spectrometer from Perkin Elmer. Solutions for ICP-OES were diluted in 5% HNO_3 (diluted from 70% HNO_3 obtained from Sigma-Aldrich).

6.3.2 Characterization of Ion-Exchange Materials

Commercially available zeolites 13X and 4A were obtained in sodium form from Thermo Fisher Scientific, and the weakly acidic organic ion-exchange resins Lewatit TP 207 (iminodiacetate functional group) and Lewatit TP 260 (aminomethyl phosphonate functional group) were obtained in sodium form from Sigma-Aldrich.

6.3.3 Batch Equilibrium Experiments

Batch equilibrium experiments were performed in CO_2-saturated solutions and in HCl solutions to determine the effect of the counterion in the forward ion-exchange step at 25°C. Equilibrium exchange capacities (EC) for ion-exchange materials were calculated by the following equation:

$$EC = \frac{(C_f - C_0) \cdot V}{W} \qquad (1)$$

where C_f and C_o are the final and initial sodium concentrations respectively, V is the solution volume, and W is the mass of solid used for ion-exchange. All experiments were performed using a solid to-liquid-ratio of 0.05 g/mL.

6.3.4 Thermodynamic Modeling

A model is developed to analyze the effect of sorbent on the syngas composition. A sequential modular simulation (SMS) approach has been used to simulate the rector. In this method, the reactor is divided into several stages where each section consists of a reformer and a carbonation reaction. Thermodynamic analysis of the chemical equilibrium was performed based on the Gibbs reactor using Aspen Plus. The Gibbs reactor was implemented using the Peng Robinson equation of state method due to its suitability in handling a system that contains hydrocarbons, water, air, and combustion gases.[30,31] This reactor calculates the reaction product distribution by the minimization of the Gibbs free energy of each participating species in the

reaction system, irrespective of the reaction network. The Gibbs reactor was preferred in the steam reforming process.[32,33]

A Gibbs reactor is based on finding the thermodynamic favorability of a system when Gibbs free energy is at a minimum value, which is achieved when the differential achieves zero for a given temperature and pressure, determined according to the following equation[31,34]:

$$(dG^T)_{T,p} = 0$$

CO_2 mineralization was performed using eRNTL as the thermodynamic property method.[35] The property method considers Hilgard thermodynamics, CO_2 reaction kinetics, and other mass transfer phenomena associated with system mixture. The model explicitly accounts for the solution chemistry, which includes dissociations of H_2O, NaOH, $CaCl_2$, and CO_2, the formation of bicarbonate, and the precipitation of calcium carbonate.

6.4 Process Description and Results

6.4.1 Steam Methane Reforming (SMR)

In conventional SMR, methane is reacted with steam using a nickel-based catalyst at the relatively high endothermic reaction temperature of 923–1273 K, and pressure equivalent to 5–40 bar, to produce carbon monoxide and hydrogen. Then, additional carbon monoxide is reacted with water to produce hydrogen in the WGS reaction.[36] Exothermic WGS operates at a temperature of 573–673 K and pressure of 6.9–31 bar through an iron-based catalyst. Typical WGS effluent consists of a mixture of 71–75% hydrogen, 5–35% CO_2, 1–4% CO, and 4–7% CH_4 on a dry basis.[14]

$$CH_4 + H_2O \rightleftharpoons CO + 3H_2 \qquad (\Delta H^0_{298} = 206.2 \text{ kJ/mol}) \qquad (1)$$

$$CO + H_2O \rightleftharpoons CO_2 + H_2 \qquad (\Delta H^0_{298} = -41.2 \text{ kJ/mol}) \qquad (2)$$

$$CH_4 + 2H_2O \rightleftharpoons CO_2 + 4H_2 \qquad (\Delta H^0_{298} = 165 \text{ kJ/mol}) \qquad (3)$$

Optimum reforming conditions were specified by performing sensitivity analysis with Aspen Plus. The chapter reports the results of the investigation to determine the temperature, steam-to-methane ratio, and pressure combination values that provide the highest H_2 yield at the lowest energy possible. In this process, steam had a substantial effect on the H_2 rate in production, increasing the ratio of steam-to-methane from 1:1 to 1:10, and increased the production of hydrogen by nearly 80% (Figure 6.2). This is consistent with the results obtained by Hegarty et al.[31,37] However, increasing the steam ratio also caused a substantial decrease in CO_2 conversion. When the ratio of steam was increased, CH_4 reacted with H_2O instead of CO_2. Hydrogen increased steadily with the increase in the steam-to-methane ratio in parallel with the CO_2 ratio. This resulted in a WGS reaction that shifted the equilibrium to the right due to the H_2O surplus. Methane and CO were not favored as the ratio of steam to methane increased. The higher the steam-to-methane ratio was, the higher the conversion was. Energy consumption also increased with increasing the steam-to-methane ratio. Thus, the optimum thermodynamic yield was achieved at a steam-to-methane ratio of 3:1.

Methane and CO_2 dominated production at low temperatures. As the temperature increased at temperatures higher than 950 K, the increment in temperature did not contribute to hydrogen production any further. In addition to temperature and steam-to-methane ratio, pressure was also a critical parameter that had an effect on the equilibrium distribution of the product (Figure 6.3). The calculation was performed using a temperature of 950 K and a steam-to-methane ratio of 3:1. The temperature and steam-to-methane ratio were selected to achieve the maximum hydrogen yield and low levels of carbon monoxide. The H_2 yield was significantly suppressed within the temperature range of 200–950 K. However, the change in pressure at a higher pressure than 950

K did not alter the results of the simulation. As the pressure increased, the hydrogen mole fraction decreased. This decrease in the hydrogen mole fraction was a result of the increase in the methane mole fraction.

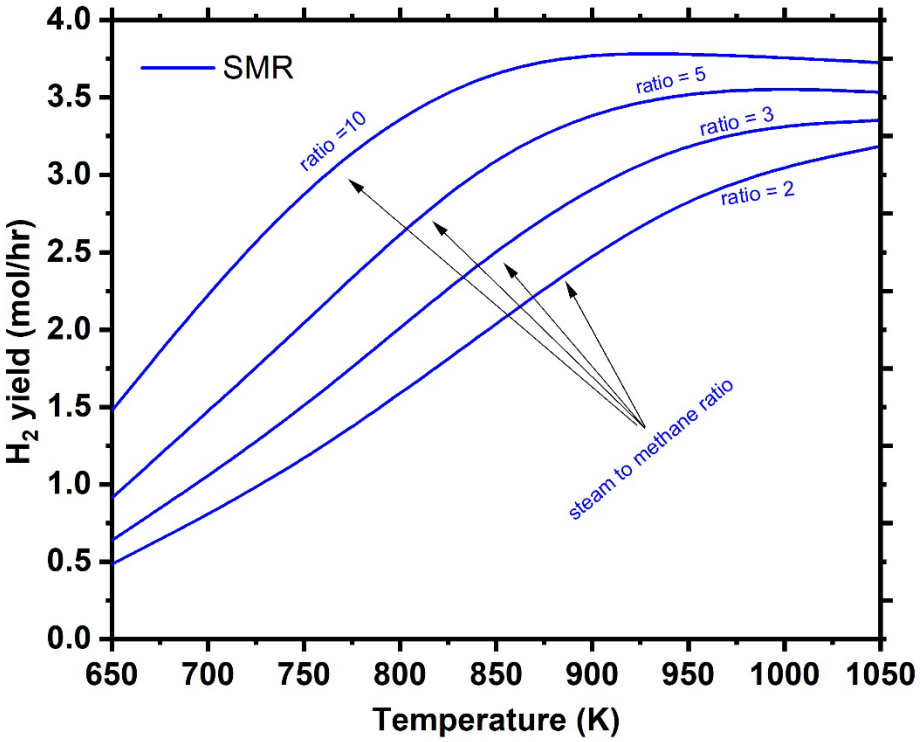

Figure 6.2. The effect of temperature on the H_2 yield product of the SMR.

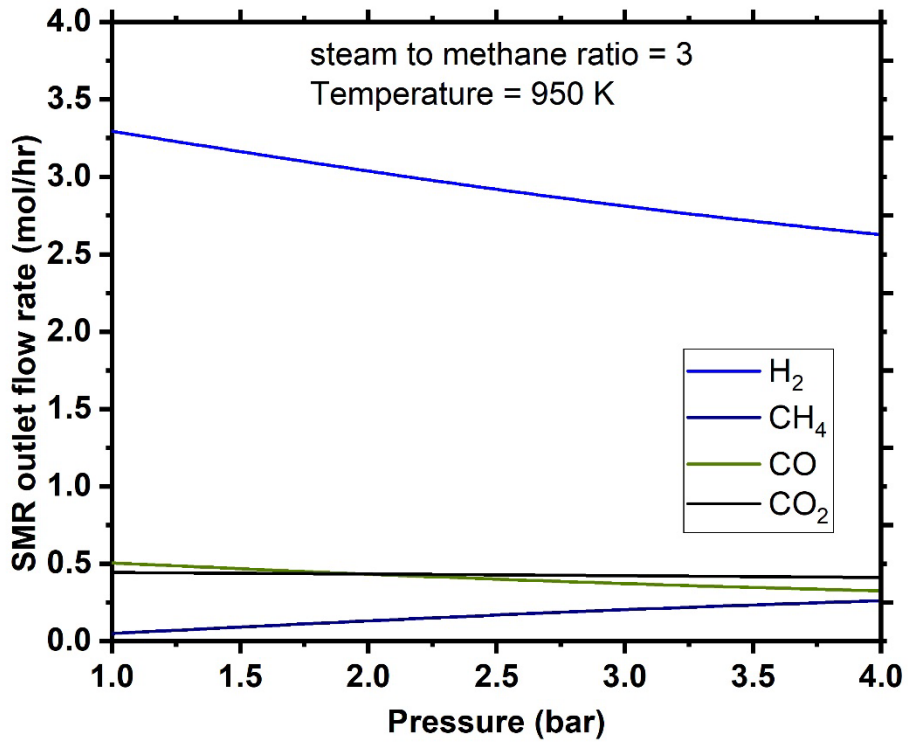

Figure 6.3. The effect of pressure on the SMR product proportions of H_2, CH_4, CO and H_2O.

6.4.2 Effect of Removing CO_2 from SMR outlet

The Sorption-enhanced steam reforming (SESR) was briefly described in the introduction section. The process flow diagram developed in the simulation SESR is shown in Figure 6.4. SESR represents a promising method for producing H_2 with high purity.[38] In a conventional SMR, a purification step is carried out by pressure swing adsorption (PSA) for the WGS effluent to produce pure hydrogen. The PSA feed is typically operates at a temperature of 293–313 K and at a pressure of 6.9–31 bar. Typical H_2 that is recovered by the PSA process (H_2 in product/H_2 in feed) is approximately 70–85% pure. The remaining waste gas impurities (H_2O, CO_2, CO, CH_4, and N_2) remain.

In this section, the separator was simulated as a splitter; having a sorbent might limit the reactor's range of temperature because sorption is an exothermic reaction. In the next section, we will use the exothermic energy of a carbonation reactor as an input to the endothermic reformer.

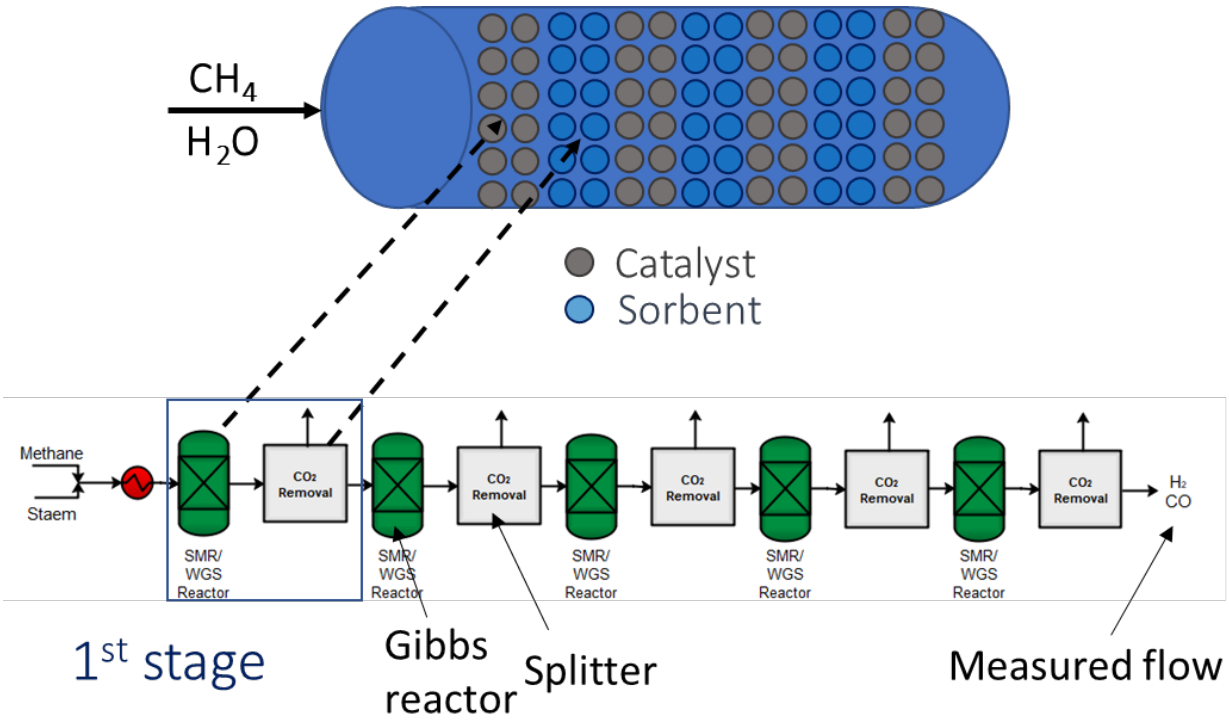

Figure 6.4. The process flow diagamr of SESR showing the varies reforming sorption stages of the process.

The proposed concept is based on Le Chatelier's principle and favors the reaction equilibrium toward hydrogen production upon CO_2 removal. H_2 production is enhanced toward completion as CO_2 is removed from products, shifting the reversible equilibrium reforming reaction and WGS reaction beyond the conventional thermodynamic limit. Figure 6.5 depicts the advantage of the SESMR process, as the removal of CO_2 results in high methane conversion levels at temperatures below 800 K which energetically enhanced steam methane reforming. This

superiority of SESMR at lower low temperatures over SMR can be observed and related to the in-situ capture of the produced CO_2.

Increasing the steam-to-methane ratio increased the equilibrium of the reforming and WGS reactions to the product side, which resulted in high methane conversion, H_2 yield and CO_2 production. Increasing the equilibrium of the WGS increased CO_2 production, thus favoring the CO_2 mineralization reaction, and producing H_2 with high purity at a lower operating temperature than that of SMR (Figure 6.5). Steam to methane ratio follows Le Chatelier"'s principle as well, whereby an increase in the water concentration moves the equilibrium toward higher water conversion, thus producing higher H_2 yield. The effect of the ratio levels off at higher values (above steam-to-methane ratio: 4 and 700–1200 K).[39,40]

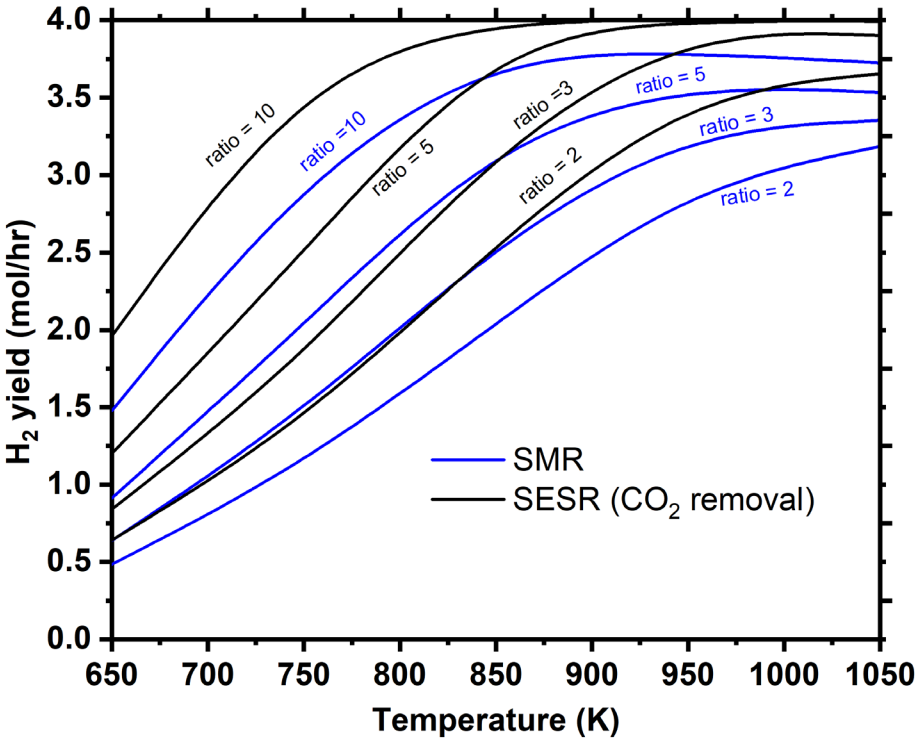

Figure 6.5. Effect of temperature on the H_2 yield product of the SESR

6.4.3 The Use of Exothermic Carbonation Energy for Reforming

The addition of a sorbent particle to the reformer reactor selectively removes CO_2. This shifts the chemical equilibrium of the reversible reaction toward a higher yield such as H_2 in the previous section based on Le Chatelier's principle and provides a means of heat via the exothermic reaction that can be applied to the reformer. Table 6.2 depicts the advantage of combining steam reforming within in situ CO_2 capture from an energy viewpoint. The addition of sorbents, such as CaO, could be favorable to the SMR process for several reasons such as:[41]

- Reforming reactions can be enhanced energetically operating at a reduced energy consumption at higher temperatures, as seen in the previous section.
- Heat released from the exothermic carbonation reaction can supply most of the energy needed for the endothermic reforming reactions, as discussed in this section.
- It captures and stabilizes CO_2 in the form of solid carbonates, which will be discussed in the following section.

In this section, the overall inlet (1 mol/hr of CH_4 and 3 mol/hr of H_2O) and the overall outlet (3.21 mol/hr of H_2 and 0.27 mol/hr of CO) are based on 80% overall conversion of CH_4. The process is displayed below (Figure 6.6), with a sequence of six reforming reactors followed by carbonation reactors in each stage. All the reactors were modeled as a conversion reactor with the feed 1 mole of CH_4 and 3 H_2O, and each reformer with the WGS reactor is followed by a carbonation reactor as follows:

$$CO_2 + CaO \rightleftharpoons CaCO_3 \qquad (4)$$

In each carbonation reactor, 0.1 mol of CaO was added. For each of the reactions in the reformer (Eq. 1, 2 and 3), 10% conversion was assumed, meaning that CH_4 was 10% converted in

Eq. 1 and 3 and 10% CO conversion in Eq. 2. This maintains the 0.1 mol/hr of CO_2 after each reformer to be consumed by each 0.1 mol CaO that was added to each carbonation reactor. From Table 6.1, we can see a summary of the flow rate over the varies stages of the flowsheet. 1 mol/h CH_4 enters the reactor with 3 mol/hr H_2O, following the first reformer stage, 0.1 mol/h. 0.70 mol/h and 0.1 mol/h of CO_2, CO and H_2 were generated, respectively through exothermic reaction of reformer -5.39 kJ/s (the first reformer was the only reformer which operated exothermally probably due to the higher contribution of WGS reaction compare to reforming reaction, following the first stage reformer, the rest of reformers operated endothermically) (Table 6.2). The 0.1 mol/hr CO_2 produced from the first reformer reacted with 0.1 mol/h CaO that was added to the first carbonation reactor generating an exothermic heat equivalent to -4.71 kJ/s. In overall, the presence of CaO sorbent in SMR lowers the CO_2 concentration (0.1 instead of 19% in SMR) and produces a richer hydrogen stream (89.4 instead of 70% in SMR). The heat duty of each reactor is exothermic reaction heat, as fed to any endothermic reactor, which was reformer-operated isothermally at 550°C with 38.32 kJ/s heater requirement. In this process, the heat released by exothermic carbonation reaction, which is equivalent to 29.48 kJ/s, was able to supply most of the heat required by the endothermic reforming reactions, which in this case is 39.29 kJ/s.

Figure 6.6. Aspen Plus flowsheet depicting each stage reactor "REF" represents the reformer and six reactors

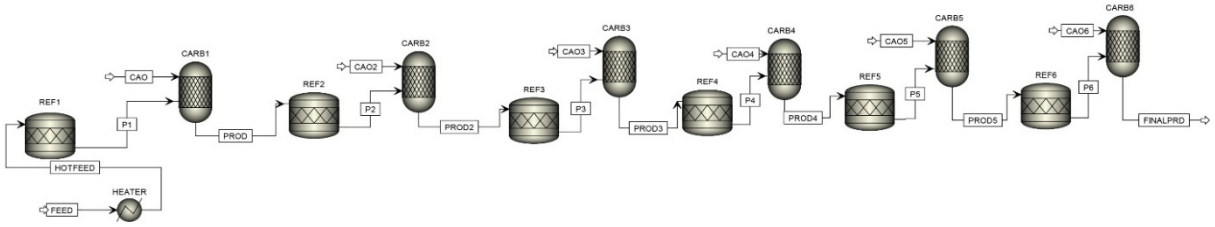

Table 6.1. Summary table of all the reactor stages flows streams.

	Feed mol/hr	1st Stage mol/hr	2nd Stage mol/hr	3rd Stage mol/hr	4th Stage mol/hr	5th Stage mol/hr	6th Stage mol/hr	Product mol/hr
Mole Flows	4.00	4.40	4.78	5.10	5.33	5.56	5.74	5.74
CaO	0.00	0.00	0.00	0.00	0.00	0.00	0.00	0.00
CO_2	0.00	0.10	0.11	0.11	0.10	0.10	0.10	0.00
$CaCO_3$	0.00	0.00	0.10	0.20	0.30	0.40	0.50	0.60
CH_4	1.00	0.80	0.61	0.45	0.33	0.22	0.13	0.13
H_2O	3.00	2.70	2.40	2.14	1.93	1.72	1.53	1.53
CO	0.00	0.10	0.18	0.24	0.27	0.28	0.27	0.27
H_2	0.00	0.70	1.38	1.96	2.40	2.84	3.21	3.21

Table 6.2. Energy streams information for reforming and carbonation reactors of each stage.

Reactor	1st reform	1st carb	2nd reform	2nd carb	3rd reform	3rd carb
name on PFD	REF1	CARB1	REF2	CARB2	REF3	CARB3
Energy (kJ/s)	-5.39	-4.71	10.17	-4.95	8.22	-4.95
Reactor	4th reform	4th carb	5th reform	5h carb	6th reform	6th carb
name on PFD	REF4	CARB4	REF5	CARB5	REF6	CARB6
Energy (kJ/s)	5.93	-4.95	5.57	-4.95	4.10	-4.95

6.4.4 Sorption-Enhanced Steam Reforming by NaOH

In this case, the reactor contained both the catalyst needed for the reforming process and an additional step that uses NaOH for the removal of CO_2 (Figure 6.7). The CO_2 capture and overall SERP reaction are formulated as follows:

$$CO_2 + H_2O \rightleftharpoons H_2CO_3 \quad (5)$$

$$H_2CO_3 \rightleftharpoons HCO_3^- + H^+ \quad (6)$$

$$HCO_3^- + \rightleftharpoons CO_3^{2-} + H^+ \quad (7)$$

$$Ca^{2+} + CO_3^{2-} \rightleftharpoons CaCO_3 \quad (8)$$

Figure 6.8 illustrates the calcium carbonation precipitation, plotting the calcium carbonation precipitation as a function of NaOH addition. The precipitation is promoted at high solution pH. The figure demonstrates that at the NaOH:CO_2 flow rate ratio of 2:1, complete purification of the product stream was achieved. Further increases in the NaOH-to-CO_2 ratio over 2:1 had no effect on the amount of CO_2 removed but had a negative impact on the overall energy because the use of more NaOH requires more energy through the electrolysis of brine solution. Therefore, the ratio of NaOH should be carefully chosen to achieve a resealable operation mode. Minimum thermodynamic energy needed for electrolysis is in the range of 0.65 - 0.81 KWh/ kg of NaOH, whereas that of the current Chlor-alkali process is approximately 2.1 - 2.2 kWh/kg of NaOH[42].

A ratio of more than 2:1 for NaOH to CO_2 did not have a significant effect. Thus, the optimum ratio of 2:1 was chosen for the addition of NaOH to the various reformer inlet steam-to-methane ratios.

Figure 6.8 illustrates the composition of the effluent stream as a function of reactor temperature, where increasing the removal fraction of CO_2 increases the production of H_2. This route provides more stable storage for CO_2 in the form of mineral carbonates compared to CO_2 capture and storage. However, it uses higher energy per tons of CO_2 utilized. Two moles of sodium carbonate are required to precipitate 1 mole of carbon dioxide. Therefore, approximately 3.78 MWh is required for each ton of CO_2 utilized using the Chlor-alkali process.

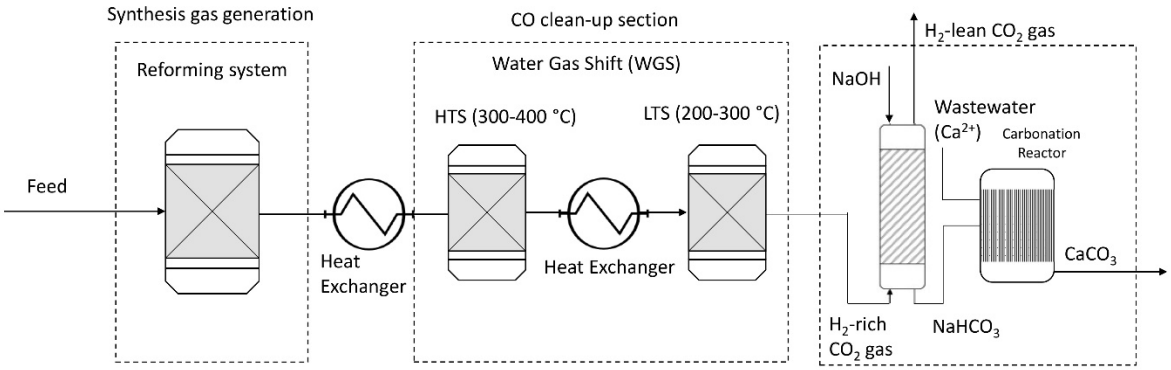

Figure 6.7. Process diagram for the proposed process of the carbonation of produced water using NaOH absorption to continuously remove CO_2. Three reactors, namely (1) a reformer and WGS reactor, (2) an absorber, and (3) a precipitation reactor, are shown.

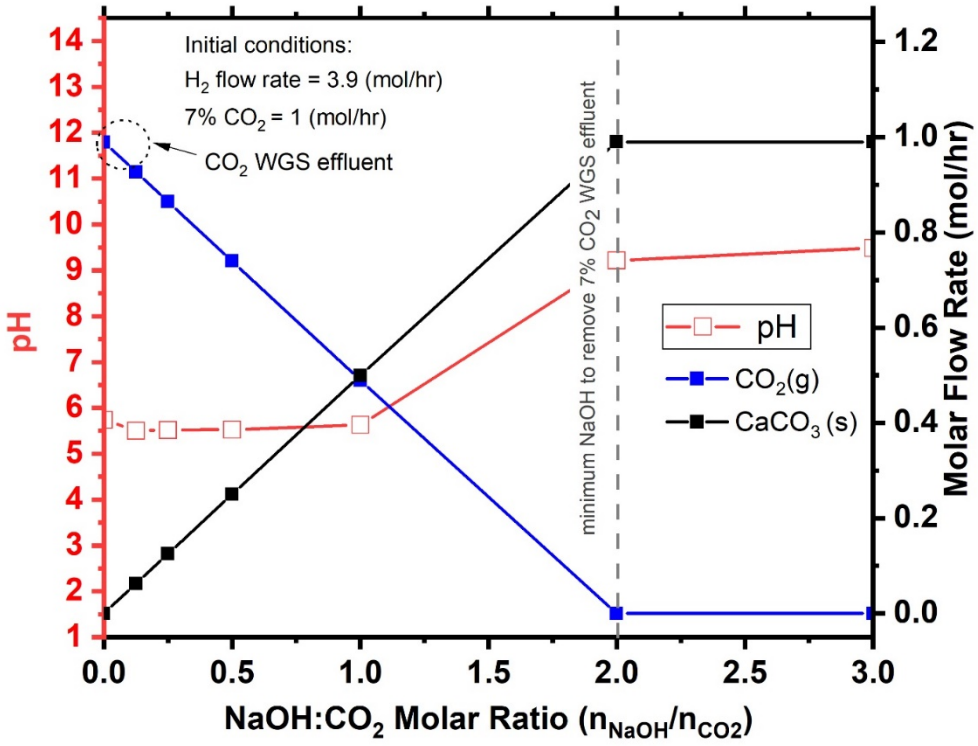

Figure 6.8. Calcium carbonation precipitation as a function of NaOH addition.

6.4.5 Ion-Exchange-Enhanced Steam Reformer

The ion-exchange-enhanced steam reformer process involves the use of regenerable solids that remove H^+ from aqueous solution during carbonation (Figure 6.9). This induces an increase in alkalinity, which is favorable for calcite precipitation. This process involves the following steps.

(1) CO_2 from a steam reformer effluent stream (~7% CO_2) is bubbled into an ion-exchanger containing water and an ion-exchanger solid. Water equilibrates with the flue gas stream and dissolves CO_2 acidifies the aqueous solution then forms H_2CO_3. As the H^+ concentration in the water increases, those ions exchange with monovalent ions contained within the ion-exchanger solid (e.g., Na^+), which prevents the pH from further decreasing. Essentially, this step captures CO_2 from steam reformer effluent passing through the ion-exchanger, inducing the reaction equilibrium toward hydrogen production upon CO_2 removal, and converting dissolved carbonic acid into $NaHCO_3$. Once the ion-exchanger solid becomes saturated with H^+, it is replaced with fresh solid and prepared for regeneration.

(2) In the next step, the $NaHCO_3$ solution exiting the ion-exchanger is mixed with Ca-rich produced water. This produces PCC that can be separated from the solution by filtering or gravitational settling. The residual solution then passes through an RO module to recycle water for reuse in step 1. As the produced water has high salinity, the RO module also produces a retentate solution with concentrated Na^+.

(3) In the final step, the retentate from the RO module is introduced to the H^+-saturated ion-exchanger solid in a regeneration reactor. The high Na^+ concentration in the retentate promotes a reverse ion-exchange reaction, in which Na^+ replaces the H^+ in the solid, thus regenerating the solid for reuse. In full-scale implementations, liquid discharge from the final step is fed into the produced water treatment process for concentration and salt crystallization.

The H^+–Na^+ ion-exchange was conducted by adding the solids (0–1.0 kg/kg) to a saturated CO_2 water (pH 4, pCO_2 = 1 ATM; Figure 6.10 b). For all types, an increase in pH coupled was observed, indicating the possibility of the ion-exchange process, and illustrating that significant basicity can be generated. The Lewatit TP 207(Na) and 260 were superior to zeolite in terms of ion-exchange and increased the solution alkalinity from 4 to approximately 10 pH. In performance, they were followed by weakly acidic ion exchangers such as zeolite 13X and 4A and then strongly acidic ion exchangers such as Amberlite 200C(Na), Amberlite IR120(Na), Diaion SK112(Na) and Lewatit M^+SP 112(Na). The strong acid resin was highly dissociated, and thus, the cation was available for exchange over the entire pH range and a considerable excess of acid was needed to convert the sodium form to the hydrogen form. The weak acid cation resin was functionalized with carboxyl groups.

Figure 6.10 (a) shows the EC of the ion-exchange materials in various concentrations of HCl solutions and CO_2-saturated solutions to indicate the effect of the initial concentration on exchange capacity. In this case, the total number of cations in the systems was constant, using 1 g of an ion-exchanger. Changing the concentration of CO_2 from 15% to 100% resulted in lower equilibrium concentrations and, thus, lower EC. As the water equilibrated with the flue gas stream, dissolved CO_2 acidified the water by forming H_2CO_3. As the H^+ concentration in the water increased, ions exchanged with monovalent ions contained within the ion-exchanger solid (Na^+), which prevented a further decrease of pH. Thus, the maximum exchange capacity was achieved at the initial CO_2 concentration of 14% with 0.6 mmol/g. This followed the same trend observed with Na^+/H^+ exchange in HCl solution. Maximum exchange capacity with organic exchange resin was achieved at 1 M HCl (~3 mmol/g Na released), whereby high amount of Na was released from zeolites due to dissolution.

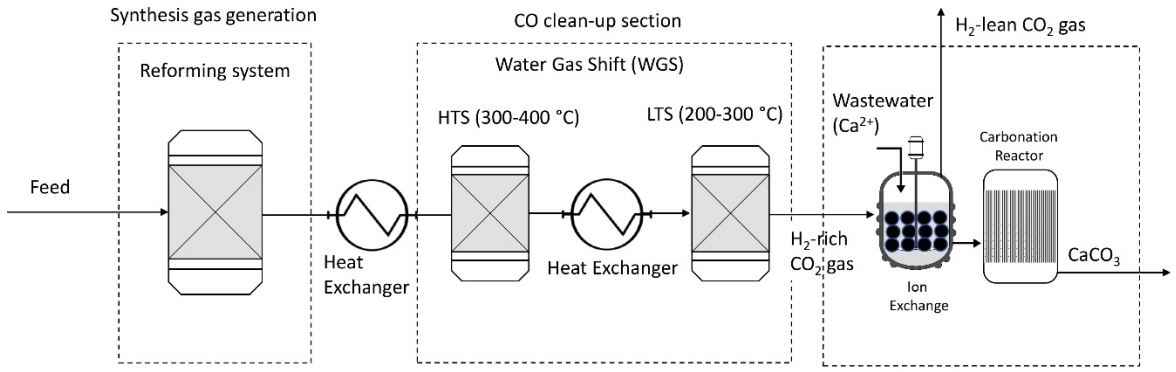

Figure 6.9. Process diagram for the proposed process of the carbonation of produced water using ion-exchange. Three reactors, namely (1) a reformer and WGS reactor, (2) an ion-exchange reactor, and (3) a precipitation reactor, are shown.

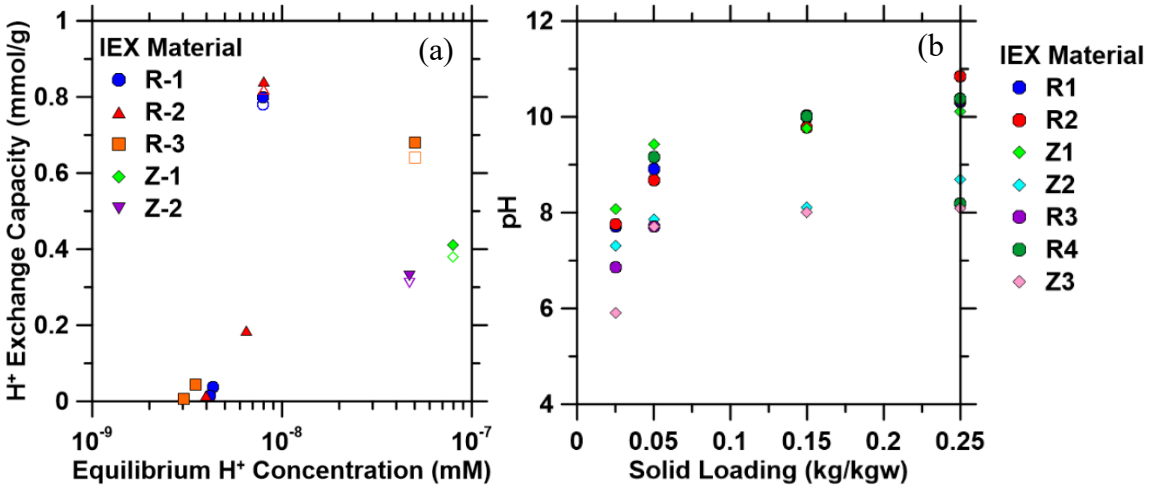

Figure 6.10. Equilibrium isotherms for CO_2 solutions developed using saturated CO_2 (pH 3.9, 100% CO_2), pH 4.5, and pH 5.3.

Ion-exchange reaction kinetics were studied at different temperatures to determine their effect on exchange rates and EC. Increasing temperature increased the reaction rate constant for all materials, due to the increased mobility of ions (Figure 6.11). Increasing temperature increased

the EC of materials further, indicating that temperature can be optimized to reach maximum exchange by utilizing the heat of the reformer outlet stream and maximum pH for the process to achieve maximum exchange capacity. Zeolitic materials have higher kinetics increments than ion-exchange resins due to the micropores structure of zeolites. Additionally, the reaction temperature is an essential operating factor for the carbonation reactor. Nucleation and growth of $CaCO_3$ are induced at high temperatures due to the decreased solubility of CO_2. Carbonation is an exothermic reaction, and an increase in temperature may lead to a decrease in the equilibrium constant.

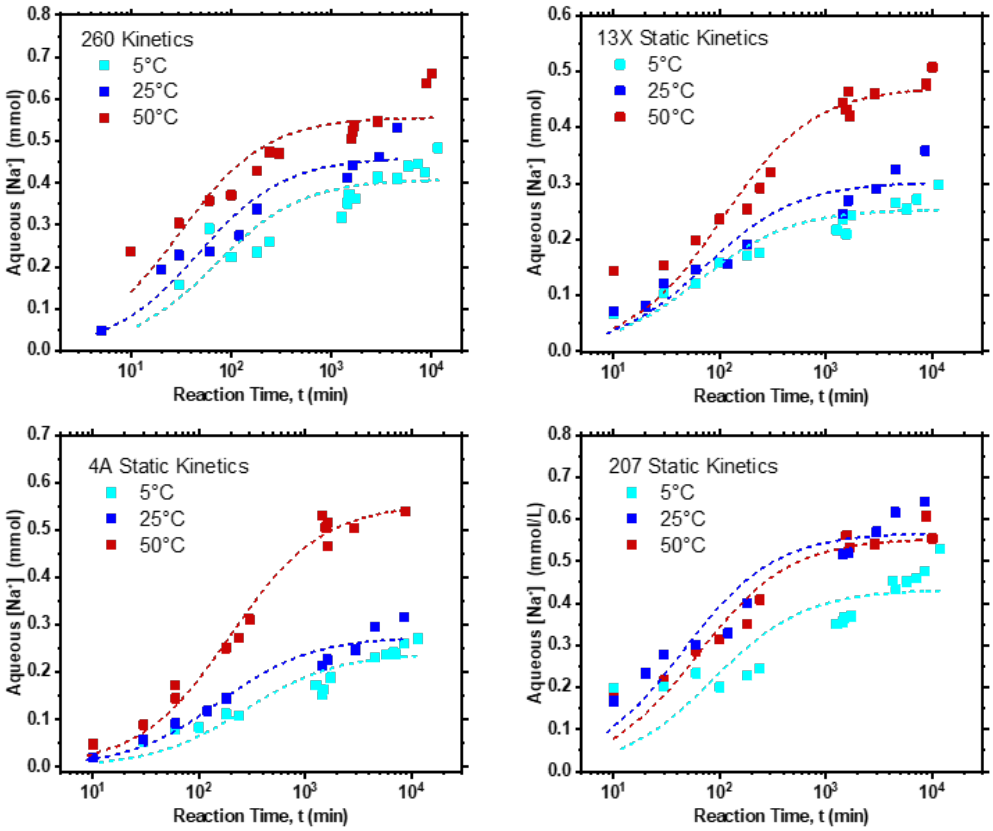

Figure 6.11. Ion-exchange reactions for different materials over time from 5 °C to 50 °C under static conditions.

6.5 Discussion

The production of hydrogen and other species at different temperatures and pressures was analyzed on the basis of thermodynamic analysis. Our simulation showed that the process was able to produce a pure H_2 stream after the mineralization step. The effect of temperature on methane conversion and hydrogen purity was illustrated for the two investigated processes. In conventional steam reforming, increased the temperature increased the conversion of methane due to the endothermic reaction, which is induced at high temperatures. The presence of CO_2 sorbent led to further methane conversion and changed the equilibrium shift of the reaction. The effect of increasing steam increased the concentration of hydrogen in the outlet stream. In this case, H_2 production and methane conversion were enhanced due to steam and CO_2 conversion, which led to the removal of CO_2 and the production of high-purity hydrogen. At a temperature of less than 650 K, CO_2 capture efficiency was above 90%. However, as the temperature increased further, CO_2 capture decreased due to the decomposition of $CaCO_3$. Thus, at high temperatures, the enhanced steam reforming process degenerated into a conventional steam reforming process. Therefore, the optimal operating condition for SESR is between 550 and 650 K. The highest quantity of hydrogen was achieved with excess steam at all temperatures.

In the ion-exchange process, weakly acidic function groups exhibited higher ion-exchange capacities than did zeolitic materials; this may be a result of the availability of exchange sites and the affinity of proton. Weak acid cation resin exhibits a higher affinity for hydrogen ions than strong acid cation due to the presence of the carboxylic functional group in their backbone structure. The ion-exchange potential of hydrogen ions is dependent on the strength of the acid functional group and hydrogen; stronger acid entails lower ion-exchange potential. This demonstrated that strong acidic resins might not be suitable candidates for ion-exchange, as their

ability to attract protons is much lower than that of sodium. Strongly acidic resin exhibited lower exchange performance than did the weakly acidic resin. Weakly to moderate acidic ion exchangers such as zeolite (13X and 4A) had less hydrogen affinity than weekly acidic resin but were able to convert dissolved carbonic acid into $NaHCO_3$. Zeolite Na-X has a cation exchange capacity of 0.6 mmol g^{-1}, a lower exchange capacity than Na-A, and does not proceed to a full exchange.

In both processes, H_2 yield was energetically enhanced the removal of CO_2. It can be observed that due to the intensification effect, CH_4 conversion was promoted to a higher value because of Le Chatelier's principle. To probe the effect of Le Chatelier's principle to improve the process more, we simulated the effect of continuous removal of H_2 from the outlet stream which can be achieved by coupling the SESR process with a selective membrane that can selectively remove H_2 (Figure 6.12) [43]. In Aspen Plus this model is a combination of component splitters. The hydrogen-rich gas was assumed to contain 98% hydrogen and 2% methane, carbon monoxide and water combined.[44] The hydrogen-rich gas was then fed to PSA unit that recovers hydrogen with a purity of 99.99%. The PSA was modeled as component splitter block in Aspen Plus.[45,46]

Results showed significant improvement in the H_2 product yield with even lower temperatures than that achieved in the SESR process (Figure 6.13).

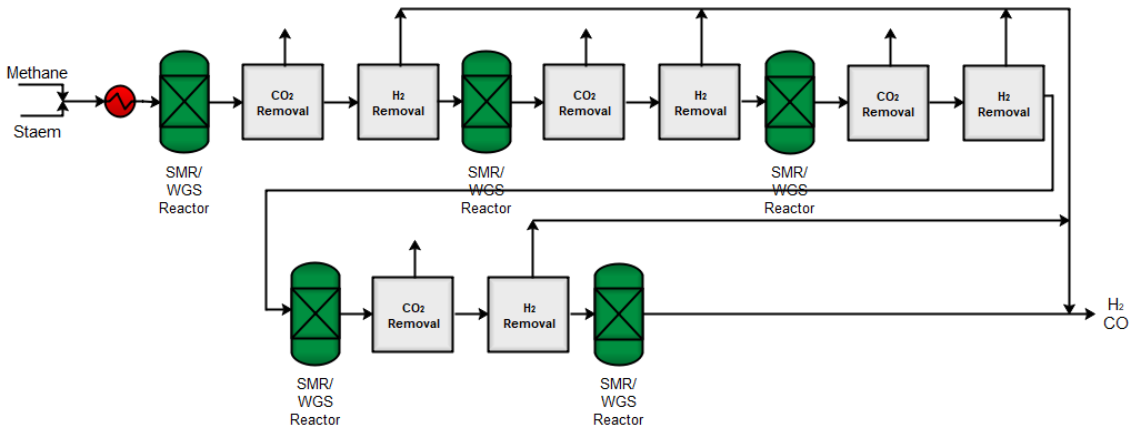

Figure 6. 12. Process Flow diagram showing the effect of temperature on the H_2 yield product of the SESR with the continuous removal of H_2 from outlet

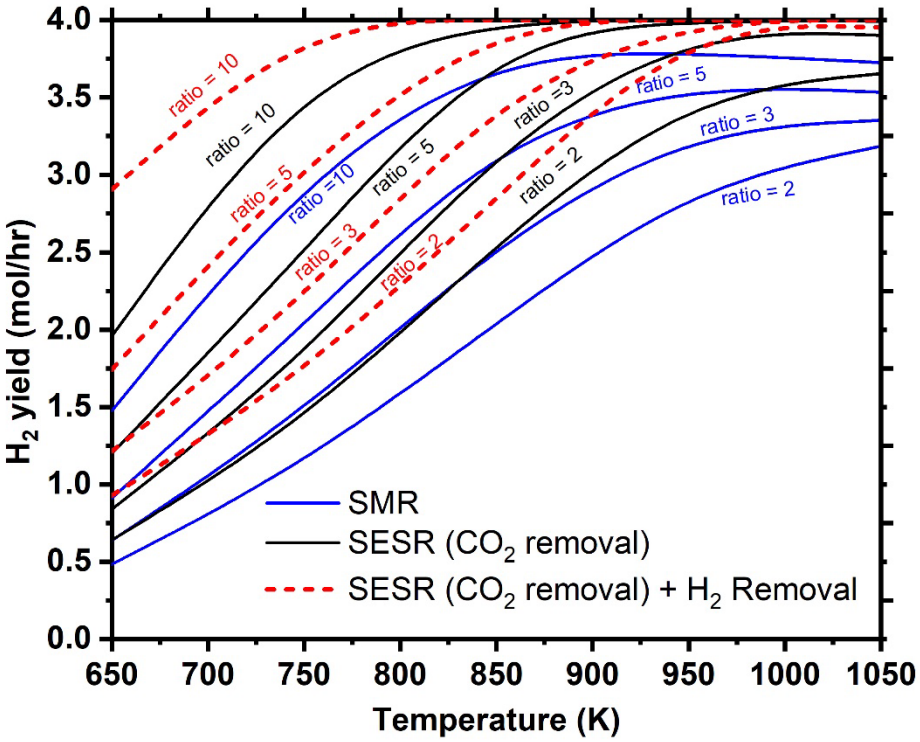

Figure 6.13. The effect of temperature on the H_2 yield product of the SESR with the continuous removal of H_2 from outlet.

6.6 Conclusion

In this study, SMR was enhanced using CO_2 mineralization. Thermodynamic calculations were made by using the method of Gibbs free energy minimization to determine the optimum conditions of temperature, steam-to-methane ratio, and pressure to produce hydrogen with high yields. The product composition at thermodynamic equilibrium was determined by minimizing the total Gibbs reaction scheme free energy at a temperature-pressure-feed composition. The results demonstrated that for all models, hydrogen yield is induced at high temperatures and high steam-

to-methane ratios. The analysis suggests that the most favorable temperature is between 800 and 950 K. Increasing the steam-to-methane ratio and temperature resulted in higher hydrogen yield, but after a certain value, the addition becomes uneconomical, due to the high energy used.

Another finding is that pressure has a negative effect on the hydrogen production yield. The combined process of reaction and separation enhanced the disappearance of carbon monoxide due to the formation of carbon dioxide, which was enhanced by the simultaneous CO_2 mineralization. Due to the more favorable position of the equilibrium of the steam reforming reaction, product formation was accelerated to a greater extent. Through use of the model, the contribution of equilibrium conversion and the sorption enhancement were quantified.

A model analysis was performed to probe the effect of producing high-purity H_2 with minimum CO concentration. Different types of ion-exchange materials were screened to examine their ability to increase the pH of the acidic solutions containing HCl and dissolve CO_2. These ion-exchange materials were screened using CO_2-rich feeds (CO_2-saturated water at atmospheric pressure has a pH of 4); ion-exchange in this system resulted in both an increase in pH and a change in the speciation of carbon in a solution to carbonate ions (which can be used for mineralization). These results indicate that both zeolite and organic exchange resins are far from their ideal EC in a CO_2-saturated solution but are able to exchange enough protons to induce a pH swing to the desired pH regions for CO_2 mineralization. An increase in temperatures yields an increase in EC and kinetics for all materials, implying that temperature may be optimized to achieve ideal capacity.

6.7 References

1. Broda, M.; Manovic, V.; Imtiaz, Q.; Kierzkowska, A. M.; Anthony, E. J.; Müller, C. R. High-Purity Hydrogen via the Sorption-Enhanced Steam Methane Reforming Reaction over a Synthetic CaO-Based Sorbent and a Ni Catalyst. *Environ. Sci. Technol.* **2013**, *47* (11), 6007–6014. https://doi.org/10.1021/es305113p.
2. Ebneyamini, A.; Grace, J. R.; Lim, C. J.; Ellis, N.; Elnashaie, S. S. E. H. Simulation of Limestone Calcination for Calcium Looping: Potential for Autothermal and Hydrogen-Producing Sorbent Regeneration. *Ind. Eng. Chem. Res.* **2019**, *58* (20), 8636–8655. https://doi.org/10.1021/acs.iecr.9b00668.
3. Kalamaras, C. M.; Efstathiou, A. M. Hydrogen Production Technologies: Current State and Future Developments. *Conf. Pap. Energy* **2013**, *2013*, 1–9. https://doi.org/10.1155/2013/690627.
4. Iulianelli, A.; Liguori, S.; Wilcox, J.; Basile, A. Advances on Methane Steam Reforming to Produce Hydrogen through Membrane Reactors Technology: A Review. *Catal. Rev. - Sci. Eng.* **2016**, *58* (1), 1–35. https://doi.org/10.1080/01614940.2015.1099882.
5. Balat, M.; Balat, M. Political, Economic and Environmental Impacts of Biomass-Based Hydrogen. *Int. J. Hydrogen Energy* **2009**, *34* (9), 3589–3603. https://doi.org/10.1016/j.ijhydene.2009.02.067.
6. Onozaki, M.; Watanabe, K.; Hashimoto, T.; Saegusa, H.; Katayama, Y. Hydrogen Production by the Partial Oxidation and Steam Reforming of Tar from Hot Coke Oven Gas. *Fuel* **2006**, *85* (2), 143–149. https://doi.org/10.1016/j.fuel.2005.02.028.
7. Muradov, N. Z.; Veziroğlu, T. N. From Hydrocarbon to Hydrogen-Carbon to Hydrogen Economy. *Int. J. Hydrogen Energy* **2005**, *30* (3), 225–237.

https://doi.org/10.1016/j.ijhydene.2004.03.033.

8. Chanburanasiri, N.; Ribeiro, A. M.; Rodrigues, A. E.; Arpornwichanop, A.; Laosiripojana, N.; Praserthdam, P.; Assabumrungrat, S. Hydrogen Production via Sorption Enhanced Steam Methane Reforming Process Using Ni/CaO Multifunctional Catalyst. *Ind. Eng. Chem. Res.* **2011**, *50* (24), 13662–13671. https://doi.org/10.1021/ie201226j.
9. Ortiz, A. L.; Harrison, D. P. Hydrogen Production Using Sorption-Enhanced Reaction. *Ind. Eng. Chem. Res.* **2001**, *40* (23), 5102–5109. https://doi.org/10.1021/ie001009c.
10. Gilles, E. D.; Lauschke, G.; Kienle, A.; Storz, M. Some Aspects of Integrated Process Operation. In *Annual Reviews in Control*; Elsevier, 1996; Vol. 20, pp 9–22. https://doi.org/10.1016/S1367-5788(97)00002-3.
11. Westerterp, K. R. Multifunctional Reactors. *Chem. Eng. Sci.* **1992**, *47* (9–11), 2195–2206. https://doi.org/10.1016/0009-2509(92)87035-O.
12. Wang, Y. N.; Rodrigues, A. E. Hydrogen Production from Steam Methane Reforming Coupled with in Situ CO2 Capture: Conceptual Parametric Study. *Fuel* **2005**, *84* (14–15), 1778–1789. https://doi.org/10.1016/j.fuel.2005.04.005.
13. Agar, D. W. Multifunctional Reactors: Old Preconceptions and New Dimensions. *Chem. Eng. Sci.* **1999**, *54* (10), 1299–1305. https://doi.org/10.1016/S0009-2509(99)00040-8.
14. Sircar, S.; Waldron, W. E.; Rao, M. B.; Anand, M. Hydrogen Production by Hybrid SMR-PSA-SSF Membrane System. *Sep. Purif. Technol.* **1999**, *17* (1), 11–20. https://doi.org/10.1016/S1383-5866(99)00021-0.
15. Le Chatelier, H. Sur La Dilatation Des Metaux Aux Temperatures Elevees. *Cornpt. rend* **1889**, *108*, 1096.
16. Al-Bassam, A. M.; Conner, J. A.; Manousiouthakis, V. I. Natural-Gas-Derived Hydrogen in

the Presence of Carbon Fuel Taxes and Concentrated Solar Power. *ACS Sustain. Chem. Eng.* **2018**, *6* (3), 3029–3038. https://doi.org/10.1021/acssuschemeng.7b02745.

17. Pichardo, P.; Manousiouthakis, V. I. Infinite DimEnsionAl State-Space as a Systematic Process Intensification Tool: Energetic Intensification of Hydrogen Production. *Chem. Eng. Res. Des.* **2017**, *120*, 372–395. https://doi.org/10.1016/j.cherd.2017.01.026.
18. Pichardo, P. A.; Manousiouthakis, V. I. Intensified Energetically Enhanced Steam Methane Reforming through the Use of Membrane Reactors. *AIChE J.* **2020**, *66* (2), e16827. https://doi.org/10.1002/aic.16827.
19. Tzanetis, K. F.; Martavaltzi, C. S.; Lemonidou, A. A. Comparative Exergy Analysis of Sorption Enhanced and Conventional Methane Steam Reforming. *Int. J. Hydrogen Energy* **2012**, *37* (21), 16308–16320. https://doi.org/https://doi.org/10.1016/j.ijhydene.2012.02.191.
20. Romano, M. C.; Cassotti, E. N.; Chiesa, P.; Meyer, J.; Mastin, J. Application of the Sorption Enhanced-Steam Reforming Process in Combined Cycle-Based Power Plants. *Energy Procedia* **2011**, *4*, 1125–1132. https://doi.org/https://doi.org/10.1016/j.egypro.2011.01.164.
21. Zhu, L.; Fan, J. Thermodynamic Analysis of H2 Production from CaO Sorption-Enhanced Methane Steam Reforming Thermally Coupled with Chemical Looping Combustion as a Novel Technology. *Int. J. Energy Res.* **2015**, *39* (3), 356–369. https://doi.org/10.1002/er.3248.
22. Balasubramanian, B.; Ortiz, A. L.; Kaytakoglu, S.; Harrison, D. P. Hydrogen from Methane in a Single-Step Process. *Chem. Eng. Sci.* **1999**, *54* (15–16), 3543–3552.
23. Fu, F.; Wang, Q. Removal of Heavy Metal Ions from Wastewaters: A Review. *J. Environ. Manage.* **2011**, *92* (3), 407–418. https://doi.org/https://doi.org/10.1016/j.jenvman.2010.11.011.
24. Klein, A. R.; Baldwin, D. S.; Singh, B.; Silvester, E. J. Salinity-Induced Acidification in a

Wetland Sediment through the Displacement of Clay-Bound Iron(II). *Environ. Chem.* **2010**, *7* (5), 413–421.

25. Avena, M. J.; De Pauli, C. P. Proton Adsorption and Electrokinetics of an Argentinean Montmorillonite. *J. Colloid Interface Sci.* **1998**, *202* (1), 195–204. https://doi.org/10.1006/jcis.1998.5402.
26. Robin, V.; Tertre, E.; Beaufort, D.; Regnault, O.; Sardini, P.; Descostes, M. Ion Exchange Reactions of Major Inorganic Cations (H^+, Na^+, Ca^{2+}, Mg^{2+} and K^+) on Beidellite: Experimental Results and New Thermodynamic Database. Toward a Better Prediction of Contaminant Mobility In. *Appl. Geochemistry* **2015**, *59* (December), 74–84. https://doi.org/10.1016/j.apgeochem.2015.03.016.
27. Teir, S.; Eloneva, S.; Zevenhoven, R. Production of Precipitated Calcium Carbonate from Calcium Silicates and Carbon Dioxide. *Energy Convers. Manag.* **2005**, *46* (18–19), 2954–2979. https://doi.org/10.1016/j.enconman.2005.02.009.
28. Said, A.; Mattila, H. P.; Järvinen, M.; Zevenhoven, R. Production of Precipitated Calcium Carbonate (PCC) from Steelmaking Slag for Fixation of CO2. *Appl. Energy* **2013**, *112*, 765–771. https://doi.org/10.1016/j.apenergy.2012.12.042.
29. Nduagu, E.; Björklöf, T.; Fagerlund, J.; Wärnå, J.; Geerlings, H.; Zevenhoven, R. Production of Magnesium Hydroxide from Magnesium Silicate for the Purpose of CO2 Mineralisation–Part 1: Application to Finnish Serpentinite. *Miner. Eng.* **2012**, *30*, 75–86.
30. Peng, D. Y.; Robinson, D. B. A New Two Parameters Equation of State. *Ind. Eng. Chem. Fundam* **1976**, *15*, 59–64.
31. Özkara-Aydnolu, Ş. Thermodynamic Equilibrium Analysis of Combined Carbon Dioxide Reforming with Steam Reforming of Methane to Synthesis Gas. *Int. J. Hydrogen Energy* **2010**,

35 (23), 12821–12828. https://doi.org/10.1016/j.ijhydene.2010.08.134.

32. Belova, A. A. G.; Yegulalp, T. M.; Yee, C. T. Feasibility Study of In Situ CO2 Capture on an Integrated Catalytic CO2 Sorbent for Hydrogen Production from Methane. *Energy Procedia* **2009**, *1* (1), 749–755. https://doi.org/10.1016/j.egypro.2009.01.099.
33. Vagia, E. C.; Lemonidou, A. A. Thermodynamic Analysis of Hydrogen Production via Steam Reforming of Selected Components of Aqueous Bio-Oil Fraction. *Int. J. Hydrogen Energy* **2007**, *32* (2), 212–223. https://doi.org/10.1016/j.ijhydene.2006.08.021.
34. Aktaş, S.; Karakaya, M.; Avci, A. K. Thermodynamic Analysis of Steam Assisted Conversions of Bio-Oil Components to Synthesis Gas. *Int. J. Hydrogen Energy* **2009**, *34* (4), 1752–1759. https://doi.org/10.1016/j.ijhydene.2008.12.019.
35. Chen, C.-C.; Song, Y. Generalized Electrolyte-NRTL Model for Mixed-Solvent Electrolyte Systems. *AIChE J.* **2004**, *50* (8), 1928–1941. https://doi.org/10.1002/aic.10151.
36. Ha-Duong, M.; Grubb, M. J.; Hourcade, J. C. Influence of Socioeconomic Inertia and Uncertainty on Optimal CO2- Emission Abatement. *Nature* **1997**, *390* (6657), 270–273. https://doi.org/10.1038/36825.
37. Hegarty, M. E. S.; O'Connor, A. M.; Ross, J. R. H. Syngas Production from Natural Gas Using ZrO2-Supported Metals. *Catal. Today* **1998**, *42* (3), 225–232. https://doi.org/10.1016/S0920-5861(98)00096-0.
38. Lysikov, A. I.; Trukhan, S. N.; Okunev, A. G. Sorption Enhanced Hydrocarbons Reforming for Fuel Cell Powered Generators. *Int. J. Hydrogen Energy* **2008**, *33* (12), 3061–3066. https://doi.org/https://doi.org/10.1016/j.ijhydene.2008.03.041.
39. Antzara, A.; Heracleous, E.; Bukur, D. B.; Lemonidou, A. A. Thermodynamic Analysis of Hydrogen Production via Chemical Looping Steam Methane Reforming Coupled with in Situ

CO2 Capture. *Int. J. Greenh. Gas Control* **2015**, *32*, 115–128. https://doi.org/https://doi.org/10.1016/j.ijggc.2014.11.010.

40. Antzara, A.; Heracleous, E.; Bukur, D. B.; Lemonidou, A. A. Thermodynamic Analysis of Hydrogen Production via Chemical Looping Steam Methane Reforming Coupled with in Situ CO2 Capture. *Energy Procedia* **2014**, *63*, 6576–6589. https://doi.org/https://doi.org/10.1016/j.egypro.2014.11.694.
41. Cheng, Y.; Wei, F.; Jin, Y. *Multiphase Reactor Engineering for Clean and Low-Carbon Energy Applications*; Wiley, 2017. https://doi.org/10.1002/9781119251101.
42. Thiel, G. P.; Kumar, A.; Gómez-González, A.; Lienhard, J. H. Utilization of Desalination Brine for Sodium Hydroxide Production: Technologies, Engineering Principles, Recovery Limits, and Future Directions. *ACS Sustain. Chem. Eng.* **2017**, *5* (12), 11147–11162. https://doi.org/10.1021/acssuschemeng.7b02276.
43. Ockwig, N. W.; Nenoff, T. M. Membranes for Hydrogen Separation. *Chem. Rev.* **2007**, *107* (10), 4078–4110. https://doi.org/10.1021/cr0501792.
44. Gabriel, K. J.; Linke, P.; Jiménez-Gutiérrez, A.; Martínez, D. Y.; Noureldin, M.; El-Halwagi, M. M. Targeting of the Water-Energy Nexus in Gas-to-Liquid Processes: A Comparison of Syngas Technologies. *Ind. Eng. Chem. Res.* **2014**, *53* (17), 7087–7102. https://doi.org/10.1021/ie4042998.
45. Yang, S. Il; Choi, D. Y.; Jang, S. C.; Kim, S. H.; Choi, D. K. Hydrogen Separation by Multi-Bed Pressure Swing Adsorption of Synthesis Gas. *Adsorption* **2008**, *14* (4–5), 583–590. https://doi.org/10.1007/s10450-008-9133-x.
46. Stöcker, J.; Whysall, M.; Miller, G. Q. 30 Years of PSA Technology for Hydrogen Purification. *UOP LLC* **1998**, 1–25.

Chapter 7: Techno-Economic Analysis of a Process to Convert Methane to Olefins Featuring a Combined Reformer Through the Methanol Intermediate

7.1 Abstract

The significant increase in the production of shale-gas in the United States has caused significant changes in the chemical and petrochemical markets. Ethylene production by steam cracking of ethane and naphtha is one of the utmost energy- and emission-intensive routes in the chemical industry. High operating temperatures, high reaction endothermicity, and complex separation create high energy demands as well as considerable CO_2 emissions. In this study, a demonstration of a transformational methane to ethylene process that offers lower emissions using energy optimization and a minimum CO_2 emission approach is presented. A process design is developed and implemented to convert methane into value-added chemicals with minimum CO_2 emissions.

7.2 Introduction

Despite significant renewable energy development efforts, carbon-based fuel sources continue to dominate global energy, representing 82.2% of the world's energy and totaling 598 quadrillion BTU in 2018.[1] The shale gas revolution has provided natural gas as an abundant, versatile, and economical alternative feedstock to conventional fuels. Natural gas (shale gas) is predominantly composed of methane and is expected to outlast oil production by a significant margin. Driven by advancements in hydraulic fracturing and horizontal drilling technologies, between 2005 and 2013, US production of natural gas increased by 33%. Production has shifted from traditional regions, such as the Gulf of Mexico, to more distant regions away from the consumption areas. This has resulted in increases in the cost of transportation. Therefore, natural gas need to be converted into more cost-effective products, such as liquid transportation fuels with a higher energy density.[2] Currently, after shale gas is purified and fractionated, the natural gas liquids (NGLs) that are produced have considerably higher market values than that of methane. The current exportation of natural gas to markets is dominated by pipelines and NGLs. These light NGLs, such as ethane, propane, and butanes, are used as a feedstock to produce olefins, and the residual heavier fractions (C_{5+} hydrocarbon) are used as gasoline stock. The use of methane gas in the production of olefins and other chemicals has high potential to be a game changer in the chemical industry. A number of researchers have attempted to develop a cost-effective methane-to-chemicals integrated process through syngas production.[3–5] Once syngas is produced, it can be transformed into numerous intermediates and products. Examples of chemicals that can be transformed into products include methanol,[6,7] ethylene,[8] propylene,[9] benzene,[10] and liquid transportation fuels.[11] Olefins are a vital chemical is the value chain because they are used to produce value-added chemicals, such as plastics, synthetic rubber, and adhesive materials.[12] The

importance of olefins is attributable to the double bond in their molecular structure; when this bond is broken, the molecules can rapidly form two new single bonds, producing a variety of reactions.

Methane dominates NGLs in shale gas, constituting 75–90% of the total gas. However, methane has a high C–H bond strength (434 kJ/mol) with considerable ionization energy, which makes it challenging to break.[13,14] Currently, 70% of methane converted to chemicals is used for ammonia production, 20% is used for methanol production, and the remainder is used in a variety of chemicals such as hydrogen cyanide, acetylene, and oxo chemicals. Methane can be converted into higher hydrocarbons (e.g., ethylene and aromatics) through indirect or direct routes. For indirect routes, methane is converted through the reforming process into syngas (a mixture of CO and H_2), which can be further used as an intermediate to produce methanol, and then olefins through a multistep catalytic reaction in a strategy that is called methanol-to-olefins (MTO).[15–17] The three main routes for producing syngas from natural gas are SMR, POX, and dry reforming of methane (DRM). Each of these routes uses a different oxidizing agent (i.e., steam, oxygen, or carbon dioxide) and operating conditions to produce different (H_2:CO) syngas ratios.[18]

SMR is the catalytic conversion of natural gas in the presence of steam.[19] Steam reforming has been the most common commercial technology with which to produce syngas and hydrogen. Partial oxidation of natural gas is an exothermic catalytic or noncatalytic reaction that involves oxygen. DRM is an endothermic reaction that involves the reaction of natural gas and carbon dioxide to produce syngas in the presence of a catalyst.[20,21] Tri-reforming is a synergetic combination of DRM, POX, and SMR in a single reactor.[22] In addition to the merits of energy integration, the tri-reforming process represents a new method for the conversion and utilization of CO_2 in flue gas without CO_2 separation. Rather than being treated as waste or stored underground, CO_2 can be used as a chemical feedstock for upscaling synthesis that does not rely

on a petrochemical source. Carbon capture and utilization rely on post computation CCS technologies to provide value-added products to offset the cost of operation and make the process profitable. It is even more viable to use flue gas CO_2 than purified CO_2. The typical furnace outlet of flue gases is usually around 1,200 °C. The injection of CO_2 allows the H_2:CO ratio to be controlled. A synergistic combination of the reforming of methane as DRM + SMR, DRM + POX, and DRM + SMR + POX has been recommended to tackle the limitations of each process individually.[22,23] The direct routes of one-step methane conversion to olefin involves conversion through oxidative coupling of methane (OCM) to higher hydrocarbons. In OCM, methane is directly converted to ethylene in a catalytic reactor. The OCM still has minimal economic potential compared to the well-established cracking process.[24] The major limitation of the OCM process is its low C_2 hydrocarbon yield (ethane and ethylene, <20 mol %) and selectivity (<50%) and a large amount of unreacted gas and byproducts. These disadvantages result in high product separation costs and a large carbon footprint.

In addition to the recent discoveries of unconventional shale gas resources, which have increased the global supply of natural gas significantly, cost reduction in renewable energies is creating opportunities for energy transitions, with wind and solar PV predicted to provide more than half of electricity generation in the United States by 2040.[1] Also, the United States is anticipated to rise its ethylene global market share from 20% in 2017 to 22% by 2025. The United States has the advantage of low-cost ethane due to an abundant natural gas supply that has resulted from the shale gas revolution.[1]

Recent publications have considered shale gas as a feedstock to produce syngas,[25] methanol,[7] and light olefins.[8,9] Ehlinger et al. performed a techno-economic analysis for shale gas conversion to methanol and concluded that this process is more profitable in comparison to the

prices of methanol and natural gas.[6] Niziolek et al. presented a framework that produced aromatics (benzene, toluene, and xylene) from natural gas via methanol as an intermediate.[26] He and You developed three processes that integrate shale gas processing facilities with ethane steam cracking to increase the overall profitability of the process.[27] The same authors later combined the conversion of shale gas and the dehydration of bioethanol to improve the economics of ethylene production.[14] Salkuyeh and Adams proposed a polygeneration process to coproduce ethylene and electricity from shale gas with zero CO_2 emissions through the OCM process.

Light olefins are manufactured commercially through three methods: a fired tubular heater using naphtha, ethane, and propane as a feedstock; auto-thermal crude oil cracking; and produced from carbon monoxide and hydrogen. Propane and ethane and are separated from natural gas through an energy-intense cryogenic process before being converted into light olefins (ethylene and propylene). Our goal was to determine whether producing light olefins directly from methane or natural gas that is composed mainly of methane is more economical than obtaining ethane and propane from NGLs and chemically convert them into light olefins.

This work considered various gas reforming technologies for methanol, such as POX, SMR, ATR, and CR. Additionally, single-step conversions of natural gas into olefins and higher hydrocarbons were considered. We developed a flexible approach to evaluate various technologies systematically, determined the appropriate process for converting methane into ethylene, and performed energy and economic analyses. For each particular reformer, specified inputs and operating conditions were analyzed to determine the syngas composition. The appropriate reformer was defined as the one able to achieve the objectives as determined by the inputs and operating conditions. We evaluate the profitability of OCM and MTO processes for the production of ethylene compared to cracking ethane. These analyses were based on an Aspen Plus simulator.

Problem Statement

- Shale gas that consists primarily of methane is an abundant, low-cost, carbon-containing feedstock that is globally widely available. The synthesis of gas followed by various processes in the production of desired chemicals is an economically viable route for producing useful chemicals from methane. The production of syngas in a large industrial plant accounts for a substantial part of the total cost. Therefore, it is important for methane to be converted into syngas and integrated in the processes used to produce methanol and ethylene, to be more efficient and economical.
- Steam cracking is a well-established industrial process for the production of ethylene. Despite optimization efforts, the process still uses a large amount of energy and is a carbon-intensive process.
- Given the considerable progress in these research areas and a significant increase in methane, significant opportunities in the advancement and eventual implementation of intensified ethylene production technologies are available.

Given the methane stream, it is desirable to develop, simulate, and integrate an olefin production plant with three different technologies for the syngas plant and then perform a techno-economic analysis to answer the following questions: (1) What does a process flowsheet look like? (2) What are the opportunities for heat integration for each syngas technology? (3) Which process route from methane to ethylene is optimal in terms of energy?

7.3 Approach and Modeling

7.3.1 Design Basis and Assumptions

The process was developed using Aspen Plus, and equipment costs were estimated using the exponential scaling expression based on the size of the equipment and cost data from the Aspen Process Economic Analyzer. Aspen Energy was used to extract hot- and cold-stream data and apply thermal pinch analysis. Modern-day catalysts are able to achieve compositions close to the equilibrium for reforming systems.[22,28] Equilibrium modeling is essential to identifying the system response because of the ability to change variables such as temperature and pressure. The Gibbs free energy minimization method has been applied widely to calculate the equilibrium composition of a system.[29] The reformer reactors of the methane to ethylene flowsheet use substantial energy. Thus, particular attention was given to modeling different reforming technologies. In most syngas processing routes, the reformer section is operated at a high temperature (800–1,200 °C).[30,31] The reformer is a complex section and depends on the downstream application of technology. The world's largest gas-to-liquid (GTL) plants, ORYX GTL operated by Sasol-Chevron and Pearl and GTL by Shell, use ATR and POX, respectively.[32] Methanol synthesis can also use different reforming approaches, such as SMR, POX, and DRM. Various studies have indicated that reformer catalysts are capable of achieving compositions close to equilibrium.[22,28,31] Therefore, equilibrium models are useful in providing an estimate for reformer conversion.

The Peng–Robinson equation of state was used to simulate the SMR, POX, DRM, and WGS sections of the flowsheet, and for the methanol and ethylene synthesis sections, the UNIFAC VLE liquid activity model and Peng–Robinson equation were used. The input streams of the flowsheet consisted of methane, oxygen, and water (as needed) at 100 kPa and 298 K, and the output streams consisted of ethylene, hydrogen, and water under the same condition. A Gibbs free

energy minimization reactor was used to represent the SMR, POX, DRM, WGS, and methanol synthesis, and the OCM reactor and ethylene synthesis reactor were modeled using a conversion reactor. The MTO reactor was modeled using the yield reactor. A simplified block flow diagram of the overall process with the different configurations for methane to ethylene routes is illustrated in Figure 7.1. The sequence of the process described was obtained from relevant literature. Operating conditions were adjusted based on guidelines in the literature that described steps to simulate these parameters.

The following assumptions were made for process flow sheet development:

- All the inputs to the flow sheet consist of pure components, and
- Pressure drop is neglected in the exchange devices (heaters and coolers).

7.4 Process Description

The proposed process is shown in Figure 7.1 and comprises the following sections: (1) methane conversion, (2) synthesis gas cleaning, (3) methanol synthesis, and (4) methanol conversion and olefin production. The process of methane separation from natural gas is not included in the analysis of this study.

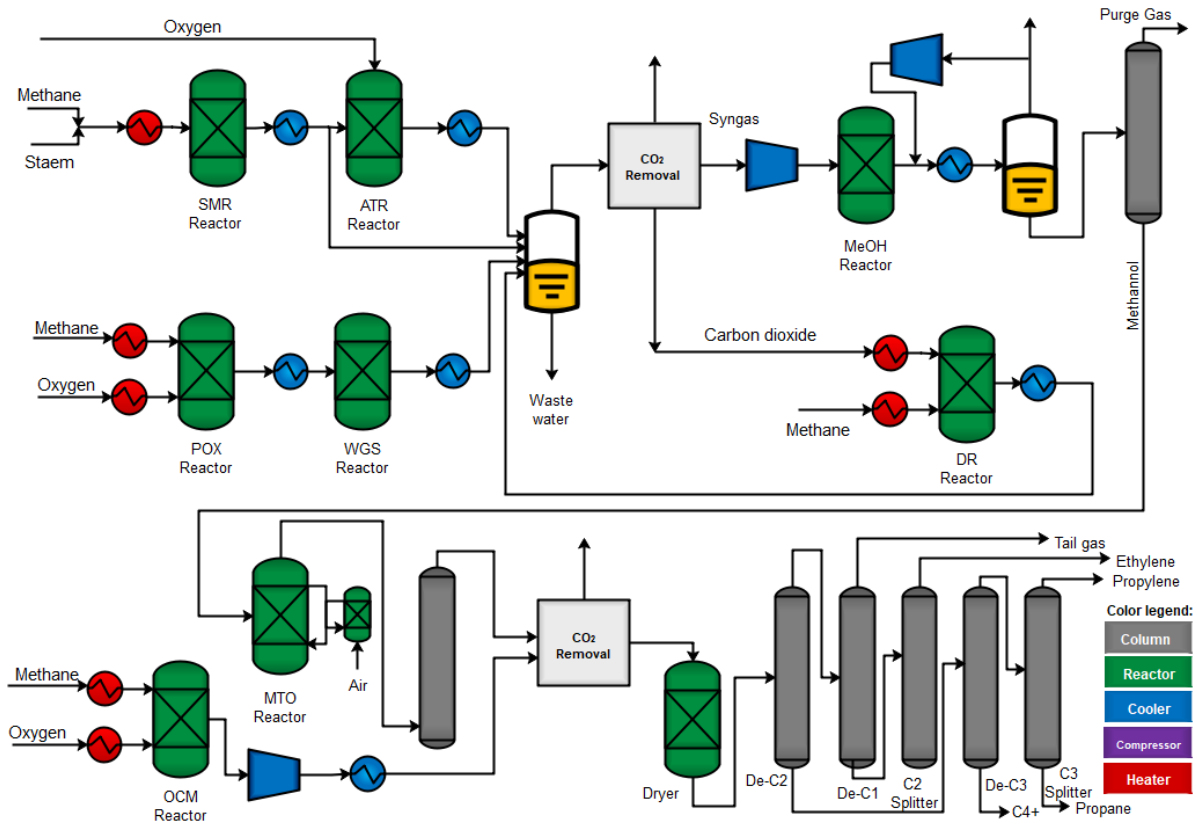

Figure 7.1 MTO flowsheet using SMR, DRM, and POX reforming technologies.

7.4.1 Catalytic Conversion

In the following sections, we consider ethane cracking as a reference, the direct and oxidative conversion of methane to olefins, as well as the task of reforming to produce methanol as an intermediate for the synthesis of olefins.

7.4.1.1 Reforming

The syngas production section consists of three primary unit operations: saturator, performer, and reformer. The ratio of steam or CO_2, in addition to reformers, depends on the type

of reformer used. In this study, CO_2 is assumed to be obtained from SMR, methanol synthesis, and OCM processes. Different reforming processes are considered here and are described below.

7.4.1.1.1 SMR

Methane is converted into syngas through an SMR process. This unit operates at a temperature of 1,073–1,173 K and a pressure of 30 bar. A nickel-based catalyst is used in the reactor tubes, where the SMR (Eq. 1) and WGS (Eq. 2) reactions reach equilibrium. Since the reforming reaction is endothermic, an external supply of heat is required.

$$CH_4 + H_2O \longrightarrow CO + 3H_2 \qquad \Delta H^0_{298K} = 206.1 \text{ kJ/mol} \qquad (1)$$

$$CO + H_2O \rightleftharpoons CO_2 + H_2 \qquad \Delta H^0_{298K} = -41 \text{ kJ/mol} \qquad (2)$$

7.4.1.1.2 POX

In this process, syngas is produced from heavy hydrocarbons. Oxygen is provided from an air separation unit.[2] The oxidation reaction in POX is as follows:

$$CH_4 + 0.5O_2 \longrightarrow CO + 2H_2 \qquad \Delta H^0_{298K} = -36 \text{ kJ/mol} \qquad (3)$$

$$CH_4 + 1.5O_2 \longrightarrow CO + 2H_2O \qquad \Delta H^0_{298K} = -519 \text{ kJ/mol} \qquad (4)$$

$$CH_4 + 2O_2 \longrightarrow CO_2 + 2H_2O \qquad \Delta H^0_{298K} = -802 \text{ kJ/mol} \qquad (5)$$

Reformer feed is heated to 650 °C before it enters the POX reactor. Oxygen is fed into the reactor at 200 °C to maintain the molar ratio of O_2/CH_4 = 0.65.[33] The converted gas leaves the POX reactor at between 1,200 and 1,500 °C.[23] Partial oxidation leads to the syngas ratio (H_2/CO)

of 1.8. This ratio can be adjusted to 2 by a WGS reaction. To obtain the desired H_2/CO ratio, the converted gas from POX is cooled to 370 °C and fed into the WGS reactor, which operates at 250–400 °C and 30 bar (Eq. 2). In this process, syngas is cooled, and water is separated with a flash unit at 45 °C and 30 bar.

7.4.1.1.3 ATR

ATR is an alternative process to SMR. This process combines the technologies of SMR and POX such that oxygen and steam react with methane in an endothermic reaction to produce syngas. The partial combustion of methane is carried out to offset the heat requirement of the endothermic reforming reaction. The steam-to-carbon ratio for the reactor inlet is constrained to be larger than 0.5, and ATR is carried out through methane oxidation by oxygen and water, as shown in the reactions described in Equations 1, 3, and 4.[33,34] The combination of SMR and POX reactions yields a unique approach in which partial combustion of the hydrocarbon feed is balanced by the endothermic requirements of the steam reforming reactions.

The stream form performer is heated to a temperature of 650 °C before the stream is fed to the ATR. Oxygen is fed into the reactor at 200 °C, and the molar ratio is kept at $O_2/CH_4 = 0.59$.[33] Superheated steam is also added to the stream to ensure that the desired molar ratio of H_2/CO is met in the produced syngas. The temperature of the converted gas at the reactor outlet stream is equal to 1,050 °C.

7.4.1.1.4 DRM

DRM is a well-defined technology of both scientific and industrial importance. This process was first studied by Fisher and Tropsch in 1928 with respect to Ni and Co catalysts and since then has been investigated by numerous studies. However, this process has not been industrialized yet.[35] DRM utilizes CO_2 to convert methane into a syngas mixture (H_2 and CO). This process is challenged by the high energy requirements (DRM = 247 kJ/mol and SMR = 206 kJ/mol), susceptibility to coke formation, and low-quality syngas (syngas ratio of H_2/CO is ~1). However, this process provides an attractive route for the cost-effective sequestration of CO_2 to make value-added chemicals and fuels. Compared with SMR and POX, DRM has the advantage of using CO_2 as an oxidant, which gains credit in the CO_2 balance in the process.

$$CH_4 + CO_2 \longrightarrow 2CO + 2H_2 \qquad \Delta H^0_{298K} = 247 \text{ kJ/mol} \qquad (6)$$

7.4.1.2 Methanol Synthesis

Syngas produced by all methods is cooled to 40 °C to separate the excess water. The dry gas is sent to the carbon dioxide extraction unit to remove CO_2 by MDEA. The purified gas then leaves the absorber and goes to the hydrogen extraction unit to maintain the syngas molar ratio of H_2/CO at the desired value (~2.2). The resulting gas is fed to the methanol reactor. The chemical reaction for methanol synthesis from syngas is as follows:

$$CO_2 + 3H_2 \rightleftharpoons CH_3OH + H_2O \qquad \Delta H^0_{298K} = -49.43 \text{ kJ/mol} \qquad (7)$$

$$CO + 2H_2 \rightleftharpoons CH_3OH \qquad \Delta H^0_{298K} = -90.55 \text{ kJ/mol} \qquad (8)$$

The reaction of RWGS is as follows:

$$H_2 + CO_2 \rightleftharpoons CO + H_2O \qquad \Delta H^0_{298K} = 41 \text{ kJ/mol} \qquad (9)$$

The routes were initially developed by Badische Anilin und Soda Fabrik (BASF) and were operated at high pressure (250–350 bar) and temperature (320–450 °C) over ZnO/Cr_2O_3 catalyst. In 1960, ICI (now called Syntex) developed a low-pressure process that operates at 35–55 bar and 200–300 °C over $Cu/ZnO/Al_2O_3$ catalysts.[7,36,37] Methanol reaction synthesis usually occurs as a combination of two reactions in the syngas mixture: the first reaction involves carbon dioxide and hydrogen (Eq. 6), and the second involves carbon monoxide and hydrogen generation in the system (Eq. 2). The net reaction is highly exothermic (Eq. 8). The methanol reactor, which is modeled as an RPlug model using Aspen Plus, operates at 83 bar and a constant temperature of 260 °C.[7] Eq 9 describes the endothermic RWGS reaction, which could also occur during methanol synthesis and produce CO, which can react with hydrogen to produce methanol. Crude methanol that leaves the reactor contains water and some impurities. Therefore, distillation columns are used to purify the methanol products. The outlet stream is cooled to 45 °C, and then methanol crude is separated. The methanol subsystem is shown in Figure 7.1. The gaseous methanol product is cooled to 308 K to separate the methanol from the unreacted syngas. The methanol pressure is reduced to 1 bar to match the operating condition of the olefin reactor.

7.4.1.3 MTO

MTO is based on the dehydration of methanol to produce olefins using a catalytic reactor. The discovery of the dual aromatic-and-olefin-based catalytic cycles in MTO catalysis on acid zeolites has provided a new context for rationalizing structure−function relationships for this complex chemistry.[38] In this mechanism, methanol forms an active pool of $(CH_2)_n$ species in

zeolite pores in which methanol reacts with the species, and this forms products (light olefins, alkanes, and aromatics).

The UOP SAPO-34 catalyst has high selectivity toward light olefins (95%) and conversion of MTO.[39,40] The effluent contains 44% hydrocarbons (ethylene, propylene, and butene) and 56% water by weight. Another catalyst (e.g., ZSM-5) can be used for this process, but SAPO-4 exhibits higher conversion (100%) and selectivity (95%).[41,42] The topology of zeolite plays an important role in the mechanism of MTO conversion. For example, the MFI-structured ZSM-5 (a 3D 10-ring structure with pore sizes of 5.1 × 5.5 and 5.3 × 5.6 Å) has been demonstrated to produce a mixture of alkanes, alkenes, and a major part of aromatics, and the CHA-structured SAPO-34 (a 3D cage structure with window openings of 3.8 × 3.8 Å) has been shown to produce mainly C_2–C_4 alkenes under the same reaction conditions.[43]

In this study, the MTO reactor was modeled using the yield and selectivity data provided in Table 7.1 and was operated at 450 °C and 1.5 bar with 100% methanol conversion.[8,44,45]

The main reactions of the MTO process are as follows[44]:

$$2CH_3OH \rightarrow C_2H_4 + 2H_2O \qquad \Delta H_{700K} = -2.8 \text{ kcal/mol} \tag{10}$$

$$3CH_3OH \rightarrow C_3H_6 + 3H_2O \qquad \Delta H_{700K} = -7.4 \text{ kcal/mol} \tag{11}$$

The outlet stream of the MTO reactor is compressed before it is cooled in a quenching tower. The product stream is compressed with a multistage compressor that includes interstage cooling; then, condensed water from the compressed stream is removed using knockout drums. The compressed stream is then treated to remove CO_2 using diglycolamine solvent (with 35 wt % water).[27] Carbon dioxide exiting the top of the regenerator column is recycled back into the reformer or methanol synthesis reactor. The hydrocarbon stream leaving the top of the absorber is

then fed into a dehydration unit to reduce the moisture content below 0.1 ppm. The dry hydrocarbon is then sent to the separation unit, which consists of a demethanizer, deethanizer, depropanizer, C_2 splitter, C_3 splitter, and a PSA unit to separate the hydrogen gas.

Table 7.1. Product distribution for the MTO reaction.[8,44]

	Yield (%)	Yield on C basis (%)
Ethylene	21.5	49.0
Propylene	14.0	32.0
Butene	4.30	10.0
Methane	0.93	2.18
Ethane	0.18	0.42
Pentane	0.95	2.00
Hydrogen	0.38	0.90
Coke	1.33	3.00
CO_2	0.21	0.50
Water	56.2	-

7.4.1.4 OCM

OCM is a direct process of converting methane into ethylene using a catalytic reactor and offers distinctive advantages in terms of the thermodynamic driving force for ethylene formation. Although this route provides favorable values for ethylene formation, the formation of other species, such as carbon monoxide, carbon dioxide, and coke, is more energetically favorable.[46] The most challenging aspect of applying the selective catalytic materials is to activate methane in the presence of more active reaction products (C_2H_4 and C_2H_6), which are the critical CO and CO_2 precursors. The process is conducted at high temperatures because doing so more readily enables improvements in efficiency on the basis of ease in heat integration.

However, disadvantages of this process are medium conversion and low selectivity.[47,48]

$$2CH_2 + O_2 \longrightarrow C_2H_4 + 2H_2O \qquad \Delta H^0_{298K} = -280.3 \text{ kJ/mol} \tag{12}$$

7.4.1.5 Ethane Steam Cracking

A plug-flow reactor was used to produce ethylene by cracking a feed stream of pure ethane to compare the energy used in the cracking process to other ethylene production processes. The reaction is irreversible, elementary, and operates isothermally at 1,100 K and a pressure of 6 atm.[49]

$$C_2H_6 \longrightarrow C_2H_4 + 2H_2 \quad (13)$$

- k = 0.072 s^{-1} at 1,000 K
- Activation Energy, E = 82 kcal/mol

Component specifications identify all of the chemical species in the process model, and for this particular study, the components were ethane, ethylene, and hydrogen. The selected property method was SYSOP0. A process model was designed for the flowsheet in Aspen Plus. RPLUG was selected, and the temperature was set to be 1,100 K. The following conditions were used: 0.072 for *k*, 82 kcal/mol for E, and 1,000 for K. The ethane steam reaction (Eq. 13) has an elementary rate law, and hence, $-rA = kC_A$.

7.5. Results and Discussion

7.5.1 Thermodynamic Trends

This section reports the determination of the equilibrium composition and reactor energy for a specific operating and feed condition.

7.5.1.1 SMR

Figure 7.2 shows the effect of varying the temperature on the equilibrium composition for SMR. Higher temperatures favor greater H_2 and CO production, higher CH_4 conversion, lower CO_2 in products, and the suppression of solid carbon formation. Higher temperatures also produce higher H_2/CO ratios of close to 3:1. In typical industrial applications, a higher H_2/CO ratio is favored to prevent coke formation and maintain high partial pressure of H_2 in the downstream synthesis. Compared with POX and DRM, SMR produces the highest ratio of syngas (H_2/CO), and oxidizing the reformer with CO_2 through DRM or with O_2 through POX does not help to achieve stoichiometric requirements. CH_4 conversion and hydrogen generation were enhanced as the steam-to-methane ratio (S:C) increased. As the amount of steam increased, more hydrogen entered the system. Thus, eventually, more hydrogen was generated. However, increasing the steam also led to lower steam conversion and CO yield. As more steam was fed into the system, the WGS reaction (Eq. 2) shifted the equilibrium toward more CO reacting with steam to produce H_2 and CO_2. Therefore, more steam increased the conversion of CO as well as the amount of CO_2 produced. Figure 7.2 illustrates that the hydrogen generation continuously increased with temperature until it became level after a specific temperature while CO yield increased continuously with temperature. These effects were caused by the competition between the SMR reaction (Eq. 1) and the RWGS reaction (Eq. 9). At high temperatures (over 1,000 K), the RWGS reaction becomes dominant, consuming the hydrogen that was produced by the SMR reaction and

producing carbon monoxide as the temperature increases. A higher steam-to-methane ratio increases hydrogen production; however, it has an adverse effect on the energy input requirement. There is a trade-off between hydrogen production and energy input with the addition of the steam-to-methane ratio.

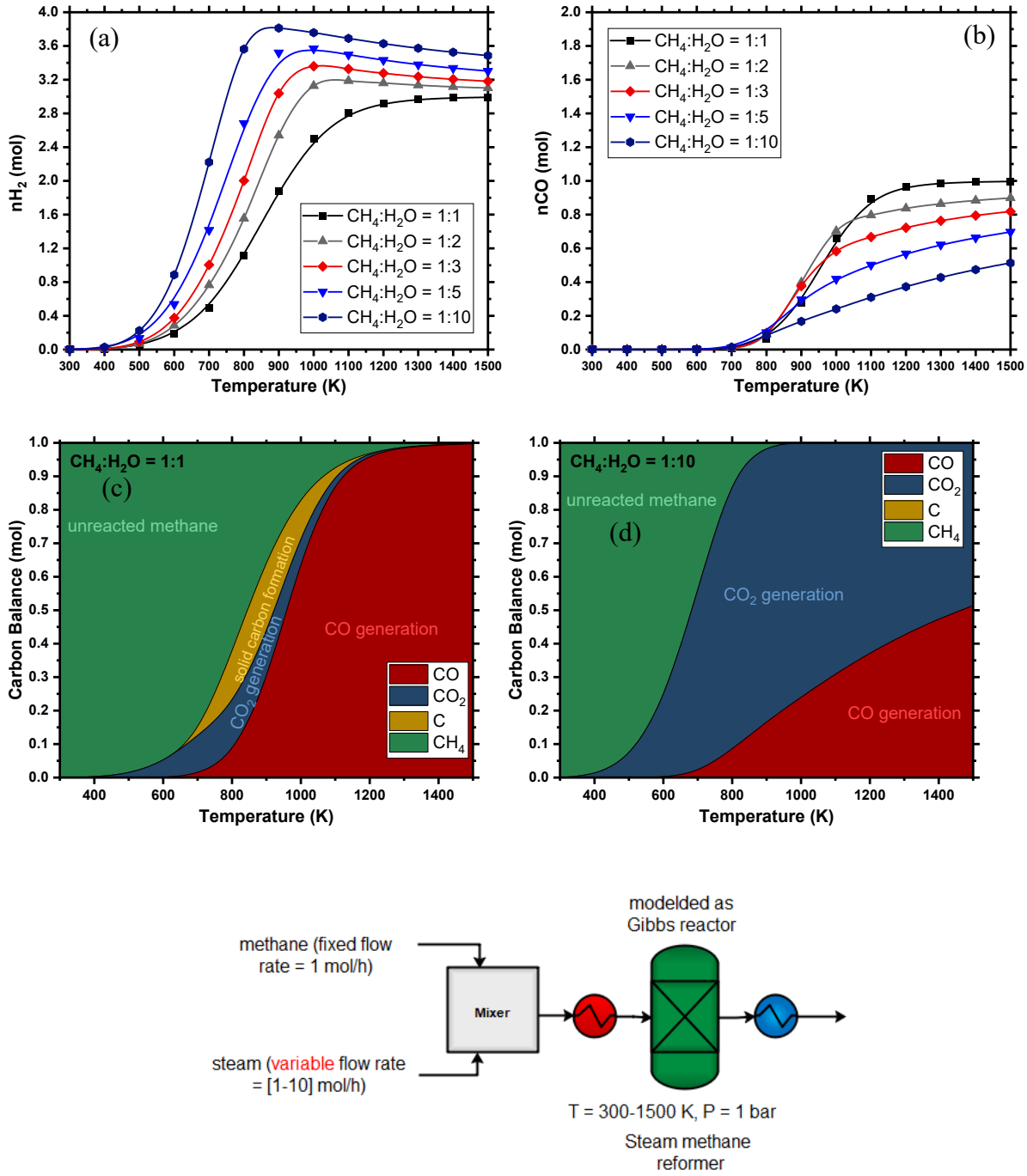

Figure 7.2. Effect of CH_4:H_2O ratio on conversion, syngas yield, CO_2 and H_2O generation, energy input, and carbon deposition in SMR (P = 1 bar).

7.5.1.2 POX

As in SMR, in POX, increasing the temperature increases CH_4 conversion, H_2 generation, and CO generation and reduces the production of CO_2 (Figure 7.3). The maximum H_2/CO ratio of 2:1 in this route is achieved at a higher temperature than the SMR ratio of 3:1 is. At higher oxygen-to-methane ratios, complete combustion is dominant, which reduces the CO and H_2 yield and increases the generation of H_2O and CO_2. In our analysis, the oxygen-to-methane ratio (O:C) varied between 0.25:1 and 1:1. The complete conversion of oxygen took place during partial oxidation and started to decrease as the O:C ratio approached 2:1. Above the 2:1 ratio, complete combustion occurred, and CO_2 formation was favored over CO. The same trend was evident for H_2 at higher O:C ratios, favoring H_2O production rather than H_2. Due to the exothermic nature of this reaction, a higher O:C ratio increased the energy output (Figure 7.3). Solid carbon formation was suppressed by increasing the O:C ratio, enabling the reactor to operate at a relatively low temperature. To maintain the syngas ratio above 2:15, this study used WGS to increase hydrogen composition.[5] The syngas was first heated to 572 °C with co-fed steam to WGS. The steam flow rate was manipulated to adjust the syngas ratio to the desired value of 2.15.

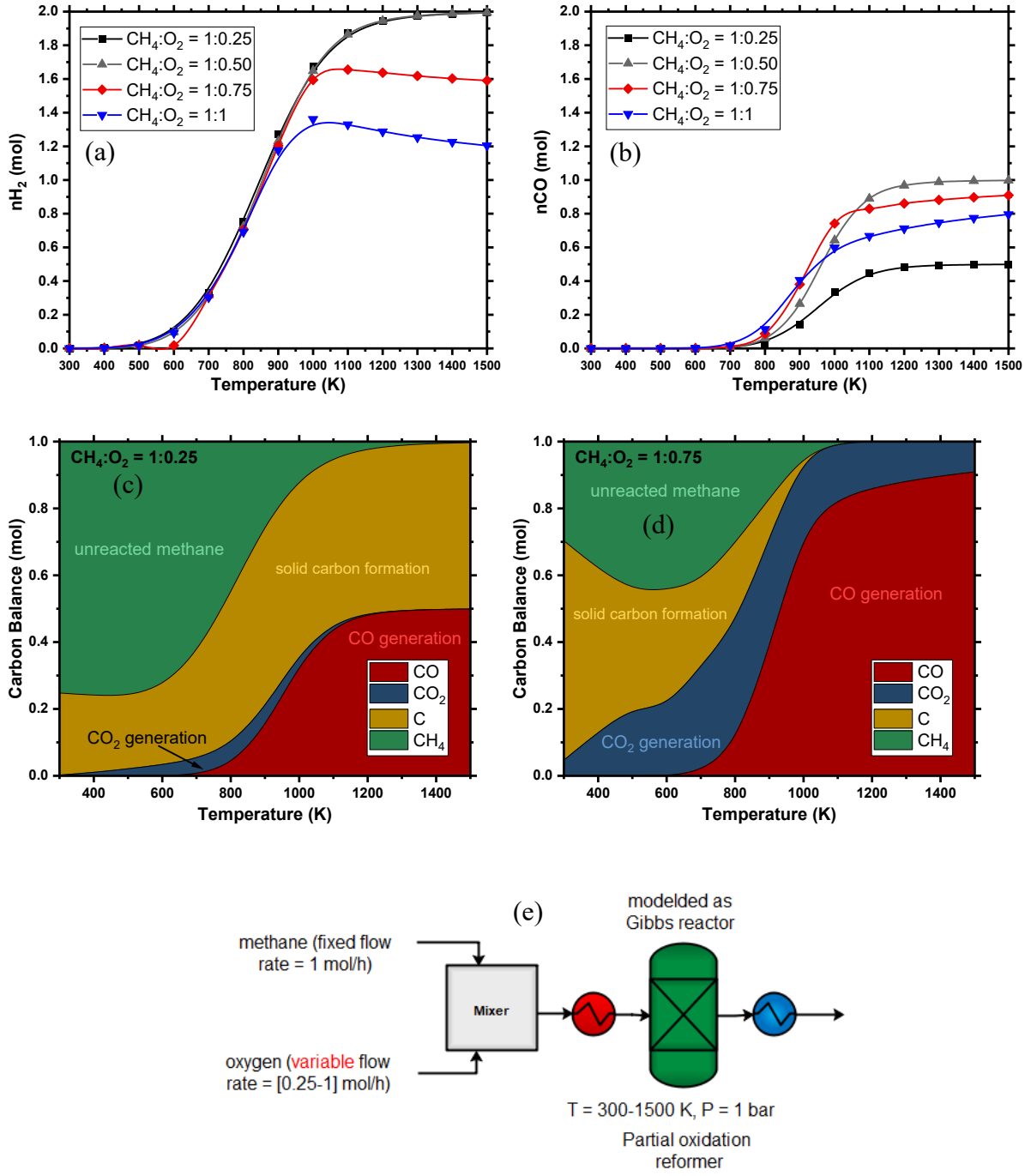

Figure 7.3. Effects of CH_4:O_2 ratio on conversion, syngas yield waste production, energy input, and carbon deposition in POX (P = 1 bar).

7.5.1.3 DRM

The conversion of CH_4 and CO_2 were assessed over a wide range of temperatures between 300 and 1,500 K (Figure 7.4). A narrower temperature range has been already studied by Nematollahi et al.[28] The conversion of CH_4 and CO_2 increased as the temperature increased. In the DRM process, the generation of hydrogen and carbon monoxide is favored at high temperatures, similar to the SMR and POX processes (Figure 7.4). The significant difference in this process is that the H_2/CO ratio is lower than that of the other reforming technologies (close to 1:1) at an initial feed ratio of CH_4:CO_2 = 1. As the ratio starts to increase (CH_4:CO_2), the ratio of syngas (H_2:CO) decreases, reaching a minimum (close to 1:0.2) at CH_4:CO_2 = 1:5. Higher temperatures help to suppress carbon formation (Figure 7.4 c and d). This is consistent with previous studies on Gibbs minimization free energy methods.[21,50] Increasing the temperature increases the hydrogen yield in low syngas ratios, whereas it exhibits a slight rise followed by a decreasing trend at higher syngas ratios. As in SMR and POX, increasing the oxidizer (H_2O, O_2, or CO_2) increases the conversion of CH_4. SMR and DRM have opposite trends with respect to H_2 and CO generation; with more CO_2 in the feed, CO generation increases while H_2 generation decreases. The carbon monoxide domination described by the endothermic RWGS (Eq. 9), which increases CO_2 in the feed, may intensify the RWGS, resulting in partial consumption of the hydrogen. Although the amount of carbon dioxide increases in the reactor outlet with the increasing CH_4:CO_2 ratio of the feed, the discrepancy among the weight of CO_2 percentage in the feed and yield decreases. The limitation of the syngas ratio allows the reformer to operate in a parallel combination of DRM with SMR or DRM with POX. A higher syngas ratio can be achieved by operating the reformer at higher temperatures (>1,373 K).

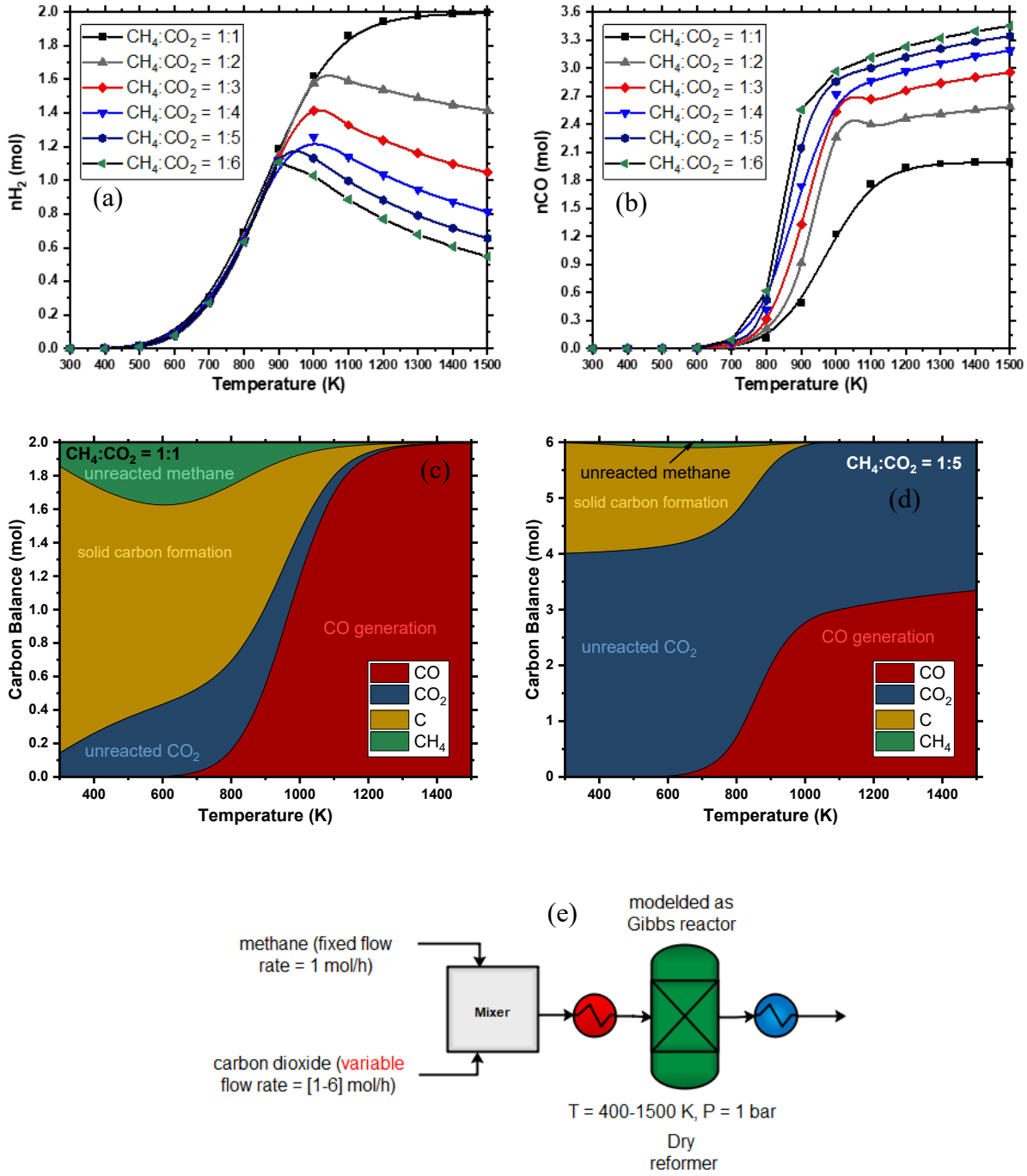

Figure 7.4. Effects of CH_4:CO_2 ratio on conversion, syngas yield, CO_2 generation, and carbon deposition in DRM (P = 1 bar).

7.5.1.4 ATR

Figure 7.5 shows the effect of adding different H_2O:O_2 ratios to the ATR reformer and the effect on the yield of the reactor (H_2, CO, and energy load). In an autothermal reformer, a higher S:C ratio can operate at 0.6–0.9, which allows ATR to produce a higher H_2/CO ratio than does POX. Various scenarios were executed in Aspen to determine the effect of adding an oxidizer (H_2O or O_2) to ATR (Figure 7.5). It was noted that the addition of H_2O or O_2 increases the conversion of methane in different H_2 and CO yield ratios. The partial oxidation reaction was more favorable than SMR was because of the more exothermic nature of this reaction, which explains the effect on O_2 conversion. The addition of an O_2 oxidizer increased the amount of CO, and the addition of H_2O increased the amount of H_2 produced. The enrichment of hydrogen at higher H_2O:O_2 ratios is expressed by the WGS (Eq. 2). The addition of oxygen may increase the exothermicity of the reaction in most cases; this addition of O_2 reaches maximum exothermicity when it is executed at higher O_2:H_2O ratios (similar to the operating conditions of POX).

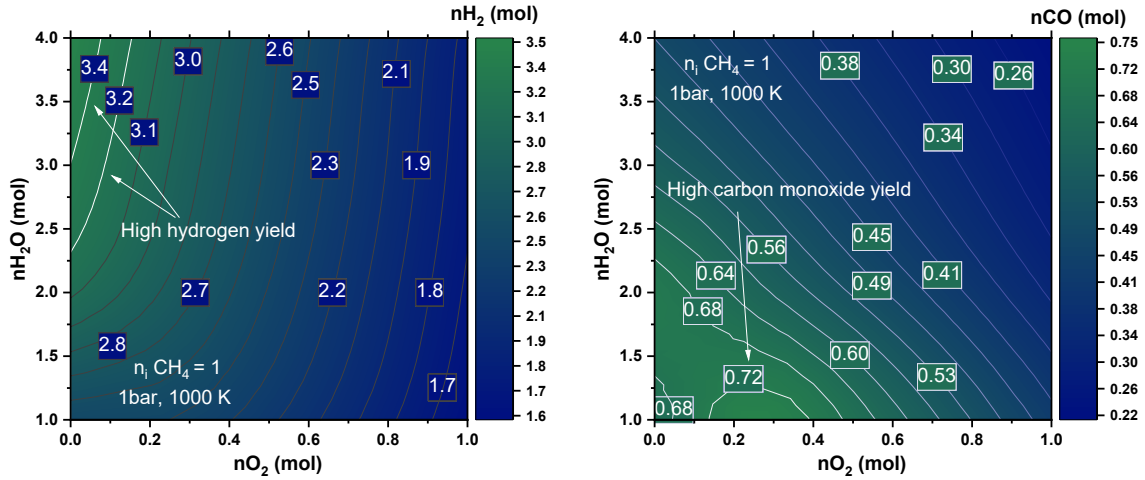

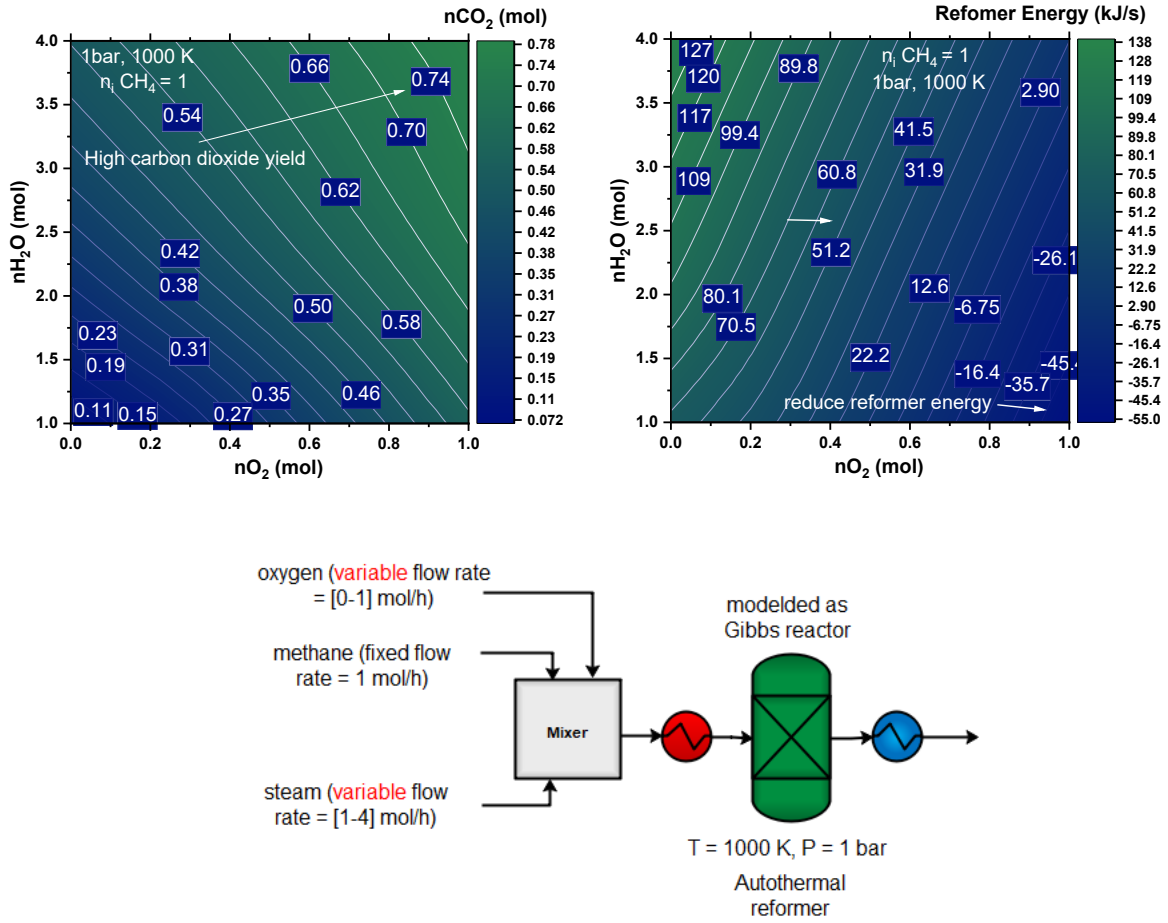

Figure 7.5. Effects of CH_4:O_2 ratio on conversion, syngas yield waste production, energy input, and carbon deposition in POX (P = 1 bar).

7.5.1.5 CR

Synergistically combining the benefits of the three reforming processes results in significant carbon dioxide conversion with a low energy requirement when this process is integrated with an MTO plant.[4,5] Combining the reforming technologies of SMR, DRM, and POX in one reactor may yield benefits by increasing the advantages and reducing the drawbacks of each technology.[4,23] The feed of oxidants (CO_2, H_2O, O_2) can be combined in a single reformer CR or implemented in individual reformers (parallel reforming), after which their outputs can be combined. Because methanol requires a 1:2 stoichiometric ratio of CO to H_2 and the excess

hydrogen produced from SMR, CO_2 is injected to react with methane through DRM (Eq. 6). The overall reaction of the process can be achieved by combining the individual reactions (Eqs. 1 and 6), and this is then multiplied by a coefficient that ultimately yields the desired product (methanol). The combination of SMR and DRM that should produce the 1:2 stoichiometric ratio of CO to H_2 is as follows:

$$3CH_4 + 2H_2O + CO_2 \rightarrow 4CO + 8H_2 \rightarrow 4CH_3OH \quad (14)$$

In addition to the combination of SMR and DRM, O_2 was added to the reformer to use the energy released from the incomplete reaction of methane in the POX reactor (Eqs. 3, 4, and 5).[51] The addition of O_2 to the feed increased CH_4 conversion, especially at a temperature below 1,100 K (Figure 7.6 c and d) because CH_4 became a limiting reactant and was consumed by both POX and DRM. The addition of O_2 increased CH_4 conversion, but it also reduced CO_2 conversion, as shown in Figure 7.6 (c and d) due to the reaction of methane oxidation, which hindered the DRM reaction (Eq. 6). The combination of SMR and DRM achieved a syngas ratio of 2.25 (Figure 6 a), whereas a combination of POX, SMR, and DRM generated a 1.5 syngas ratio (Figure 7.6 b). The presence of O_2 in the combined reformer was shown to increase conversion of CH_4 and CO_2.[28] Song reported catalytic tri-reforming of methane achieved high conversion (>97%) and high CO_2 conversion (roughly 80%) to produce syngas with H_2:CO = 1.5–2.0 over a Ni catalyst at 1,130–1,273 K and 1 bar without carbon formation on the catalyst.[22] Water formation increased as more O_2 was added to this process, implying that with the addition of high quantities of O_2, CH_4 tends to convert into H_2O and CO_2 instead of CO and H_2. The addition of O_2 reduced the ratio of H_2:CO at low temperature due to the influence of POX reactions (Eq. 3) and RWGS (Eq. 9), whereas at a higher temperature, the syngas ratio was dictated by DRM (Eq. 6).[52] Increasing O_2 content caused a considerable decrease in CO_2 conversion due to the predominance of the reaction of CH_4 total

combustion (Eq. 5), which formed CO_2 and H_2O.[53] However, carbon formation was reduced to a minimum at 1,000 K when O_2 was added compared to the formation in the cases of DRM and SMR (Figure 7.6 c and d). In this combined reactor was demonstrated the competition of the two oxidants (O_2 and CO_2) to be the oxidant agent for CH_4, showing that O_2 was consumed in all conditions, whereas CO_2 conversion depended on temperature and the addition of O_2. Overall, the optimal condition of this section was based on the maximization of CH_4 conversion and the production of a suitable H_2/CO ratio for methanol synthesis. This comparison illustrates the importance of studying the reforming network configuration to optimize the interlink parameters. Coupling POX with SMR and DRM can facilitate heat transfer between endothermic and exothermic reactions.

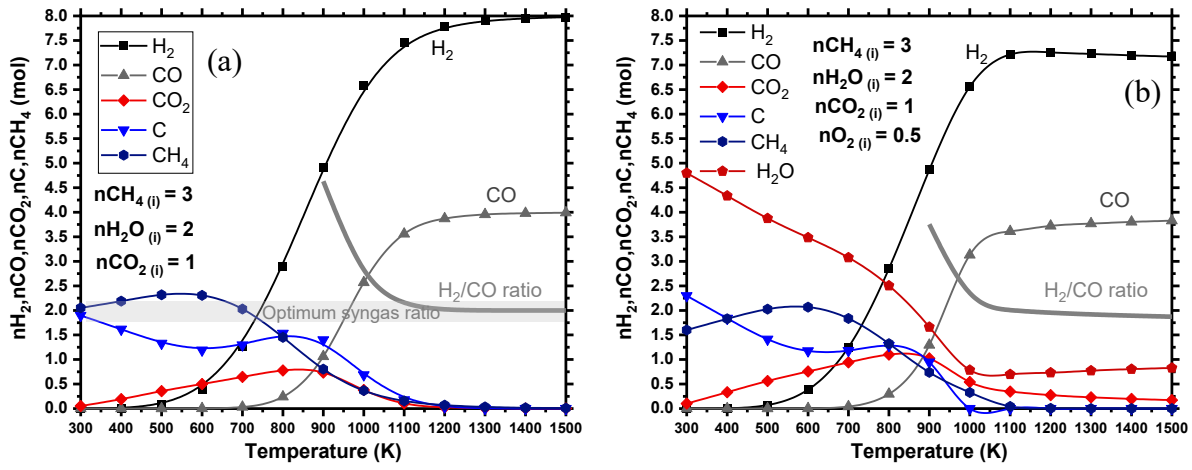

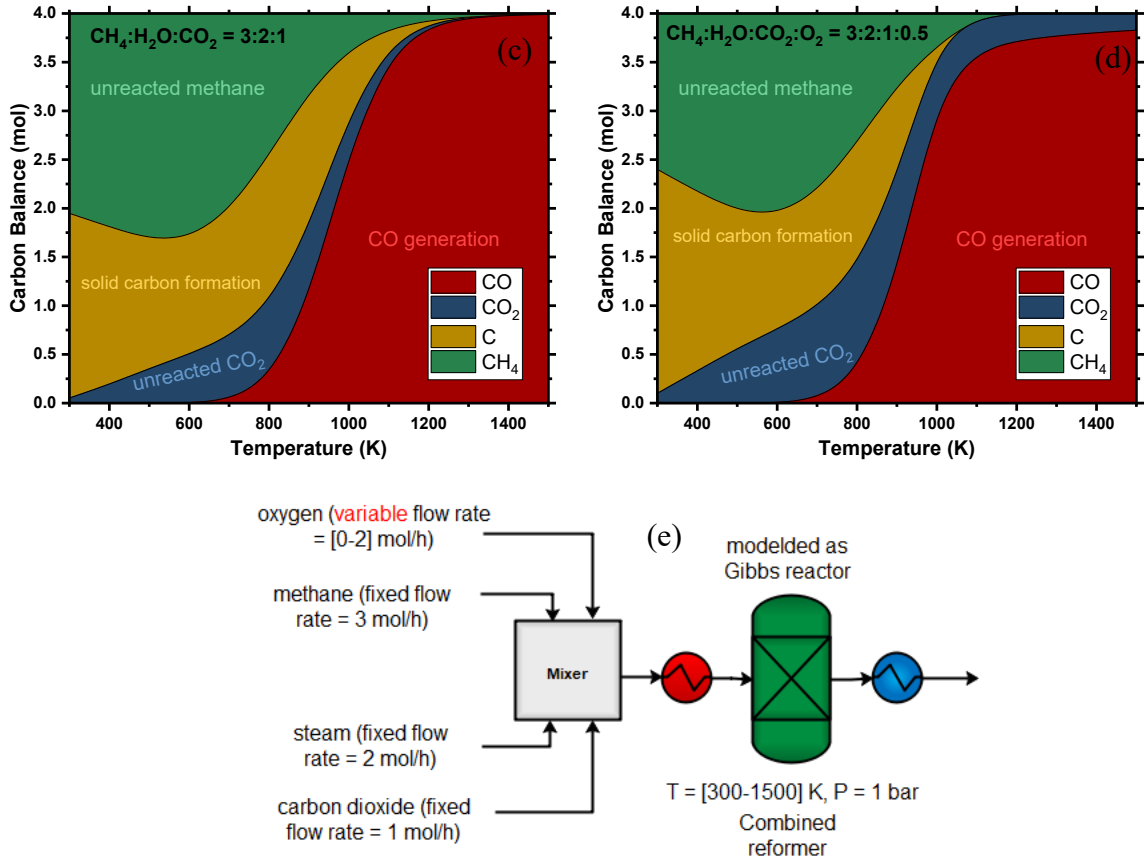

Figure 7.6. Effects of CH_4:O_2 ratio on conversion, syngas yield, energy input, and carbon deposition in POX (P = 1 bar).

7.5.1.6 Methanol Production

The effect of reactor temperature, pressure, and the stoichiometric ratio of reactants on the methanol yield in the method described in this section is shown in Figure 7.7. For modeling and optimization purposes, reaction conditions of 210–270 °C and 1 bar were used.

The amount of methanol produced increased with temperature and reached a maximum of approximately 923–973 K. Methanol can be produced from syngas (CO, H_2, and CO_2) at lower temperatures. An analysis was conducted using an RGIBBS reactor to study the influence of a feed composition of CO_2 and CO with a constant H_2 feed on the methanol yield to optimize methanol synthesis for the optimal combination of syngas feeds. The CO_2 hydrogenation of methanol and

the RWGS reaction were found to be acting competitively. Methanol synthesis is an exothermic reaction and RWGS is endothermic, and RWGS dominated the process at higher temperatures. By increasing the pressure, CO selectivity decreased while methanol selectivity increased. This resulted in CO hydrogenation of methanol being more favorable than CO_2 hydrogenation. Methanol yield increased with increasing CO concentration in the feed, which decreased the selectivity of forming CO from RWGS due to the presence of CO in the feed. Due to the low equilibrium conversion to methanol, the recycling of syngas is necessary. As Figure 7.7 illustrates, CO_2 conversion decreased with the addition of CO and even became negative at high CO concentrations. This was due to the WGS reaction, which produced additional CO_2 in the presence of CO. H_2 conversion increased with increases in the addition of CO.

Figure 7.7 (c) shows the two reformers and methanol synthesis reactors that were placed in a series. The effect of varying reformer inlet conditions on the outlet of the methanol reactor was analyzed. The initial feed ratios of methane, water, and carbon dioxide were similar to the ratio that was used in the combined reformer in Figure 7.6 (a and b). The results of using these ratios are presented in Figure 7.7 (c and d). As shown in Figure 7.7, a maximum of 2.1 moles of methanol was achieved at 373 K and 30 bar. A similar yield was obtained by the trade-off between pressure and temperature.

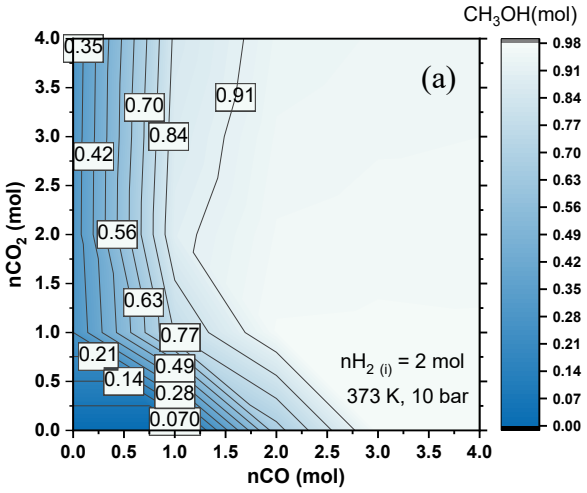
CH3OH(mol)
(a)
nH2 (i) = 2 mol
373 K, 10 bar
nCO2 (mol)
nCO (mol)
0.35
0.42
0.56
0.63
0.70
0.77
0.84
0.91
0.21
0.14
0.49
0.28
0.070

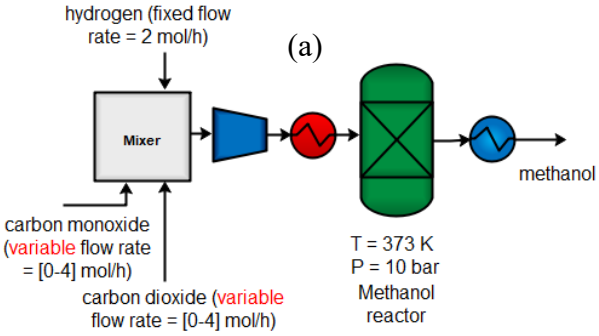
hydrogen (fixed flow rate = 2 mol/h)
(a)
Mixer
methanol
carbon monoxide (variable flow rate = [0-4] mol/h)
carbon dioxide (variable flow rate = [0-4] mol/h)
T = 373 K
P = 10 bar
Methanol reactor

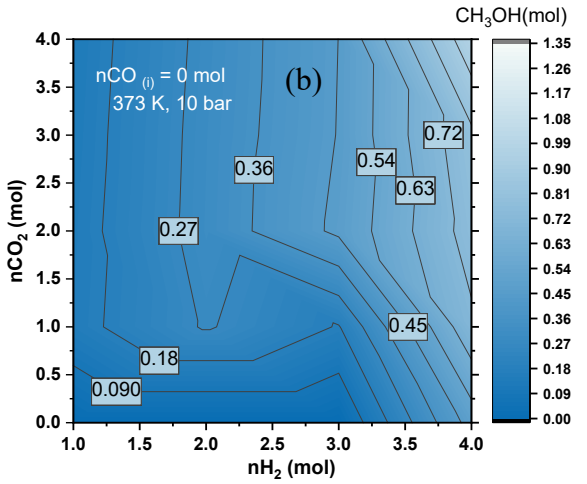
CH3OH(mol)
nCO (i) = 0 mol
373 K, 10 bar
(b)
nCO2 (mol)
nH2 (mol)
0.72
0.54
0.36
0.63
0.27
0.45
0.18
0.090

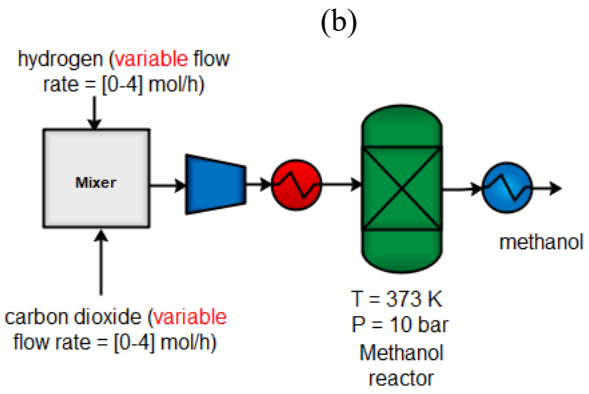
(b)
hydrogen (variable flow rate = [0-4] mol/h)
Mixer
methanol
carbon dioxide (variable flow rate = [0-4] mol/h)
T = 373 K
P = 10 bar
Methanol reactor

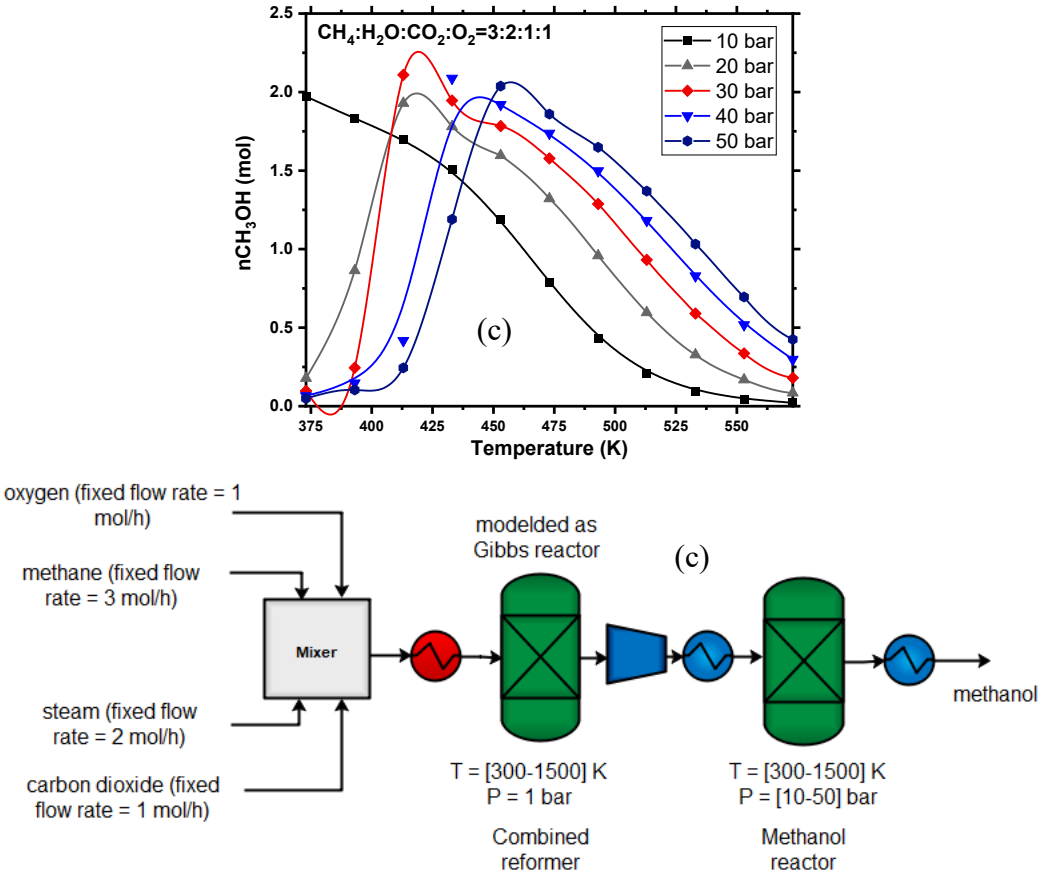

Figure 7.7. (a) Effects of varying the CO:CO_2 ratio with fixed H_2 (nH_2 = 2 mol) feed on the conversion of syngas to produce methanol at 373 K and 10 bar (b) effect if varying both CO and H_2 in the reactor feed without CO_2 as a co-feed at 373 K and 10 bar; (c) the same outlet composition obtained from the CR was used as a feed for methanol reactor.

7.5.2 Material and Energy Balances

All three of the process designs discussed in the previous section were assessed for material and energy balances, with results presented in Figure 7.8. The operating energy at different syngas ratios of the SMR, DRM, and POX reformers is shown in Figure 7.8. The external heat input for each recovery was calculated from the reactor energy balance. A positive $H_{External}$ means that the reactor is endothermic and needs heat, and a negative $H_{External}$ means that the reactor is exothermic and that heat must be removed. In this process, the highest demand for energy was from the SMR, followed by DRM, and then the POX reactor. The energy of SMR indicated an increased use of steam to obtain a higher syngas ratio, which increased the energy. SMR requires a heat supply and produces syngas with H_2:CO = 1:3, which is a relatively higher ratio than that of methanol synthesis. POX is more economical to heat than SMR is, and the process does not require a catalyst. Additionally, syngas with H_2/CO = 1:2 is produced, which is ideal for methanol synthesis. The results indicate that POX and ATR have higher efficiency than SMR in terms of energy usage. However, POX requires high-purity O_2, which requires an air separation plant to supply the required O_2. Compared with the high cost of SMR, an ATR reactor is moderately cheap to operate. The ATR process is flexible, allowing for an option of oxygen or steam. However, the process requires extensive operational control to ensure proper robust operations.

The need to have a transformative approach to optimize syngas production has been widely investigated.[4,5,23] Significant energy is lost in the current process in the SMR and DRM reactors due to fuel consumption and low energy recovery. All methods involve high costs and are subject to similar activation mechanisms. The combined reactor integrates SMR, POX, and DRM and has the advantage of performing catalyst deactivation by oxidizing the coke, which increases catalyst life and process efficiency. Thus, CR was chosen for the MTO plant, as illustrated in Figure 7.10.

Integrating SMR and POX with DRM is an encouraging concept whereby the undesired CO_2 generated from the SMR and POX processes is exploited to reform the unreacted methane and achieve autothermal reactions within the integration reactors. In the Aspen flowsheet, a methanol synthesis reactor was modeled using a Continuous stirred-tank reactor (CSTR) with kinetic values obtained from the literature. The methanol produced was then fed into the MTO reactor, which was modeled in this case as three RSTOICH reactors to produce ethylene, propylene, and butene. This split fraction allocated to each reactor was decided on the basis of experimental yields illustrated in Table 7.1.[8,44] Downstream compression and cryogenic energy separation were not included in this study; however, in the conventional cracking process, they result in additional energy loss. Higher ethane conversion can reduce compression and separation load. However, this approach is not practical, owing to reaction limitations and the tendency of ethylene to undergo secondary reactions that form coke on the tubes' inner surfaces.[54]

In MTO, methanol is converted to ethylene, propylene, butene, and water in a set of net-exothermic reactions. MTO offers overall process exothermicity because ethane conversion is not limited by a reaction equilibrium, as is the case with steam cracking (Figure 7.9). However, the low ethylene yield (<20% ethylene) and the considerable ethane by-products require intensive downstream separation and the recycling of the unconverted methane and ethane.[55,56] Figure 7.8 shows a section-wise comparison of energy consumption. The simulation indicates that the energy demand is higher for steam cracking than for MTO. It should be noted that both MTO and steam cracking processes require intensive separation and coproduce propylene and butene. These coproducts can either be credited to the process as fuels or purified and sold as by-products.

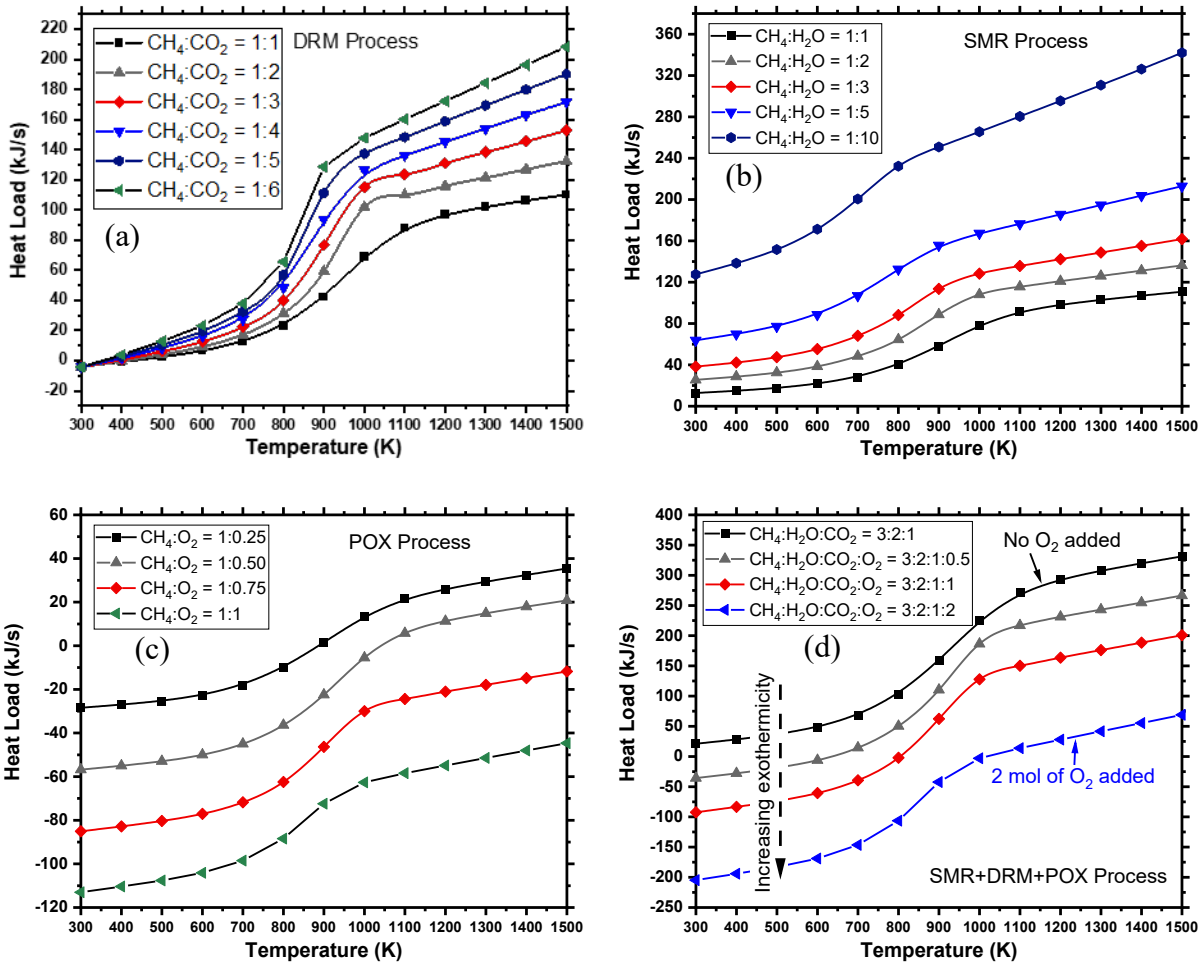

Figure 7.8. Energy input for syngas production from various routes: (a) DRM, (b) SMR, (c) (POX), and (d) CR.

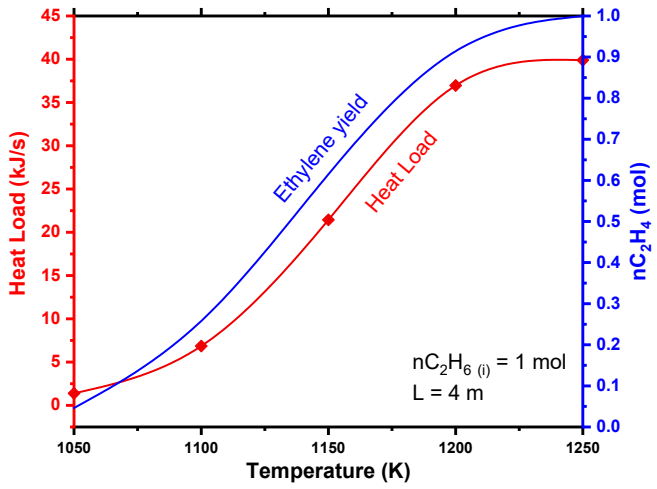

Figure 7.9. Energy input for ethane steam cracking.

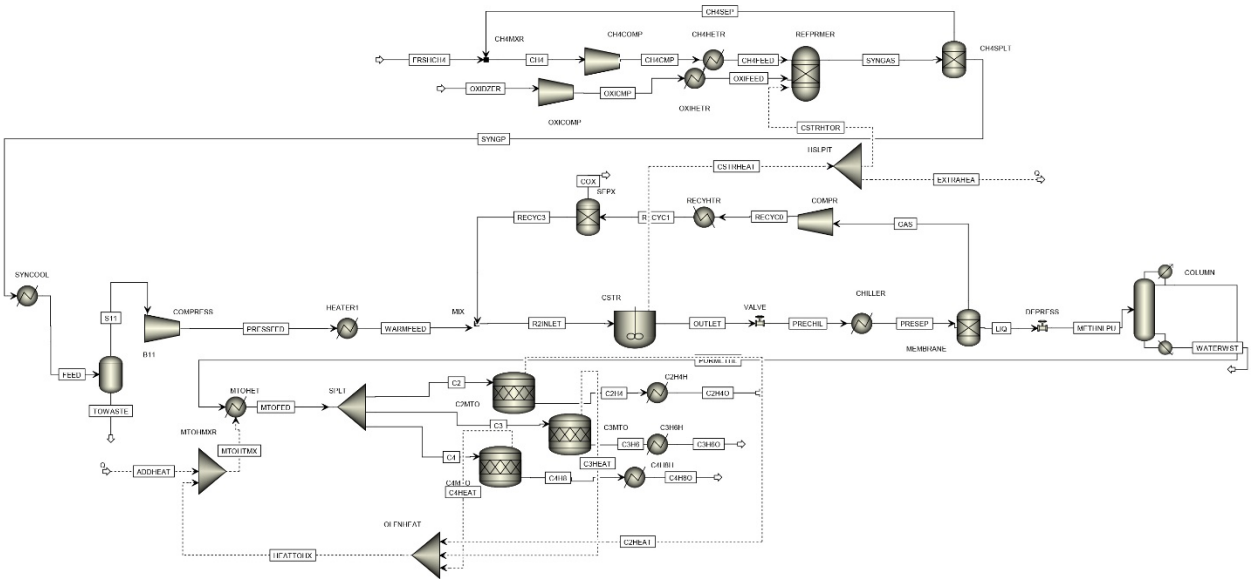

Figure 7.10. Proposed methane-to-olefin design process flow sheet.

7.5.3 Economic Evaluation

The olefin plant economics were estimated on the basis of the assumption of 330 operating days per year, a tax rate of 30%, and a 10-year linear depreciation scheme to calculate the annualized fixed cost.[57,58] The selling price for ethylene was set at \$1,200/ton, and for the propylene by-product, the price was \$1,340/ton. The feedstock market and product prices are listed in Table 7.2. The products ethylene and propylene were assumed to be sold from the plant gate and did not include the costs of transportation to end-users. Annual operating cost (*AOC*) included operating and maintenance costs for steam (C_{steam}), solvent, refrigerant (C_{refri}), cooling/boiling water (C_{water}), and electricity ($C_{electric}$), as given by the following equation:

$$AOC = \sum_{\mathrm{LPS,MPS}} C_{steam} + \sum_{\mathrm{CW,BW}} C_{water} + \sum_{\mathrm{MDEA}} C_{solvent} + C_{electric} + C_{refri} \qquad (15)$$

The total capital investment (*TCI*) was estimated using the six-tenths rule based on data obtained for methanol and olefin plants. The profitability of each process was estimated using a return on investment (*ROI*) equation, as follows:

$$ROI = \frac{(Annual\ incomes - Operating\ costs - Annualized\ fixed\ cost) \times (1 - tax\ rate) + \text{Annualized fixed cost}}{TCI} \quad (16)$$

The cost of shale gas was assumed to be \$3.50/kscf. The lifetime of the catalysts was not considered as part of the operating cost estimation.

Table 7.2. Cost parameters for the economic evaluation of the process.

Item	Best value
Shale gas	\$5.6/MMbtu
Ethane	\$0.50/gal
Ethylene	\$1,200/ton
Propane	\$1.00/gal
Butene	\$1.60/gal
Hydrogen	\$1.76/kg
Propylene	\$1,340/ton
Electricity	\$0.07/kWh

Based on the simulation results, capital costs and variable operating costs of most of the process equipment (i.e., reactors, flash tanks, and distillation columns) in addition to fixed operating costs for the plant (i.e., labor, insurance, and maintenance) were estimated using Aspen Process Economic Analyzer. Vacuum pumps are not standard simulation blocks in Aspen, and thus, they were analyzed separately. Feedstock and utilities were assumed to be available at the prices listed in Table 7.3. The total capital and operating costs for the process are presented in Table 7.4. For a base case plant size that is capable of processing 1,000 ton/yr^{-1} of methane, the total installed equipment costs were \$16.4 million.

Table 7.3. Process utilities and feedstock prices.

Methane purchase price ($ kscf^{-1})[59]	3.5
Grade 1 refrigerant	2.74×10^{-6}
Cooling water ($ kg^{-1})[a]	3.08×10^{-5}
Steam, 100 PSI ($ kg^{-1})[a]	0.0179
Fired heater, 1273K ($ kJ^{-1})[a]	4.2×10^{-6}
Electricity ($ kg^{-1})[a]	0.0775

[a] Estimated using Aspen Process Economic Analyzer

Table 7.4. Total capital and operating costs for the methane-to-olefin plant.

Total Capital Cost [$MM]	17.54
Total Operating Cost [$MM/Year]	55.31
Total Raw Materials Cost [$MM/Year]	7.23
Total Utility Cost [$MM/Year]	4.92
Desired Rate of Return [Percent/Year]	20
Equipment Cost [$MM]	6.76
Total Installed Cost [$MM]	9.50

7.5.4 Energy Integration

The heat integration of each process design was investigated using Aspen Energy Analyzer. Thermal pinch analysis was performed on the base case to identify the recovery of heat within the process streams. Pinch analysis is a heat exchanger network (HEN) optimization algorithm that can be used to reduce the energy consumption in a process by setting feasible energy targets to be achieved by the optimization of the heat recovery systems, methods of energy supply, and process conditions for a reduction in energy.[60] The composite curve is achieved by summing all the heat loads over a range of temperatures. The composite curve is presented in Figure 7.11. The process had several heating and cooling duties. The heat exchanger took inlet stream and heated it to 1,000

K before it entered the CR reactor. The heat recovery exchangers cooled the syngas mixture stream from the CR reactor to 323 K and then compressed the mixture to a pressure of 40 bar. The condensed liquid was separated from the syngas stream in the flash column, and then the gas stream was heated again in the methanol heat exchanger to 543 K before the stream entered the methanol reactor. The product outlet was then sent to cool exchangers to cool them to 323 K. The heat load for each of the types of equipment used in the process flow sheet is shown in Figure 7.5. It was determined that the operating energy of this process can be reduced by using heat integration. The minimum hot and cold utility requirements were 153 kJ/s and 12,230 kJ/s, respectively. High values of hot utility were due to the large heating requirement of the fired heater and reboiler. The high cold utility was due to the reactor effluent cooler and condenser. There was potential for heat exchange in the temperature range of 273–1,000 K. Therefore, the composite curve could be further optimized for the heat exchanger network to provide the lowest energy consumption for the external utilities. Given these high energy values for the utilities, an integrated case was developed to reduce the energy consumption from external sources by utilizing some of the process heat. For this modification, the combined reactor effluent cooling duty was reduced. The syngas leaving the reformer had a hot stream that could serve as effective heat recovery.

Figure 7.11 (c) shows the grand composite curve that was developed in the process. The analysis shows that the target values can be reduced to minimal values. Cooling utilities can be reduced by 39.3%, and the 98.5% heating requirement can be reduced by 95%. Such reductions in energy requirements have the potential to provide savings equivalent to MM$2.79/year (Figure 7.13 and Table 7.6).

In addition to the heat exchange network, which is illustrated in Figure 11 (b), the methanol reactor has the potential for mass and heat integration with a methane reformer reactor.[24] The heat

released from the exothermic methanol reactor can partially supply the heat required for the endothermic methane-reforming reaction (Figure 7.11). Another integration is to release heat from the MTO reactor, a strategy which can be applied to the MTO feed heat exchanger.

Table 7.5. Heat load for methane-to-olefin design process flow sheet.

Equipment	Heat Load	Unit
COMPR	522.2	kWh
COMPRESS	5968	
OXIHETR	12.22	
CH4HETR	7.29	
RECYHTR	0.11	
C3H6H	4.00	
HEATER1	9.56	MMBtu
SYNCOOL	15.81	
C2H4H	6.10	
C4H8H	1.01	
CHILLER	14.36	

Table 7.6. Impact of heat integration on operations of the methane-to-olefin plant.

	Current [kJ/s]	Target [kJ/s]	Saving Potential [kJ/s]	Energy Cost Savings [$/Yr]	Energy Cost Savings [%]	ΔT_{min} [K]
LP Steam	4,442	0	4,442	266,340	100.00	10.0
Fired Heater	5,752	153.4	5,599	750,922	97.33	25.0
Total Hot Utilities	1.02×10^4	153.4	1.00×10^4	1,017,263	98.02	-
Cooling Water	4,155	1.22×10^4	−8,043	−53,808	−193.56	5.0
Refrigerant	1.99×10^4	29.87	1.99×10^4	1,724,930	99.85	3.0
Total Cold Utilities	2.41×10^4	1.22×10^4	1.19×10^4	1,671,122	95.20	-

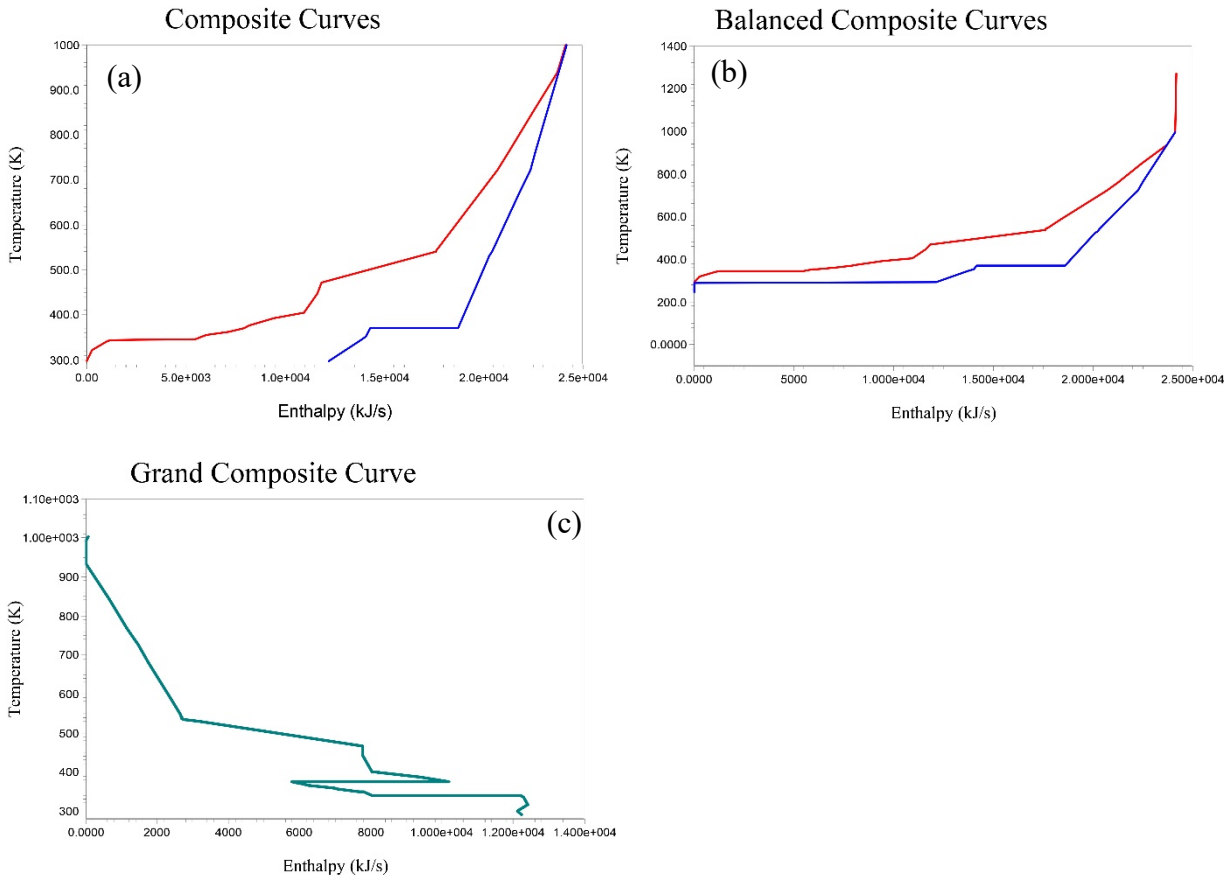

Figure 7.11. Temperature−enthalpy change diagram for (a) the baseline and (b) integrated approaches and (c) the grand composite curve for heat integration of the methane-to-olefin plant.

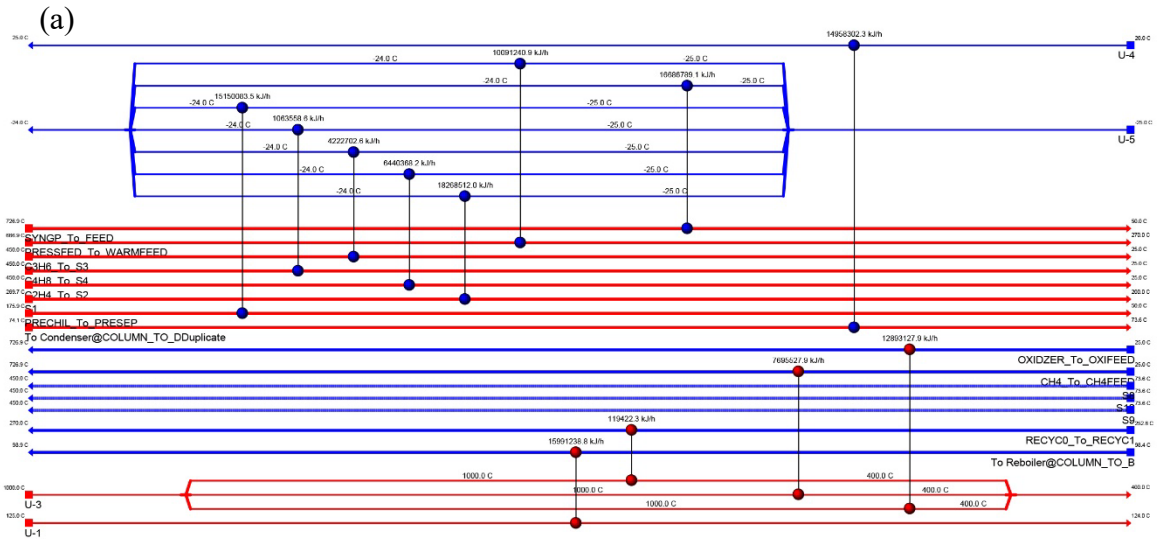

(b)

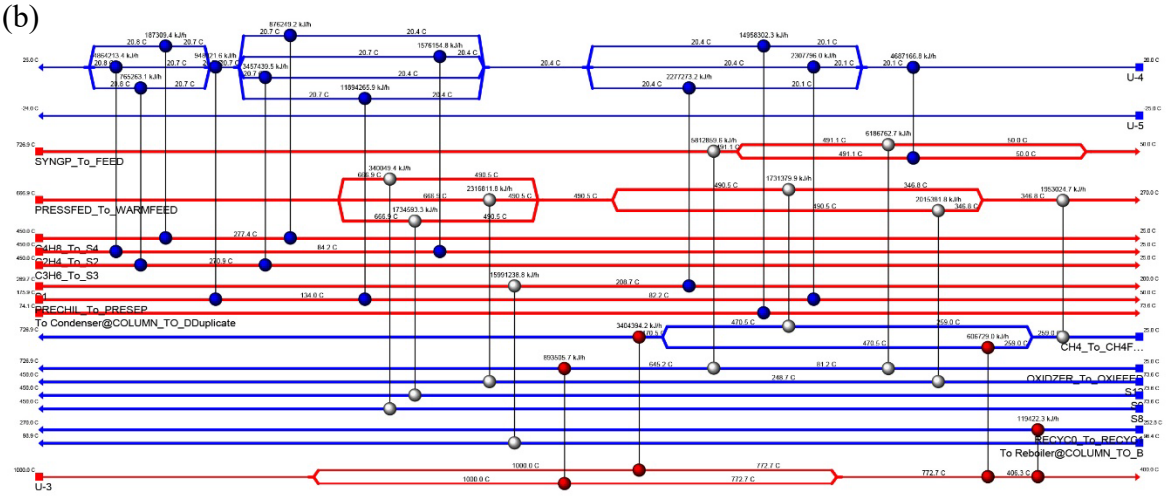

Figure 7.12. Heat exchanger network (HEN) diagram obtained using ASPEN Energy Analyzer, where red lines show hot streams and blue lines show cold streams for (a) the baseline and (b) the proposed heat integration network.

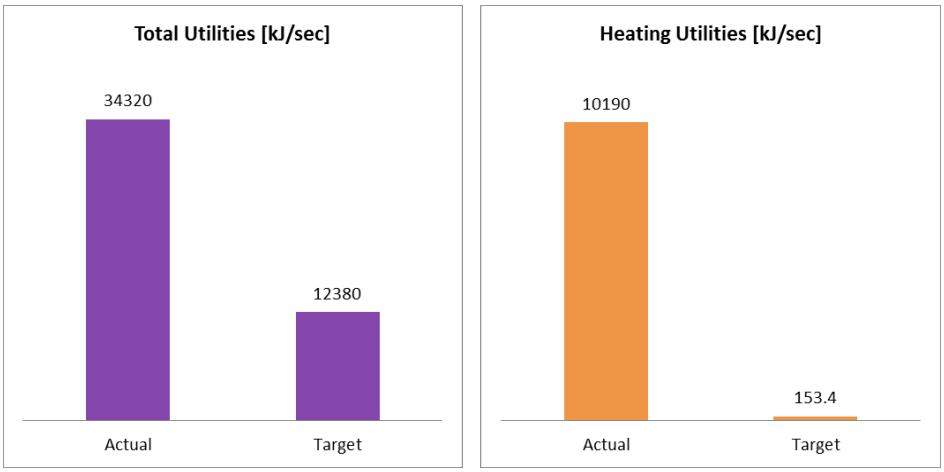

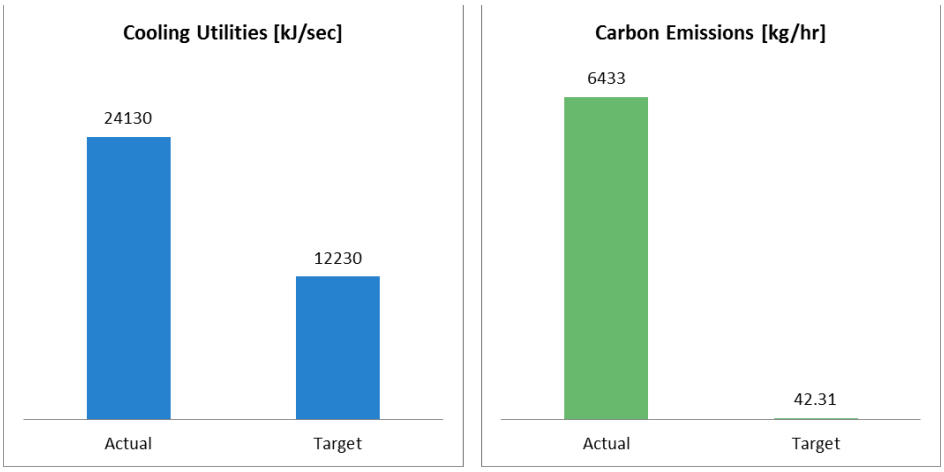

Figure 7.13. Effect of energy integration on heating and cooling requirements and carbon emissions.

7.5.5 Environmental Impact

CO_2 emissions were analyzed in order to determine the effect on the atmosphere of each operation. Based on actual CO_2 emissions and energy-related emissions, the carbon emissions were calculated. CO_2 emissions can be directly generated by burning fuels. The CO_2 equivalent of outlet streams was obtained from Aspen Plus simulations, whereas CO_2 emissions from the consumption of electricity were calculated using a factor of 0.73 MT of CO_2/MW.[8] Emissions from heating utilities were estimated using the Environmental Protection Agency's energy calculation method of stationary combustion.[61] The resulting CO_2 emissions of the process were determined to be 6,433 kg/h. Combining DRM and SMR can produce syngas with H_2:CO close to a ratio of 2:1, resulting in minimal CO_2 emissions. The analysis revealed the differences in the environmental impact after applying energy integration resulted in a CO_2 reduction from 6,433 to 43.2 kg/h.

7.6 Conclusion

Technical analyses for ethylene, propylene, and other products produced from methane were presented. Four reforming technologies were analyzed to produce syngas: POX, SMR, ATR, and CR. Of all the cases considered in this study, we found the case of using CR and MTO to be the most promising route to produce ethylene with low energy demand and CO_2 emissions. There is a >50% reduction in the energy consumption for the proposed route compared with the conventional reforming units. Aspen Plus was used to assess the performance of each option. Thermodynamically, the equilibrium conversion of CH_4, CO_2, and O_2 was preferred between 700 and 1,100 K. The highest yield of H_2 was obtained at CH_4/CO_2 and CH_4/O_2 ratios of 1.0 and 4.0, respectively, and a temperature of 1,100 K. The results show that POX and ATR have higher efficiency than SMR does in terms of energy usage. The impact of each process on the carbon footprint was evaluated, and the overall CO_2 emissions for a specific H_2/CO ratio were compared. The comparisons indicate that DRM has a negative carbon footprint at a low syngas ratio of 1 and below and more carbon emissions can be reduced through integrating heating and cooling utilities, resulting in a CO_2 from 6,433 to 43.2 kg/h.

7.7 References

1. *World Energy Outlook 2019*. (OECD, 2019). doi:10.1787/caf32f3b-en
2. York, A. P. E., Xiao, T., Green, M. L. H. & Claridge, J. B. Methane Oxyforming for Synthesis Gas Production. *Catal. Rev.* **49**, 511–560 (2007).
3. Martinez-Gomez, J. *et al.* Involving economic, environmental and safety issues in the optimal purification of biobutanol. *Process Saf. Environ. Prot.* **103**, 365–376 (2016).
4. Noureldin, M. M. B., Elbashir, N. O., Gabriel, K. J. & El-Halwagi, M. M. A process integration approach to the assessment of CO2 fixation through dry reforming. *ACS Sustain. Chem. Eng.* **3**, 625–636 (2015).
5. Gabriel, K. J. *et al.* Targeting of the water-energy nexus in gas-to-liquid processes: A comparison of syngas technologies. *Ind. Eng. Chem. Res.* **53**, 7087–7102 (2014).
6. Ehlinger, V. M., Gabriel, K. J., Noureldin, M. M. B. & El-Halwagi, M. M. Process design and integration of shale gas to methanol. *ACS Sustain. Chem. Eng.* **2**, 30–37 (2014).
7. Julián-Durán, L. M., Ortiz-Espinoza, A. P., El-Halwagi, M. M. & Jiménez-Gutiérrez, A. Techno-economic assessment and environmental impact of shale gas alternatives to methanol. *ACS Sustain. Chem. Eng.* **2**, 2338–2344 (2014).
8. Ortiz-Espinoza, A. P., Noureldin, M. M. B., El-Halwagi, M. M. & Jiménez-Gutiérrez, A. Design, simulation and techno-economic analysis of two processes for the conversion of shale gas to ethylene. *Comput. Chem. Eng.* **107**, 237–246 (2017).
9. Jasper, S. & El-Halwagi, M. A techno-economic comparison between two methanol-to-propylene processes. *Processes* **3**, 684–698 (2015).
10. Pérez-Uresti, S. I., Adrián-Mendiola, J. M., El-Halwagi, M. M. & Jiménez-Gutiérrez, A. Techno-economic assessment of benzene production from shale gas. *Processes* **5**, 33

(2017).

11. Bao, B., El-Halwagi, M. M. & Elbashir, N. O. Simulation, integration, and economic analysis of gas-to-liquid processes. *Fuel Process. Technol.* **91**, 703–713 (2010).

12. An, Y. *et al.* Advances in direct production of value-added chemicals via syngas conversion. *Sci. China Chem.* **60**, 887–903 (2017).

13. Guo, X. *et al.* Direct, nonoxidative conversion of methane to ethylene, aromatics, and hydrogen. *Science (80-.).* **344**, 616–619 (2014).

14. He, C. & You, F. Toward more cost-effective and greener chemicals production from shale gas by integrating with bioethanol dehydration: Novel process design and simulation-based optimization. *AIChE J.* **61**, 1209–1232 (2015).

15. Bao, J., Yang, G., Yoneyama, Y. & Tsubaki, N. Significant Advances in C1 Catalysis: Highly Efficient Catalysts and Catalytic Reactions. *ACS Catal.* **9**, 3026–3053 (2019).

16. Spivey, J. J. & Hutchings, G. Catalytic aromatization of methane. *Chem. Soc. Rev.* **43**, 792–803 (2014).

17. Taifan, W. & Baltrusaitis, J. CH 4 conversion to value added products: Potential, limitations and extensions of a single step heterogeneous catalysis. *Appl. Catal. B Environ.* **198**, 525–547 (2016).

18. Cho, W. *et al.* Optimal design and operation of a natural gas tri-reforming reactor for DME synthesis. *Catal. Today* **139**, 261–267 (2009).

19. Kalamaras, C. M. & Efstathiou, A. M. Hydrogen Production Technologies: Current State and Future Developments. *Conf. Pap. Energy* **2013**, 1–9 (2013).

20. Wilhelm, D. J., Simbeck, D. R., Karp, A. D. & Dickenson, R. L. Syngas production for gas-to-liquids applications: Technologies, issues and outlook. *Fuel Process. Technol.* **71**, 139–

148 (2001).

21. Rostrup-Nielsen, J. R. & Bak Hansen, J. H. CO2-reforming of methane over transition metals. *J. Catal.* **144**, 38–49 (1993).

22. Song, C. & Pan, W. Tri-reforming of methane: a novel concept for catalytic production of industrially useful synthesis gas with desired H2/CO ratios. *Catal. Today* **98**, 463–484 (2004).

23. Noureldin, M. M. B., Elbashir, N. O. & El-Halwagi, M. M. Optimization and Selection of Reforming Approaches for Syngas Generation from Natural/Shale Gas. *Ind. Eng. Chem. Res.* **53**, 1841–1855 (2014).

24. Godini, H. R. *et al.* Techno-economic analysis of integrating the methane oxidative coupling and methane reforming processes. *Fuel Process. Technol.* **106**, 684–694 (2013).

25. Martinez-Gomez, J., Nápoles-Rivera, F., Ponce-Ortega, J. M. & El-Halwagi, M. M. Optimization of the production of syngas from shale gas with economic and safety considerations. *Appl. Therm. Eng.* **110**, 678–685 (2017).

26. Niziolek, A. M., Onel, O. & Floudas, C. A. Production of Benzene, Toluene, and the Xylenes from Natural Gas via Methanol. *Comput. Aided Chem. Eng.* **38**, 2349–2354 (2016).

27. He, C. & You, F. Shale gas processing integrated with ethylene production: Novel process designs, exergy analysis, and techno-economic analysis. *Ind. Eng. Chem. Res.* **53**, 11442–11459 (2014).

28. Nematollahi, B., Rezaei, M. & Khajenoori, M. Combined dry reforming and partial oxidation of methane to synthesis gas on noble metal catalysts. *Int. J. Hydrogen Energy* **36**, 2969–2978 (2011).

29. Meissner, H. P., Kusik, C. L. & Dalzell, W. H. Equilibrium composition with multiple

reactions. *Ind. Eng. Chem. Fundam.* **8**, 659–665 (1969).

30. Foust, T. D., Aden, A., Dutta, A. & Phillips, S. An economic and environmental comparison of a biochemical and a thermochemical lignocellulosic ethanol conversion processes. *Cellulose* **16**, 547–565 (2009).

31. Phillips, S., Aden, A., Jechura, J. & Dayton, D. *Thermochemical ethanol via indirect gasification and mixed alcohol synthesis of lignocellulosic biomass*. *Ethanol Biofuel Production* (National Renewable Energy Lab.(NREL), Golden, CO (United States), 2010).

32. Asaro, M., Smith, R. M. & Davis, B. H. Gas to Liquid Technologies. in *Encyclopedia of Sustainability Science and Technology* (ed. Meyers, R. A.) 1–48 (Springer New York, 2017). doi:10.1007/978-1-4939-2493-6_72-3

33. Steynberg, A. & Dry, M. *Fischer-Tropsch Technology*. (Elsevier Science, 2004).

34. Aasberg-Petersen, K. *et al.* Natural gas to synthesis gas - Catalysts and catalytic processes. *J. Nat. Gas Sci. Eng.* **3**, 423–459 (2011).

35. Snoeck, J. W., Froment, G. F. & Fowles, M. Steam/CO2 reforming of methane. Carbon filament formation by the Boudouard reaction and gasification by CO2, by H2, and by steam: Kinetic study. *Ind. Eng. Chem. Res.* **41**, 4252–4265 (2002).

36. Tijm, P. J. A., Waller, F. J. & Brown, D. M. Methanol technology developments for the new millennium. *Appl. Catal. A Gen.* **221**, 275–282 (2001).

37. Vanden Bussche, K. M. & Froment, G. F. A steady-state kinetic model for methanol synthesis and the water gas shift reaction on a commercial Cu/ZnO/Al2O3 catalyst. *J. Catal.* **161**, 1–10 (1996).

38. Arora, S. S. & Bhan, A. The critical role of methanol pressure in controlling its transfer dehydrogenation and the corresponding effect on propylene-to-ethylene ratio during

methanol-to-hydrocarbons catalysis on H-ZSM-5. *J. Catal.* **356**, 300–306 (2017).

39. Lee, Y. J., Baek, S. C. & Jun, K. W. Methanol conversion on SAPO-34 catalysts prepared by mixed template method. *Appl. Catal. A Gen.* **329**, 130–136 (2007).

40. Chen, J. Q., Bozzano, A., Glover, B., Fuglerud, T. & Kvisle, S. Recent advancements in ethylene and propylene production using the UOP/Hydro MTO process. *Catal. Today* **106**, 103–107 (2005).

41. Mokrani, T. & Scurrell, M. Gas conversion to liquid fuels and chemicals: The methanol route-catalysis and processes development. *Catal. Rev. - Sci. Eng.* **51**, 1–145 (2009).

42. Onel, O., Niziolek, A. M. & Floudas, C. A. Optimal Production of Light Olefins from Natural Gas via the Methanol Intermediate. *Ind. Eng. Chem. Res.* **55**, 3043–3063 (2016).

43. Khare, R., Millar, D. & Bhan, A. A mechanistic basis for the effects of crystallite size on light olefin selectivity in methanol-to-hydrocarbons conversion on MFI. *J. Catal.* **321**, 23–31 (2015).

44. Vora, B. V. *et al.* Economic route for natural gas conversion to ethylene and propylene. in *Studies in Surface Science and Catalysis* **107**, 87–98 (Elsevier, 1997).

45. Wilson, S. & Barger, P. The characteristics of SAPO-34 which influence the conversion of methanol to light olefins. *Microporous Mesoporous Mater.* **29**, 117–126 (1999).

46. Gao, Y. *et al.* Recent Advances in Intensified Ethylene Production—A Review. *ACS Catal.* **9**, 8592–8621 (2019).

47. Gradassi, M. J. & Wayne Green, N. Economics of natural gas conversion processes. *Fuel Process. Technol.* **42**, 65–83 (1995).

48. Zaman, J. Oxidative processes in natural gas conversion. *Fuel Process. Technol.* **58**, 61–81 (1999).

49. Fogler, H. S. *Essentials of Chemical Reaction Engineering*. *Focus on Catalysts* **2017**, (Pearson Education, 2017).

50. Fan, M. S., Abdullah, A. Z. & Bhatia, S. Catalytic technology for carbon dioxide reforming of methane to synthesis gas. *ChemCatChem* **1**, 192–208 (2009).

51. O'Connor, A. M. & Ross, J. R. H. The effect of O2 addition on the carbon dioxide reforming of methane over Pt/ZrO2 catalysts. *Catal. Today* **46**, 203–210 (1998).

52. Souza, M. M. V. M. & Schmal, M. Combination of carbon dioxide reforming and partial oxidation of methane over supported platinum catalysts. *Appl. Catal. A Gen.* **255**, 83–92 (2003).

53. Tomishige, K., Nurunnabi, M., Maruyama, K. & Kunimori, K. Effect of oxygen addition to steam and dry reforming of methane on bed temperature profile over Pt and Ni catalysts. *Fuel Process. Technol.* **85**, 1103–1120 (2004).

54. Neal, L. M., Haribal, V. P. & Li, F. Intensified Ethylene Production via Chemical Looping through an Exergetically Efficient Redox Scheme. *iScience* **19**, 894–904 (2019).

55. Ahari, J. S., Sadeghi, M. T. & Zarrinpashne, S. Effects of operating parameters on oxidative coupling of methane over Na-W-Mn/SiO2 catalyst at elevated pressures. *J. Nat. Gas Chem.* **20**, 204–213 (2011).

56. Elkins, T. W. & Hagelin-Weaver, H. E. Characterization of Mn–Na2WO4/SiO2 and Mn–Na2WO4/MgO catalysts for the oxidative coupling of methane. *Appl. Catal. A Gen.* **497**, 96–106 (2015).

57. El-Halwagi, M. M. Overview of Process Economics. in *Sustainable Design Through Process Integration* (ed. El-Halwagi, M. M. B. T.-S. D. T. P. I.) 15–61 (Butterworth-Heinemann, 2012). doi:10.1016/b978-1-85617-744-3.00002-3

58. Peters, M. S. & Peters, J. I. *Plant design and economics for chemical engineers*. *Engineering Economist* **5**, (McGraw-Hill New York, 1959).

59. Davis, R. *et al. Process Design and Economics for the Conversion of Lignocellulosic Biomass to Hydrocarbons: Dilute-Acid and Enzymatic Deconstruction of Biomass to Sugars and Biological Conversion of Sugars to Hydrocarbons*. *National Renewable Energy Laboratory-NREL* (National Renewable Energy Lab.(NREL), Golden, CO (United States), 2013). doi:10.2172/1107470

60. Linnhoff, B. & Boland, D. *A user guide on process integration for the efficient use of energy*. (Elsevier, 1982). doi:10.1016/0300-9467(83)80027-6

61. Albina, D. O. & Themelis, N. J. Emissions from Waste-to-Energy: A Comparison with Coal-fired Power Plants. in *Energy Conversion and resources - 2003* 169–184 (American Society of Mechanical Engineers Digital Collection, 2003). doi:10.1115/imece2003-55295